THE IMPACT OF GRAPHENE NANOPLATELET LOADING AND UREA HARD SEGMENT FRACTION ON MORPHOLOGY AND MECHANICAL PROPERTIES OF POLYUREA NANOCOMPOSITES

By

Demetrios A. Tzelepis

A DISSERTATION

Submitted to
Michigan State University
in partial fulfillment of the requirements
for the degree of

Materials Science and Engineering - Doctor of Philosophy

2025

ABSTRACT

Lightweighting of automotive and ground vehicles has facilitated the use of a wide range of materials such as high strength aluminum, advanced high strength steel alloys, ceramics along with various composites based on the desired application. This inevitably leads to multi-material joints, where fusion welding process is not possible. Adhesive bonding offers an alternative to fusion welding for mixed or multi-material joints. In military ground vehicle applications, these types of multi material joints not only undergo quasistatic and fatigue loading but also high strain rate events such as a mine blast and ballistic penetration. Adhesives that exceed 10.0 MPa in shear strength and a displacement failure greater than 3.81 mm are classified as 'Group-1 adhesives' as they exhibit excellent stiffness-toughness balance which are needed for high strain rate applications.

In this work a multidisciplinary approach (experimental and modeling) is used to elucidate the effect of the GnP on the processing (chemistry), structure (phase separation), and properties (quasi-static, and viscoelastic) relationship of PUa based nanocomposite. A model polyurea with hard segment weight fraction (HSWF) of 20, 30 and 40 percent was developed to explore the combined effect of HSWF and nano-additions of 0.5, 1.0 and 1.5 weight percent GnP on the quasi-static and viscoelastic properties. For model PUa formulation with higher HSWF the additions of GnP on quasi static tensile and viscoelastic properties were negligible but at lower HSWF some improvement was seen in the viscoelastic properties and simultaneously improvements in strength and ductility were seen. Despite the complexity of the phase separated microstructure of the PUa and the nanocomposite, time-temperature (TTS) super position was shown to be valid for both the neat PUa's and the PUa-GnP nano composite. Although the TTS shifts didn't fit Arrhenius nor the WLF models, they did fit a more recently developed two-state, two-(time) scale model.

Furthermore, a micro mechanical model utilizing fractional calculus-based modeling showed excellent correlation between the experimentally obtained TTS curves and the mechanical modeling for both neat and composite PUa. The micromechanical model developed utilizes a few physical properties such as modulus and relaxation time to predict material viscoelastic behavior instead of the conventional Prony series which has a large number of parameters with no relation to material properties. The micro-mechanical model parameters were evaluated at various nano-loading and hard segment weight fraction which showed that the effect of GnP was significantly less pronounced than the effect of HSWF.

In addition, Single Lap Joints were used for an initial exploration of multiple formulations from both a chemistry perspective (changing isocyanate type and diamine type) and a microstructural perspective (weight fraction of hard segments). Results indicate that Group-I adhesive with cohesive failures can be achieved with PUa, showcasing the potential of PU as an adhesive.

Overall, this work supports the feasibility of utilizing PUa's in adhesive applications. The detailed characterization of PUas with varying HSWF and GnP content shows that the HSWF had a far greater effect on the properties of PUa than the additions of GnP. GnP did not have adverse or detrimental effects on the performance of the PUa. Future work can explore the advantage of GnP in creating multifunctionality to PUa such enhancing thermal and electrical conductivity. At the same time, GnP showed significant improvement in PUas with low HSWF creating a wide range of potential applications for PUa based bonded joints. Future work should also explore the high strain rate behavior of the PUa bonded joints.

To my beloved wife Maria,
who sacrificed her career,
moved from Toronto
so that I may pursue a dream.

ACKNOWLEDGEMENTS

Glory be to God for all things!

In a way this thesis marks the end of a long academic career. It was definitely not the route that I intended for my life, but none-the-less, it is route that I took. It has been a long a difficult journey with its ups and downs, and the many delays, some of my own doing and some of circumstance. In retrospect, I would do nothing different! For, through this journey I learned a lot, and not just the "technical" but of myself.

I first would like to thank my family, especially my mother and father for their continuous support; they put me on this journey so long ago. I would like to thank my wife Maria for her patience, sacrifice, emotional support and encouragement during the last leg of my academic career. If it was not for her, I would not have finished. I would be remised not to thank all the financial support and encouragement from my leadership at US-ARMY GVSC, especially Dr. David Gorsich, Ms. Parminder Khabra, Mr. Micheal Foley, Ms. Amanda Mieksztyn and Mr. Brandon Pender. If it was not for the leave of absence, they granted me, this Doctorate would not have been possible.

I would like to also thank my committee Dr. Lawrence Drzal, Dr. Mahmood Haq, Dr. Valeriy Ginzburg, Dr. Andre Lee, and Dr. Jayaraman. Dr. Haq who encouraged and brought me to MSU, who gave me a home at CVRC. I know we started down one research path and ended somewhere else; it has been quite the ride, and I look forward to our future. Dr. Drzal for his infinite patience, and his technical advice on all things GnP and polymer composites. I especially would like to thank Dr. Ginzburg for without his knowledge of polymer physics, polyureas and modeling this thesis would not have been possible.

Additionally, I would like to thank Dr. Mohsen Zayernouri, Dr. Jorge Suzuki and Mr. Arman Khoshnevis for introducing me to the Fractional Maxwell Model and helping model the PUa system. It was my first foray into mathematical modeling of materials, and I look forward to our next steps. I would also like to thank Dr. Per Askeland, for running the XPS at CMSC and his SEM advice, Dr. Su, Dr. Wang and Dr. Lim at Oak Ridge National Laboratory for the TEM help. I am fairly certain I am forgetting to thank many additional people that helped me, especially my colleagues at work who had to endure my endless complaints. I look forward to the next stages of my research career.

Finally, to my brother Christ, I actually finished! There will be no more degrees after this.

Funding Acknowledgement: This work was funded by PPG Industries Inc, Grant/Award Number: 201825-140909, and an In-House Laboratory Independent Research (ILIR) grant from the US-Army Ground Vehicle System Center.

TABLE OF CONTENTS

Chapter 1 - Introduction

1.1 Motivation

Design engineers are constantly evaluating the use of multiple material classifications, such as high strength aluminum, advanced high strength steel alloys, ceramics along with various composites in combat vehicle design. This inevitably leads to multi-material joints, where fusion welding process is not possible or will lead to a less than desirable joining efficiency. Adhesive bonding offers an alternative to fusion welding for mixed or multi-material joints, especially in metallic joints where the two materials are not considered weldable through a fusion process such as aluminum to steel or steel to titanium and in some cases, it would be advantages to join composite materials to the metallic. In military ground vehicle applications, these types of multi material joints not only undergo quasistatic and fatigue loading but also high strain rate events such as a mine blast and ballistic penetration. As an example, a typical composite armor can be composed of layers of fibers laminates, ceramics, rubbers, and metals [1]. Jensen et al. illustrate the importance of adhesive bonding by stating that adhesive failure represents a significant portion of the global failure modes in ceramic integral armor panels and little understanding of the adhesives response during a ballistic event is known. In a second work in an attempt to start classifying adhesives for ballistic performance, Jensen et al define four categories of adhesives based on using a single lap joint (SLJ) shear test. The four categories are summarized as follows: Group I, with are Maximum SLJ strength (S_{max}) of $\geq$ 10 MPa and a displacement at complete failure of ($d_{failure}$) > 3.81 mm, Group II is defined as S_{max} > 10 MPa and 1.5 $\leq d_{failure}$ < 3.81 mm, Group III is defined as S_{max} greater than 10 MPa and $d_{failure}$ < 1.5 mm, and Group IV is defined as S_{max} < 10 MPa and no limit on $d_{failure}$ [2]. The four categories along with results from SLJ test of various adhesives classification are shown in Figure 1-1[2]. They continue by mentioning that both

high strength and low elongation to failure adhesives and low strength and high elongation to failure both demonstrate poor damage tolerance traits for army applications, but that Group I adhesives show optimal adhesive performance. This suggests that the goal is to develop adhesives that are in Group I of Figure 1-1, with excellent stiffness-toughness balance.

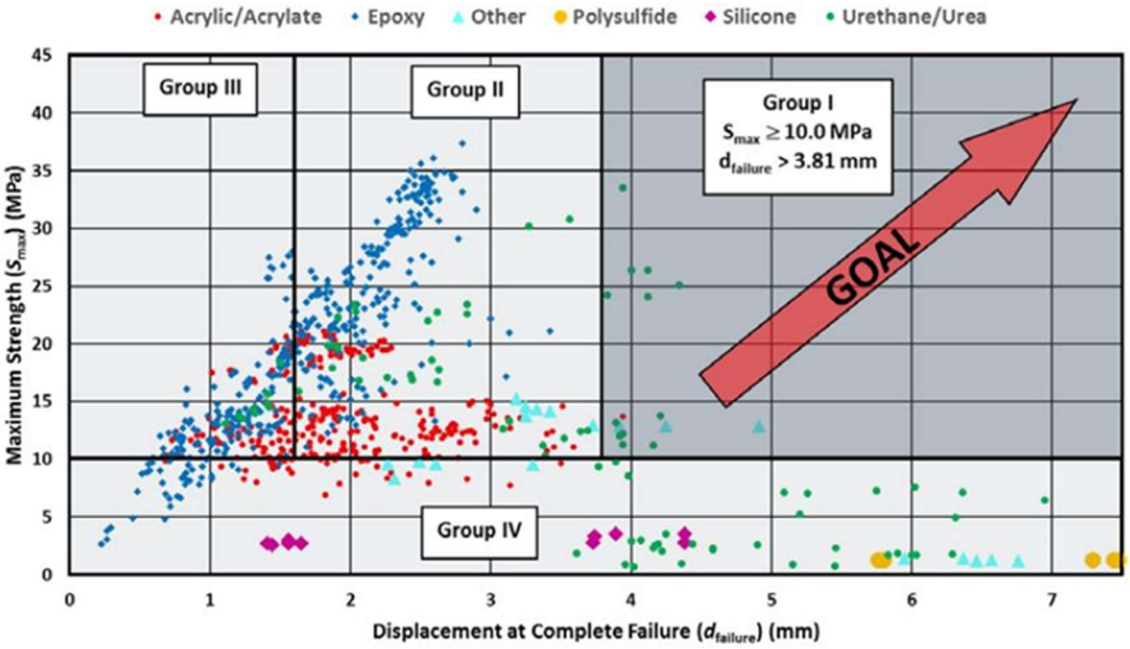

Figure 1-1. Adhesive grouping per ARL-ADEHS-QA-001.02 Rev1.0, including ARL experimental population of SLJ adhesive chemical classifications [2].

In most traditional material systems, ductility and strength are inversely related. When the system is modified to increase the strength, ductility is sacrificed and conversely when the system is modified to increase the ductility the strength is sacrificed. The balancing of strength and ductility can be thought of as toughness. Conceptually what is sought is a tougher adhesive by balancing the strength and ductility to increase toughness. From Figure 1-1 one can identify two approaches to achieving the desired outcome. First is to modify or toughen existing high-strength, low-ductility adhesives and the second is to strengthen the high-ductility, low-strength adhesives. Most of the current Group I adhesives are based on urethane/urea chemistry [2]. Thus, it is important to understand how to improve both stiffness and toughness of those materials. In

particular, one can consider two pathways – (1) optimization of the PU/PUa formulation and (2) addition of the hard nano- or micro-particles such as clay, graphene, metals, or a mixture of them.

1.2 Background

1.2.1 Polyurethanes – History, Chemistry and Application

Polyurethanes (PU), polyureas (PUa) and poly(urethane-ureas) (PUU), represent a class of polymers with a wide variety of applications. These include elastomeric coatings, adhesives, and sealants, as well as rigid foams for thermal insulation and flexible foams for furnishings and transportation industries [3]–[6]. Historically, PU's and PUa's were developed in the 1930s by Bayer. The initial works focused on the reaction between diisocyanates and diamines (PUa), later reactions between diisocyanates and glycol were explored. Commercial polyisocyanate became available in 1952 and soon after commercial scale production of PU, reaction between toluene diisocyanate and polyester polyols was realized. Development of PU, PUa formulations continued through the 60's and 70's with the development of polyether polyols and Poly(tetramethylene ether) glycol (PTMG) [7], [8]. In 1969, PUa Reaction Injection Molding technology was developed which culminated in the development of fully automotive body components in the 1980's. The advantage of using PUa and PUU over PU is the rapid gel times and dry times, which can be 2-3 seconds and less than 10 seconds respectfully. These two component systems have evolved into spray foam and coating technologies used in roofing, insulation, and linear systems [9].

In terms of defense industry applications, PUa's have been used as explosion resistant coatings (ERC) that can suppress the rupture of thick steel plates, or the spallation of masonry wall structures by dissipating the energy from the shock wave [10]. The mechanisms of energy dissipation in ERCs are related to the unique nanophase-separated microstructure, which will be

described later. The mechanisms include: 1) Shock-wave-induced hard domain ordering resulting from the hard-domain compaction and attenuating the shockwave. 2) Shock-wave-induced hard domain crystallization/densification where the hard domains experience an irreversible compaction and densification with an increase in their degree of order. Microstructural changes lead to the absorption of kinetic energy from the shockwave. 3) Shock-wave-induced hydrogen bond cleavage and formation where the hydrogen bond found in the urea linkages of the hard domains are cleaved, rearranged, and reformed when exposed to shock loading. 4) Viscoelastic stress relaxation within the hard-domains/soft matrix interfacial regions; the viscoelastic nature of PUa allows for the dissipation of large amounts of energy through the dissipation of heat. 5) Shockwave-capture-and-neutralization. Shockwave mitigation is not the emphasis of this work but a brief summary, with respect to multiphase materials, is offered here. The ability of material to mitigate shockwaves is related to width of the shockwave profile. In homogenous materials shockwave travels as a single wave (leading wave), but in a heterogeneous multiphase structure such as PUa's shock-waves form a two-wave structure, a leading shock wave followed by a more complex wave pattern that varies with time. This two-wave structure leads to additional shock wave attenuation in PUa [11].

1.2.2. Structure of Polyurethanes and Polyureas – A brief Overview.

A review of the materials science of polyurethane polymers, Polyureas, polyurethanes and their copolymers, polyurethane-urea and polyurea-urethanes, shows they represent a class of polymers that often exhibit a nanophase-separated structure, a hard phase (higher density, higher stiffness, higher glass transition temperature) and a soft phase (lower density, lower stiffness, lower glass transition temperature). The hard phase (comprised primarily of PU or PUa hard segments [HS]) can be percolated or dispersed. The soft phase (comprised primarily of the

polyether or polyester soft segment [SS] and some dissolved HS]) is usually a continuous or a co-continuous phase for those PUs and PUa's used in adhesives and coatings applications. In general, polyurethanes are purely a reaction between a polyisocyanate (typically a diisocyanate) and a polyol typically in the presence of catalysts [9]. The hydroxyl functional group of the polyol reacts with the isocyanate functional group of the isocyanate to form the urethane linkage as shown in Figure 1-2a. The urethane linkage results in a monodentate hydrogen bond, between the neighboring urethane linkages. Like polyurethanes, polyureas involve the reaction of a diisocyanate but in the case of a polyurea the polyol is replaced with a polyamine. Figure 1-2b shows the reaction between isocyanate functional group of the generic diisocyanate and the amine functional group of a generic polyamine to form the urea linkage. The urea linkage is bidentate; two hydrogens are available to form hydrogen bonds.

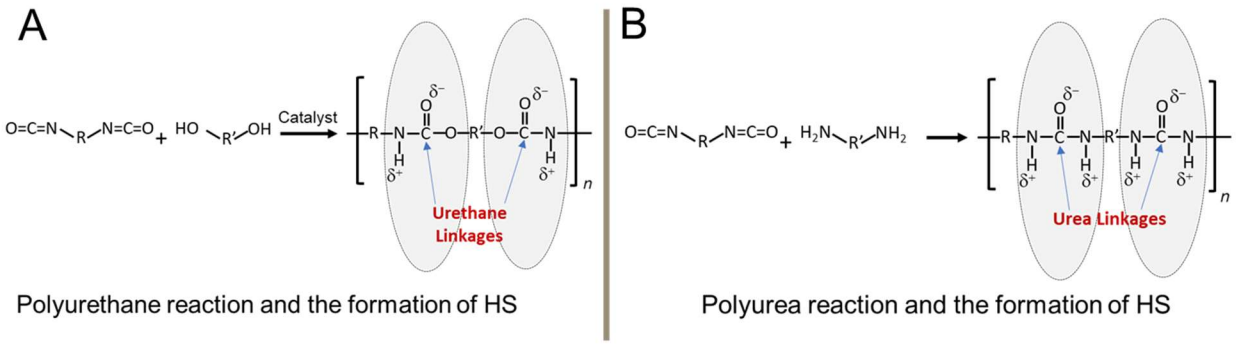

Figure 1-2. Schematic representation of the polyurethane and polyurea reaction and the formation of hard segments for polyurethane (A) and polyurea (B).

There are two potential production methods for polyureas/urethanes, a one-shot method and a prepolymer method [8], [9]. Both approaches utilize a step growth polymerization process. The one-shot method combines all reactants, the isocyanate, the amine/polyol and the chain extender in one step. This gives little control over the reaction sequence and the final structure depends on the relative reactivity of the various functional groups. The prepolymer method, which is typical of most industrial uses of polyurea, utilizes a two-step process. The first step is that the

diol or diamine is reacted with a large excess of a diisocyanate to form an isocyanate terminated pre-polymer. This prepolymer is then reacted with a chain extender and/or additional long chain diol or diamine. The prepolymer method allows for additional flexibility. Here, the diamine can be replaced with a polyol in the isocyanate terminated pre-polymer, a diamine or polyol, can be used as a chain extender and the final reaction can be a long chain diol or diamine. Note that utilizing diamine results in PUa hard segments that are exclusively made from these urea linkages. These urea linkages have two hydrogens which are available for hydrogen bonding with the oxygen from adjacent chains. In polyurethanes, the urethane linkages, have only one hydrogen available for hydrogen bonding with adjacent chains. Figure 1-3 compares the hydrogen bonding in polyurea to polyurethane. Polyurethane only has one available hydrogen for hydrogen bonding while polyurethane has two.

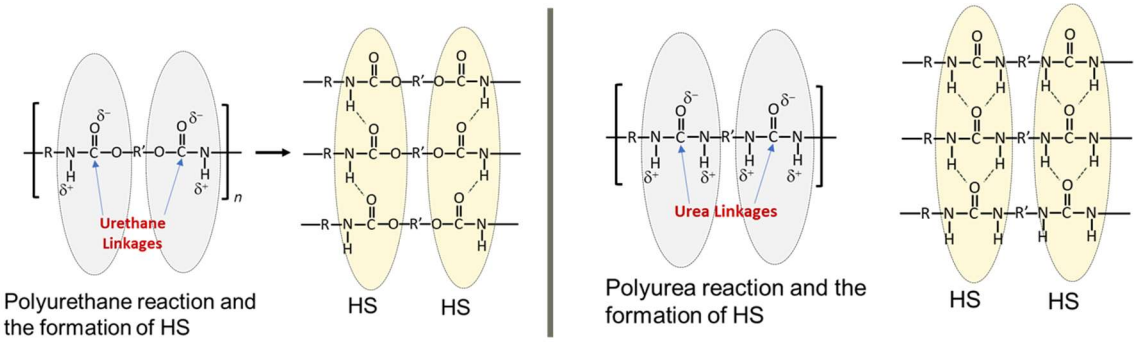

Figure 1-3. Comparison of the formation of hard segments in polyurethane and polyurea.

In polyurea and polyurethane systems, the percentage of hard segments and soft segments are defined with respect to the reaction chemistry. They are the total mass of the chemical constituents that react to form the hard segments divided by the total mass of the system. Equation 1.1 defines the percentage of hard segments (%HS)

$$\%HS = \frac{(m_{iso} + m_{cha\ \ extender})}{m_{iso} + m_{chai\ \ extender} + m_{amine}} \times 100 \qquad (1.1)$$

Here m_{iso} is the mass of the isocyanate, $m_{chain\_extender}$ is the mass of the chain extender and m_{amine} mass of the high molecular weight amine[1]. The percentage of soft segments (%SS) is defined as

$$\%SS = 100 - \%HS \tag{1.2}$$

In examing Equation 1.1, we can see that the % HS is equal to the mass reactants involved in the hard segment formation divided by the total mass of all components. Therefore there are only two methods to affect the percent hard segements when designing a formulation. The first one is to vary the molecular weight of the chemical constiuents involded in the reaction, i.e., increase or decrease the molecular weight of the soft segments. A decrease in the molecular weight of the soft segements will increase the amount of hard segments. A second method is to range the stoichiometric ratios of the isocyanate prepolymer (A-side) and the amine blend (B-side). The effect of these on the mechancial properties will be expolered in a later section.

In the polyurea the hard segments align to form hard domains. These hard domains are made from the urea/urethane linkages from the diisocyanate and chain extender reaction leaving the rest of the chain, the high molecular weight amine, to form soft domains [12]. Figure 1-4 shows a schematic representation for the formation of hard and soft domains which result in the phase segmented microstructure.

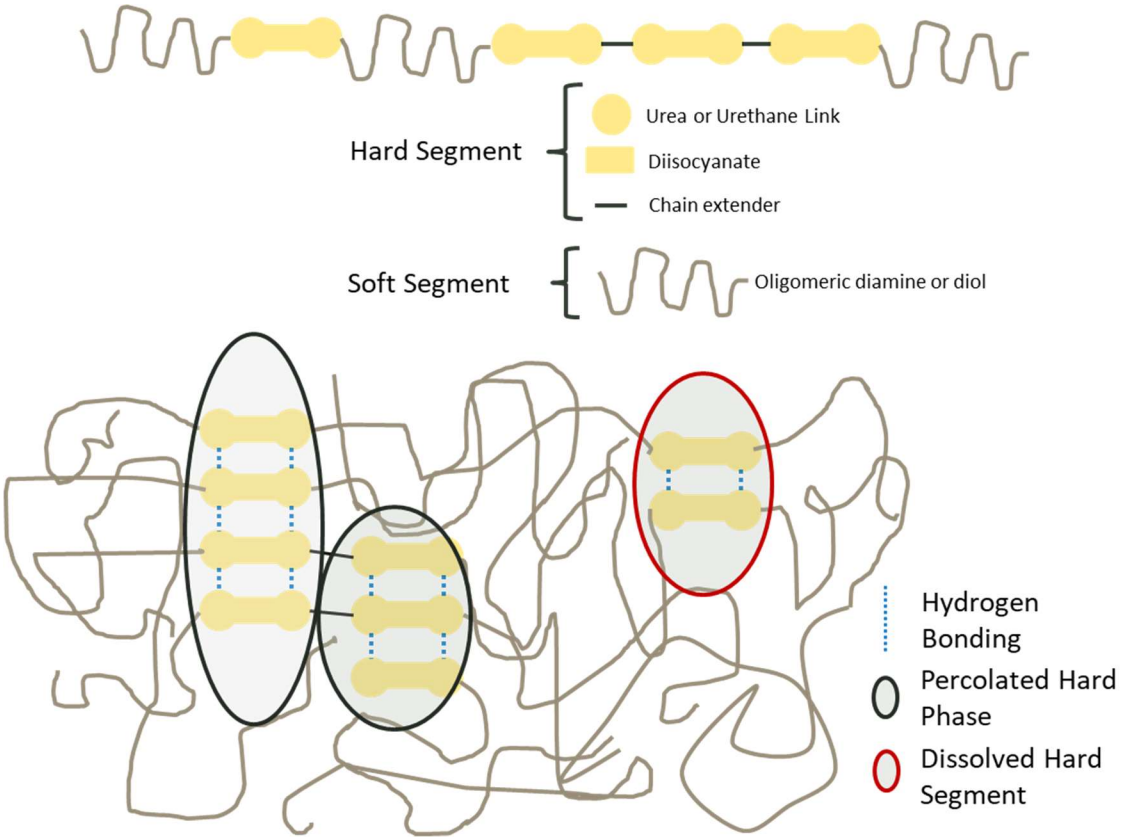

Figure 1-4. Schematic representation of the formation hard and soft domains which results in a phase segmented microstructure. Schematic adopted from He et al [12].

The hard segments align (due to the strong urea hydrogen bonding) to form hard domains in polyurea. These hard domains are made from the urea/urethane linkages from the diisocyanate and chain extender reaction leaving the rest of the chain, the high molecular weight amine, to form soft domains thus, creating a two-phase polymer solution. The schematic in Figure 1-4 shows the formation of hard and soft domains which result in the nanophase-separated microstructure. These microstructures have been observed by many research groups using transmission electron microscope (TEM) and atomic force microscopy (AFM) [13], [14]. As an example, Pangon et. al [13] studied the effect soft segment molecular weight, poly(tetramethylene oxide)-(PTMO), on microphase separation. He notes, through AFM, that the morphology of the hard domain depends on the molecular weight of the soft domains. For the higher molecular weight P1000 (1000 g/mol

PTMO), the structure of the hard domains is acicular/rod-like, but as the lower-molecular-weight polyol P250 (250 g/mol PTMO) is added, the morphology changes to a more spherical one [13].

Factors that can affect the microphase-separated structure are the polymerization method (one shot vs. prepolymer), concentration of hard segments within the soft domain, chemical structure of the chain extender, average chain length, and process parameters such as temperature, melting cooling rate, and solvent evaporation rates [15]–[17].

From a polymer physics viewpoint, PU and PUa's and their derivatives are considered A-B block copolymers where the A counterpart is the reaction between the isocyanate and the amine-based or hydroxyl-based chain extender which forms the hard segment, and the B counterpart is the polymer chain of the long chain diamine or polyol which forms the soft segment [18]. Their phase separation behavior and its associated nano-structure is defined by two factors, a composition parameter (f_A), which is the weight fraction of HS, and an incompatibility parameter, $\chi_{AB}(N_A + N_B)$, where χ_{AB} is the Flory-Huggins parameter, and $N_{A,B}$ are the chain lengths of the A and B block respectively. Following previous work [19]–[22], Agrawal and Drzal [23]–[25] used the difference in solubility between hard and soft blocks (segments) as the driving force for phase separation. In their work the calculated the Flory-Huggins interaction parameter, χ_{HS}, for the hard segments utilizing Equation 1.3.

$$\chi_{HS} = \frac{V_R}{RT}(\delta_H - \delta_S)^2 \qquad 1.3$$

where V_R is the reference molar volume, R is the universal gas constant, T is the temperature and δ_H and δ_S are the solubility parameters of hard and soft segments respectively. To determine if phase separation occurred, they compared it to a critical interaction parameter, χ_C, Equation 1.4.

$$\chi_C = \frac{1}{2}\left[\frac{1}{\sqrt{N_A}} + \frac{1}{\sqrt{N_B}}\right]^2 \qquad 1.4$$

where Na and Nb are the number of repeat units in polymer A (hard segments), and B (soft segments). If $\chi_{HS} > \chi_c$ then phase separation would occur. Their investigation of the phase separation behavior of PU on soda-lime glass showed that the PU at the interface of the PU and the soda-lime glass had different phase separation than the bulk PU. It was noted that PU at the interface was rich in the soft phase which affected the strength of the interface [23]–[25].

According to Matsen and Bates AB block copolymers have ordered phases that include spherical, cylinder and lamellar [26]. Furthermore, they state that it is the composition, i.e., the volume fraction (*f*) of block A, of the block co-polymer that controls the geometry of the structure. For a nearly symmetric diblock, $f \sim 0.5$ a lamellar structure occurs. At higher asymmetries, i.e., as *f* approaches 0 of A or 1 of B, a completely disordered structure exists. In between the disordered (D) phase and the lamellar (L) phase, the phase separation can form cylinders (C) or spheres (S) of the minor constituent. Ginzburg et al. approximated the phase diagram for a polyurethane using an A-B block copolymer model [27]. Equation 1.5 is used to predict the degree of phase separation and phase boundaries for the various regions of the phase diagram.

$$(\chi N)_i = (\chi N)_o \left(\frac{1}{1 - \frac{0.25 - f_i(1-f_i)}{0.25 - \alpha_i}} \right) \tag{1.5}$$

were $(\chi N)_i$ defines the boundary between the disordered-spherical (DS), SC (spherical-cylindrical) and CL (cylindrical-lamellar), *i* is the index for DS, SC and CL, $\alpha_i = f_i(1\text{-}f_i)$; $\alpha_{DS} = 0$, α_{SC}=0.098, a_{CL}=0.206. For block copolymers the prefactor $(\chi N)_0$ ranges 15-20, depending on the total number of blocks per chain. Equation 1.6 is used to estimate the Flory-Huggins interaction parameter (χ_{hs}) between the hard segments (h) and the soft segments (s).

$$\boldsymbol{\chi_{hs} = v_{ref}\left(\frac{(\delta_h - \delta_s)^2}{RT}\right) = v_{ref}\left(\frac{\left(\sqrt{(E_{coh})_h} - \sqrt{(E_{coh})_s}\right)^2}{RT}\right)} \quad (1.6)$$

where v_{ref} is the reference volume which was set to 58 cm^3/mol, δ_{hs} is the hard and soft segment solubility parameters, $(E_{coh})_{hs}$ is the hard and soft segment cohesive energy density. The chain lengths for hard and soft segments N_h and N_s are calculated by Equations 1.7 and 1.8 respectively.

$$N_h = \frac{\bar{M}_H}{2(\varrho_h v_{ref})} \quad (1.7)$$

where $\bar{M}_H$ is the number average molecular weight of the hard segments, ρ_h is the density of the hard segments and v_{ref} is defined above.

$$N_s = \frac{E_s}{2(\varrho_h v_{ref})} \quad (1.8)$$

where Es is the equivalent weight of the soft segment, ρ_s is the density of the soft segments and v_{ref} is defined above. The equivalent weight of the soft segment is simply the molecular weight of the soft segment (M_s) divided by the molecule's amine functionality (f_p). The number average molecular weight of the hard segments is calculated using Equation 1.9.

$$\bar{M}_H = 2E_s \frac{f}{(1-f)} \quad (1.9)$$

where f is the total hard segment weight fraction. Just like in polyurethanes, the prefactor of 2 reflects that fact that urea bonds consist of 2 amines and 2 isocyanates. Finally, the Flory-Huggins interaction parameter can be calculated using Equation 1.10.

$$\chi N = \chi_{hs}[N_h + N_s] = \frac{(\delta_h - \delta_s)}{RT}\left[\frac{\bar{M}_H}{2\rho_H} + \frac{E_s}{\varrho_s}\right] \quad (1.10)$$

Based on the above procedure, a phase diagram can be plotted where the interaction parameter can be plotted as function of weight fraction of HS (f_{HS}). The phase diagram model [27] is based on a simple polyurethane system where one component is used in the isocyanate prepolymer (A-side).

This model will be extended to a more complex PUa system to predict the phase separation behavior of the model PUa system developed in this thesis.

1.2.3. Mechanical Properties of Polyurethanes and Polyureas

The phase separation of PU and PUa, which is influenced by factors such as isocyanate type, chain extender type, non-percolated hard segments, soft segment molecular weight (chain length) and isocyanate and amine functionality, controls the mechanical properties. This was seen in O'Sickey's [15]–[17] work on polyurethanes where he showed an increase in the tenacity (toughness/resilience) with increasing hard segments regardless of soft segment chain length. Iqbal et al. published a series of studies that explored the above-mentioned properties of spray type and solvent cast formulations [28]–[32]. In their work, they varied many of the above variables. In "*Tuning the properties of segmented polyurea by regulating soft-segment length"* [29], Iqbal varied the percentage of hard segment by varying the soft segment molecular weight of poly(propylene) oxide PPO diamines and varying the molecular. They showed that increasing the percent hard segments increased the quasi-static tensile strength and decreased elongation of the polymer. They also explored the effect of the viscoelastic properties of PUa's through Dynamic Mechanical Analysis (DMA). They showed that a higher hard segment weight fraction (HSWF) resulted in a higher modulus in the glassy region, as well as a higher modulus in the rubbery region. Finally, they showed a shift in T_g as higher temperatures as the hard segments increased. Though these studies showed the effects of hard segments on PUa, they controlled the hard segment by varying the molecular weight of the soft segment thus confounding hard segment weight fraction with molecular weight. Dynamic mechanical analysis, and differential scanning calorimetry, showed only a small shift in T_g when compared to the previous paper. The crosslinking T5000 had no effect on the glassy region of the storage modulus but did increase the rubbery plateau slightly.

Fragiadakis et. al [33] varied the percentage of hard segments by varying the reaction stoichiometry of an MDI-PTMO based PUa system. The percentage of hard segments were 35.4, 33.9 and 32.7. They reported a 32 MPa increase in tensile stress and 6 MPa increase in the secant Modulus in tensile strength.

In, "l*arge deformation rate-dependent stress–strain behavior of polyurea and polyurethanes"* [34], Yi et al explored the large deformation and rate dependency behavior of a 37 wt% HS PUa and 3 PUs at 55, 54 and 44 percent HS. The polyurethanes, 55 % HS PU were made with 2,2-dimethyl-1,3-propanediol (DMPD) as the chain extender which results in a non-crystalline hard segment. The 44% and 54% hard segments PUs were made from 1,4 butanediol chain extender which results in crystalline hard segments. The isocyanate and polyol soft segments were the same for all the PUas. The PUa was an MDI-PTMO based PUa. They reported a strong strain rate dependency on the stress-strain behavior, utilizing split Hopkinson bar testing (SHPB). They showed that the flow stress taken at 0.15 and 0.30 strain increased with an increase in the strain rate for all the samples. A glass transition temperature shift effect was noted with strain rate by a change in the slope of the flow stress curves at strains between 10^2 and 10^3 1/s. It was also confirmed through DMA testing (1, 10, and 100 Hz) showing a T_g shift between 4 and 5 ^oC per decade of strain rate. In their study, the percentage of hard segment had little effect on the Tg shift, crystallinity of the hard segments had an incremental shift (0.1 ^oC/decade strain rate), the largest shift (0.6 ^oC/decade strain rate) was seen between the PUa and all three Pu's. This behavior was confirmed by Sarva, et al [35]. They studied the stress-strain behavior of the PUa and the non-crystalline hard segment (DMPD chain extender) across strain rates ranging from 0.001 s^{-1} to 10,000 s^{-1}. It should be noted that these are the formulations that show the largest Tg shift in the Yi et al paper [34]. The polyurea underwent transition from a rubbery-regime behavior at low rate

to a leathery-regime behavior at the highest strain rates, while the PU exhibit rubbery-regime behavior to glassy behavior at the highest strain rates. The fact that PUa's can avoid glassy behavior at high strain rates is one of the reasons why PUa's are utilized in high strain rate applications [36]. This Tg shift due to increasing strain rate, and corresponding mechanical behavior shift shows the importance of using a time-temperature super-position (TTS) principle to the DMA and corresponding relaxation time to explain the rheology PUa's and PU's through decades of frequency.

1.2.4. Rheology and Modeling.

In polymer science, rheology is the study of deformation or flow of a polymer (pre-gel or gelled state) under an applied force. For polymeric materials in both the liquid pre-gel state, and the solid viscoelastic state, polymer chain configurations such as large side groups, molar mass, chain entanglements, and other microstructural features such as polymer crystallinity, and multi-phase systems can influence the rheological properties of the polymer in both liquid and solid state. In the case of polymer solutions like polyurea and polyurethanes, the rheological properties, such as relaxation time (τ), are affected by the phase separation behavior which as previously discussed is affected by the relationship between hard segment and soft segments. Therefore, studying the rheological behavior of the polymer can give insight to its microstructure. Experimentally, rheological behavior can be characterized using small oscillatory testing such as Dynamic Mechanical Analysis (DMA).

DMA can be used to describe various transitions (T_g, T_β, etc.) of segmental motions of polymers. The segmental motions depend not only on temperature, but also on frequency. In many polymers, including PU's and PUa's the glass transition will shift with increasing or decreasing frequency. There are also limitations in the frequencies that testing equipment can achieve, at the

high frequency end and the time it takes to test a material at extremely low frequencies. For PUa's that are used in high strain rate applications, as previously noted, they undergo vitrification at higher strain rates. Time-temperature-superposition principle allows for developing modulus curves in a small range of frequency, typically two to three decades, at various temperatures and then shifting the curves along the frequency axis (x-axis) to develop a master curve at a chosen reference temperature [37]. Master curves are constructed using shift factors derived from the Williams, Landel, Ferry (WLF) equation, Equation 1.11.

$$log(\alpha_T) = \frac{C_1(T-T_r)}{C_2+T-T_r} \tag{1.11}$$

where α_T is shift factor and is equal to $\eta_T/\eta_{Ts}=\tau_T/\tau_{Ts}$ (η represents the viscosity and τ represents a characteristic segmental relaxation time), T is the test temperature of the frequency sweep, T_r is the reference temperature C_1 and C_2 are empirically determined constants [38]. The shift factor can also be described by an Arrhenius function, Equation 1.12.

$$\ln a_T = \left(\frac{E_a}{R}\right)\left(\frac{1}{T}-\frac{1}{T_r}\right) \tag{1.12}$$

where α_T is the shift factor, E_a is an apparent activation energy, R is the universal gas constant, T is the temperature of the frequency sweep and Tr is the reference temperature [38]. However, the WLF equation overpredicts the relaxation time below the T_g. Recently, the two state, two-time scale (TS2) has been developed to model the shift factor. The TS2 model describes the glass transition as smooth transformation between two Arrhenius-type regions. The shift factor is modeled by Equation 1.13.

$$ln(a_T) \equiv ln\left(\frac{\tau[T]}{\tau[T_o]}\right) = \frac{E_1}{RT} + \frac{E_2-E_1}{RT}\left(\frac{1}{1+exp\left\{\frac{\Delta S}{R}\left(1-\frac{T^*}{T}\right)\right\}}\right) - \frac{E_1}{RT_o} + \frac{E_2-E_1}{RT_o}\left(\frac{1}{1+exp\left\{\frac{\Delta S}{R}\left(1-\frac{T^*}{T_o}\right)\right\}}\right) \tag{1.13}$$

were E1 and E2 are activation energies (in J/mol), ΔS is a dimensionless transition entropy between the solid and liquid states of matter. T* is the transition temperature (K), and is typically approximated by the T_g, and T_o is the reference temperature of the TTS shifts [39]. The TS2 model captures the high temperature Arrhenius activation energy in E_1, a WLF-like region (apparent activation energy is very large and T-dependent), and a low-T Arrhenius activation energy in E_2, which deals with the low-T discrepancy between the WLF fit and experimental shift factors [39]. Through DMA and the TTS principle, master curves describing the polymer rheology or polymer stiffness can be developed and used to describe properties of the polymer microstructure. Specifically, these methods in conjunction with mathematical modeling can give us insight on the relaxation time (τ) and subsequent microstructural aspects such as phase separation.

Mathematically, constitutive modeling in rheology considers an elastic element typically described by a Hookean spring, and viscous element described by a Newtonian dashpot. In traditional modeling of viscoelastic materials both elements can be combined in either series, Maxwell, or in parallel, Voigt-Kelvin, to model the complexity of the polymer systems [38]. As an example, the Maxwell element the constitutive relationship between the shear stress and strain is,

$$\sigma + \frac{\eta_o}{G_o}\frac{d\sigma}{dt} = \eta_o \frac{d\gamma}{dt} \tag{1.14}$$

where σ is the shear stress, γ is the shear strain, η_o is the viscosity and G_o is the elastic modulus of the material. A time-dependent relaxation modulus *G(t)* can be derived by finding the stress response to an applied step strain function.

$$G(t) = G_o e^{\left(\frac{-t}{\tau}\right)} \tag{1.15a}$$

Where $\tau = \eta_o/G_o$ and represent a single relaxation time of the Maxwell model [40]. Note that the mathematical representation utilizes the shear modulus, but this can also be represented using the elastic modulus which is shown in Equation 1.15b.

$$E(t) = E_o e^{\left(\frac{-t}{\tau}\right)} \tag{1.15 b}$$

A Fourier transform of Equation 1.15b will result in Equation's 1.16 a and 1.16b which describe the effect of small oscillator deformations, such as what is utilized in DMA, on the moduli.

$$E'(\omega) = E_o \left(\frac{(\omega)^2}{1+(\omega\tau)^2}\right) \tag{1.16a}$$

$$E''(\omega) = E_o \left(\frac{(\omega\tau)}{1+(\omega\tau)^2}\right) \tag{1.16b}$$

Where E' and E" are the storage and loss modulus, ω is angular velocity and τ is the relaxation time. In Equations 1.14, 1.15, the viscoelastic model is represented by one single Maxwell element and one single relaxation time. However, complex polymeric systems cannot be described as a single element with a single relaxation time; more complex combination of elements in series or in parallel are needed [38]. This results in a spectrum of relaxation times describing the relaxation modulus, Equation 1.17,

$$E(t) = \sum_{i=1}^{n} E_i exp\left(-\frac{t}{\tau_i}\right) \tag{1.17}$$

or as a continuous function,

$$E(t) = E_{eq} + \int_{-\infty}^{+\infty} H(t)\, exp\left(-\frac{t}{\tau_i}\right) d(ln\tau) \tag{1.18}$$

Where E_{eq} is the relaxed (equilibrium) modulus and $H(\tau)$ is the relaxation time spectrum. For small oscillatory deformations, Equation 1.18 the dynamic moduli can be written as

$$E'(\omega) = E_{eq} + \int_{-\infty}^{+\infty} H(t) \frac{(\omega)^2}{1+(\omega\tau)^2}\, d(ln\tau) \tag{1.19}$$

$$E''(\omega) = \int_{-\infty}^{+\infty} H(t) \frac{(\omega\tau)}{1+(\omega\tau)^2}\, d(ln\tau) \tag{1.20}$$

Holzworth et al. utilized this methodology to explore the effect of isocyanate content on the relaxation times of various stoichiometric ratios of MDI-PTMO (Versilink P1000) PUa [41]. They found that relaxation spectrum begins to flatten as isocyanate content increased and that the equilibrium modulus also increased with increase in isocyanate content. Note that an increase in isocyanate content increases the percentage of hard segments.

Complex polymeric systems, such as those involving crosslink polymers [42], and soft glassy materials [43], are best described as a power-law in relaxation time i.e., the modulus is a proportional or equivalent to the relaxation time to an inverse power i.e., $G(t) \sim t^{-b}$ [40], [44]. To describe these "power-law" materials, multiple Maxwell and/or Voight elements are placed in series or parallel (like what is described above) to provide for the additional modes of relaxation time needed to characterize the materials response to an applied strain. In most cases a very large number of elements must be used to describe the material's viscoelastic response. From a modeling standpoint this becomes unwieldly and from a microstructural viewpoint it lacks any real physical meaning.

To simplify the modeling for "power-law materials", Scott-Blair (spring-pot) elements can be introduced. The Scott-Blair element can be thought of as spring-pot which interpolates between and Hookean spring and a Newtonian dashpot. Figure 1-5 shows the relationship between a Scott-Blair, Maxwell, and Dashpot elements [44].

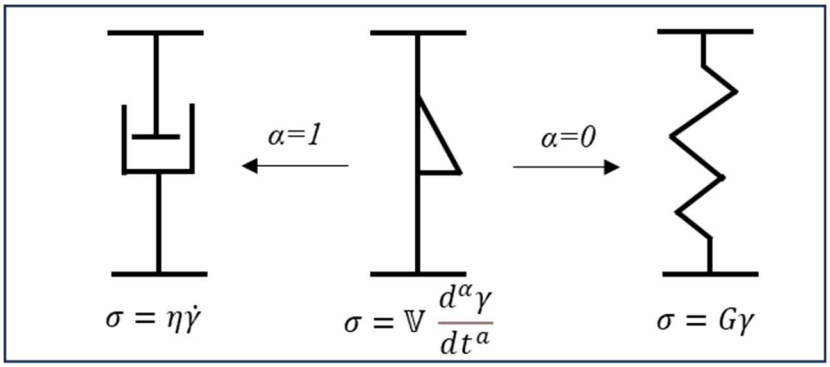

Figure 1-5. Schematic representation showing three different elements. The Scott-Blair element which interpolates between a dashpot and a spring.

The Scott-Blair element is described by the constitutive equation in terms of a fractional derivative, Equation 1.21.

$$\sigma(t) = \mathbb{V}\frac{d^{\alpha}\gamma(t)}{dt^{\alpha}} \tag{1.21}$$

Where $0<\alpha<1$, $\mathbb{V}$ is a quasi-material property, d^{α}/dt^{α} is a fractional derivative operator. Note that when $\alpha=0$, the Scott-Blair element reduces to a Hookean Spring with the quasi-material property, $\mathbb{V}$, equaling the modulus, and when the $\alpha=1$ the Scott-Blair element reduces to a dashpot with $\mathbb{V}$ is now the viscosity. The advantage of the Scott-Blair element is that only two parameters, $\mathbb{V}$ and α are required to characterize the material. By combining Scott-Blair elements more complex constitutive models can be developed. One such model is the fractional Maxwell model, FMM where two Scott-Blair elements are arranged in series, Figure 1-6.

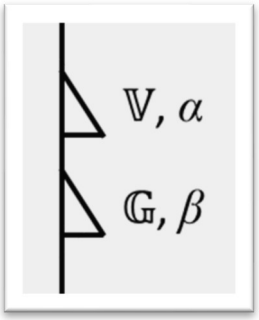

Figure 1-6. Schematic representation of an FMM utilizing two Scott Blair elements.

The intent here is not to give a detailed formulation of the Fractional Maxwell Model, as this has already been done in the literature [40], [44] but to show that the general form of the FMM, and its two limiting cases. Rathinaraj et al [40] utilized fractional calculus to develop a mathematical model, Equation 1.22 to describe the linear viscoelastic properties of multi-scale complex fluids.

$$\frac{E^*(\omega)}{E_o} = \frac{(i\omega\tau_c)^\alpha}{1+(i\omega\ _c)^{\alpha-\beta}} \tag{1.22}$$

were E^* is the complex elastic modulus, E_o is a characteristic modulus, τ_c is a characteristic relaxation time, α and β are power law exponents which can describe the spectrum of realization times. The real and imaginary parts can be split into the storage and loss modulus, Equations 1.23 and 1.24 respectively.

$$\frac{E'(\omega)}{E_o} = \frac{(\omega\tau_c)^\alpha \cos\left(\frac{\pi\alpha}{2}\right)+(\omega\tau_c)^{2\alpha-\beta}\cos\left(\frac{\pi\beta}{2}\right)}{1+(\omega\tau_c)^{\alpha-\beta}\cos\left(\frac{\pi(\alpha-\beta)}{2}\right)+(\omega\tau_c)^{2\alpha-\beta}} \tag{1.23}$$

$$\frac{E''(\omega)}{E_o} = \frac{(\omega\tau_c)^\alpha \sin\left(\frac{\pi\alpha}{2}\right)+(\omega\tau_c)^{2\alpha-\beta}\sin\left(\frac{\pi\beta}{2}\right)}{1+(\omega\tau_c)^{\alpha-\beta}\cos\left(\frac{\pi(\alpha-\beta)}{2}\right)+(\omega\tau_c)^{2\alpha-\beta}} \tag{1.24}$$

There are two limiting cases in the FMM, the first is the Fractional Maxwell Liquid (FML) where the exponent α is set to 1 and is used to describe complex fluid in the pre-gel state, and the Fractional Maxwell Gel (FMG) which describes the elastic behavior of viscoelastic materials beyond the gel point. Both the storage and loss modulus are defined by three parameters the characteristic modulus and characteristic relaxation time along with the exponents α and β. In the limiting case of the Fractional Maxwell Gel (FMG), the exponent β is constraint to 1.

Note the similarity between utilizing a continuum number of Maxwell elements (Equations 17a and 17b) and use of the FMM. Both determine a characteristic modulus, and both determine characteristic relaxation times. But in the case of an FMM a model can be built to explore multiphase systems where a single Scott-Blair element can be used to describe one phase and a second Scott-Blair element can be used to describe a second phase, with each element representing

the viscoelastic properties of its respective phase. In the context of this PUa and PU one element can represent the hard phase, and the second element can represent the soft phase. A third element representing a nano-filler such as GnP can be added to study the effect of the filler on the microstructure of PU or PUa.

1.2.5. Polyurethane, Polyurea Composites – the Impact of Nanofillers

Fillers, such as carbon nanotubes (CNT), nano-clays, chopped glass fiber, exfoliated graphene nanoparticles (GnP), and graphene oxides, alumina (Al_2O_3), and silica, have been used as reinforcing particles for polymers for a very long time. These various nanoparticles can improve mechanical properties, especially the modulus. Additions of graphene and its derivatives can also affect electrical, thermal, and mechanical properties of the composites as compared to the pristine matrix [45]. As an example, Zhao et al. investigated the use of graphene (prepared through a graphene oxide reduction route) in Poly(vinyl alcohol) composites [46]. They showed that the addition of up to 1.8 vol% of graphene resulted in a 150% improvement in tensile strength and nearly 10 times increase in the Young's modulus. Interestingly, the additional increase in the graphene loading did not result in any further increases in the tensile strength. The increase in strength was coupled, however, with a decrease in ductility as seen through a drop in percent elongation. The authors were able to demonstrate that the graphene nanosheets were fully exfoliated and well dispersed in the PVA matrix. The experimental modulus was compared to Halpin-Tsai [47] equations for both unidirectional and randomly distributed filler-reinforced composite. The experimental results were in a good agreement with the Halpin-Tsai randomly distributed particle model for up to 0.6wt% and then slightly deviated toward unidirectional, at about 2.0 wt%, and finally deviating back towards the randomly distributed at 3.0 wt%, indicating that the graphene was well distributed throughout the polymer [46].

Yadav and Cho studied the effect of a 4-aminophenthyl alcohol functionalized and non-functionalized graphene nano-plates (pristine GnPs with thickness and length values of 5 nm and 20 μm respectively) on a single PU formulation. Nano-particle loading ranged from 1 to 2 wt% [48]. They showed a similar increase in modulus between functionalized and non-functionalized and nano-graphene, indicating that both were well dispersed. The fracture stress for both nano-particle conditions showed a 35% increase in the functionalized nano particles while only an 8% increase in the non-functionalized. Both conditions showed a decrease in fracture strain. Both nano-particle conditions did show an increase in thermal stability, through TGA measurements, with the functionalized GnP showing a 30% shift at 50% weight loss. The non-functionalized GnP showed a smaller shift. The shift was attributed to graphene fillers acting as thermal barriers in the polymer matrixes and for the functionalized GnP a strong interaction between with the polymer matrix which was confirmed with SEM images. Finally, DSC showed that both functionalized and non-functional GnP shifted the crystallization temperature to higher temperature suggesting a role of graphene as nucleus from which crystallization of PU initiates.

Rana et al. investigated the effects of graphene (GnP) and CNT addition to polyurethane [49]. The pristine polyurethane had approximately 40% HSWF. Increases in both stiffness and strength as well as a significant loss in elongation was seen. In their work the nanoparticles were not functionalized but underwent a long (12 hour) ultrasonication process. Which did affect the nano particles as seen through Raman spectra and XPS. XPS showed oxygen containing functional groups on the graphene surface. Note in this study no chain-extension was used for the nano composite only for the neat PU and the weight ratios between the diisocyante and the polyol were maintained throughout all the formulations. This would hint that at least some the oxygen containing functional groups would react with the diisocyanate forming a crosslink between the

hard segments, but not the soft segment, since no isocyanate functionalization was seen in the GnP. In both CNT and GnP nano composites a shift in the crystallization temperature to lower temperatures along with an accompanied drop in heat of crystallization (ΔH_c) was seen in the DSC thermograms, which the authors noted was due to the cross-linking effect.

Qian et al. investigated the additions of both graphene and graphene-oxide (GO) to PUa. In this case the PUa was synthesized from IPDI and D2000 with a DEDTA chain extender [50]. The base PUa had a hard segment content of 29 %. The nano-composite films were made through a solvent cast process (DMF was used as the solvent). The nano particles were added to the DMF and sonicated at room temperature. The IPDI was introduced into the mixture for 5 hours. Finally, the D2000 was added, and the solution was cast. Although not stated by the authors the order of addition of IPDI and D2000 may influence the synthesis, since the IPDI may react with the hydroxyl groups of the GO or the graphene. The mechanical properties of the PUa composites are shown in Table 1-1. Additions of 0.2 and 0.5 wt% graphene increased the tensile strength of the PUa. Note that the addition also increases the elongation; this is counter-intuitive since most materials lose ductility with increase in strength. Note that the GO additions degraded the properties of the PUa. DMA was also used to evaluate the effect of the nano particles. They report an over 30% increase in storage modulus for the PUa-GO 0.2 and 0.5 wt% nano-composites at -75 ^{o}C, in the glassy region of the storage modulus curve. The graphene additions showed improved storage modulus in the low and high temperature regimes (glassy and rubber region). They attributed this to the good dispersion and the strong mechanical strength of graphene. The authors explored the interaction between the nano-particles and the PUa using DSC. For the graphene PUa composite they noted a shift in Tg to higher temperatures (~1 ^{o}C) over the neat but for the GO nano-composite it shifted to lower temperatures (~0.5 ^{o}C). The claim the Tg shift is in

accordance with the DMA and tensile results. They suggest the incorporation of the GO the movability of the PUa molecules. Finally, SEM images showed good dispersion and no agglomeration of the nano-particles.

Table 1-1. Mechanical properties of PUa neat and nano-composite at various loadings.

Samples	**Component**	**Tensile Strength (MPa)**	**Elongation (%)**
PUa	Neat	13.0 +/- 1.9	609 +/- 26
PUa/graphene-0.2	0.2 wt% Graphene	23.6 +/- 1.9	735 +/- 32
PUa/graphene-0.5	0.5 wt% Graphene	21.3 +/- 0.9	751 +/- 34
PUa/graphene-1	1 wt% Graphene	17.5 +/- 0.8	697 +/- 21
PUa/graphene-2	2 wt% Graphene	14.1 +/- 0.7	603 +/- 28
PUa/GO-0.2	0.2 wt% GO	13.8 +/- 1.8	631 +/- 35
PUa/GO-0.5	0.5 wt% GO	9.2 +/- 1.1	462 +/- 18
PUa/GO-1	1.0 wt% GO	5.8 +/- 0.9	311 +/- 23
PUa/GO-2	2.0 wt% GO	3.6 +/- 0.8	129 +/- 12

In a follow up second paper Qian et al compared the same PUa formulation accept this time synthesized nano-composite from GO and GO-functionalized with D400, which is a lower molecular weight diamine [51]. Through FTIR and XPS they showed successful grafting of the D400 to the GO. In this case the f-GO increased the strength of the nano-composite but only by 30% over the neat. This was significantly better than the 43 % decrease when comparing the PUa neat to the PUa non-functionalized GO. It is important to note here that the f-GO was not as effective as the PUa graphene nano-composite in the previous study which had an 82 % increase in tensile strength. In this study the Tg was measured as the peak of tan δ curve form DMA. They report shift to lower temperatures for the GO but to slightly higher temperatures f-GO. The authors interpret this as a measure of single sheet morphology and surface modification of the GO "afford better interaction with the PUa matrix compared to the un-modified."

Finally, Toader et al look at various loadings of epoxy functionalized multi-walled carbon nano tubes (MWCNTs) in a PUU [52]. The PUU was MDI based PUU with a mixture of

poly(propylene glycol) PPGs the soft segment and the 4,4'-diaminodiphenylmethane (DADPHM) as the chain extender. (Note the weight of each constituent during the synthesis is not reported therefore the percentage of hard segments cannot be calculated nor were the stated in the paper). Two molecular weights of the PPG were used 2000 and 4000 g/mol. As with the previous studies the mechanical properties increased with additions of the f-MWCNTs. The lower molecular weight PPG nano-composite had maximum of 27% increase in tensile strength and a 71% increase in modulus at a 0.2 % nano-loading f-MWCNT. For the high molecular weight PPG the increases were similar. Two T_g's reported for both PUU formulations. They speculated that the low the low temperature T_{g1} (-55 ^oC to -63 ^oC) is related to the soft segment and the higher temperature T_{g2} (5 ^oC to 10 ^oC). For the lower molecular weight PPG based PUU only a 0.2 ^oC shift was seen for T_{g1}, but a more significant shift (9.2 ^oC) was seen in the higher molecular weight samples for T_{g1}. The shift in the T_{g1} is also seen in the DMA curves, compare the PUU higher molecular weight neat vs its corresponding f-MWCNT, where a shift in the max of the loss modulus was seen to higher temperature implies a that the MWCNTs could also hinder the mobility of the polymer chains.

There has been a great deal of work incorporating nanoparticles into PU and PUa and their derivative's. Various nanoparticles have been used in both the pristine state and the functionalized state. All show that when properly mixed the mechanical properties will increase to varying extents, but few papers have studied the effect of adding nanoparticles to the phase separation behavior of the PUs and PUa. As shown earlier the phase separation behavior drives the microstructure which in turn drives the mechanical properties of the PU and PUa.

1.3 Objectives

The intent of this work is to improve the fundamental understanding of the structure-property relationships in polyureas and their composites and to use the new knowledge for the design of better adhesives. The overall objectives can be summarized by the following questions:

- Do additions of GnP to polyurea impact the overall mechanical performance?
- Despite the microstructural complexity of polyurea and especially the nano-composite can the time-temperature-superposition principle be applied and can a mathematical model be developed to help elucidate the combined effect of HSWF and GnP additions?
- If one considered PUa's as a composite of hard domain and soft domains, which has a greater effect on the mechanical property's variation in HSWF or additions of GnP, and can the work synergistically?

1.4 Method / Approach

In this work a multidisciplinary approach (experimental and modeling) is used to explore the effect of the GnP on the processing (chemistry), structure (phase separation), and properties (quasi-static, and viscoelastic) relationship of PUa based nanocomposite. We begin experimentally being exploring the effect of isocyanate and diamine type on single lap joints utilizing a two-part adhesive cartridge with a 50:50 by volume ratio of isocyanate prepolymer (A-side) to amine blend (B-Side).

A solvent cast PUa formulation has been developed and analyzed. The base polymer is comprised of the isophorone diisocyanate (IPDI), diethyl-toluene-diamine (DETDA) chain extender, and Polyetheramine Jeffamine D2000 and D5000 diamines as soft segments. The hard segment weight fraction (HSWF) is varied by changing the ratio of isocyanate (IPDI) and the

diamine (T5000) in the prepolymer (A-side) and the weight percentage of chain extender (DEDTA) and diamine (D2000) in the amine blend (B-side).

Three separate polymers with hard segment levels of 20, 30, and 40 percent have been synthesized, and each formulation was characterized using DMA, DSC, FTIR, TGA, and tensile testing. To understand mechanical properties, and specifically linear viscoelasticity measured by DMA, a new micromechanical model was developed. The model is based on the fractional Maxwell model (FMM) in which a fractional Maxwell gel (FMG) element describes the contribution of the percolated hard phase and a second FMG that of the filled soft phase. For the first time, the model can successfully describe linear viscoelasticity of polyurethane-type material in a broad range of temperatures and frequencies. The model parameters such as the modulus, the characteristic relaxation time (τ_c), and the FMG Scott-Blair power-law exponent (α) have been shown to depend substantially on the hard segment fraction and relate to the polymer morphology. DSC, FTIR, and TGA confirmed these results.

Additions of GnP will be made at three levels -- 0.5, 1.0 and 1.5 weight percent. The composites were characterized in the same way as the neat polymers in the earlier study. For the DMA results, the fractional Maxwell model was utilized to determine the effect of the GnP on the FMG parameters.

1.5 Organization

- The dissertation has been organized in five chapters. The first chapter introduces the work with a brief background, scope, and objectives of this work.
- Chapter 2 explores PUa as adhesive through the utilization of a two-part adhesive cartridge. Here the HSWF is varied and the effects of HSWF on the single lap joint are reported. Additions of GnP to PUa are made and results are reported.

- Chapter 3 reports on the development of a solvent cast PUa with varying HSWF. Solvent extraction is tracked through TGA, and curing is tracked through DMA. The structure-properties relationship of the PUa is explored through DSC, DMA and tensile testing.
- Chapter 4 reports on the development of a solvent cast nanocomposite with three different GnP loadings (0.5, 1.0 and 1.5 wt%). The structure-properties relationship of the PUa is explored through DSC, DMA and the tensile testing and the results are compared to the neat PUa at identical HSWF.
- Chapter 5 lays out the mathematical modeling framework for the characterization of the viscoelastic properties. The time-temperature-super position (TTS) principle along with a novel approach in materials modeling using fractional calculus is used elucidate the visco-elastic properties of neat and filled PUa.
- Chapter 6 provides concluding remarks, future research needs and recommendations.

Chapter 2 - Polyurea Based Adhesives

2.1 Introduction

In this chapter single lap joints (SLJ) were used to study the effect of hard segment weight fraction (HSWF) on two polyurea (PUa) type adhesives. Nanocomposites of the same PUa formulations were manufactured using GnP and characterized using the SLJ, Dynamic mechanical analysis (DMA), Fourier-transform infrared spectroscopy (FTIR), and differential scanning calorimetry (DSC).

The first PUa is a novel Isophorone diisocyante (IPDI) based PUa where the ratio of chemical constituents was varied to control the hard segment weight fraction (HSWF). A two-component adhesive extrusion cartridge with a bayonet style static mixing nozzle was utilized to mix and apply the adhesive. The A-side of the extrusion cartridge was the isocyanate prepolymer. This was obtained in a separate reaction vessel in which the isocyanate was partially reacted with an amine blend of (high molecular weight diamine and triamine) to obtain an isocyanate prepolymer. The B-side of the cartridge is a second amine blend which contains a diamine chain extender and the high molecular weight diamine. The reaction of the A-side and B-side occurs very rapidly, in the static mixing nozzle, during the adhesive application.

A second methylene diphenyl diisocyante (MDI) based PUa was also studied. The MDI based PUa was also a two-part method, but the reaction was slow enough not to utilize the two-part adhesive cartridges. In this case the MDI used is a polycarbodiimide-modified diphenylmethane diisocyante prepolymer (DOW143LP) product which is an isocyanate prepolymer manufactured by DOW Chemical Corporation. The amine on the B-side was poly(tetramethylene oxide) (PTMO) based diamine. The molecular weight of the diamine was varied to achieve three different levels of HSWF.

Adhesive bonding should be designed with a systems level approach considering the substrate, its surface preparation, adhesive type, etc., This research is primarily focused on the adhesive type and not the substrate surface chemistry, therefore substrate surface chemistry is not optimized or addressed in this research, except to ensuring cohesive failure in the SLJ. Two different surface treatments on the aluminum substrate were used. The first is per ASTM D2651 and the second was an automotive electrophoretic (e-coat) coating. PUa is used as an automotive coating such as a truck bed liner. These components are typically e-coated therefore it would be the most likely surface treatment to produce cohesive failure of the adhesive joint and hence considered for this work.

2.2 Polymer Synthesis and Lap Joint Construction

2.2.1 Polymer Synthesis

In this chapter two different PUa formulations were explored. The first is a novel formulation IPDI formulation, where the HSWF was varied from 20% to 40% HS by varying the relative amounts of isocyanate, amine chain extender, and the amine blend.

In formulating the polyurea compositions, two basic conditions must be met. The first is that the reactive mixture should be close to stoichiometric ratio, and the second is that the volume ratio of Isocyanate prepolymer (A-side) to amine resin blend (B-Side) should be close to unity [31]. The following was the method used to formulate experimental polyureas. It was based on a technical bulletin published by Primeaux Associates LLC [53]. In this report, the IPDI-2K-20HS formulation is illustrated as an example, and all other formulations were designed in a similar manner. The isocyanate component, (a quasi-prepolymer) was calculated first. In this formulation, the (A-side) quasi prepolymer is a reaction between IPDI plus Jeffamine D2000, and T5000 blend at a 1:4 ratio T5000:D2000. The initial input values for the mass of isocyanate (m_{iso}), the mass of

T5000 (m_{T5}), and the mass D2000 (m_{D2}) are arbitrary but the ratio of 1:4 by weight of triamine to diamine was maintained. Table 2-1 shows the input and initial results of the isocyanate prepolymer.

Table 2-1. Initial and final results of the isocyanate prepolymer.

Component	Molecular Weight (g/mol)	Percent by Weight (PBW)	Equivalent Weight	MEQ	Specific Gravity (g/ml)	Volume (ml)
IPDI	222	40	111	360.4	1.06	37.7
T5000	5000	12	1666	7.20	0.997	12.0
D2000	2000	48	1000	47.9	0.991	48.4

Using Equation 2.1 the equivalent weight for each component is calculated.

$$MEQ = \frac{PBWx1000}{Eq.\ Wt} \tag{2.1}$$

where MEQ is the milliequivalent, PBW is the percent by weight of each component, and Eq. Wt is the equivalent weight of each component. The equivalent weight is the molecular weight of the component divided by its functionality. In the case of the diamine and the IPDI, the functionality is 2 and for the triamine the functionality is 3. Equation 2.2 is used to calculate the total MEQ.

$$MEQ(Total) = MEQ\ for\ IPDI - (MEQ\ D2000 + MEQ\ T5000) \tag{2.2}$$

Equation 2.3 calculates the MEQ on a per gram basis.

$$MEQ/g = MEQ(Total)/PBW(Total) \tag{2.3}$$

where PBW(Total) is the sum of PBW of each individual component in the prepolymer. Note that the sum of PBW can exceed 100 for these calculations. The actual formulation weight percent will be determined once the system is balanced. This also applies to the Amine Blend calculations. The Eq.Wt. of the prepolymer is calculated using Equation 2.4.

$$Eq.WT(prepoly.) = {(PBW(total) \times 1000)}/{MEQ(total)} \quad (2.4)$$

The % NCO is estimated using Equation 2.5 and the specific gravity of the prepolymer is calculated using Equation 2.6.

$$\%NCO = \frac{MEQ}{g} \times \frac{42g}{eq} \times \frac{1eq}{1000\ MEQ} \times 100\% \quad 2.5$$

$$S.G = \frac{PBW(total)}{V(total} \quad 2.6$$

where S.G. is the specific gravity and V is the total volume of each component.

For the amine blend only two components were used, the Jeffamine D2000 and DETDA as the chain extender, both are diamines with a functionality of 2. Again, an arbitrary value for the chain extender is chosen to facilitate the calculation for the 1:1 volume ratio. The milliequivalent for the individual components of the amine blend are calculated using Equation 2.3, and the total milliequivalents for the amine blend is calculated using Equation 2.7. This is based on the total PBW for the amine blend which was arbitrary. To obtain the MEQ for 100 PBW a simple ratio is used, see Equation 2-8.

$$MEQ(Total) = MEQ_{D2000} + MEQ_{DETDA} \quad (2.7)$$

$$\frac{MEQ(Total)}{PBW(arbitray)} = \frac{MEQ(100)}{100} \quad (2.8)$$

The specific gravity (SG) for the amine blend is calculated by Equation 2.9.

$$SG(amine\ blend) = {PBW(Arbitray)}/{Volume(total)} \quad (2.9)$$

Table 2-1 and Table 2-4 summarize the inputs and results for the sample calculations for the amine blend.

Table 2-2. PUR adhesive Side B Materials: Summary of sample calculation for amine blend.

Component	Molecular Weight (g/mol)	Percent by Weight (PBW)	Equivalent Weight	MEQ	Specific Gravity (g/ml)	Volume (ml)
D2000	2000	90	1000	89.8	0.991	9.8
DEDTA	178	10	89	112.4	1.022	90.8

As previously mentioned, for the polyurea systems a 1:1 volume ratio of isocyanate prepolymer (A-side) to Amine Blend (B-Side) was used. While the isocyanate-amine stoichiometry is desired in theory, in practical applications it is common to have a slight excess of isocyanate, i.e., isocyanate index i_{iso} » 1.05. For these calculations we start with the assumption that we have 100 PBW amine blend. Therefore, the mass of isocyanate need is described by Equation 2-10.

$$m_{iso\_blend} = {(i_{iso} \times MEQ(total\ resin) \times EqW(iso\_prepoly))}/{1000} \quad (2.10)$$

Where m_{iso_blend} is the mass of isocyanate prepolymer, i_{iso} is the isocyanate index, MEQ(total resin) is the milliequivalents of the resin, and EqW(iso_prepoly) is the equivalent weight of the isocyanate prepolymer. From this the isocyanate:amine blend weight ratio was calculated using Equation 2.11.

$$Iso{:}\,Amine\ Weight\ Ratio = {m_{iso\_blend}}/{m_{amine\_blend}} \quad (2.11)$$

Using Equation 2-12 we can calculate the Isocyanate to amine volume ratio.

$$Iso{:}\,Amine\ Volume\ Ratio = {(Iso{:}\,Amine\ Weight\ Ratio \times SG(amine)}/{SG(iso)} \quad (2.12)$$

If the volume ratio is not 1.00, the composition can be modified to obtain a volume ratio of 1.00. The percent hard segment (%HS) can be calculated using Equation 2-13.

$$\%HS = \frac{(m_{iso}+m_{chain\ extender})}{m_{iso}+m_{chain\ extender}+m_{amine}} \times 100 \quad (2.13)$$

Table 2-1 summarizes the initial and final results based on the inputs and calculations from Tables 1 and 2.

Table 2-3. PUR adhesive sample calculations. Results of the first and last iterations from Excel spreadsheet and the goal seek function in Excel.

Iteration	%NCO	S.G of Isocyanate Prepolymer	m_{iso_blend}	Iso to Amine Weight Ratio	Iso to Amine Volume Ratio	%HS
1 (Initial)	12.8	1.02	69.5	0.695	0.678	22.3
Final	8.73	1.01	102.1	1.02	1.003	20.2

In the first iteration the volume ratio is not 1.00 therefore the PBW for the IPDI, D2000 T5000, and DETDA were adjusted until the volume ratio is equal to 1.00. A third constraint is added to this calculation. The percent hard segment was targeted to be approximately 20%. The most efficient way of finalizing the formulation design is to set up a spreadsheet in Microsoft Excel where the goal seeker function can be used to adjust the component weights until the desired hard segment content is obtained, while simultaneously keeping the volume ratio to 1:1. Multiple iterations of the calculations were conducted until desired results were obtained. Table 2-4 shows final target composition of the IPDI formulations.

The reactants used in formulating the novel PUa were IPDI-Vestanat which was obtained from Evonik Corporation. Jeffamine T5000 and D2000 polyetheramines were obtained from the Huntsman Corporation. The diethyltoluene diamine (DETDA) (Lonzacure) was obtained from Lonza and was used as the chain extender.

Table 2-4. Summary of chemical constituents and quantity used in the IPDI based PUa using the two-part adhesive cartridge system.

	Component	IPDI-2k-20HS	IPDI-2k-30HS	IPDI-2k-40HS
Isocyanate Prepolymer (A-Side)	**IPDI**	30.8	41.6	52.1
	T5000	14.5 g	12.1 g	10.1 g
	D2000	57.1 g	48.5 g	40.4 g
	%NCO	14.5	12.1	10.1
Amine Blend (B-Side)	**DETDA**	10 g	19.4 g	29.3 g
	D2000	90 g	80.6 g	70.7 g
Processing	**Index**	1.05	1.05	1.05
	Iso:Amine Vol.	1.00	1.00	1.00
	Iso:Amine Wt.	1.02	1.02	1.17
	%HS	20.2 %	30.2 %	40.0 %

The polyurea prepolymer was made by placing the required amount of IPDI into a double walled reactor. The amine blend (Jeffamine T5000 and D2000) for the prepolymer was mixed for 5 minutes in a separate 250 ml beaker at room temperature followed by degassing for approximately 10 minutes. The amine prepolymer blend was poured into an addition funnel. The reactor was assembled and then a vacuum was drawn for five minutes, after which N_2 gas at 0.3-0.4 l/min flow rate was introduced to the reactor. The reactor temperature was raised to 80 ^{o}C and then the A-side amine blend was added dropwise under mechanical stirring at 120 RPM. The solution was stirred for an additional hour at 80 ^{o}C after the last drop of the A-side amine blend was added. The reactor was tapped and the IPDI-base prepolymer was placed in a glass container, degassed for 10 minutes and capped. The amine blend for the B-side, a mixture of the Jeffamine D2000 and Lonzacure DETDA, was mixed for 5 minutes in separate 250 ml beaker. The amine blend was

then poured into a glass container and followed by vacuum degassing for approximately 10 minutes.

Using a syringe, 25 ml of the prepolymer and 25 ml of the B-Side amine blend were carefully drawn so as to not create any air pockets and placed into a two-component adhesive extrusion cartridge. A standard Bayonet type 20 element static mixer was placed on the cartridge and the adhesive was applied to the lap joints. For all formulations the adhesive gelled within 10 minutes from application.

For the IDPI based PUa nanocomposite, exfoliated nano-graphene grade C300, obtained from XG Sciences was used as received. Approximately 0.4g of GnP was placed in a 250 ml beaker with the amine blend, see paragraph above. The slurry was stirred using a combination of magnetic stirring and a Qsonica sonicator, manufactured by Qsonica L.L.C, Newtown, CT, USA. The amplitude was set to 20% and the process time was set to 30 min with a pulse time of 10s on and 10s off. The temperature of the slurry never exceeded 32 °C, and the total run time was ~1 h. The B-Side slurry was immediately transferred, via syringe to the two-component adhesive cartridge. The SLJ was manufactured as described earlier.

For the MDI system the molecular weight of the soft segments, a poly(tetramethylene oxide) (PTMO) based diamine with molecular weights of 650 g/mol, 1000 g/mol, and 2000 g/mol, was varied to control the HSWF. The time for reaction and joint assembly was sufficient as to not require the use of the two-part adhesive cartridges, therefore the reaction calculation is much simpler. The weight of MDI (isocyanate) necessary to react with 100 g of Amine (PTMO) is calculated using Equation 2-14.

$$\frac{Wt\ of\ PTMO}{Eq.Wt.of\ the\ PTMO} \times Eq.Wt.of\ MDI \times Index = Wt\ of\ MDI \tag{2.14}$$

where Eq. Wt. is the equivalent weight of the constituents, Wt is the mass of the constituents in grams, Index is the stoichiometric index which was set at 1.03. The MDI used was Isonate 143LP which is a polycarbodiimide-modified diphenylmethane diisocyante prepolymer manufacture by DOW Chemical Company. The PTMO based diamines were obtained from Evonik and are listed under the Versalink product line as P650, P1000, and P2000. Note for calculations, the equivalent weights of the PTMO were not estimated but were taken from the Evonik Inspection Certificates and the equivalent weight of the MDI was taken from the Isonate 143LP product information sheet. Table 2-5 and Table 2-6 summarizes the inputs and final target compositions, respectively.

Table 2-5. Summary of the equivalent weights of the constituents used in the reaction calculations for the MDI based PUa.

Constituents	**Equivalent Weight (g/eq)**
MDI DOW143L	143
P650 (PTMO)	436
P1000 (PTMO)	619
P2000 (PTMO)	1134

Table 2-6. Final target composition for the MDI based PUa.

	MDI-P650	**MDI-P1000**	**MDI-P2000**
MDI	33.7 g	23.8 g	13.1g
PTMO	100.0 g	100.0 g	100.0 g
%HS	25 %	19 %	12 %

The MDI based PUa was manufactured by the following method. 100 g of the PTMO was placed in a 500 ml beaker and heated to 70 ^{o}C on a hot plate. An over-head stirrer was utilized, and the required amount of isocyanate was dripped in using an addition funnel. Once all the isocyanate was incorporated, the beaker was removed and the PUa adhesive was poured into the SLJ fixtures.

For the MDI PUa-GnP nanocomposites system, exfoliated nano-graphene (grade R-10, obtained from XG Sciences) was heat-treated at 400 °C, in a nitrogen atmosphere, for 1 h and allowed to cool gradually in the convection oven. The reaction procedure was modified to assist with the dispersion of the GnP. Toluene was used as a solvent to disperse GnP. The desired amount of GnP was added to a 250 ml beaker, along with 95 ml of toluene and ultrasonically stirred, using a Qsonica sonicator, manufactured by Qsonica L.L.C, Newtown, CT, USA. The amplitude was set to 20 % and the process time was set to 30 min with a pulse time of 10 s on and 10 s off. The temperature of the slurry never exceeded 32 °C, and the total run time was ~1 h. The total amount of energy input was 38,610 J. The required amount of PTMO (see Table 2-6) was placed in a 500 ml beaker and heated to 70 ºC. The GnP-toluene slurry was transferred into the 500 ml beaker and stirred for 10 minutes using an overhead stirrer. The required amount of MDI (see Table 2-6) was placed in an addition funnel and dripped into the 500 ml beaker. Once all the isocyanate was incorporated, the beaker was removed and the PUa adhesive was poured into the SLJ fixtures. A second set of neat MDI-PUa (without GnP) with added toluene were also created to compare the effect of residual Toluene solvent (if any) on the resulting PUa adhesives.

2.2.2 Single Lap Joint Construction

The single lap joints (SLJ) were assembled per ARL-ADHES-QA-001.01 Rev 2 [2]. The lap joints were constructed from 1.6 mm 6061-T6 aluminum substrate. The bond line thickness was approximately 1mm. Two separate surface treatments were utilized, the first was the sulfuric acid/sodium Dichromate chemical etching as per ASTM D2651. The Etching solution was 24.51 wt% H_2SO_4, 6.66 wt% $Na_2Cr_2O_7$, and 68.83 wt.% DI water. The substrate pretreatment steps were: 1) Degreased and wipe with IPA, 2) sand blast with 120 grit sand, 3) clean with IPA, 4) immerse

for 20 minutes @25 ºC in the etching solution, 5) rinse with tap water, 6) rinse with DI water, oven dry for 30 minutes at 70 ºC followed immediately by joint manufacturing.

The second surface treatment was a commercial e-coat designed for aluminum substrates. The e-coat was recommended by PPG industries and was applied by Spectrum E-Coat Inc. in Grand Rapids, Michigan. The e-coated substrates were used as is with only a mild wipe using a cloth rag.

2.3 Single Lap Joint and PUa Adhesive Characterization

All adhesive joints were tested on an electromechanical screw-driven Instron model 5984 with a 10kN load cell. The displacement was measured utilizing cross head displacement and the crosshead speed was set to 50 mm/min. Adjustable grips which align the SLJ samples to ensure symmetric and aligned loading along the shear plane were used, thereby eliminating effects of any bending due to misalignment of grips.

Solvent extraction efficiency was measured using thermogravimetric analysis (TGA) techniques. TA instruments Q5000 was utilized to measure presence of any residual toluene solvent. Platinum pans were placed on the Q5000 and approximately 15 mg to 20 mg of the PUr was placed on the pan. The initial sample weight was measured by the Q5000. The samples were heated at a rate of 3 ºC/min and the weight change with temperature was recorded.

A Thermo Scientific Nicolet IS50 Fourier Transform Infrared (FTIR) spectrometer was determined to follow the chemical reaction. A germanium crystal was utilized, and the spectrometer was set to the attenuated total reflectance mode.

Differential scanning calorimetry (DSC) was performed on TA instruments DSC2500 machine. Approximately 15 mg of the PUr was placed in premeasured hermetically sealed pan. The samples were heated at a rate of 3 ºC/min and the change in heat flow (q) with temperature

was recorded. Each sample pan was cycled through a heat-cool-heat experiment, where the sample was equilibrized at -90 ºC then heated up to 200 ºC depending on the formulation. Subsequently the sample was cooled to -90 ºC at a rate of 3 ºC/min followed by a second heating cycle.

Dynamic mechanical analysis (DMA) was conducted using a TA Instruments RSA-G2 rheometer. All film samples were loaded in tension. Temperature sweeps, at a rate of 3 °C/min, were conducted from −95 °C to a maximum temperature that depended on the polyurea formulation hard segment content.

2.4 Results

2.3.1 IPDI based Adhesive Joints – 2-Part Adhesive Cartridge

Figure 2-1 shows the results of the single lap joint testing for the PUa adhesives for both neat (a, b, c) and filled (e, f, g) system. The shear stress (τ)-displacement (d) response of the 20% HS and 30% HS joints can be divided into three segments: (i) an initial steep slope representing the elastic regime in region 1, followed (i) a gentler slope representing hardening mechanisms in region 2 followed by (iii) final failure of the joint in region 3. As HSWF is increased from 20% to 30% the slope of region 1 increases from approximately 7 MPa/mm to 12 MPa/mm. For region 2 the slope, approximately 2.5 MPa/mm remains the same for both formulations, but the range of the displacement decreases between the 20% HSWF (2 mm) and the 30% (1mm). For the 40% HS joint it is only defined by 1 region; its slope is approximately 12 MPa/m. Figure 2-2 shows the substrate/adhesive surfaces, after failure for all three IPDI based formulations. The 20% and 30% (Figure 2-2a and b) hard segment joints failed interfacially. For the case of 20% HS, the peeling starts at the edge of the joint and progresses until the adhesive fillets at the end. For joints with 30%HS the peeling starts at the edges and converges on the middle of bonded area subjecting the adhesive in the joint to pure tension load until final failure. The 40% HS (Figure 2-3c) failed within

the linear elastic regime in a partially cohesive/partially interfacial fashion. Figure 2-1 also shows the effect of GnP additions. Regardless of the HSWF the initial slopes (region 1) for all three formulations were similar, indicating that the nanoparticle additions did not significantly affect the stiffness of the resulting adhesives. For the 20% HS and 30% HS formulations the addition of GnP reduced the ultimate displacement (displacement at failure). For 40% HS, to recall, the response of the neat (without GnP) adhesive was linear elastic, but with the presence of GnP, a non-linear response beyond yield was observed. Interestingly, the load drops at the end of the linear elastic regime similar to when failure occurs in 20% and 30% HS. It is then followed by a gradual hardening behavior until failure. Nevertheless, this hardening is not significant enough to increase the failure loads. In short, the maximum load is still governed by the linear elastic response. Figure 2-3 compares the ultimate shear stress (a) and the displacement at ultimate shear (b) for both neat and filled systems. As HSWF increases so does the ultimate shear stress; this is accompanied by a loss in the displacement at ultimate shear. For this chemical formulation of PUa, the additions of GnP had minimal influence on the overall performance of the joint and did not have any detrimental effect on the key characteristics (ultimate shear stress and displacement at ultimate shear) of the joint.

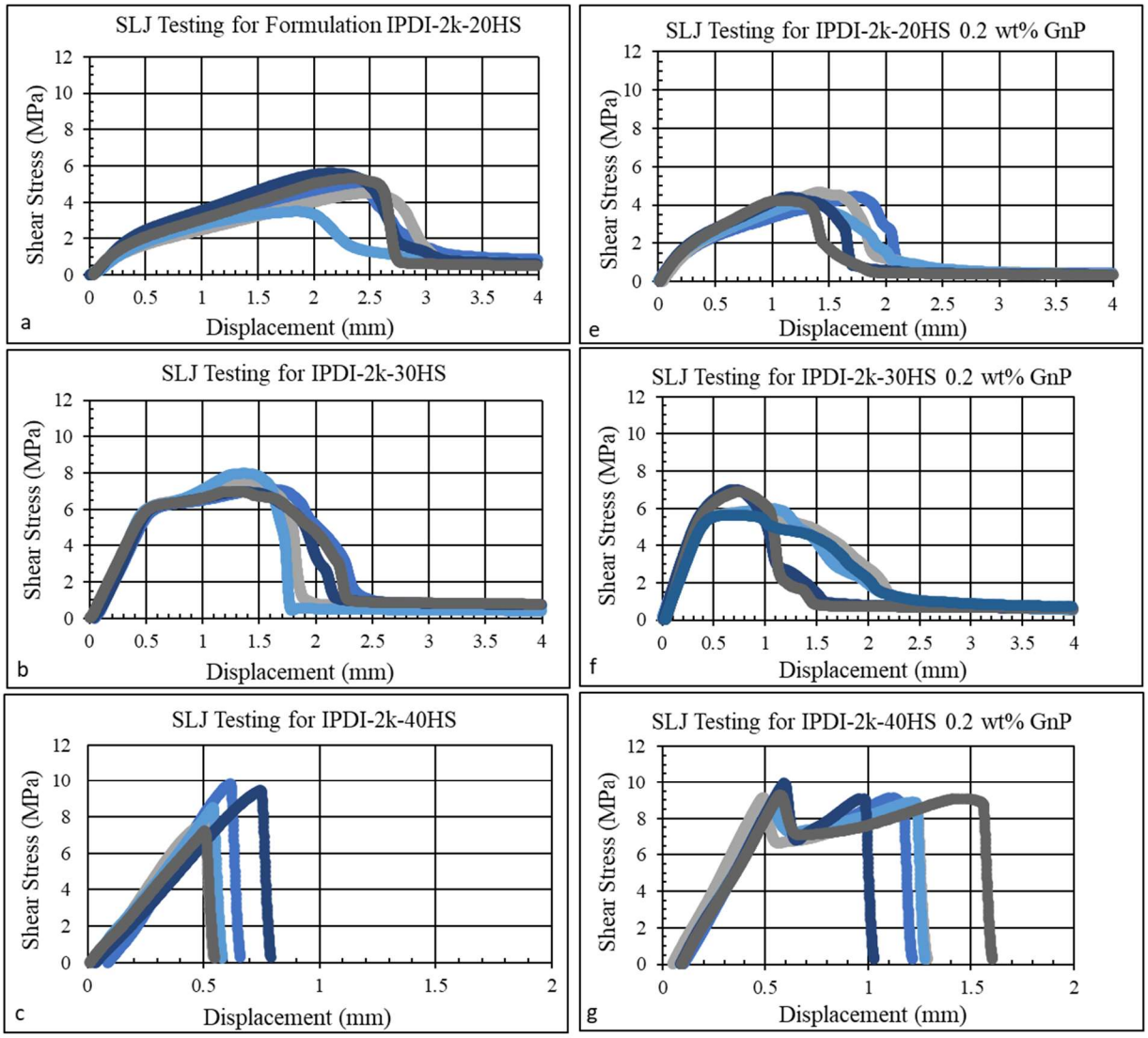

Figure 2-1. SLJ testing for neat (a,b,c) PUa adhesive joint, and filled (e,f,g) PUa adhesive joint. The GnP grade used was C3000 and the aluminum substrate surface treatment was per ASTM D2651.

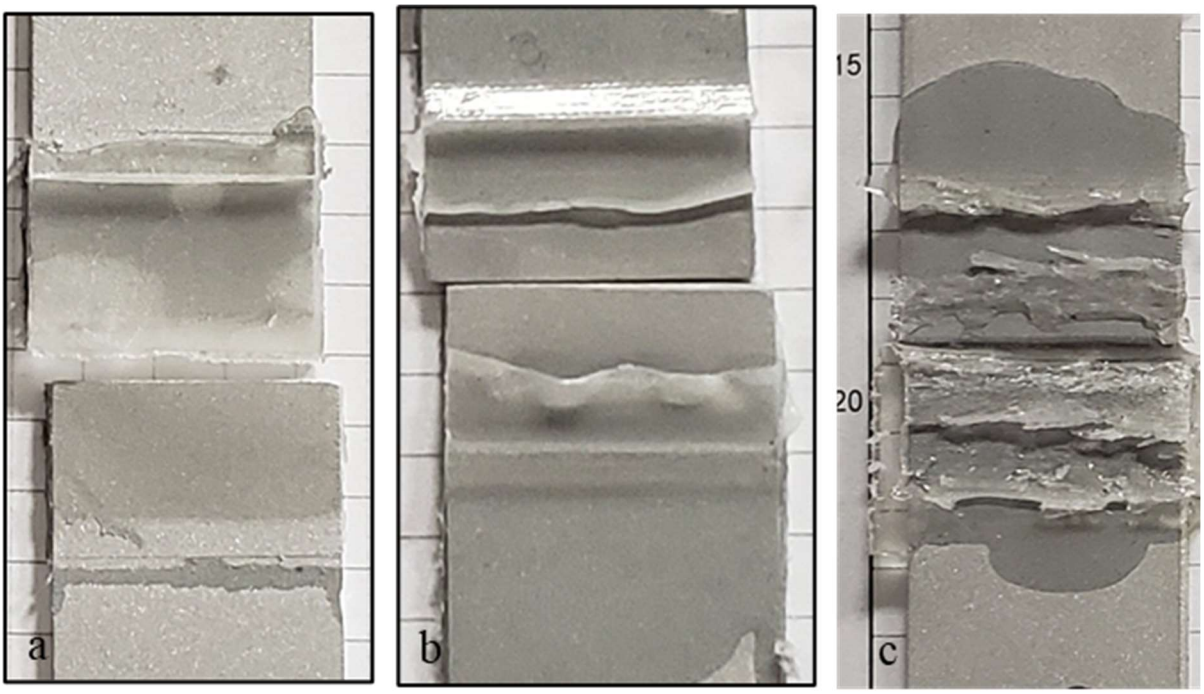

Figure 2-2. Photograph of the neat IPDI adhesive. a) IPDI-2k-20HS, b) IPDI-2k-30HS, c) IPDI-2k-40HS.

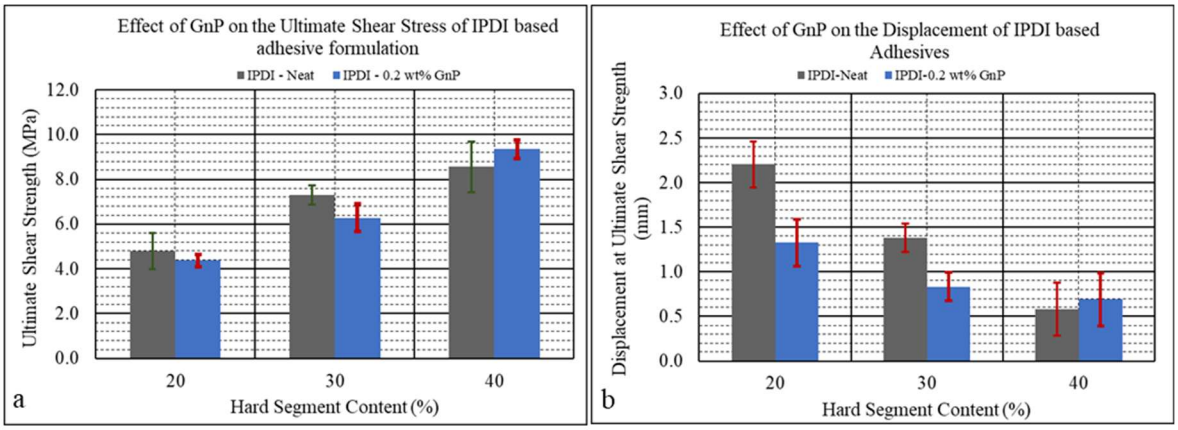

Figure 2-3. Comparison of the Ultimate Shear Stress and displacement at Ultimate Shear Strength for neat and filled PUa adhesive.

2.3.2 MDI based adhesive joints – cast joints.

Figure 2-3 shows the results of single lap joint testing for the two MDI based adhesives. The stress-displacement response showed similar trends as those observed in the IPDI based adhesives. As HSWF increases so does the ultimate shear stress and the displacement at ultimate shear stress decreases with the increase HSWF. Regardless of HSWF the joints failed in the interface as shown in Figure 2-5. At this point, it was decided to e-coat the surface of the aluminum substrate to see if the failure mode of the joint can be changed from interfacial to cohesive. Figure 2-6 shows the results of the single lap joint while Figure 2-7 compares the two surface treatments. The e-coat surface treatment results in a cohesive failure with both the 12% and 18% HS PUa exceeding the requirements for a group I adhesive.

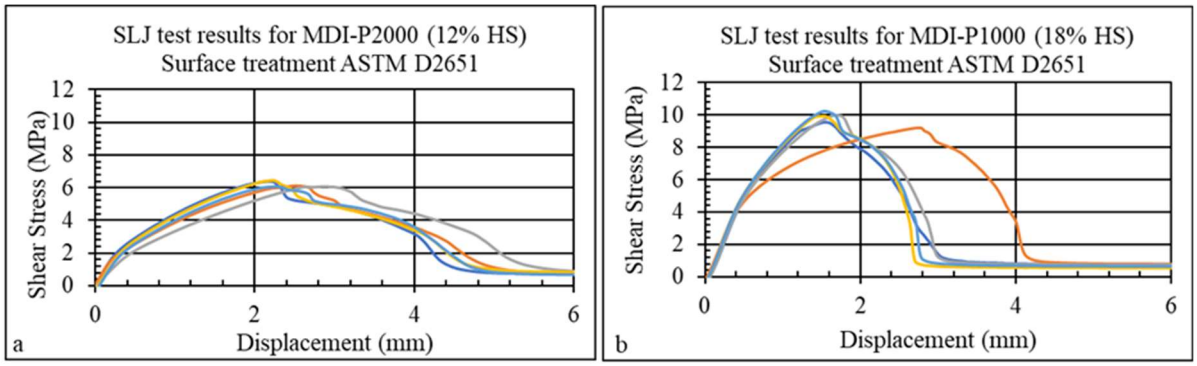

Figure 2-4. Single Lap Joint testing using a cast system the MDI-PTMO system a) MDI-P2000 (12% HS) and b) MDI-P1000 (18%HS).

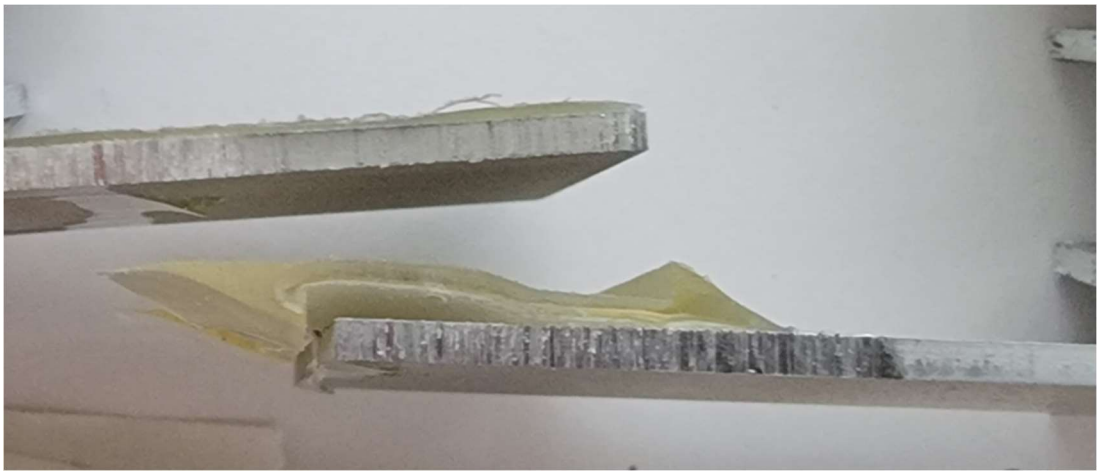

Figure 2-5. Photograph showing the adhesive fracture representing both the MDI-P2000 and MDI-P1000 system.

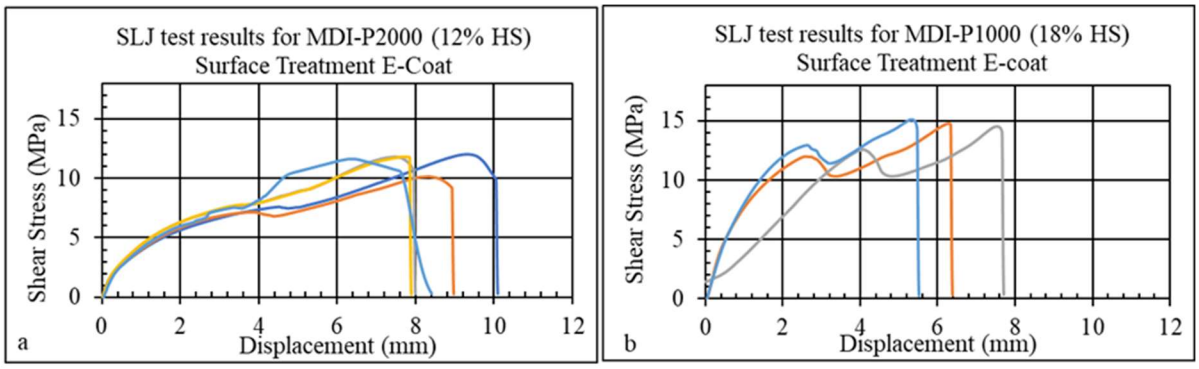

Figure 2-6. Single Lap Joint testing using a cast system the MDI-PTMO system a) MDI-P2000 (12% HS) and b) MDI-P1000 (18%HS).

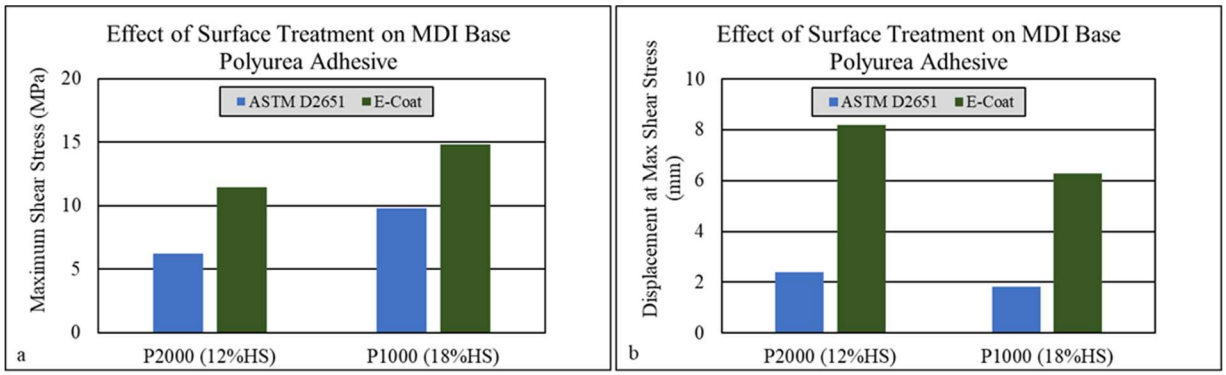

Figure 2-7. Comparison of aluminum surface treatments a) maximum shear stress, b) displacement at max shear.

In this adhesive study, the grade of GnP nano particles was changed to R10 grade, and the solvent cast process was used. Although DMF is a better solvent for preparing PUa formulations, it was decided to use toluene as it would be better for dispersion of the GnP. To ensure that the solvent in the system was removed and that it didn't affect the SLJ properties, thermogravimetric analyses were performed on adhesives immediately after SLJ testing to measure any residual solvent. This was done only for the MDI-P2000 system. The same parameters were used for solvent extraction and curing for the lap joints for the MDI-P1000 and MDI-P650. Figure 2-8 shows the TGA curves for the 5 tested samples. Table 2-7 summarizes the TGA and single lap joint test results. Sample 1 is the first sample extracted and tested 24 hours after the joints were assembled. The results represent room temperature solvent extraction and curing. All subsequent samples were evaluated at 24 hours intervals. Sample 5 showed the least amount of toluene remaining and the highest shear strength.

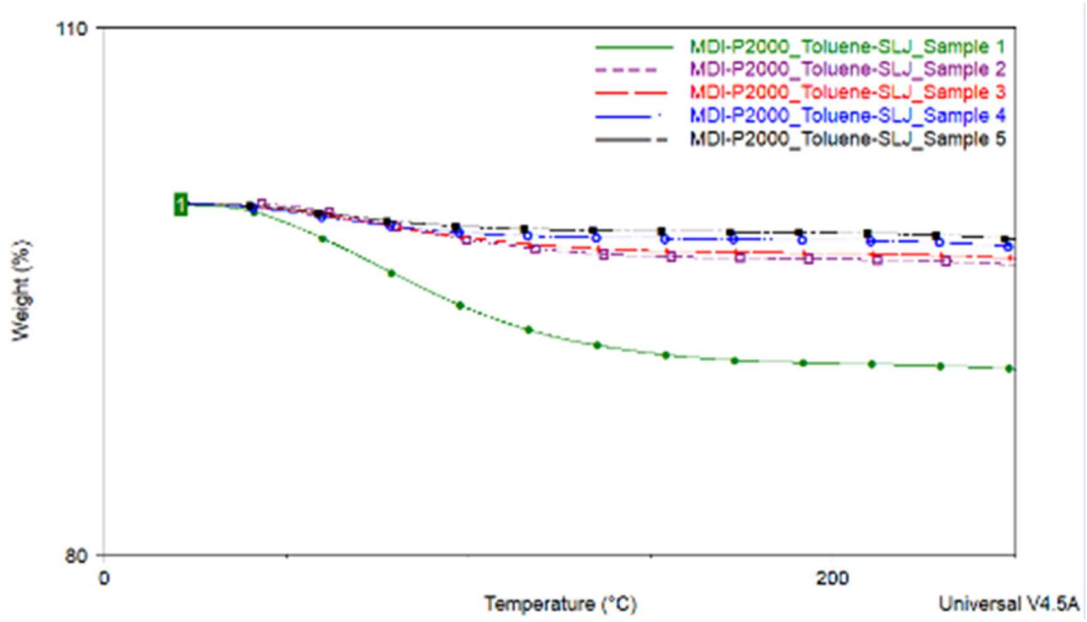

Figure 2-8. TGA results for the single lap joints after testing. Sample 1 was extracted and tested 24 hours after creating the joint. All subsequent samples were evaluated in 24-hour intervals.

Table 2-7. Results from the solvent extraction process.

Sample	Time After SLJ Assembly (hrs.)	Maximum Shear Stress (MPa)	Toluene Remaining (wt%)
Sample 1	24	3.44	6.732
Sample 2	48	8.06	2.323
Sample 3	72	Evaluated but results not saved by machine	2.156
Sample 4	96	Evaluated but results not saved by machine	1.777
Sample 5	120	12.71	1.402

Table 2-8 summarizes the single lap joint testing seen in Figure 2-9. The stress-displacement response of neat samples were found to be similar for both 12% HS and 18% HS formulations with similar average ultimate shear stress and max displacement to failure. A further increase in HSWF (25%HSWF, MDI-P650-25HS) resulted in a decrease in the max displacement to failure, although the ultimate shear stress remained the same. Figure 2-10 shows the fracture surfaces of the joints representing each formulation. Regardless of the HSWF the average cohesive zone failure area was similar when considering the 1σ variation as shown in Table 2-8. For the nano modified PUa, the addition of GnP did not have a detrimental effect on any of the ultimate shear stress and the max displacement at ultimate shear. It did however increase the average area of the cohesive zone relative to its respective neat formulation for both the 19% and 25% HS samples. This increase is more dramatic in the higher HS PUa. While this is not explicitly reported elsewhere, this may be attributed to the increase in resistance to peel stresses due to the presence of GnP. This can be directly correlated to the increase in cohesive fracture area. Further testing, especially in peel, is needed to confirm this phenomenon.

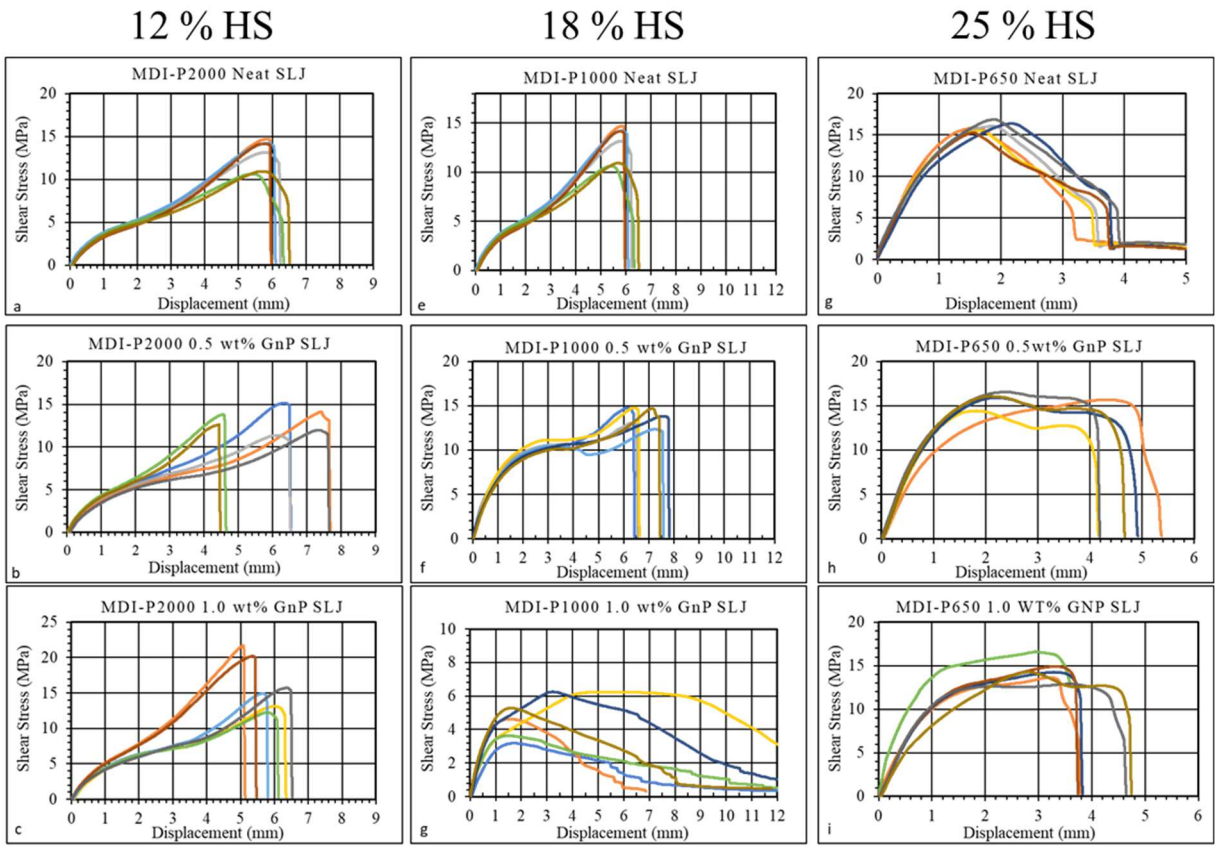

Figure 2-9. Lap joint testing for the MDI PUa system. The first column is the MDI-P2000 system (12%HS) a) MDI-P2000 neat, b) MDI-P2000 0.5 wt% GnP, c) MDI-P2000 1.0 wt% GnP. The middle column is the MDI-P1000 system (18%HS). The last column is the MDI-P650 system (25%HS) h) MDI-P2000 neat, i) MDI-P2000 0.5 wt% GnP, j) MDI-P2000 1.0 wt% GnP.

Table 2-8. Summary of single lap joint testing for the MDI based PUa system.

Formulation	Ultimate Shear Stress (MPa)	Displacement at Ultimate Shear Stress (mm)	Average Cohesive Zone Failure Area (mm^2)
P2000 – Neat	12.7 +/- 1.8	5.28 +/- 1.76	128 +/- 55
P2000 – 0.5 wt% GnP	13.2 +/- 1.4	6.04 +/- 1.31	183 +/- 28
P2000 – 1.0 wt% GnP	16.3 +/- 3.8	5.71 +/- 0.45	165 +/- 31
P1000 – Neat	14.1 +/- 2.5	4.31 +/- 0.44	174 +/- 26
P1000 – 0.5 wt% GnP	13.9 +/- 1.0	6.80 +/- 0.56	213 +/- 9
P1000 – 1.0 wt% GnP	4.2 +/- 0.89	1.54 +/- 0.14	265 +/- 36
P650 – Neat	16.0 +/- 0.6	1.78 +/- 0.25	72 +/- 3
P650 – 0.5 wt% GnP	15.9 +/- 0.8	2.45 +/- 0.94	182 +/- 18
P650 – 1.0 wt% GnP	14.0 +/- 0.6	3.22 +/- 0.24	229 +/- 17

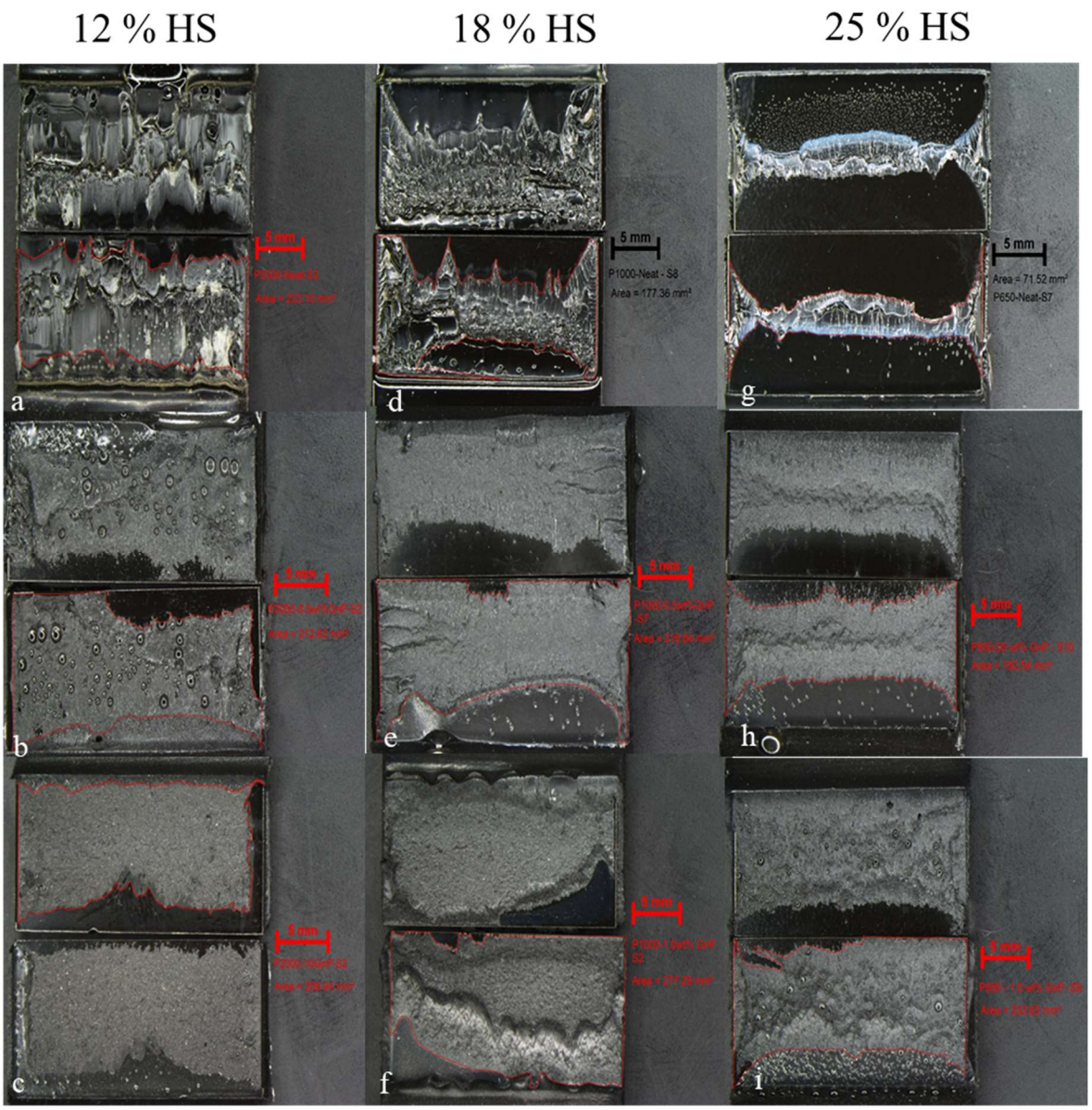

Figure 2-10. Fracture surfaces of the single lap joint for the MDI PUa system. The first column is the MDI-P2000 system (12%HS) a) MDI-P2000 neat, b) MDI-P2000 0.5 wt% GnP, c) MDI-P2000 1.0 wt% GnP. The middle column is the MDI-P1000 system (18%HS). The last column is the MDI-P650 system (25%HS) h) MDI-P2000 neat, i) MDI-P2000 0.5 wt% GnP, j) MDI-P2000 1.0 wt% GnP.

FTIR, DSC and DMA results for the IPDI based systems for both the neat and filled systems are addressed in the following chapters and are not discussed within this discission of the single lap joint testing. Since the MDI based system was only studied for the lap-joint testing,

FTIR, DSC and DMA results for the MDI based system alone are presented here. Figure 2-11 show the FTIR spectra for the MDI based PUa. The key peaks involved in the PUa reaction are an isocyanate peak located at wavelength of 2250- 2275 cm^{-1} and the amine stretching peaks forum between 3400 and 3500 cm^{-1}, Figure 2-11a. The absence of peak in the isocyanate range and the presence of secondary amines suggest that the reaction between the isocyanate (MDI) and the diamine (Versilink©) has gone to completion and there is no free isocyanate. Figure 2-12 compares the FITR spectra for the neat and fille PUa. Again, the reaction has gone to completion as shown by the absence of the Isocyanate peak, no additional peaks were found (Figure 2-12 b and c) when comparing the neat to the filled system, suggesting that no new covalent bonds were formed between the PUa and the GnP.

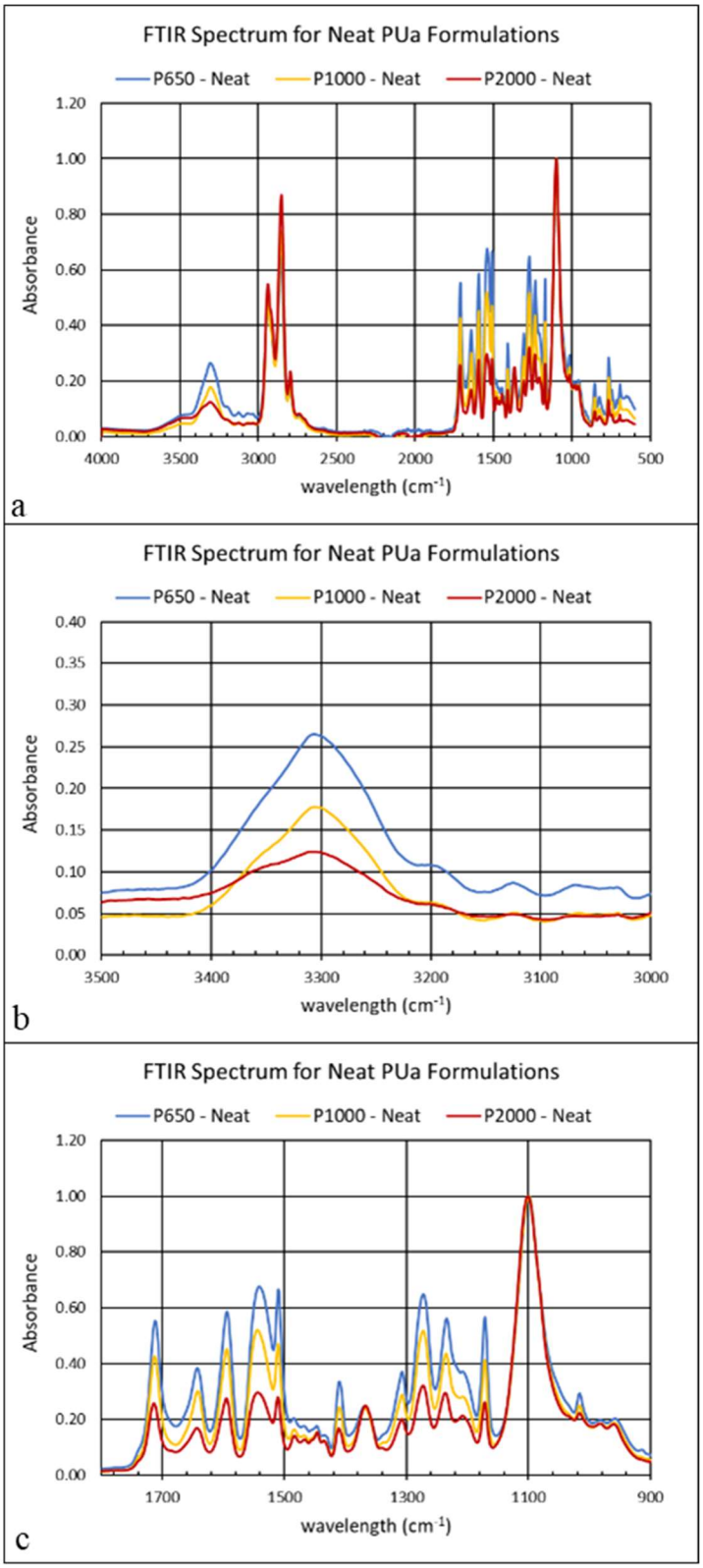

Figure 2-11. FTIR spectra comparing the neat MDI based PUa. a) overall spectra, b) the amine region of a, c) the carbonyl region of a.

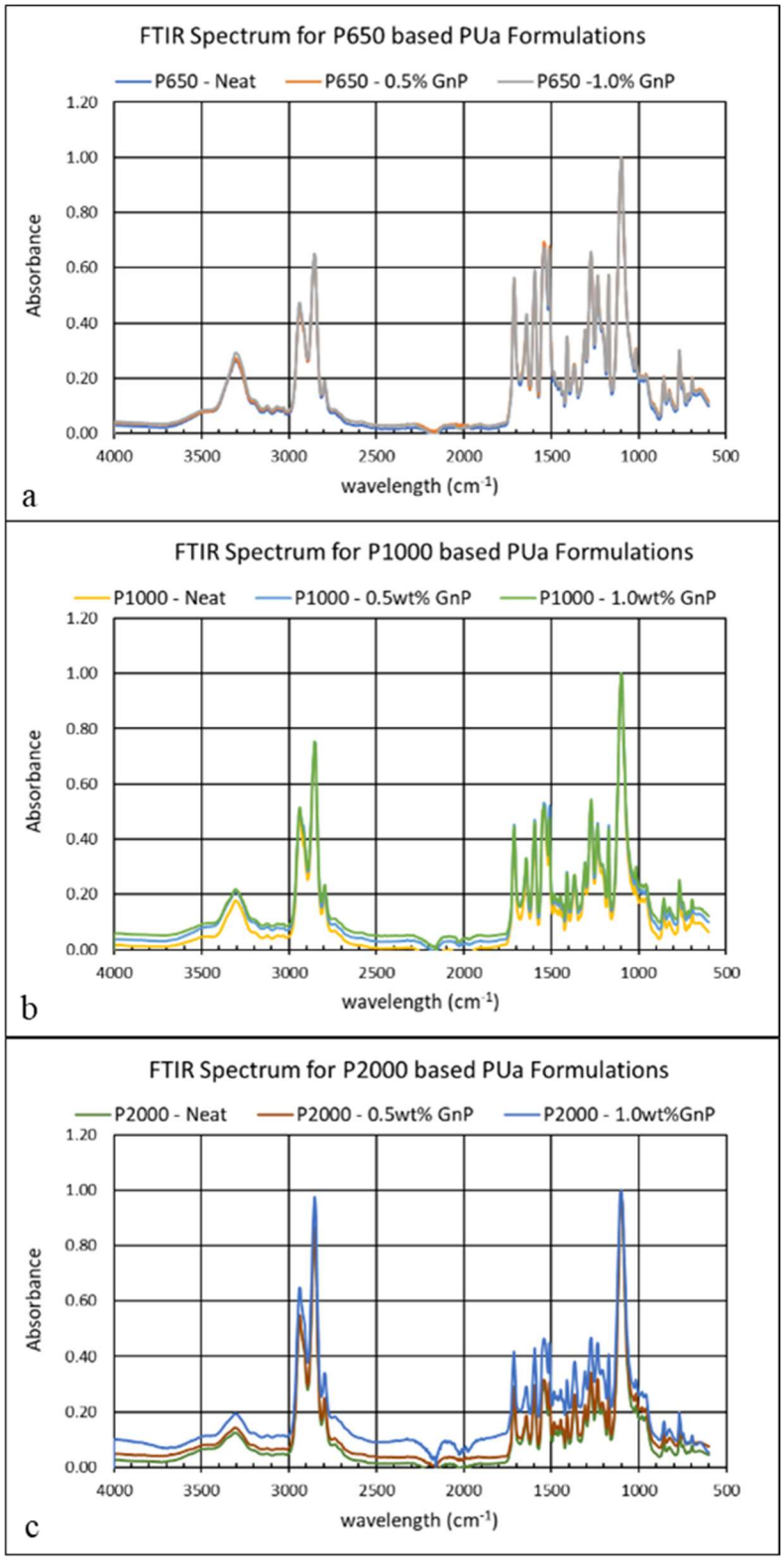

Figure 2-12. FTIR spectra comparing the neat MDI and filled based PUa. a) overall spectra, b) the amine region of a, c) the carbonyl region of a.

Figure 2-13 through Figure 2-15 show the DSC thermographs for the MDI based PUa. Table 2-9 summarize the thermodynamic glass transition temperatures (T_g). It should be noted that the Tg for the MDI-P2000 neat and filled system is not obvious and difficult to interpret and should be considered an approximation. Furthermore, the starting temperature of the DSC runs was -90 ºC, which is only 15 ºC above the approximated Tg which is insufficient; the starting temperature should be a minimum of 20 ºC above Tg. The Tg is included here for completeness. As the HSWF increases so does the Tg. At high temperatures, in the first heating run, a second transition, corresponding to the transformation within the hard-phase domains is seen. Upon subsequent slow cooling and re-heating, no high temperature transitions were observed. Indicating that the high temperature transition in the first run was a non-equilibrium structure, and a single thermal anneal was enough to equilibrate the system. For both the 18% and 25% HSWF the additions of GnP did decrease the T_g. For the 18% PUa the decrease was ~10 ºC while for the 25% system the decrease was considerably smaller at approximately 2 ºC. The most dramatic effect for GnP addition was found in the higher molecular weight system Versalink system (P1000, P2000). In the neat P1000 and P2000 systems, Figure 2-13 and Figure 2-14, a strong exothermic peak was observed between 0 and 50 ºC. The temperature and enthalpy are summarized in Table 2-10. The peak is associated with a degree of crystallization of the soft segments. For the P1000 system the additions of GnP completely suppress the peak. For P2000, the GnP additions do not suppress the peak completely but do reduce the enthalpy.

Table 2-9. Summary of the glass transition temperature seen in the Neat and filled MDI-PUa system.

Formulation	HSWF	Tg 1st Heat Run	Tg Cooling Run	Tg 2nd heating Run
P2000 – Neat	12	-75.76	-42.14	-58.90
P2000 – 0.5 wt% GnP		-75.92	-67.51	-68.00
P2000 – 1.0 wt% GnP		-74.10	-73.52	-85.87
P1000 – Neat	18	-51.67	-49.65	-61.54
P1000 – 0.5 wt% GnP		-63.75	-64.00	-63.68
P1000 – 1.0 wt% GnP		-64.26	-60.50	-62.14
P650 – Neat	25	-48.81	-44.12	-41.92
P650 – 0.5 wt% GnP		-51.57	-46.2	-44.41
P650 – 1.0 wt% GnP		-51.36	-47.43	-49.00

Table 2-10. Summary of Enthalpy for the crystallization peaks seen in the higher molecular weight soft segments. Note peak not present is abbreviated as NP in the table.

Formulation	1st heating run		Cooling Run		2nd heating run	
	T (°C)	ΔH (J/g)	T (°C)	ΔH (J/g)	T (°C)	ΔH (J/g)
P2000 – Neat	10.45	29.75	3.36	25.30	25.30	62.30
P2000 – 0.5 wt% GnP	7.14	23.84	-15.99	21.23	21.23	42.20
P2000 – 1.0 wt% GnP	4.75	25.96	-13.01	21.67	21.67	43.97
P1000 – Neat	11.91	28.77	-18.56	22.35	NP	NP
P1000 – 0.5 wt% GnP	NP	NP	NP	NP	NP	NP
P1000 – 1.0 wt% GnP	NP	NP	NP	NP	NP	NP

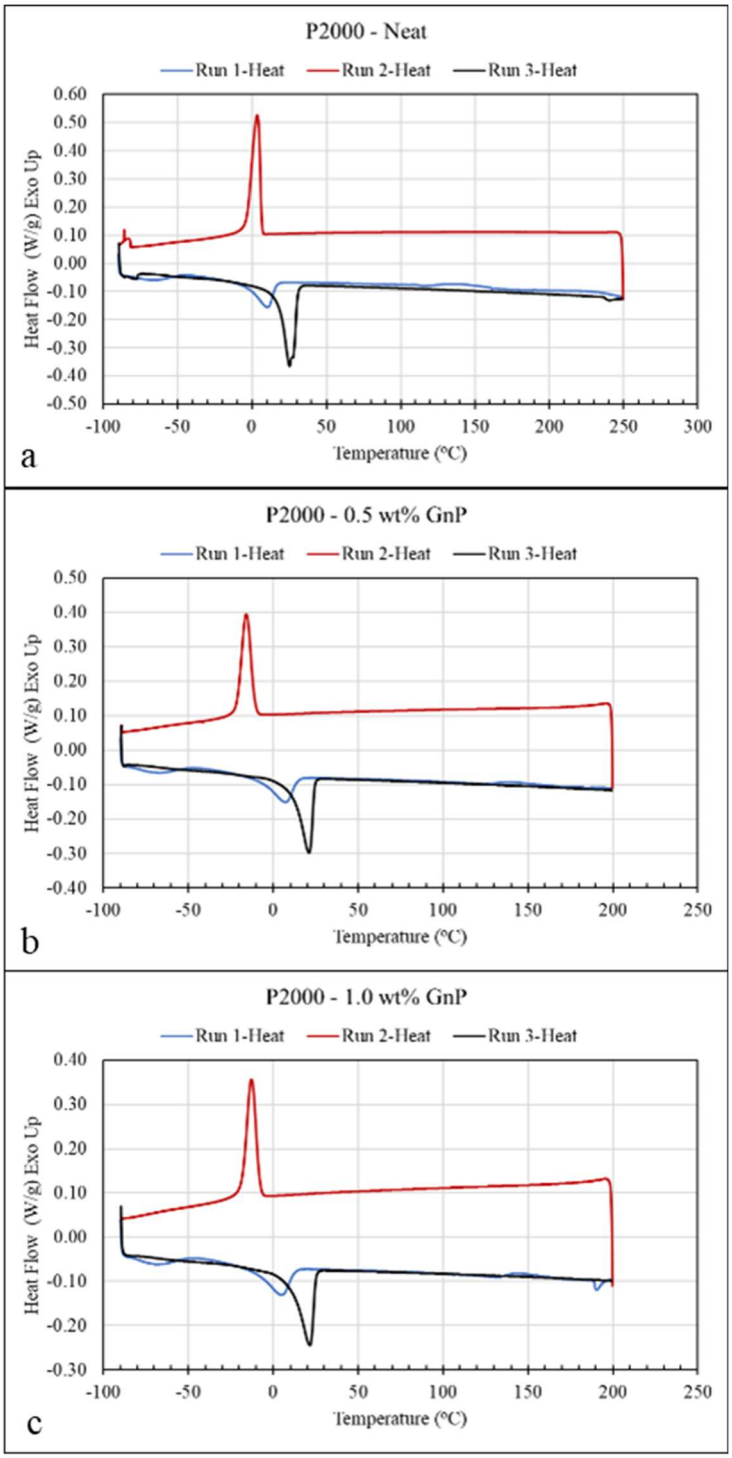

Figure 2-13. DSC curves comparing P2000 neat and filled polymers. a) neat, b) 0.5wt% GnP, c) 1.0 wt% GnP.

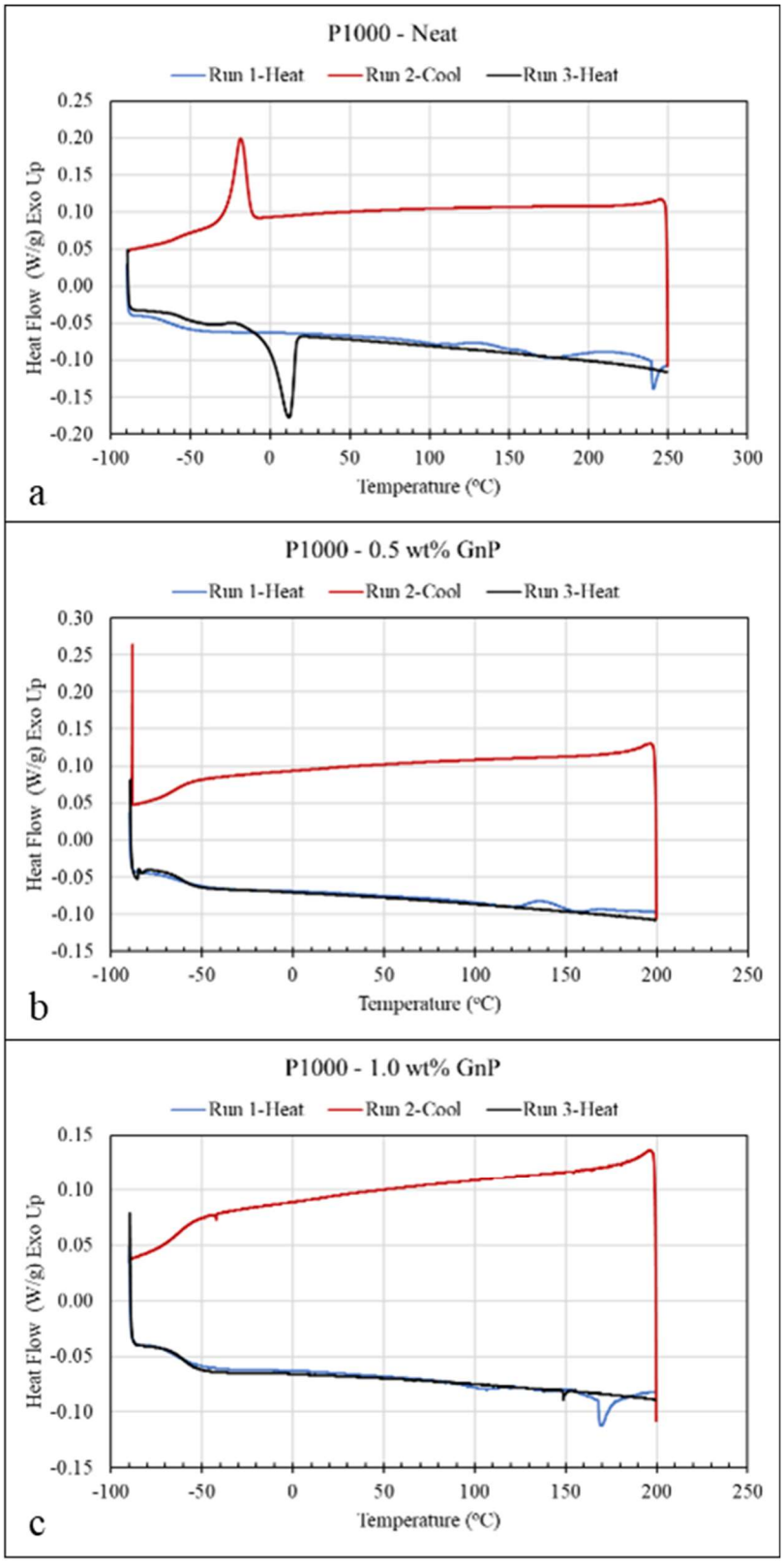

Figure 2-14. DSC curves comparing P1000 neat and filled polymers. a) neat, b) 0.5wt% GnP, c) 1.0 wt% GnP.

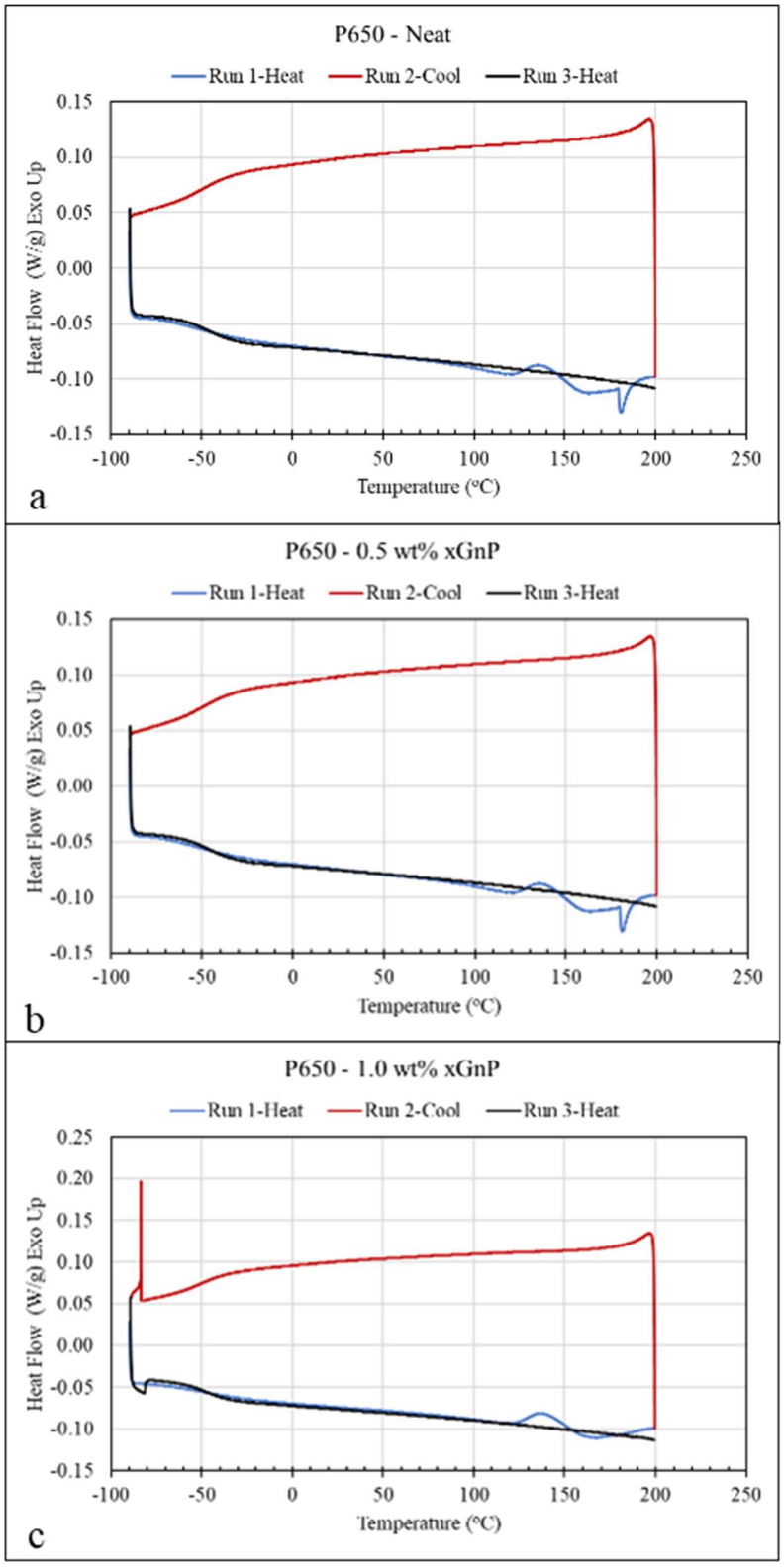

Figure 2-15. DSC curves comparing P650 neat and filled polymers. a) neat, b) 0.5wt% GnP, c) 1.0 wt% GnP.

Figure 2-16 through Figure 2-18 show the DMA curves for both neat and filled systems. The Tg for the system decreases with increasing HSWF (or decrease in molecular weight of the PUa), in almost linear fashion, Table 2-7 compares the Tg for all PUa formulations. Doubling the HSWF increased the Tg by nearly 25 ^{o}C, (as measured by the onset point of the storage modulus). Increasing the HSWF dramatically increased the room temperature storage modulus. Increasing the HSWF by 6% resulted in a modulus increased by a factor of 4.5 while the increase from 18% to 25% (an increase of 7%HS) resulted in a modulus increase by a factor 3.5.

The addition of GnP had very little effect on the T_g of the PUa. The more dramatic effect is seen on the storage modulus. The additions of GnP to the PUa also resulted in increases of the Storage Modulus. For the lower HSWF formulation (12%) the addition of 0.5 wt% GnP and 1.0 wt% GnP increased the room temperature storage modulus by a factor of 2 for each addition GnP. As the HSWF is increased the effect of the GnP additions decreases. For the 18% HSWF samples the increase is only about 2 for the 0.5 wt% GnP but the subsequent increase in GnP addition decreases the modulus. Similarly for the 25% HS PUa the addition of 0.5 wt% GnP increase the modulus by a factor of 1.1 and 1.5 for the subsequent 1.0 wt% GnP addition.

Table 2-11. Effect of HSWF and Soft Segment molecular weight (SSMW) on the Tg and room temperature storage modulus of neat and fill PUa.

Formulation	HSWF	SS MW (g/mol)	T_g E' (°C)	T_g E'' (°C)	T_g tan(δ) (°C)	E' at 25 °C (MPa)
P2000 – Neat	12	2000	-78.50	-73.8	-63.33	8.5
P2000 – 0.5 wt% GnP			-80.58	-74.96	-65.65	16.7
P2000 – 1.0 wt% GnP			-79.67	-74.14	-61.8	30.5
P1000 – Neat	18	1000	-66.83	-60.35	-42.78	38.3
P1000 – 0.5 wt% GnP			-67.82	-60.35	-45.16	71.9
P1000 – 1.0 wt% GnP			-67.13	-59.77	-43.98	44.7
P650 – Neat	25	650	-53.38	-43.38	-15.37	136.4
P650 – 0.5 wt% GnP			-56.76	-44.55	0.46	150.9
P650 – 1.0 wt% GnP			-56.66	-43.39	-10.68	228.64

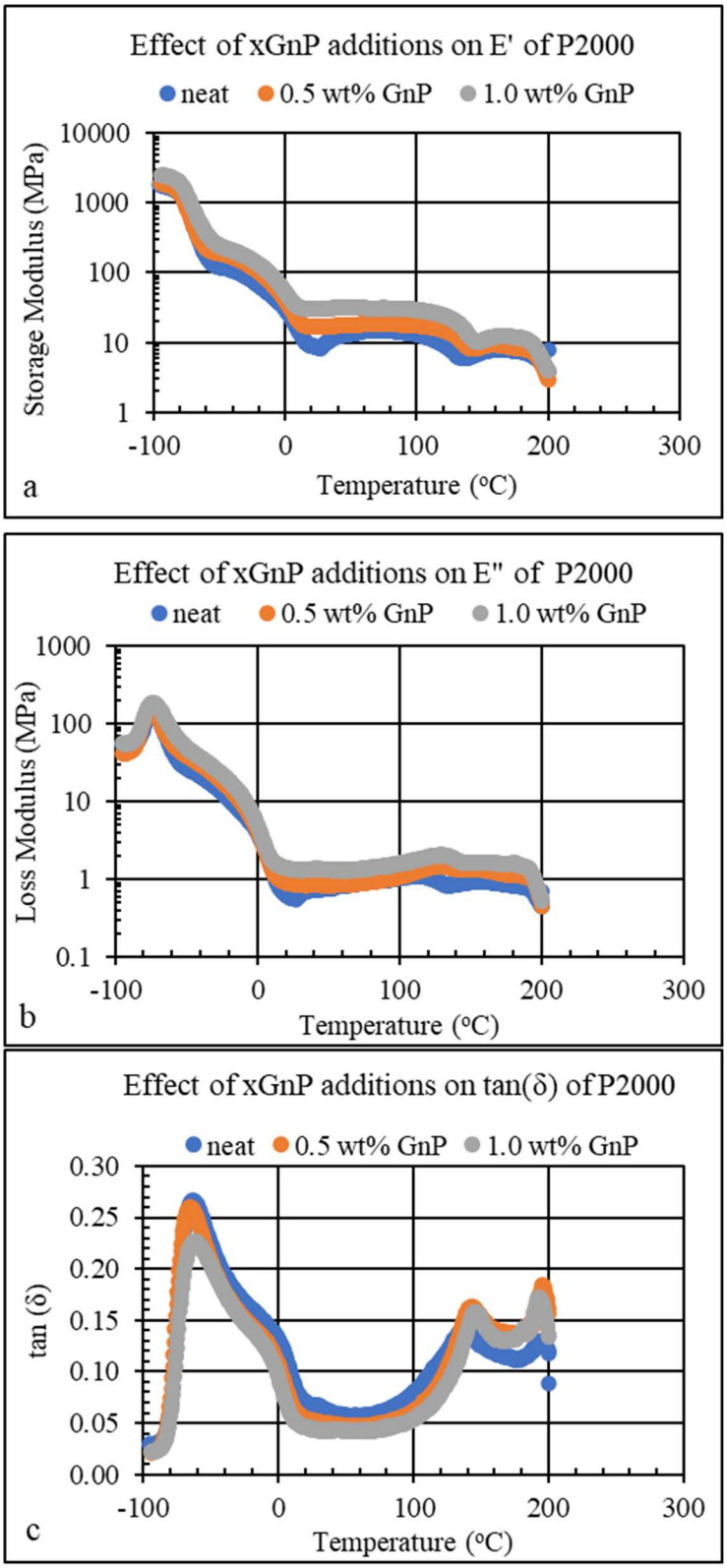

Figure 2-16. DMA curves for Neat and Filled MDI-P2000 (12% HS) system, a) Storage Modulus, b) Loss Modulus, c) tan(δ).

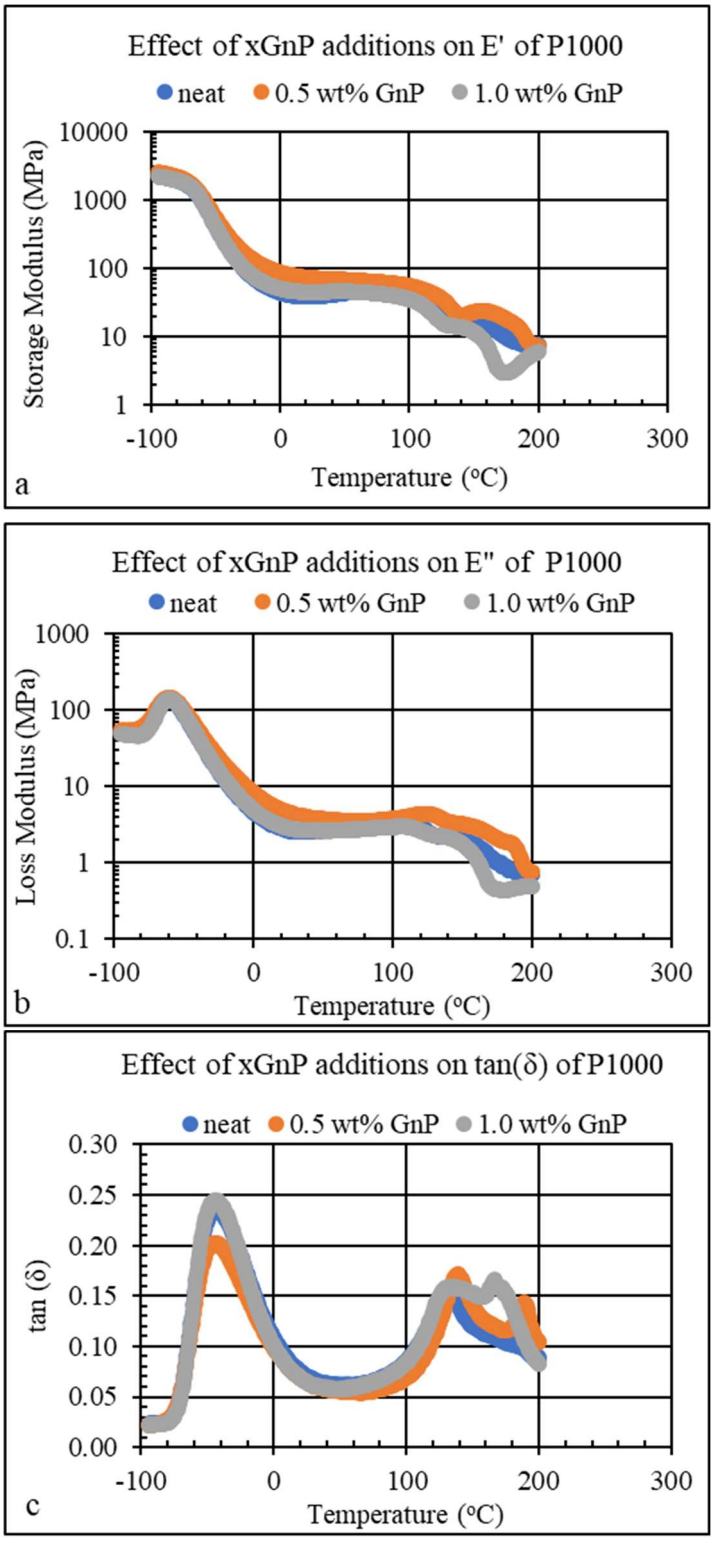

Figure 2-17. DMA curves for Neat and Filled MDI-P1000 (18% HS) system, a) Storage Modulus, b) Loss Modulus, c) tan(δ).

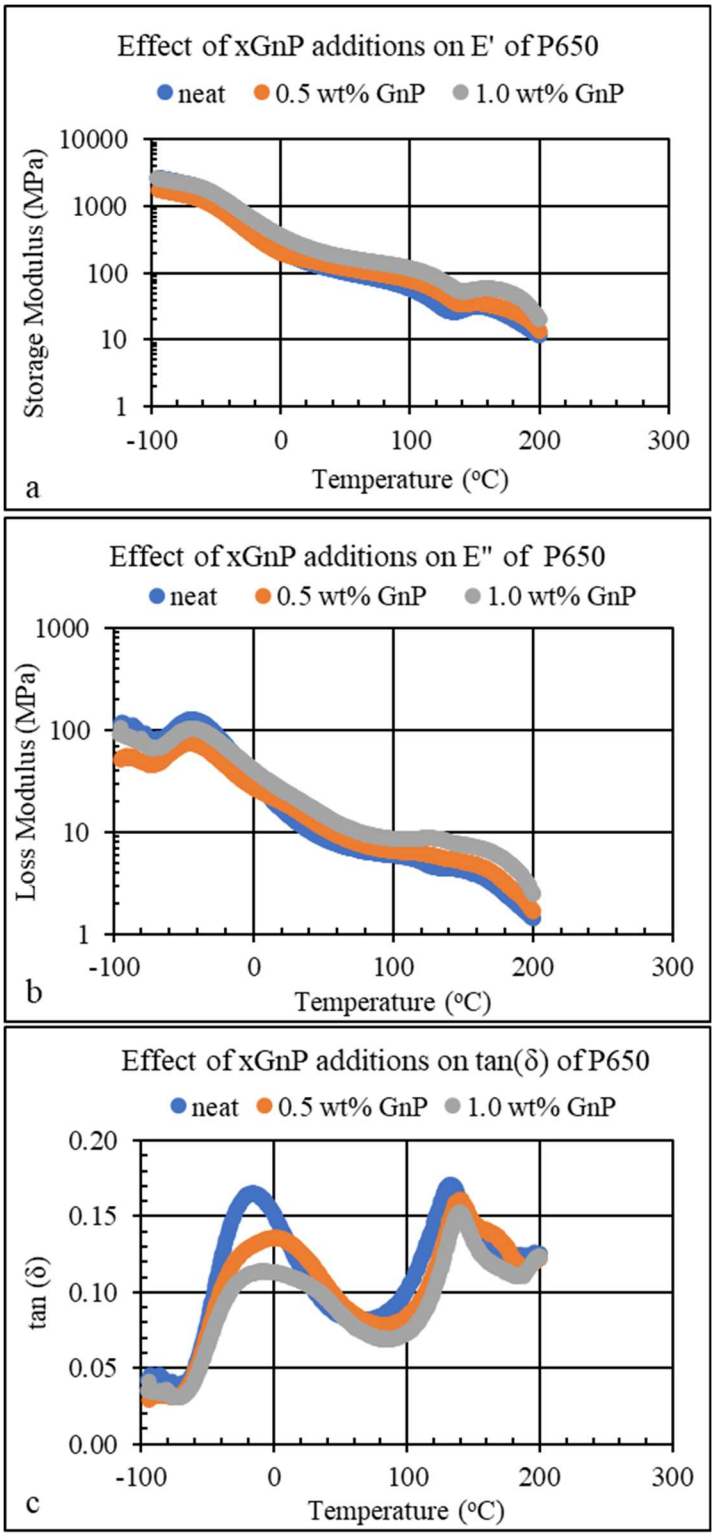

Figure 2-18. DMA curves for Neat and Filled MDI-P650 (25% HS) system, a) Storage Modulus, b) Loss Modulus, c) tan(δ).

2.4 Discussion

The lap-shear single lap joints with the IPDI and the MDI based adhesives revealed that with increase in HSWF the lap shear strength also increased, but the displacement at failure was reduced. The addition of 0.2 wt.% GnP had no detrimental effect on the SLJ properties. The increase in HSWF also changed the failure mode of the SLJ. From Figure 2-2 it was observed that for adhesives with 20%HS and 30%HS interfacial failure occurred along the aluminum surface, but the adhesive at the end of joint remained bonded to the Aluminum surface. Once the PUa debonded from regions of high peel stresses the failure propagated until the end of the bonded areas on both adherends of the SLJ. The tests were stopped at this time and progressing with the loading led to the adhesive being tested in pure tension. Figure 2-19 shows a schematic representation of the different region of the SLJ as well as the failure locations.

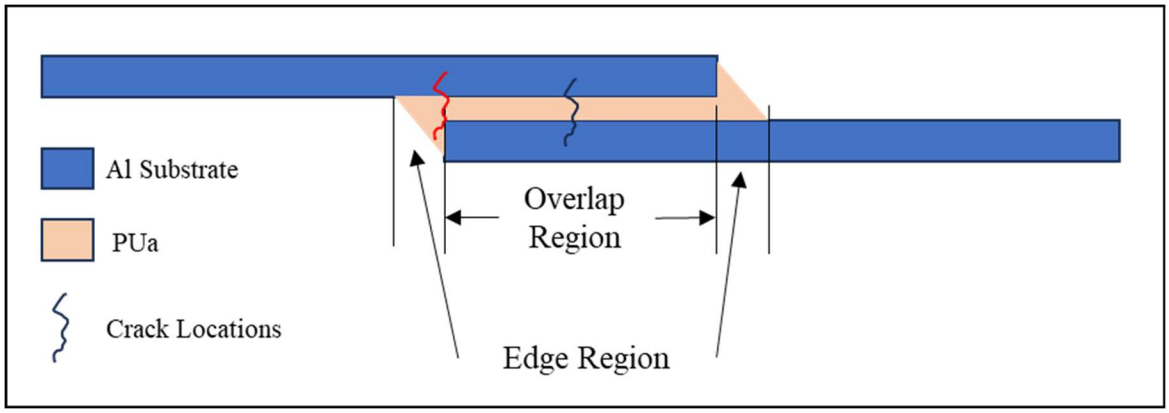

Figure 2-19. Schematic representation of the SLJ. The jagged red line represents the location of the cracks for the 20% HS samples and the jagged black represents the fracture location the of the 30% HS samples.

This phenomenon of failure wherein the peel stresses initiate the failure can be partially attributed to stiffness mismatch between the aluminum substrate and the PUa. Stiffness mismatch can cause stress concentrations at a much higher magnitude relative to materials with similar stiffness. Stiffness is a combination of the modulus of a material and the geometry of substrate. In pure shear configuration, the axial stiffness is dominant while in peel stresses the flexural stiffness

is dominant. In this case the adhesive has a very low modulus of elasticity, in the range of 1 MPa to 500 MPa depending on formulation type and HSWF, while the Aluminum has a modulus of approximately 70 GPa. As the SLJ is loaded, it causes the overlap region to twist in the initial stages of loading which results in peel stress at the edge. This is also highlighted in the MDI system, see Figure 2-5. The aforementioned observation is not seen in the 40% HS samples as their axial and peel stiffness is relatively much higher and thereby failure occurs in a partially interfacial and partially cohesive manner.

In general, the MDI based system produced significantly higher SLJ strengths and displacements at lower HSWF. In fact, the P1000 based MDI-PUa had properties close to the stated target of Group I adhesives with 10 MPa ultimate shear stress and 3.81 mm of displacement, (See Chapter 1). Since the stiffness mismatch will always be present and cause peel type loading, to improve the SLJ properties it was decided to change the surface treatment from the ASTM D2651 to an e-coat. This resulted in a dramatic increase in the SLJ properties, as seen in Figure 2-7. Further exploration of the MDI system, neat and filled, that P2000 and the P1000 systems (12% HS and 18% HS respectively.) showed that a group 1 adhesive can be achieved irrespective of the nanoparticle concentration. The 25% HS samples did not meet the group 1 requirements. In general, and similar to the IPDI system, the GnP additions had no effect on the single lap joint properties. The interesting sample was the MDI_P1000 1.0 wt% GnP which resulted in a drop of both the shear strength and the displacement at ultimate shear. This correlated with a drop in the storage modulus seen in the DMA results. Figure 2-10 confirms that peel loading can occur in the SLJ, note that the edge of the overlap region shows evidence of peel loading but the shifts to completely shear. For the MDI system with GnP toluene was added to assist in GnP dispersion. Although the majority of the toluene was evaporated it will have had an effect on the performance

of the adhesive. Gas bubbles, as a result of the degassing of the toluene, was seen on many of the adhesive joints. It should be noted that while GnP additions did not show any significant enhancements, it did not show any detrimental effect. This opens opportunities for using GnP loading to increase multifunctionality such as sensing properties and tailoring the electrical and thermal properties of resulting adhesives. This is beyond the scope of this work and one of the future recommendations of this work.

For completeness the FITR, DSC and DMA were run for the MDI system, but only one replicate. The FITR showed that the PUa reaction has gone to completion and that there is no free isocyanate in the adhesive. From a DMA perspective the addition of GnP did not shift the T_g significantly. Some increases were notable with the addition of GnP. As noted above the storage modulus (E') did drop for the MDI_P1000 1.0 wt% GnP system and is similar to what is seen in the neat sample; it is not clear if this is a result of insufficient GnP dispersion.

The most significant change seen in the addition of the GnP to the MDI PUa was in the DSC curves. For the P1000 and P2000 formulations a soft segment crystallization peak was observed. The addition of GnP completely suppressed the peak for the P1000 samples and decreased its enthalpy for the P2000 formulations.

2.5. Conclusion

In this chapter, the feasibility of polyureas as a structural adhesive was explored. The main intent was to see if Group 1 type of adhesive can be achieved using polyurea and evaluate the effects of GnP inclusions on the resulting adhesives and joints. To that extent the work was successful, such that Group 1 adhesives can be achieved using an MDI system, but additional work on the bonding between the adhesive and the substrate is necessary, and beyond the scope of this

body of work. Furthermore, this body of work studies the combined effect of HSWF and GnP on the properties of PUa, the effect of GnP on soft segments is the concern of future work.

Chapter 3 - Neat Polyurea Formulations

3.1. Introduction

As shown in the introduction, the processing-structure-property relationship of PUa has been extensively studied. The overall goal of this work is to test the effect of GnP additions on PUa. The previous chapter explored various PUa formulations as an adhesive. A novel PUa formulation was developed utilizing a two-component cartridge with a static mixing nozzle to mix and apply the adhesive. In this chapter the novel adhesives will be utilized, in a solvent cast process, to explore the phase separation behavior, and its effect on the properties of the PUa. In later chapters the results from this chapter will be used to compare to PUa-graphene composite. Much of this chapter has been published in *Experimental and modeling studies of IPDI-based polyurea elastomers – The role of hard segment fraction* [54]. The PUa components and formulation calculation are discussed in Chapter 2 but are also summarized here. The components are isophorone diisocyanate (IPDI), Jeffamine D2000 polyetheramine, which is a difunctional primary amine with an average molecular weight of 2000 g/mol, and Jeffamine T5000 polyetheramine, which is trifunctional primary amine with an average molecular weight of 5000 g/mol. Note the ratio of the D2000 and T5000 were kept the same in the prepolymer therefore soft segment cross-linking of the PUa is consistent across all three model PUa's.

3.1.1. Model PUa phase diagram

As discussed extensively in the literature [3], [31], [35], [41], [55], the mechanical properties of polyurethanes and polyureas depend on the phase separation between the hard and soft phases. Here, to guide the formulation development, a model phase map [27] based on a simple polyurethane system where one component is used in the isocyanate prepolymer (A-side).

A thorough review of the equations used to develop the model phase map was introduced in Chapter 1, Section 1.2.2. The key equations are summarized here.

Equation 3.1 is used to predict the degree of phase separation and phase boundaries for the various regions of the phase diagram.

$$(\chi N)_i = (\chi N)_o \left(\frac{1}{1-\frac{0.25-f_i(1-f_i)}{0.25-\alpha_i}} \right) \tag{3.1}$$

were $(\chi N)_i$ defines the boundary between the disordered-spherical (DS), SC (spherical-cylindrical) and CL (cylindrical-lamellar), i is the index for DS, SC and CL, $\alpha_i = f_i(1-f_i)$; $\alpha_{DS} = 0$, $\alpha_{SC}=0.098$, $\alpha_{CL}=0.206$. For block copolymers the prefactor $(\chi N)_0$ ranges 15-20. Equation 3.2 is used to estimate the Flory-Huggins interaction parameter (χ_{hs}) between the hard segments (h) and the soft segments (s).

$$\boldsymbol{\chi_{hs} = v_{ref}\left(\frac{(\delta_h-\delta_s)^2}{RT}\right) = v_{ref}\left(\frac{\left(\sqrt{(E_{coh})_h}-\sqrt{(E_{coh})_s}\right)^2}{RT}\right)} \tag{3.2}$$

where v_{ref} is the reference volume which was set to 58 cm^3/mol, δ_{hs} is the hard and soft segment solubility parameters, $(E_{coh})_{hs}$ is the hard and soft segment cohesive energy density. The chain lengths for hard and soft segments N_h and N_s are calculated by Equations 3.3 and 3.4 respectively.

$$N_h = \frac{\bar{M}_H}{2(\varrho_h v_{ref})} \tag{3.3}$$

where $\bar{\boldsymbol{M}}_H$ is the number average molecular weight of the hard segments, ρ_h is the density of the hard segments and v_{ref} is defined above.

$$N_s = \frac{E_s}{2(\varrho_h v_{ref})} \tag{3.4}$$

where E_s is the equivalent weight of the soft segment, ρ_s is the density of the soft segments and v_{ref} is defined above. In the chapter 1 equations only one type of amine was used, therefore the equivalent weight of the soft segment is simply the molecular weight of the soft segment (M_s)

divided by the molecule's amine functionality (f_p). In the model polyurea system there are two amine components to the prepolymer. Since the model system contains both difunctional and trifunctional amines with varying molecular weights, the phase diagram model is adjusted for average functionality and average molecular weight of the soft segments. Equation 3.5 is used to calculate the average molar mass (M_{avg}) for the binary prepolymer amine blend.

$$M_{avg} = X_d M_d + (1 - X_t) M_t \tag{3.5}$$

where X_d is the mole fraction of the diamine and M_d and M_t are the molar mass of the diamine or triamine, respectively. Equation 3.6 is used to calculate the average functionality.

$$fP_{avg} = f_d X_d + f_t (1 - X_t) \tag{3.6}$$

Here $f_d = 2$, $f_t = 3$ and are the functionalities of the diamine and triamine, respectively. Finally, the average equivalent weight of the soft segments (Eq_{avg}) can be calculated using Equation 3.7 and replaces E_s in Equation 3.4.

$$Eq_{avg} = \frac{M_{avg}}{fP_{avg}} = \frac{[X_d M_d + (1 - X_d) M_t]}{[2X_d + 3(1 - X_d)]} \tag{3.7}$$

The number average molecular weight of the hard segments is calculated using Equation 3.8.

$$\bar{M}_H = 2E_s \frac{f}{(1-f)} \tag{3.8}$$

where f is the total hard segment weight fraction. Just like in polyurethanes, the prefactor of 2 reflects that fact that urea bonds consist of 2 amines and 2 isocyanates. Finally, the Flory-Huggins interaction parameter can be calculated using Equation 3.8.

$$\chi N = \chi_{hs}[N_h + N_s] = \frac{(\delta_h - \delta_s)}{RT}\left[\frac{\bar{M}_H}{2\rho_H} + \frac{E_s}{\varrho_s}\right] \tag{3.9}$$

Based on the above procedure, a phase diagram can be plotted where the interaction parameter can be plotted as function of weight fraction of HS (f_{HS}).

The solubility parameters, δ_h and δ_s, were estimated using the Synthia function in Materials Studio. The molecules for both the hard segments and soft segment were drawn in Materials Studio utilizing the sketching toolbar. The clean function was used to optimize the geometry of the hard and soft segments. Figure 3-1a shows the molecules for the hard segment. It contains one IPDI and one DEDTA molecule connected by the isocyanate functional group. The hydrogen atoms at each end were chosen for the head and tail of the hard segment, highlighted in light blue and magenta, respectively. Figure 3-1b shows the molecule for the soft segment. It contains just the polypropylene glycol back bone. The carbon atoms at each end were selected as the head and tail of the soft segment, highlighted in light blue and magenta, respectively. Table 3-1 summarizes the results of the solubility parameters obtained from Materials Studio calculations.

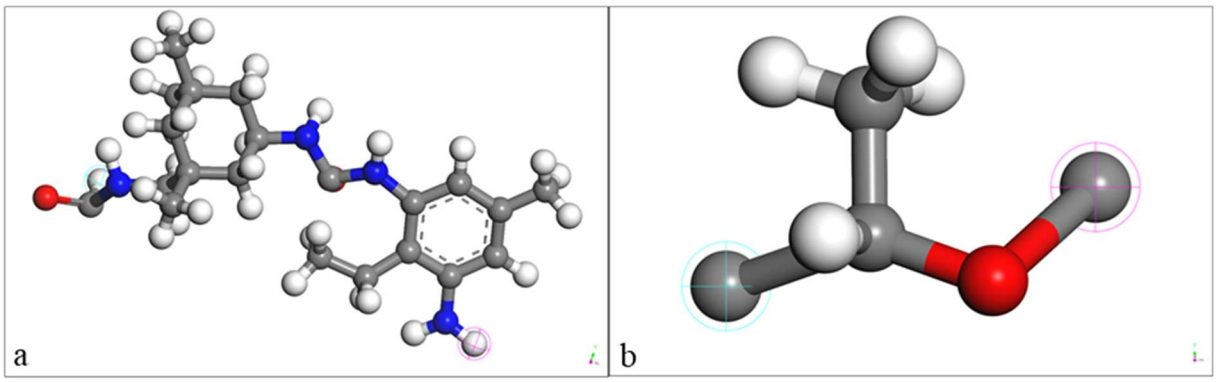

Figure 3-1. Material Studio sketch of the PUa hard segment a), and the PUa soft segment b). The hard segment consists of DETDA and IPDI. The soft segment consists of the polypropylene glycol backbone. The red atom is oxygen, the grey atoms are carbon and white atoms are hydrogen.

Table 3-1. Solubility Parameters obtained from Materials Studio.

	Hard Segment Solubility Parameter (δh)	**Soft Segment Solubility Parameter (δs)**
van Krevelen	20.57	17.42
Fedors	25.07	16.98
Average	22.82	17.20

Figure 3-2 plots the Flory-Huggins interaction parameter as a function of hard segment weight fraction. Note the van Krevelen solubility parameter predicts that the microstructure would be completely disordered but the Fedor solubility parameter predicts phase separation. Often, a better estimate of a true segregation strength is obtained by using the average of the two solubility parameters (V. Ginzburg, unpublished).

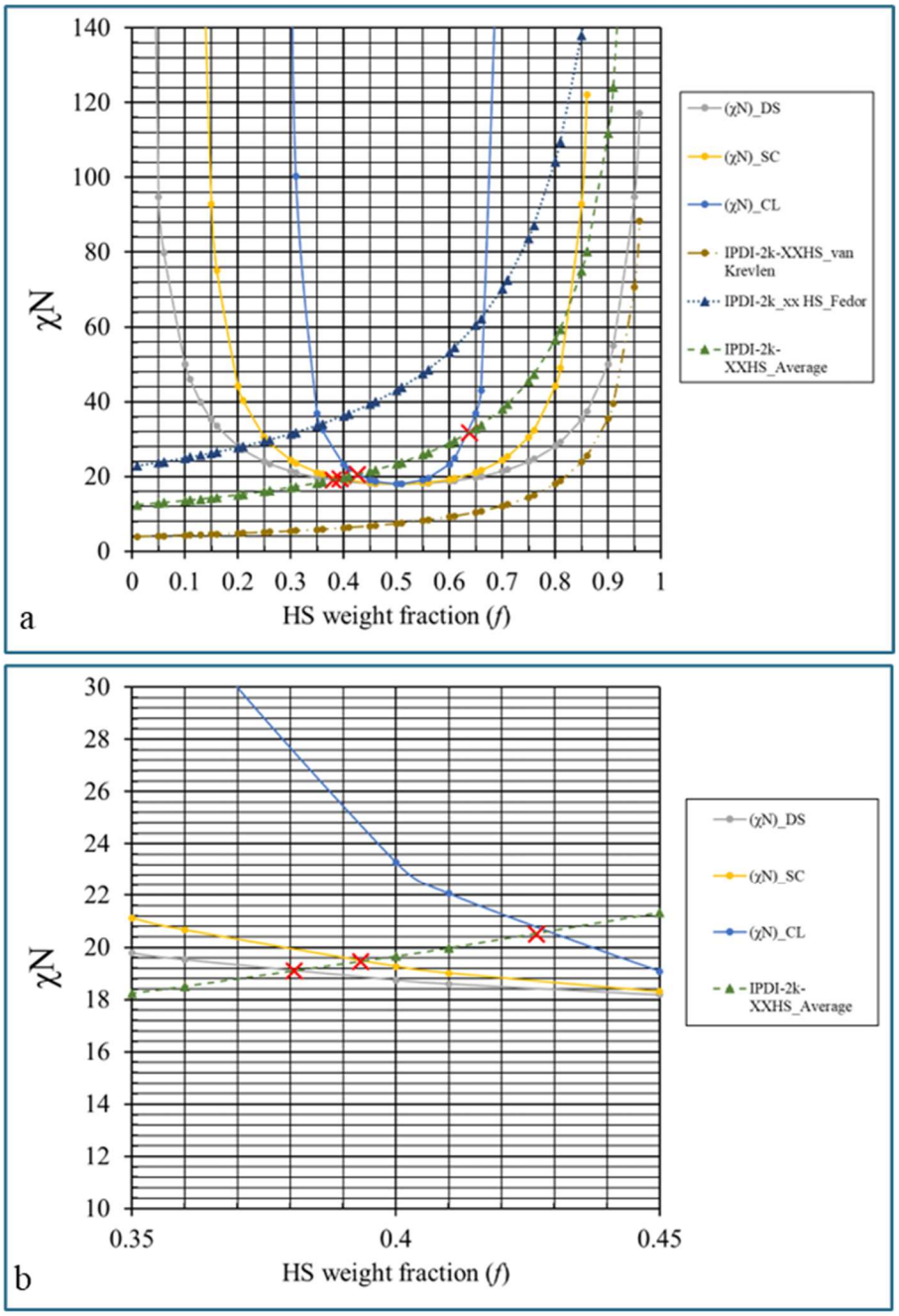

Figure 3-2. Flory-Huggins interaction parameter as a function of weight fraction of hard segments. a) showing the Flory-Huggins interaction parameter using the van Krevelen, Fedor, and the average solubility parameter. b) an enlarged portion of a) showing the intersection of the Flory-Huggins interaction parameter using the average solubility parameter and the intersection of the phase field boundaries.

3.1.2 Formulation Desing and Polymer Synthesis

The formulation design and its calculations are identical to the two-part adhesive cartridges, see Chapter 2.2.1 for detailed calculations. Here the process was switched from the two-part adhesive cartridge with a static mixing nozzle to a solvent cast process. Note that the chemical constituents and quantities were identical, Table 3-2. The solvent cast process slows the reaction time to allow for thorough mixing of the various components during the reaction. Also note that in later chapter GnPs are introduced and a dispersion media is needed to properly disperse the GnP.

Table 3-2. Summary of chemical constituents and quantity used in the IPDI based PUa using the solvent cast process.

	Component	**IPDI-2k-20HS**	**IPDI-2k-30HS**	**IPDI-2k-40HS**
Isocyanate Prepolymer (A-Side)	**IPDI**	30.8 g	41.6 g	52.1 g
	T5000	14.5 g	12.1 g	10.1 g
	D2000	57.1 g	48.5 g	40.4 g
	Toluene	82.7 g (95 ml)	165.3 g (190 ml)	208.8 g (240 ml)
	%NCO	8.7 %	12.9 %	15.3 %
Amine Blend (B-Side)	**DETDA**	10 g	19.4 g	29.3 g
	D2000	90 g	80.6 g	70.7 g
Processing	**Index**	1.05	1.05	1.05
	Iso:Amine Vol Ratio	1.00	1.00	1.00
	Iso:Amine Weight Ratio	1.02	1.02	1.17
	%HS	20.2 %	30.2 %	40.0 %

3.2 PUa Casting Process

IPDI-Vestanat was obtained from Evonik Corporation. Jeffamine T5000 and D2000 polyetheramines were obtained from the Huntsman Corporation. The diethyltoluene diamine (DETDA) (Lonzacure) was obtained from Lonza. Toluene was purchased from Fisher Scientific. All materials were used as received with no further processing.

The polyurea prepolymer was made by placing the required amount of IPDI into the reactor. The target weights of each component are listed in Table 3-2. Toluene was added to prevent the high hard segment formulations for gelling in the reactor. The amine blend for the prepolymer, a mixture Jeffamine D2000 and T5000 was mixed for 5 minutes in a separate 250 ml beaker at room temperature followed by degassed for approximately 10 minutes. The amine prepolymer blend was poured into an addition funnel. Similarly, the amine blend for the B-sided, a mixture of Jeffamine D2000 and Lonzacure DETDA, was mixed for 5 minutes in separate 250 ml beaker followed by vacuum degassing for approximately 10 minutes and then poured into a separate addition funnel. The reactor was assembled and then a vacuum was drawn for five minutes, after which N_2 gas at 0.3-0.4 l/min flow rate was introduced to the reactor. The reactor temperature was raised to 80 ^oC and then A-side amine blend was added dropwise under mechanical stirring at 120 RPMs. The solution was stirred for an additional hour at 80 ^oC after the last drop of the A-side amine blend was added. After the hour, the reactor was chilled to 0 ^oC and the B-side amine blend was added dropwise. Mechanical stirring is kept at 120 RPMs. Once all the B-side was added, the reactor was bottom tapped and into a 600 ml beaker and then degassed for 5 minutes, followed by pouring into molds. The molds were constructed from 145 mm glass petri dishes. 6.35 mm plate glass is placed in the petri dish and a spray on mold release was used. The petri dishes were then covered and placed on a level surface. The molds sat for 24 hours to allow for gelation and solvent extraction. After 24 hours the samples were placed in an oven at 40 ^oC, for 12-24 hours, to increase the rate at which the solvent is extracted. Curing of the PUa was completed at 60 ^oC for 72 hours.

3.3 PUa Characterization

Solvent extraction was measured using thermogravimetric analysis (TGA) techniques; a TA instruments Q5000 was utilized. Platinum pans were tared on the Q5000 and approximately 15 mg to 20 mg of the PUa was placed on the pan. The final weight was measured by the Q9000. The samples were heated at a rate of 3 ^{o}C/min and the weight change with temperature was recorded.

Differential scanning calorimetry (DSC) was measured on a TA instruments DSC2500. Approximately 15 mg of the PUa was weighted out and placed in a premeasure Tzero hermetically sealed pans. The samples were heated at a rate of 3 ^{o}C/min and the change in heat flow (q) with temperature was recorded. Each sample pan was cycled through a heat-cool-heat experiment, where the sample was equilibrized at -90 ^{o}C then heated to between 200 and 250 ^{o}C depending on the formulation. Subsequently the sample was cooled to -90 ^{o}C at a rate of 3 ^{o}C/min followed by a second heating cycle.

Dynamic mechanical analysis was conducted using a TA instruments RSA-G2 instrument. The curing of the polymer was determined by measuring the change in storage modulus with respect to time. All film samples were loaded in tension. To determine the linear elastic region of the PUa, strain sweeps were run at -95 ^{o}C from 0.001% to 1% strain, at 0 ^{o}C from 0.001% to 5% strain, at 50 ^{o}C, 0.01% to 5% strain, and 0.1 to 5% strain. All subsequent DMA testing was conducted within the linear viscoelastic region. Temperatures sweeps were conducted from -95 ^{o}C to a max temperature depending on the polyurea formulation hard segment content. The reference temperature for the TTS, 25 ^{o}C, was also included in the frequency sweeps. All TTS shifts were completed with TA instruments TRIOS software package.

Tensile properties were measured on an Instron 5586A tensile tester. An Instron 1 kN load cell was used to measure the force and the extension was measured utilizing an Instron AVE-2 non-contact video extensometer. The crosshead speed was set 200 mm/min. Finally, the ISO37 Type 3 tensile specimens were used. All tensile specimens were stamped using electromechanical stamper and a pre-certified stamping die.

Thin TEM specimens were sectioned from the bulk polymers of 20%, 30%, and 40% HS formulations using a Leica EM FC7 attached on the Leica UC7 ultramicrotome. The thickness of samples ranged from 75 to 100 nm. After sectioning, the TEM specimens were stained with a 0.5% ruthenium tetroxide (RuO_4) solution for 15–30 min at room temperature. Microstructure image and electron energy loss spectroscopy (EELS) analysis were carried out using a JEOL JEM-2100F equipped with a Schottky field emission gun and Gatan GIF Quantum image filter and spectrometer. In the present work, the microscope was operated at 200 kV for both image and EELS analytical work. Images were taken under TEM bright-field (BF) mode, whereas EELS analysis was done in scanning transmission electron microscopy (STEM) mode with a probe size of 1 nm and convergence and collection semi angles of 7 and 13 mrads, respectively.

3.3 Results

3.3.1 Gelation Time

The gelation time was measured using a standard gelation timer from Gardco. A low torque synchronous motor rotates a specially shaped stirrer in resin mixture. As gelation occurs, drag exceed torque and the motor stall. The gel time is recorded at motor stall. Approximately 50-52 grams of the liquid polyurea formulations were poured into a measured cup. The time to stall was recorded.

In the solvent cast process of polyureas, DMF is a better choice as a solvent but for GnP dispersing toluene is a better solvent [REF]. For this work toluene was chosen as a solvent because it showed greater GnP dispersion in the nanocomposite, as will be shown in Chapter 4. For processing reasons of these PUa it was important to balance the working time in the reactor including the bottom tapping and vacuum degassing of the final PUa with the amount of solvent used. The higher the hard segments the quicker the reaction would gel and, in some cases, would gel either in the reactor or during the vacuum degassing. Therefore, enough toluene was added to ensure the time to mix in the B-Side, tap the reactor and degas without gelation of the PUa Table 3-3 shows the gelation time for each Polyurea Formulation along with the total solvent used. The gelation time decreases with an increase in the number of hard segments regardless of the volume of toluene added. In general, the gelation time gives an indication of the time the reaction takes to go to completion and the polymer molecular weight increases to point where the polyurea becomes a gel.

Table 3-3. Gelation time of the polyureas.

	IPDI-2k-20HS	**IPDI-2k-30HS**	**IPDI-2k-40HS**
Toluene Solvent	82.7 g (95 ml)	165.3 g (190 ml)	208.8 g (240 ml)
Solvent to PUa ratio	0.29	0.45	0.51
Gelation Time	84 min	51 min	23 min

In general, as the percentage hard segments increased more toluene was needed to keep the reaction from gelling inside the reactor. For the 30 and 40% HS the ratio of toluene to PUa components was as high as 50%. This resulted in high levels of distortion and cracking in the higher high segment films. To address the cracking issue the 40% HS was placed in a freezer (at -12 ^{o}C) to slow the degassing process allowing the PUa to completely gel and slightly harden.

3.3.2 Fourier Transform Infrared Spectroscopy

A Thermo Scientific Nicolet IS50 Fourier Transform Infrared (FTIR) spectrometer was determined to follow the chemical reaction. A germanium crystal was utilized, and the spectrometer was set to the attenuated total reflectance mode.

Figure 3-3 shows the FTIR spectrum for all reactants used in the PUa reaction. The key peaks involved in the PUa reaction are the strong isocyanate peak of the IPDI seen at 2255 cm^{-1}, the N-H stretching peak of the primary amine peaks found between 3400 – 3500 cm^{-1} in the DEDTA. Although the structure of D2000 and T5000 contain primary amines no N-H stretch peak was found. This is most likely due to fact that the primary amine is only a small portion of the molecular structure of both the D2000 and T5000 diamines.

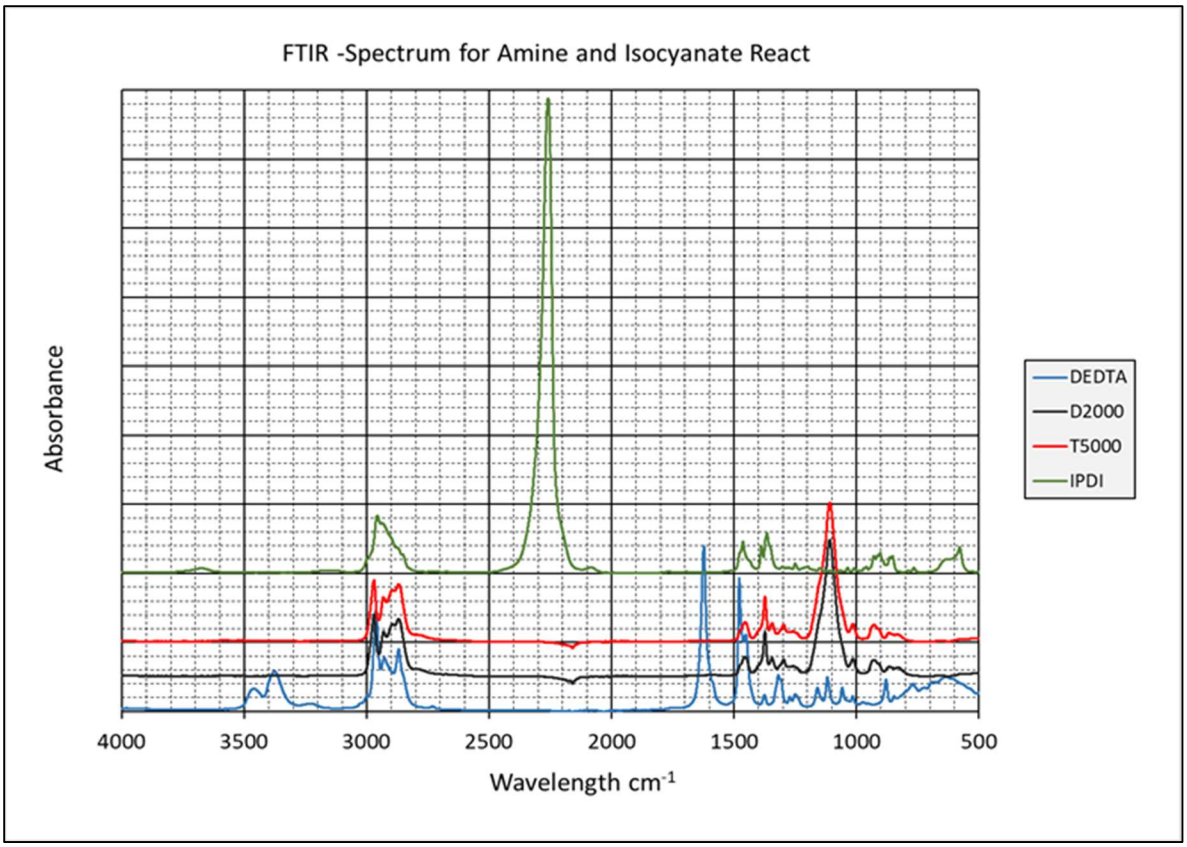

Figure 3-3. FTIR spectra for the D2000, T5000, DETDA, and IPDI.

Figure 3-4 shows the FTIR spectrum for the IPDI based polyureas. The strong isocyanate peak found in the IPDI has disappeared and the deconvoluted N-H stretching peaks found at 3400-3500 cm^{-1} are now convoluted indicating that the amines are now secondary. The absence of the Isocyanate peaks and the convolution of the N-H stretching peaks indicate the urea reaction has gone to completion and no free isocyanate remains. An absorption band was found at 2263 cm^{-1} indicating in the 20% HS sample indicating a small amount of free isocyanate remaining.

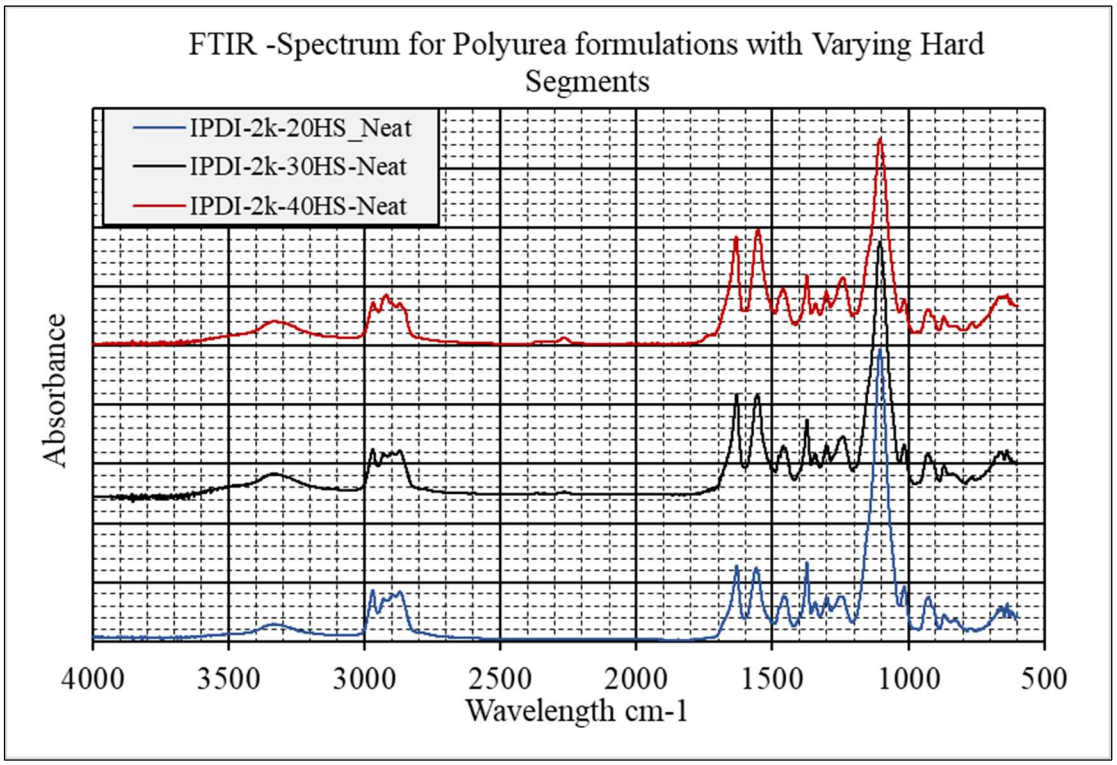

Figure 3-4. FTIR Spectra as function of the weight fraction of PUa.

Figure 3-5 compares the FTIR spectra for the isocyanate prepolymers (first half of the reaction sequence). In the case of the prepolymers, there are three peaks, 1638 cm^{-1}, 1678 cm^{-1} and 1720 cm^{-1}. The peaks at 1720 cm^{-1} indicate the presence of a free or non-hydrogen bonded carbonyl [32]. The peaks at 1678 cm^{-1} indicate the presence of "disordered' hydrogen structure where only one N-H is interacting with the carbonyl group in an interphase of hard and soft segments [56]. Finally, the peaks at 1638 cm^{-1} are associated with a more "ordered" hydrogen

bonding structure where two N-H groups are interacting with the carbonyl forming the hard phase. Figure 3-6 shows the spectra in the carbonyl region after the reaction is complete and the polymers are cured. For all three formulations, the free carbonyl peak at 1720 cm^{-1} disappears. The "order" peaks at 1638 cm^{-1} increase in intensity, and the disorder peak 1678 cm^{-1} now convoluted within the "ordered" peak. Figure 3-6 also shows that as the hard segment content increases so does the intensity of the "order peak", possibly indicating a large amount of hard phase formation. A similar trend is seen in the amine region of the spectra, Figure 3-7.

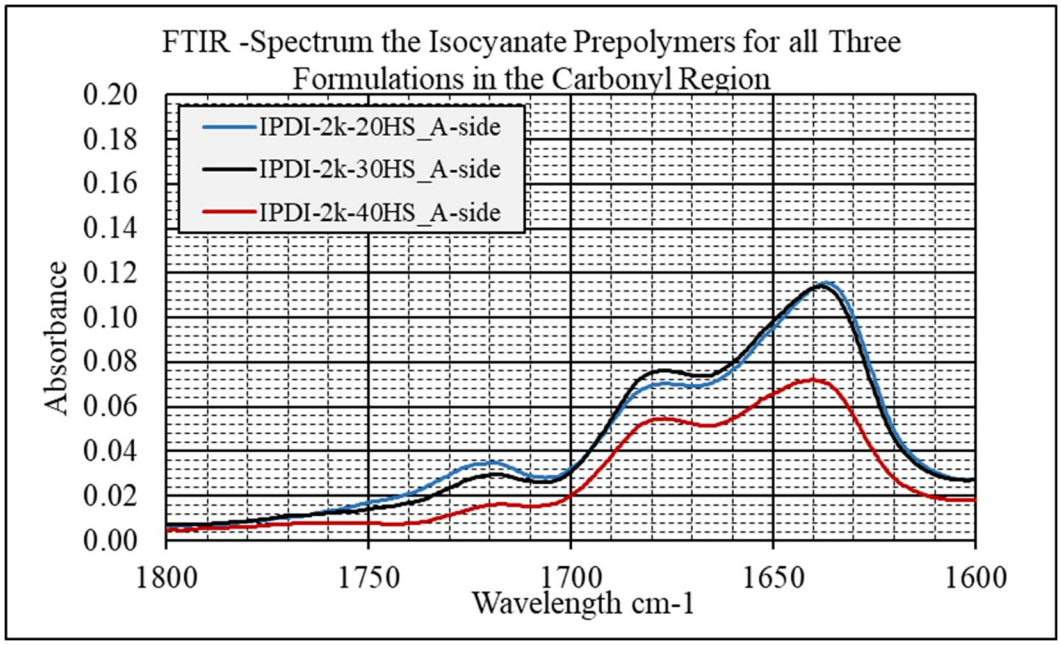

Figure 3-5. The carbonyl region of the FTIR Spectrum for the isocyanate prepolymers (A-side) used in all three formulations.

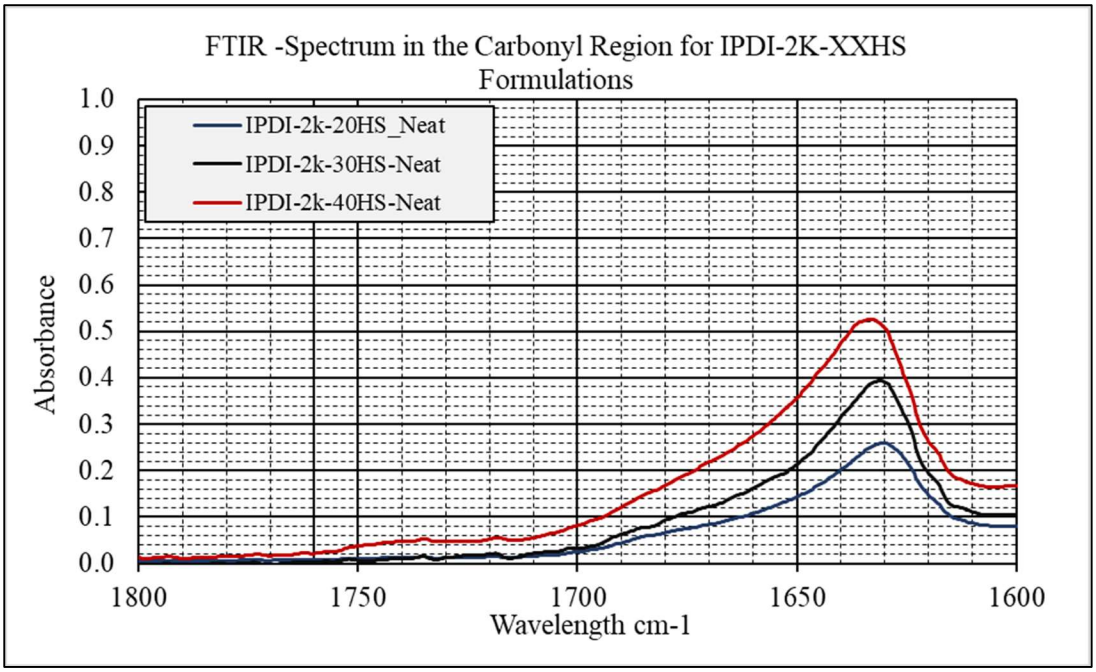

Figure 3-6. The carbonyl region of the FTIR spectra in the carbonyl region for all three formulations after reaction is complete.

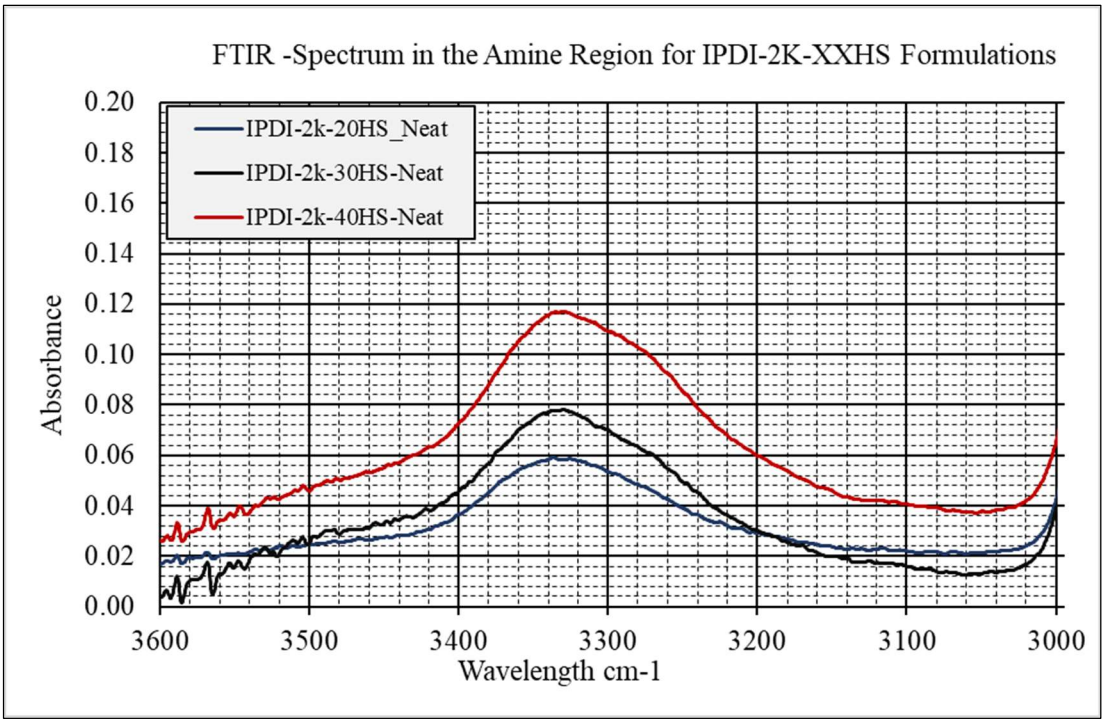

Figure 3-7. FTIR spectra in the amine region for all three formulations.

3.3.3 Thermogravimetric Analysis

Solvent extraction was monitored by TGA and the weight loss at the boiling point of toluene (110.6 ºC). Figure 3-8 a-c shows the TGA thermograms for IPDI-2k-30HS, IPDI-2k-20HS, and IPDI-2k-40HS respectively.

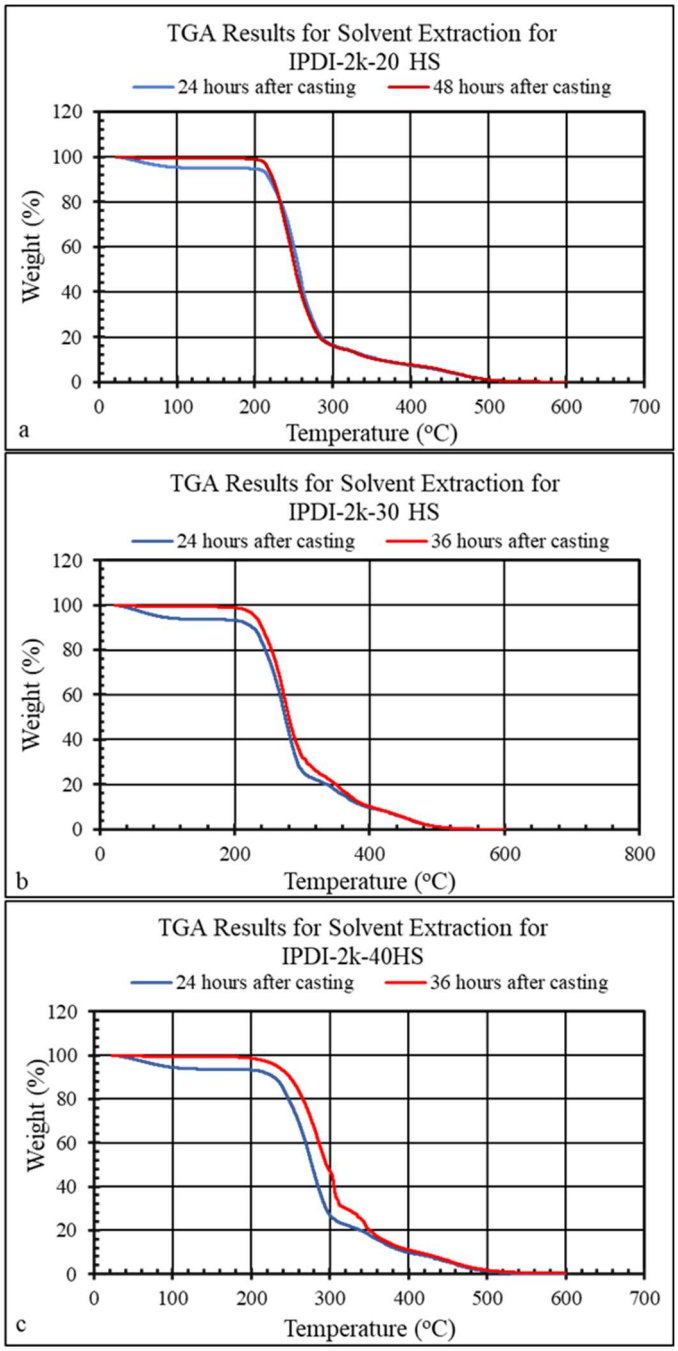

Figure 3-8. TGA results for the solvent extraction process of a) IPDI-2k-20HS, b) IPDI-2k-30HS PUa, c) IPDI-2k-40HS.

The figures show two thermograms, one at approximately 24 hours after the PUa was cast and one after the solvent extraction process was completed, i.e., a minimum of 24 hours at 40 ºC. Table 3-4 summarizes the weight loss at 110.6 ºC at both 24 hours after casting and at the end of solvent extraction process. For all three formulations the weights loss at 110.6 ºC is less than 1 percent of the weight and may not be completely associated with the loss toluene. To determine if the solvent extraction process was sufficiently completed, TGA thermograms were also run-on samples that were created through a 2-component adhesive static mixing system where no solvent was used. Table 3-4 compares the weight loss at 110.6 ºC for approximately 24 hours, end of the solvent extraction and non-solvated samples. The weight loss after the solvent extraction process was similar to the samples where no solvent was added. Therefore, most of the toluene is extracted and any remaining toluene would be considered trace.

Table 3-4. Summary of Thermogravimetric Analysis for the solvent extraction process.

	IPDI-2k-20HS	**IPDI-2k-30HS**	**IPDI-2k-40HS**
24 hours after casting	4.737 %	5.914 %	7.179 %
End of solvent extraction	0.581 %	0.601 %	0.535 %
No added solvent	0.852 %	0.531 %	0.697 %

Figure 3-9 compares the thermograms of the polyurea for all three formulations after curing. Increasing the percentage of hard segments in the formulations causes the thermograms to shift to high temperatures. This is illustrated by the extrapolated onset temperature, which defines the point where the polyureas start to degrade, and the temperature at which 50% of the mass loss has occurred. As the HSWF increases the onset temperature increases, Table 3-5 summarizes these results.

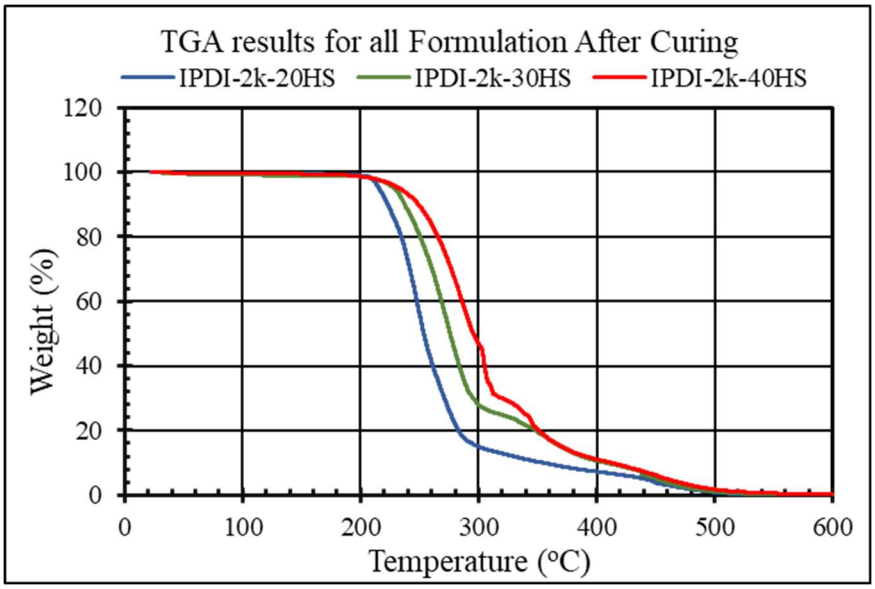

Figure 3-9. Thermograms for all formulations after the solvent extraction.

Table 3-5. TGA summary of PUa formulation after curing.

	IPDI-2k-20HS	IPDI-2k-30HS	IPDI-2k-40HS
Onset Temperature	214 ºC	229 ºC	246 ºC
@ 50 % weight loss	254 ºC	276 ºC	296 ºC

3.3.4 Differential Scanning Calorimetry

Figure 3-10 shows the results of the DSC runs for all three formulations. In the first run there is an approximately 6 °C shift in the low temperature T_g (summarized in Table 3-6) as the number of hard segments are increased,

Table 3-6. DSC results for all three formulations.

Formulation	**T_g 1st heating run**	**T_g Cooling Run**	**T_g 2nd heating run**
IDPI-2k-20HS	-61.2 °C	-64.5 °C	-62.6 °C
IPDI-2k-30HS	-58.6 °C	-65.1 °C	-62.3 °C
IPDI-2k-40 HS	-55.4 °C	-66.0 °C	-63.4 °C

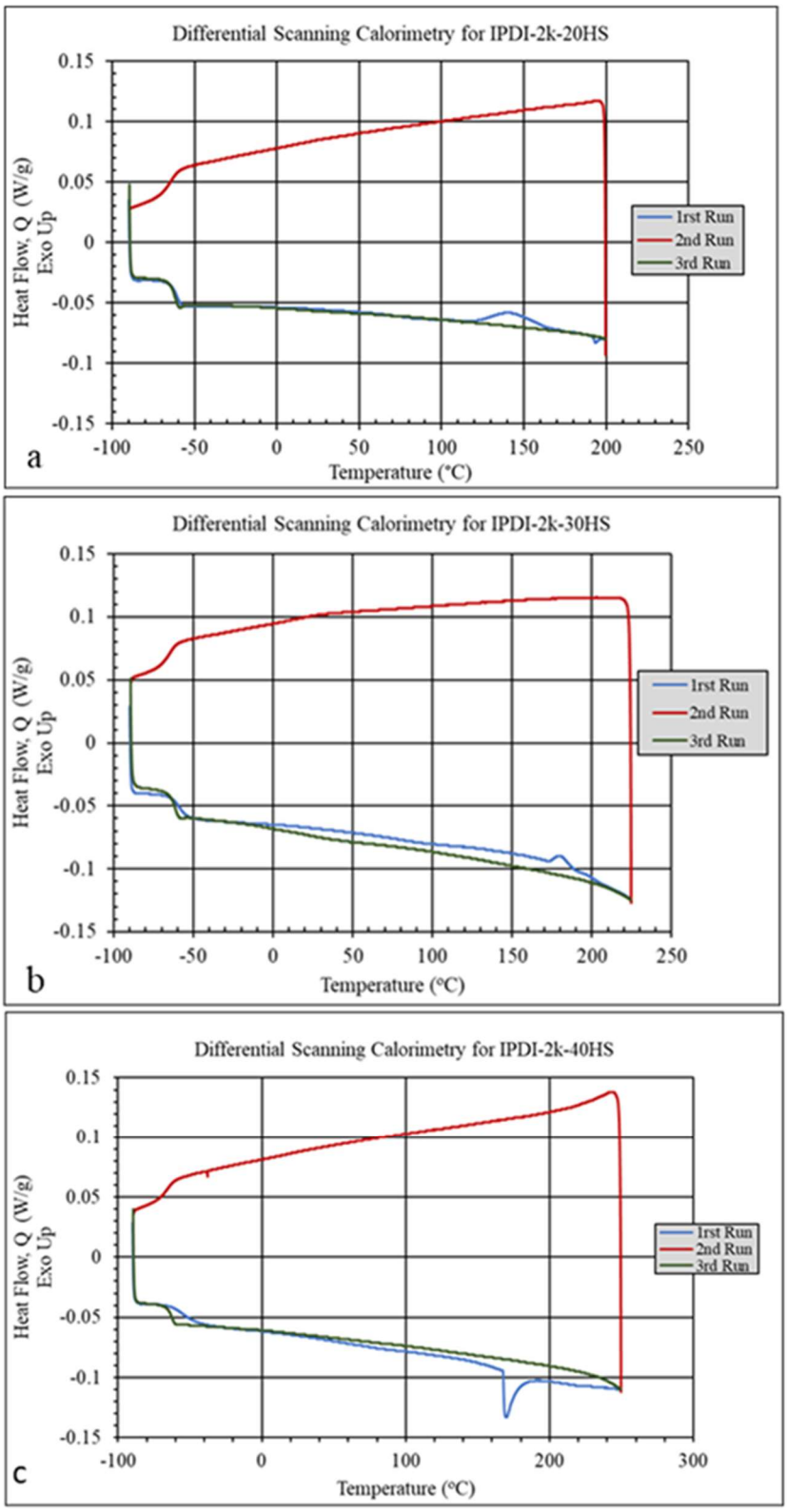

Figure 3-10. DSC curves for all three PUa formulations.

As the HSWF is increased, the soft-phase T_g for the first heating run increases in a nearly linear fashion. This is similar to, for example, Iqbal et al. [28], [57] or Christenson et al [58] and can be attributed to the increase in the hard segments dissolved in the soft phase and thus increasing its glass transition temperature. The effect becomes less pronounced for the cooling and the second heating run. At higher temperatures, in the first heating run, there is a second transition corresponding to the transformations within the hard-phase domains. This transition is strongly exothermic ($\Delta H = 5.4$ J/g) for the 20% HSWF material, weakly exothermic ($\Delta H = 1.5$ J/g) for the 30% HSWF material, and strongly endothermic ($\Delta H = -7.3$ J/g) for the 40% HSWF material. This transition is due to thermal annealing of the hard domains, with multiple hydrogen bonds inside the domains breaking and re-forming. For the 20% HSWF material, the first heating run results in the "net" decrease in the overall hydrogen bond density ("melting-like behavior"), for the 30% HSWF material, the overall hydrogen bond density is nearly unchanged, and for the 40% HSWF material, the overall hydrogen bond density increases ("crystallization-like behavior"). Upon subsequent slow cooling and reheating, no high temperature transitions were observed, suggesting that a single thermal annealing was enough to equilibrate the system.

3.3.5 Dynamic Mechanical Analysis.

Dynamic Mechanical Analysis (DMA) was used to determine the time needed to cure the samples. Figure 3-11 tracks the storage modulus over time for the three polyurea samples. Initially a steep increase in storage modulus is seen, but after about 100 min only small increases are seen. Effectively the cure time at 60 ^{o}C is approximately 100 minutes but a final curing time of 3 days was chosen. This was done for convenience; the curing process was done over weekends.

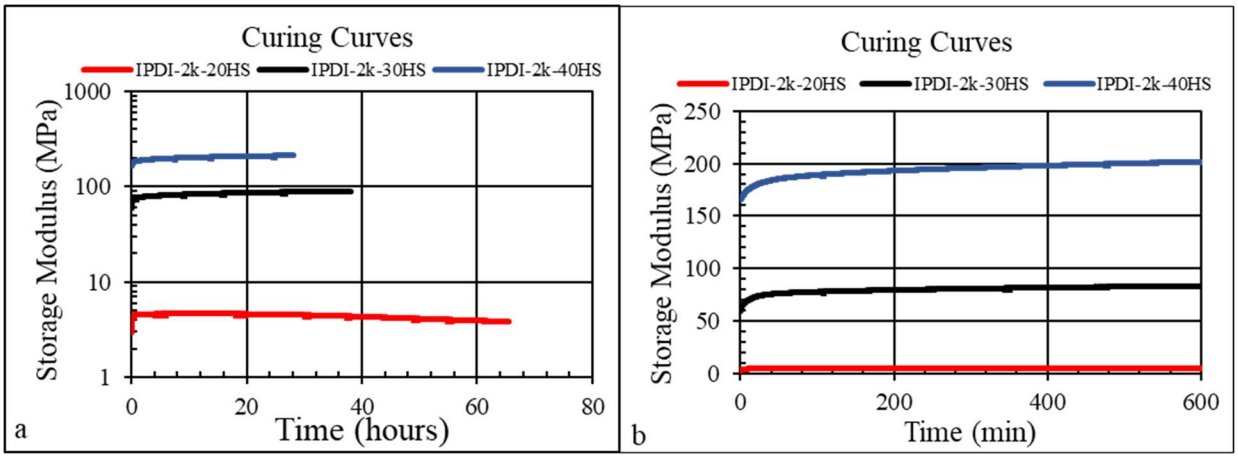

Figure 3-11. - DMA curves tracking the storage modulus as curing of the PUa occurs. a) shows the evolution of the modulus over longer periods of time. b) is the same curve as (a) but in this case showing most of the change in modulus occurs over the first 200 min of curing.

Figure 3-12 shows the DMA temperature sweeps (at frequency 1 Hz) for the three PUa formulations. Based on these results, we first calculate the soft-phase T_g based on the onset temperature of the storage modulus and the peak temperatures of the loss modulus and the tan (δ) curves [59]. Table 3-7 summarizes the glass transition temperatures. The glass transition is relatively broad (given the spread between the different Tg measures); also, the DMA-measured T_g agrees well with the DSC-measured one, as one would expect. Figure 3-13a compares the storage moduli of all three formulations. In the glassy region, below the T_g, the three materials differ very weakly. There is a slight increase of the glassy modulus as the HSWF is increased, consistent with the standard "nanocomposite" description of segmented PUas and the likely slight difference between the modulus of the hard phase and the glassy modulus of the soft phase [18]. In the transition and rubber regions of the curves a significantly more pronounced effect is seen with respect to the hard segment content. The temperature range of the transition from the glassy state to the amorphous state increases with increasing hard segment content. The rubbery plateau increases in both modulus and temperature range with increasing HSWF. The room temperature (25 °C) storage modulus has increased with the increase in HSWF from 20% to 40% by a factor

of approximately 35, consistent with the concept of hard-phase percolation [6], [18], [58], [60]. This increase is also seen in the loss moduli, Figure 3-19 b.

The increase in HSWF is also influencing the rubbery region of the storage modulus, Figure 3-19 a. For the 20% HS polymer, a rubbery plateau is almost non-existent, while for the 30% and 40% HS a plateau is pronounced and extends to fairly high temperatures (>120 ^{o}C) where both hydrogen and polyether covalent bonds begin to break. In general, the breadth of the plateau increases with increasing hard segment content. Similar trends are seen in the loss moduli curve, Figure 3-13 b. Supporting Figure 3-13 c shows the effect of HSWF on the tan (δ) of the model polymers. As the hard segment content is increased, the peak of the tan (δ) curves decreases -- indicating that the higher hard-segment polymers have a smaller dissipative capacity.

Table 3-7. Glass Transition of the IPDI-based polyureas for 20, 30 and 40 % hard segments.

	T_g (^{o}C) Onset Storage Modulus	**T_g (^{o}C) Peak Loss Modulus**	**T_g (^{o}C) Peak Tan Delta**
IPDI-2k-20HS	-59.6	-57.2	-49.1
IPDI-2k-30HS	-58.2	-54.5	-48.7
IPDI-2k-40HS	-57.9	-56.0	-44.0

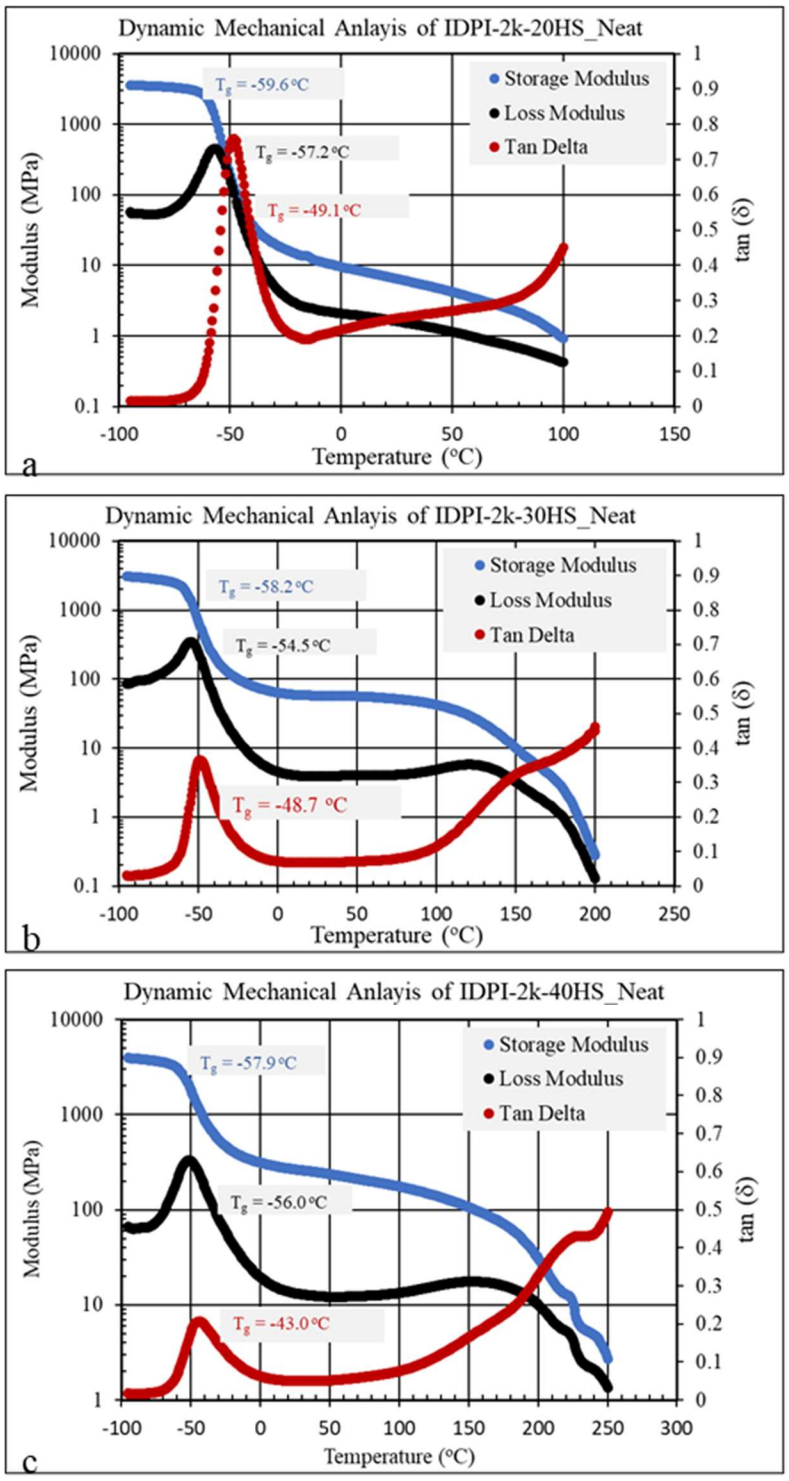

Figure 3-12. Dynamical mechanical analysis temperature sweep showing the storage and loss moduli, and tan (δ) for all three PUa formulations. (a) 20% hard segment; (b) 30% hard segment; (c) 40% hard segment.

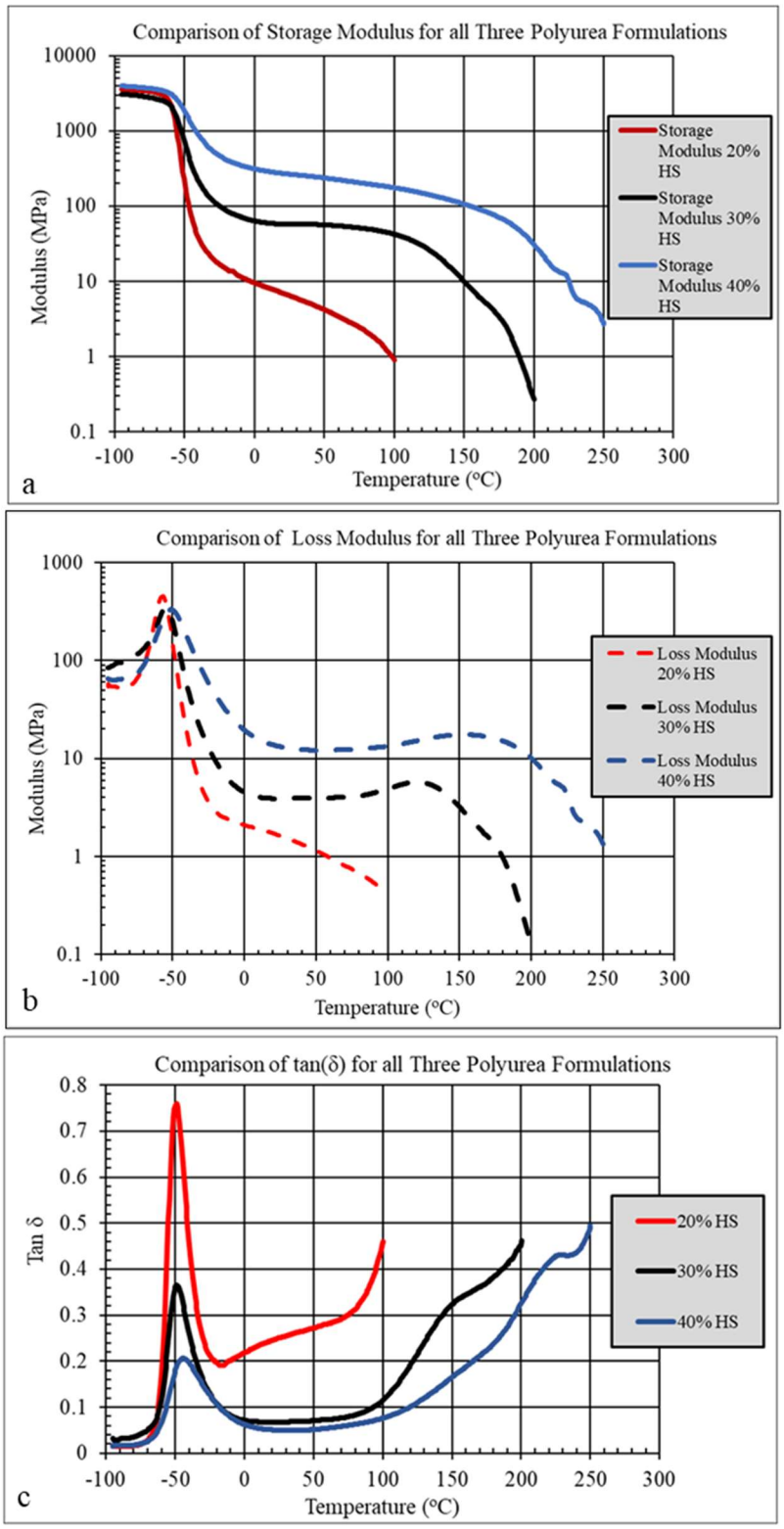

Figure 3-13. Comparison of the Storage Modulus (a), Loss Modulus (b), and tan(δ) for all three formulations.

3.3.6 Tensile Testing

Figure 3-14 shows the tensile curves for the IPDI-2k-20HS, 30HS and 40HS formulations. The pertinent mechanical properties are summarized in Table 3-8. The toughness (area under the stress strain curve) of all three formulations by integrating the area under the stress strain curve. The toughness (U_T) was calculated for all formulations utilizing Equation 3-10.

$$U_T = \int_0^{\varepsilon_f} \sigma d\varepsilon \tag{3.10}$$

where ε_f is the failure strain, σ is the stress, ε is the strain. The trapezoidal rule was utilized to estimate the integral. The toughness from 20 to 30 % HS increases and then decreases from 30 to 40% HS.

Table 3-8. Summary of Tensile Data for all three neat IPDI formulations.

Formulation	**Secant Modulus**	**Tensile Strength @ Failure (MPa)**	**Tensile Strain @ Failure (%)**	**Toughness (J/m^3) $x10^7$**
IPDI-2k-20HS	3.3 +/- 0.52	2.7 +/- 0.1	814 +/- 15	2.0 +/ 0.1
IPDI-2k-30HS	63.0 +/- 6.3	18.2 +/- 1.21	782 +/- 33	8.2 +/- 0.5
IPDI-2k-40HS	203.9 +/- 8.9	17.1 +/- 0.5	397 +/- 22	5.0 +/- 0.7

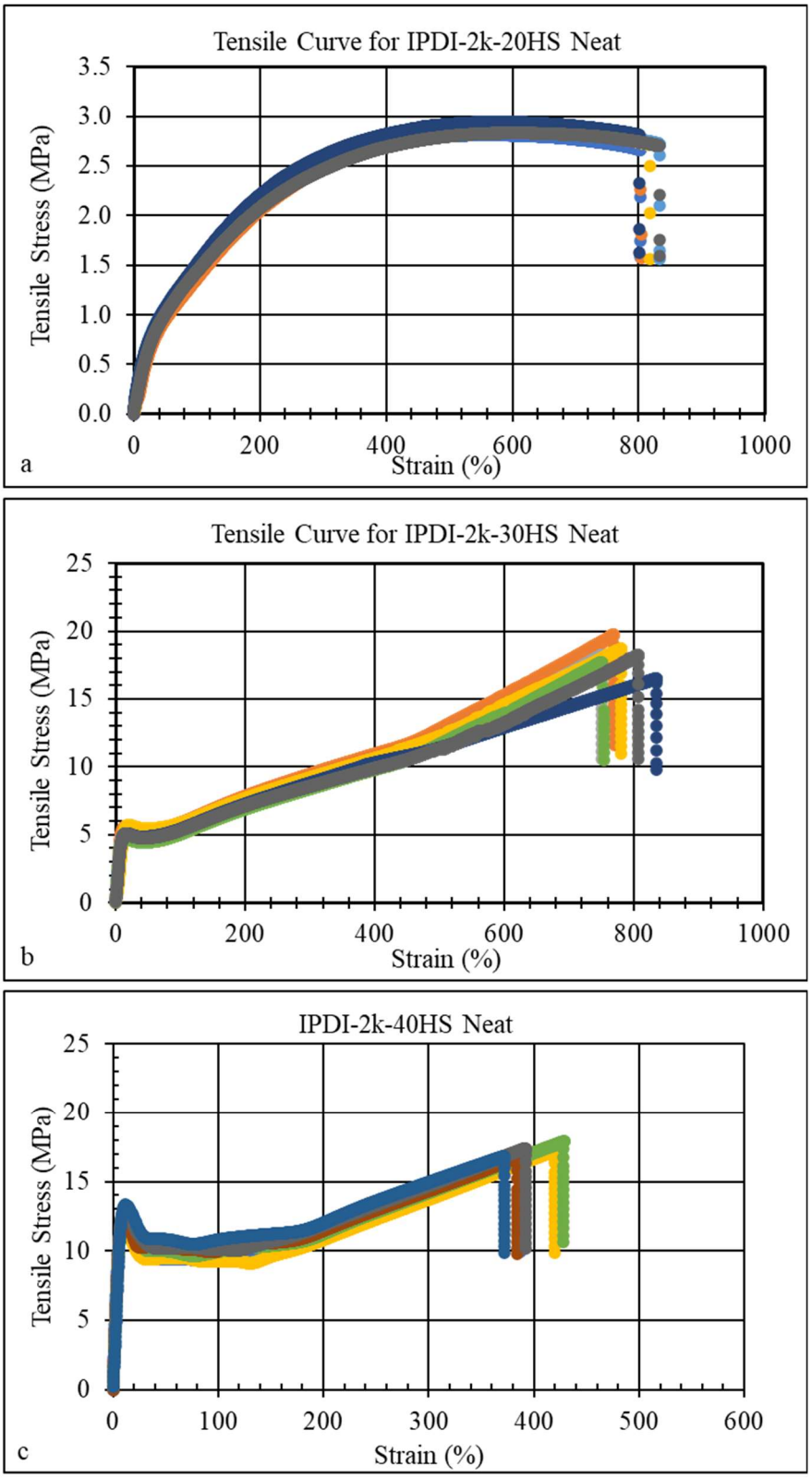

Figure 3-14. Tensile curves for the PUa formulations a) 20 % HS, b) 30% HS, c) 40% HS.

The 2% secant modulus was calculated as a function of the HSWF. As expected, the higher the HSWF the higher the modulus [33], [55]. The 20%HS PUa did not show a definitive yield point. The yield strength increased by a factor of 2, between the 30% HS and 40% HS samples. It was interesting to note that tensile curves for the 20% HS sample do not show a drop in stress (due to necking) typically seen in polymers and no necking was visual observed during the testing. In fact, the tensile curve exhibited a stain hardening region between 40 and 400 percent, which a plateau region between 400 and 600 percent followed by a slight drop in stress until final fracture. Note the SEM examination of the fracture surface of the polymer showed no distinguishing fracture features, Figure 3-15.

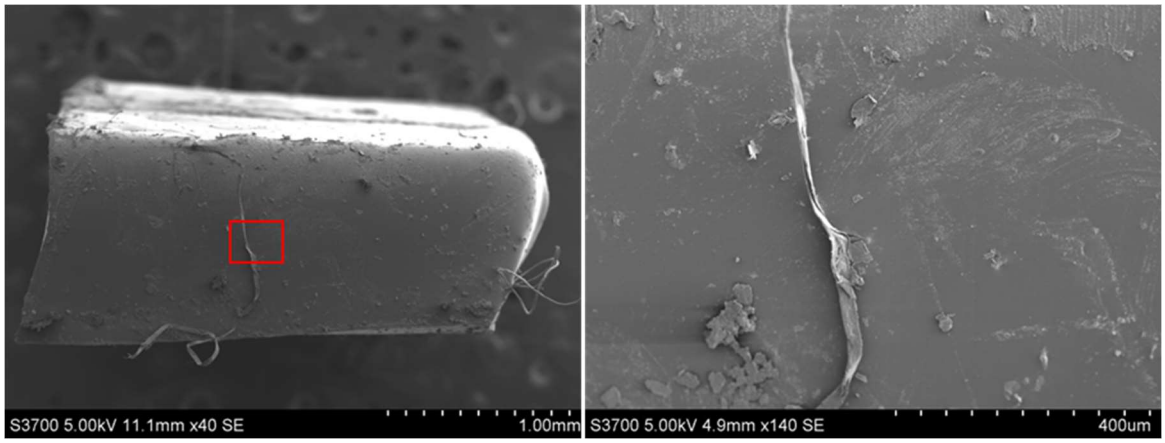

Figure 3-15. SEM fractography showing the fracture surface of the 20% HS PUa. a) low magnification showing the complete fracture surface, b) higher magnification of the red box from a). Note the absence of fracture features such as dimples, cleavage facets, etc.

As previously mentioned, the IPDI-2k-30HS did have a distinct yield point with a necking short region, especially when compared to the 40% HS PUa. The cold drawn region was short, only approximately 60% strain, but significant amount of strain hardening was evident. Two separate strain hardening slopes were seen for both the 30% and 40% HSWF.

The SEM examination of the fracture surface for the 20% HS showed hackle lines, outwardly divergent “river pattern” pointing back to the fracture origin, lower right corner in Figure 3-16a. The hackle line represents multiple crack surfaces being formed during crack

propagation and failure. The SEM examination of the 40% HS fracture surface also showed Hackle lines, Figure 3-17, similar to what is seen in the 30% HS. In comparing the fracture surface of the 40% HS back to the 30% HS surface the Hackle lines are more visual numerous. It is interesting to note that as the HSWF weight fraction is increased the Hackle lines increase. This would indicate the HS may be providing a more tortuous path for the crack to travel. This will be further explored in Chapter 4.

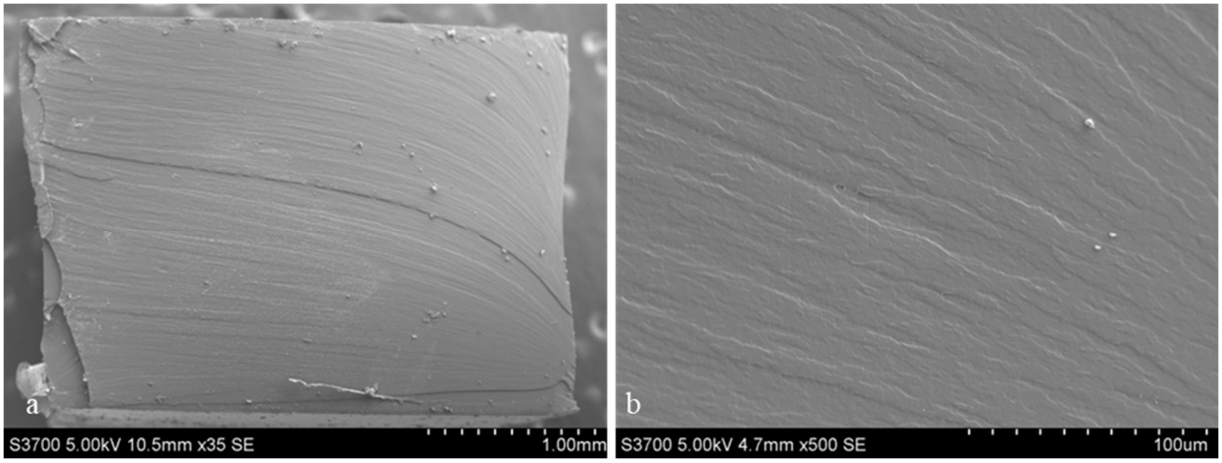

Figure 3-16. Fracture surface of the 30% HS PUa. a) low magnification showing the complete fracture surface, Note the hackle lines ("river pattern") points to the corner where the fracture initiated b) higher magnification of a).

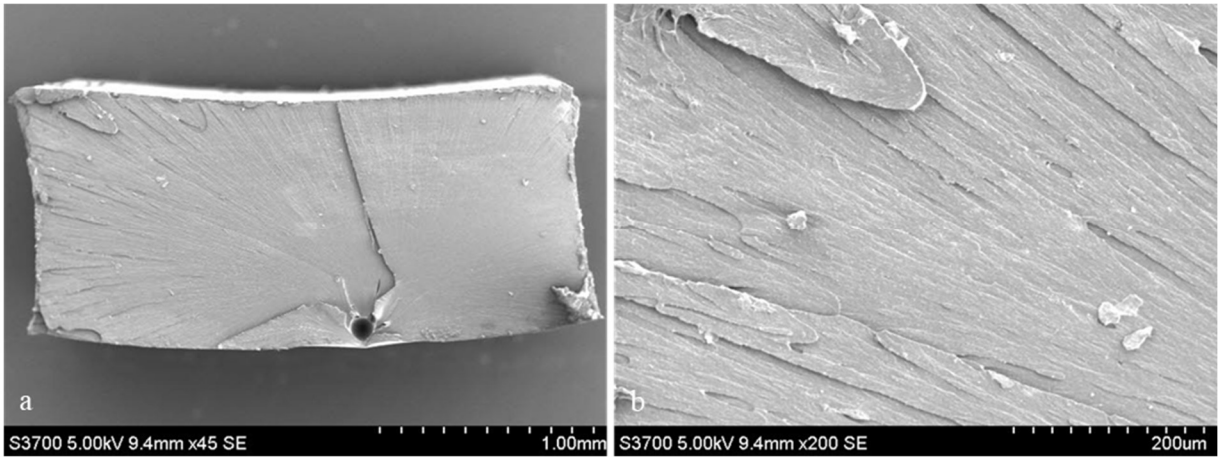

Figure 3-17. Fracture surface of the 40% HS PUa. a) low magnification showing the complete fracture surface, Note the Hackle lines (river pattern) points to the center where the fracture initiated from a pore b) higher magnification of a).

3.3.7 Transmission Electron Microscopy

The Transmission Electron Microscope along with EELS spectroscopy was utilized to view the nanostructure of the formulations after the RuO_4 etching. Figure 3-18 shows the TEM survey image of IPDI-2k-40HS which captured areas of dark and light. With-in the survey image 5 regions of interest were identified of various contrast for EELS spectroscopy. All low loss spectra were nearly identical for both π+σ bulk plasms at ~23 eV and π-π* transition at ~7 eV. All five regions contain an aromatic structure, and no purely aliphatic structure was found. The aromatic structure is found only in the hard segments. This shows that non-percolated hard segments exist with-in the soft phase. Figure 3-19 shows a TEM image of IPDI-2k-30HS along with 2 ROI. One in area in the percolated hard phase (dark area) and one in the non-percolated soft phase (light area). Comparing the low loss spectra from the light area to the dark area, both contain a π-π bond, but the dark area also contains a nitrogen functional group on the aromatic ring. Comparing the core loss spectra between the light and dark areas the N-K peak is found in the dark area, but the N-K is barely visible. The Ru M3 and M2 lines are found in both samples but the Ru is sharper in the darker areas. Since nitrogen is associated only with the hard segments and the Ru is attached to the double bonded oxygen of the hard segments. It adds further credence that the dark areas are rich in hard segments and that spherical nano-domains are present in all three samples. Figure 3-20 through Figure 3-22 shows the TEM images of the 20, 30 and 40% HS formulations at various magnifications. Figure 3-23 compares all three formulations at equivalent magnifications.

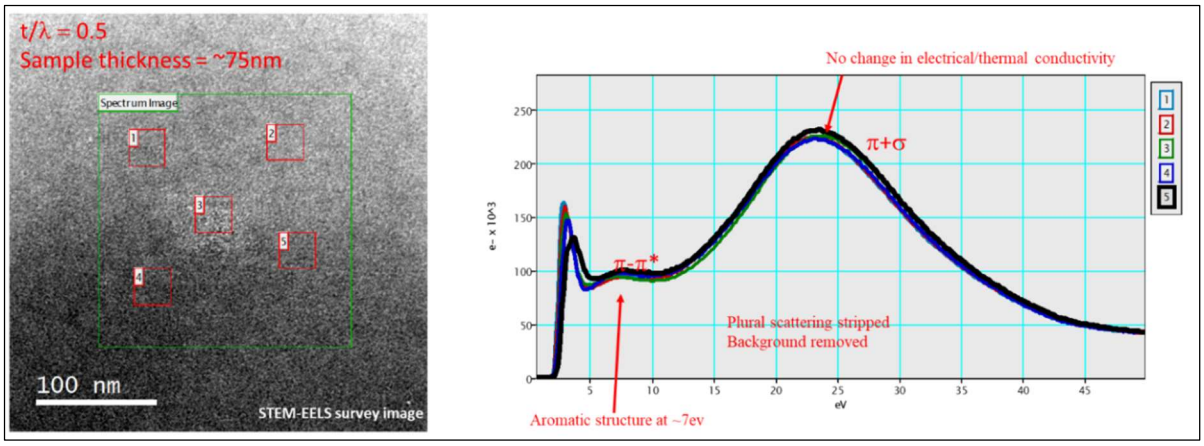

Figure 3-18. TEM image (left) and EELS low loss spectra (right) extracted from 5 areas (red boxes) from IPDI-2k-40HS with different contrast within the green region of interest. The low loss spectra are virtually identical for both π+σ bulk plasms at ~23 eV and π-π* transition at ~7eV.

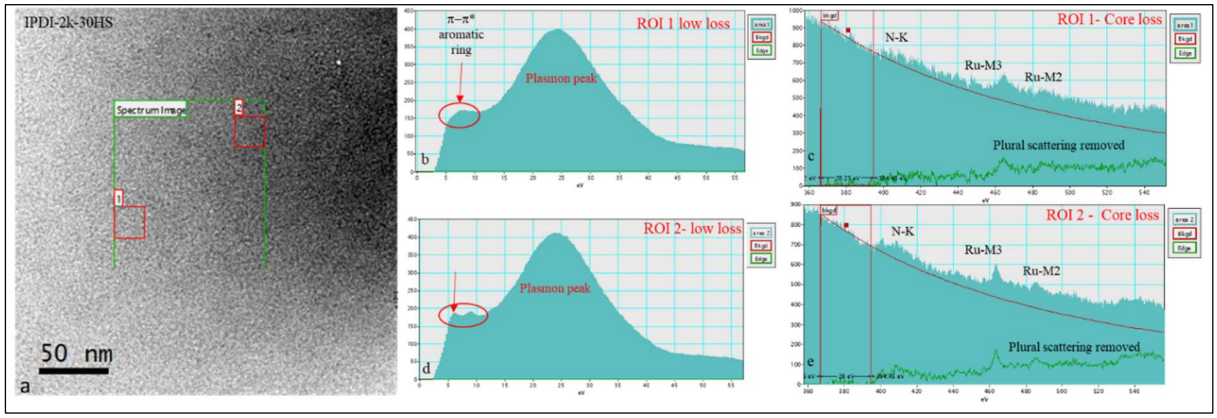

Figure 3-19. a) TEM image of IPDI-2k-30 HS. Two regions of interest (ROI) for EELS analysis. RIO 1 in the light areas, hard segment poor area, of the microstructure and ROI 2 in the hard segment rich domain of the microstructure. The ROIs are 22nm x 22nm. B) Low loss EELS spectra for ROI showing the presence of the π-π* bonds from the aromatic ring. c) Core loss spectrum for ROI 1. Along with t Ru M2 and Ru M3 edge a faint N K edge is seen d) Low loss EELs spectra of ROI2. The additional peak at ~5-6 eV, when compared to ROI 1(b) is attributed to the fact that the nitrogen on an aromatic ring[34]. e) Core loss EELS spectrum for ROI 2. The Ru M2 and M3 edge is sharper while the N peak is sharper.

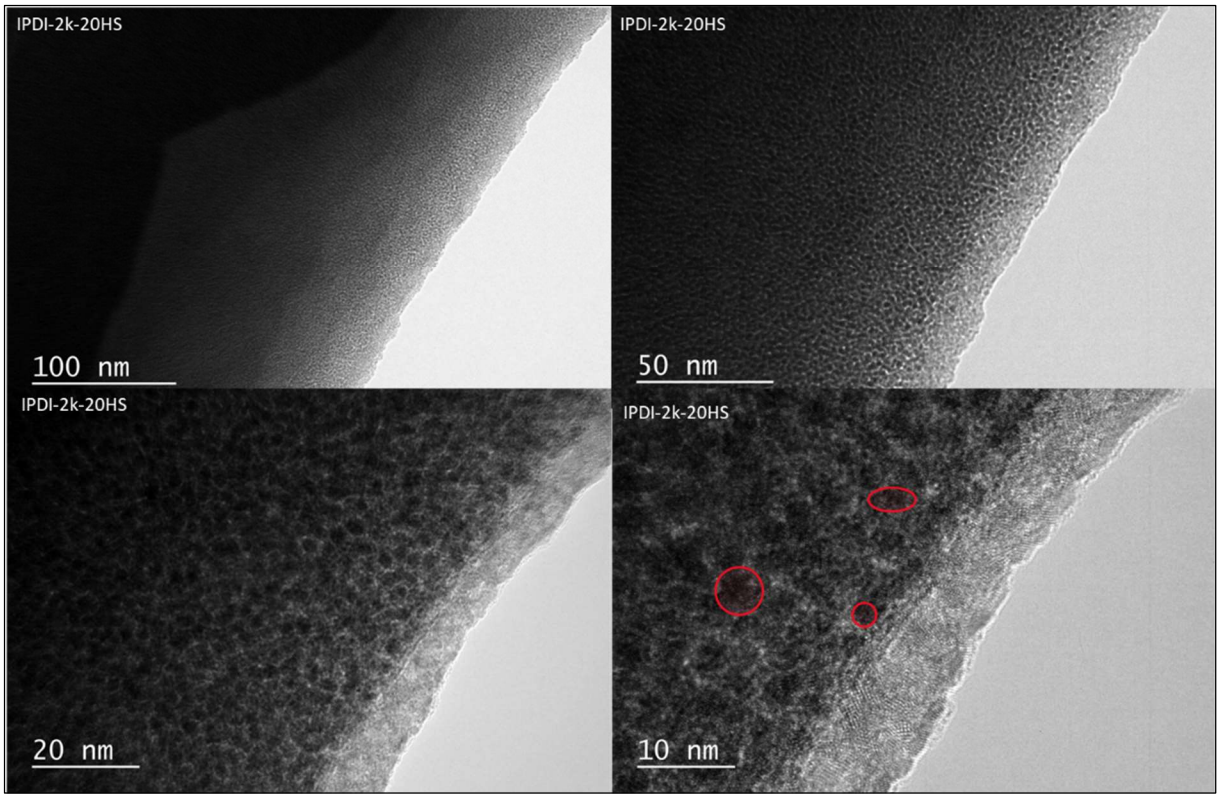

Figure 3-20. TEM images at various magnifications for the IPDI-2k-20HS. Spherical hard nano-domains are highlighted in red.

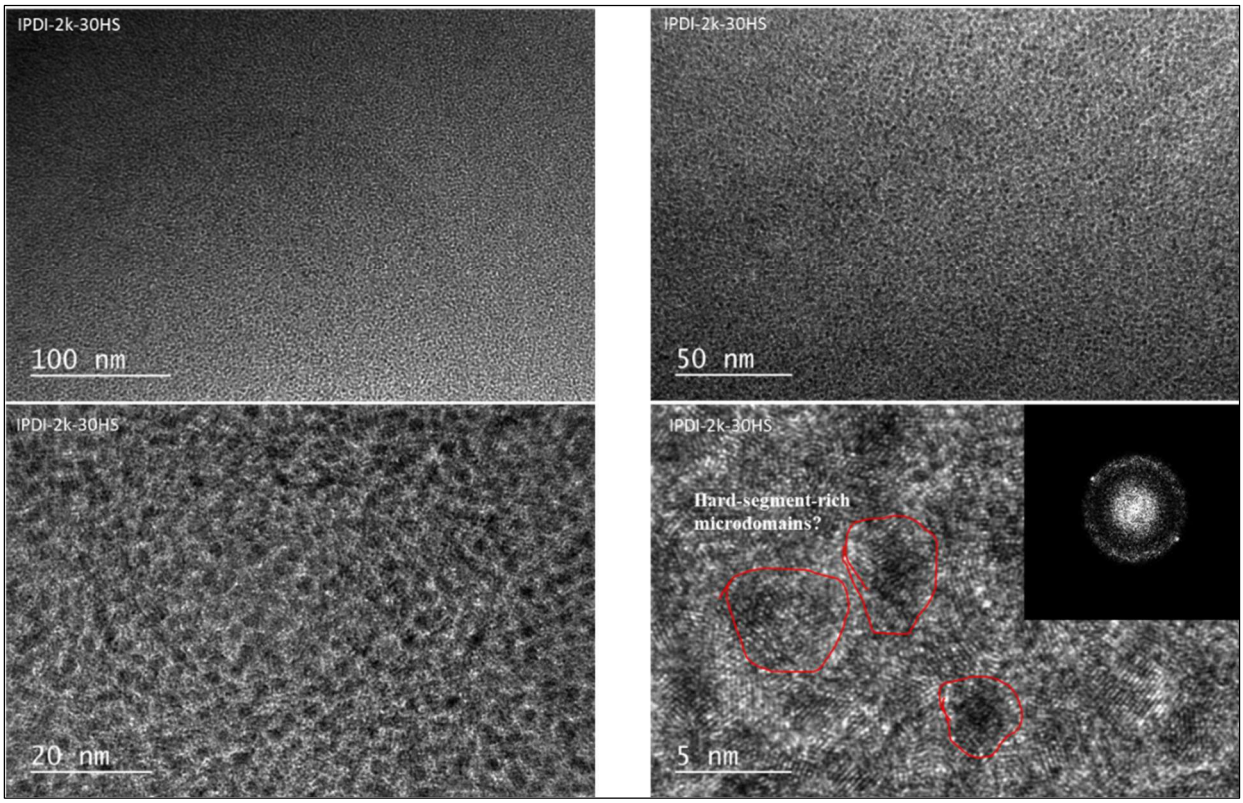

Figure 3-21. TEM images at various magnifications for the IPDI-2k-30HS. Sperifical hard nano-domains are highlited in red.

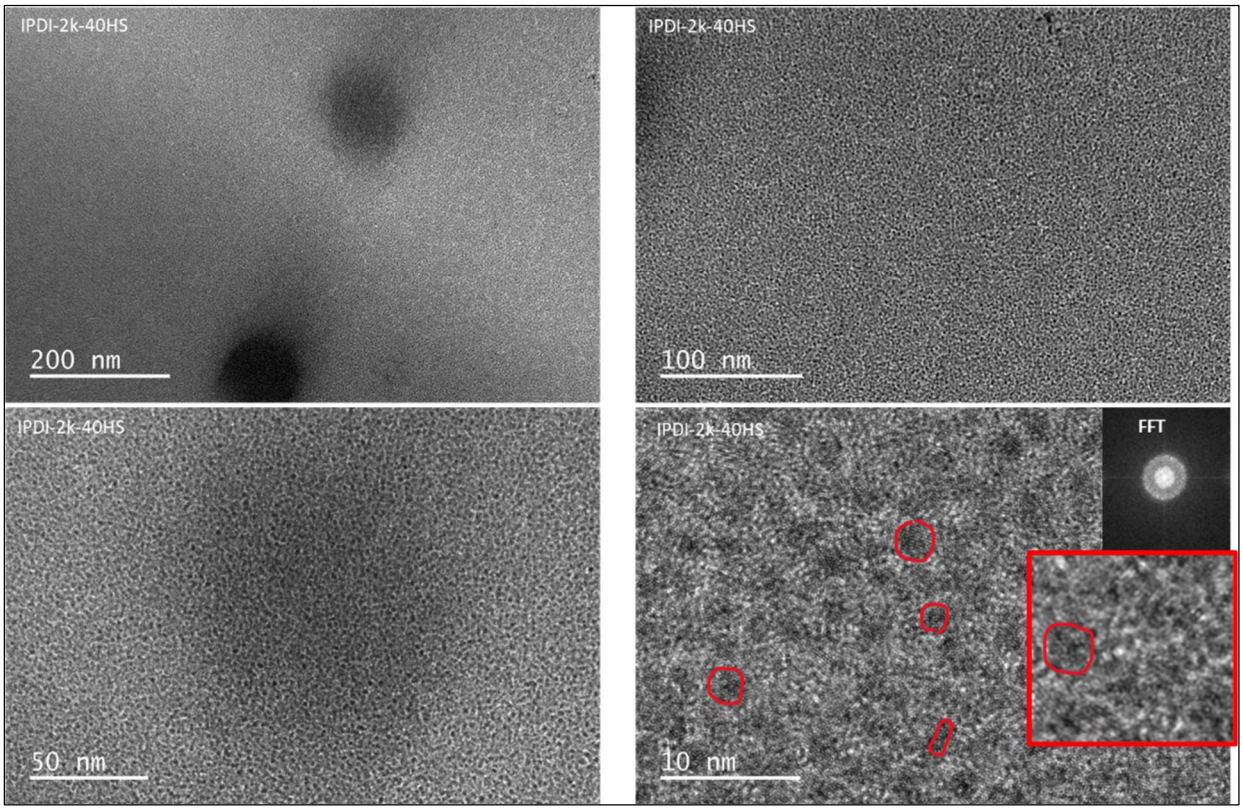

Figure 3-22. TEM images at various magnifications for the IPDI-2k-40HS. Sperifical hard nano-domains are highlited in red.

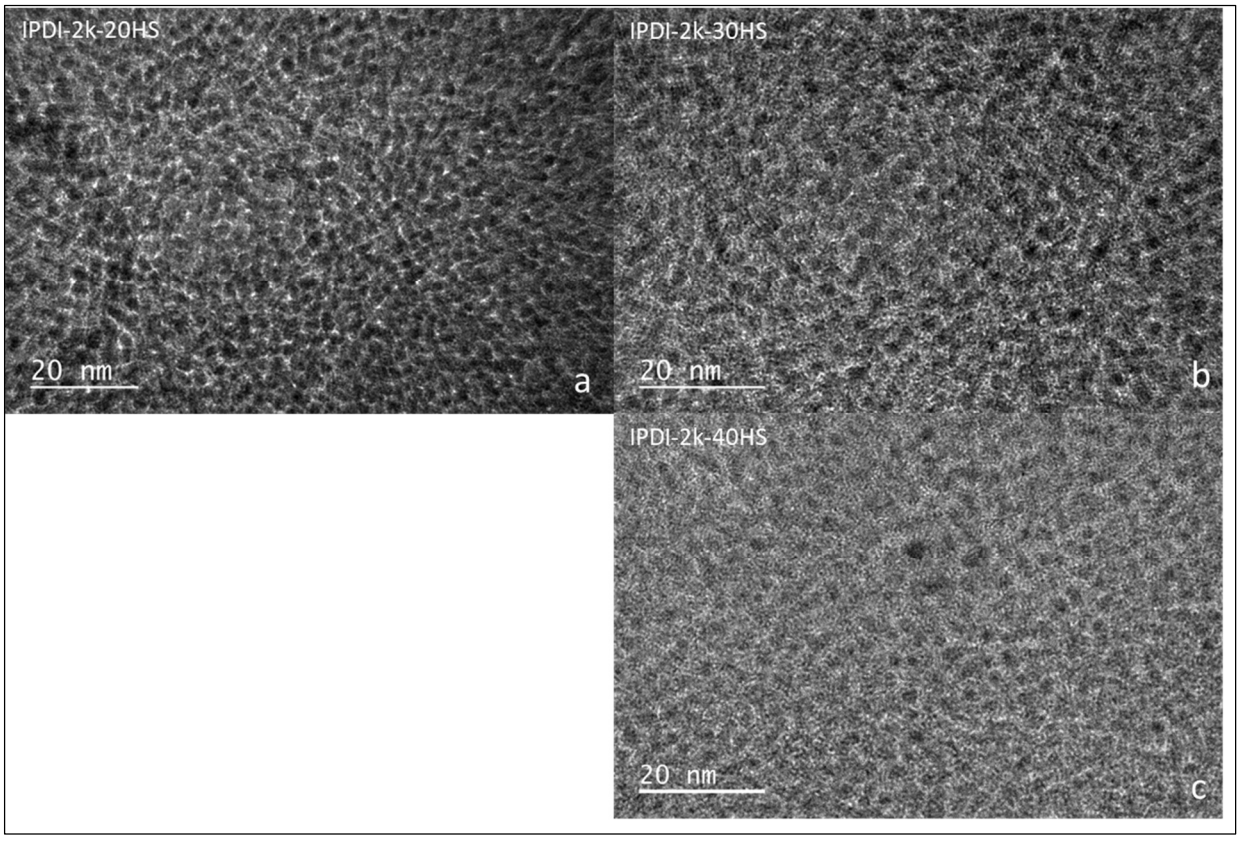

Figure 3-23. TEM images at equivalent magnification for all three formulations.

3.4 Discussion

TEM was used to help elucidate the potential structure of the various polyurea formulations. The TEM micrographs, show strong microphase separation for all three PUas. Some hard segments did remain dissolved in the soft phase as indicated by the fact that EELS spectroscopy which revealed the presence of an aromatic structure in both the darkly RuO_4 stained region and lightly RuO_4 stained regions. This is also confirmed with the Tg shift seen in the first heat run of the DSC. This shift was attributed to non-percolated hard segments in the soft phase. The TEM and DSC show that the final microstructure, which mechanical properties was investigated, consists of a percolated hard phase, in a soft phase matrix which contains some dissolved hard segments for all three model polyurea's. Note the structure is not an equilibrium type structure, neither from soft phase perspective (shift in low temperature Tg) nor in the hard

phase, disappearance of the high temperature transition. The dissolved hard segments do increase with increasing HSWF.

Both the TGA and the DSC show that as the HSWF increases the thermal stability increases. In the TGA runs both the onset temperature, where thermal decomposition begins, and the 50% weight loss temperature shift to higher temperatures. The PUa formulations have the same chemical constituents thus this shift is entirely related to the increase in hydrogen bonding that an increase in HSWF would bring. This is consistent with the DMA temperature sweep, the temperature range with rubbery plateau region increases with increasing HSWF. At lower HSWF, the rubbery plateau is nonexistent, and the modulus continues to decrease with increasing temperature and the modulus drops below 1 MPa at 100 ºC. For the 30% HS and 40 %HS a rubber plateau is seen and the temperature at which the modulus begins to rapidly drop is approximately 120 ºC for the 30% HS and 150 ºC for the 40% HS, Figure 3-13.

Increasing HSWF has a dramatic shift in the mechanical properties as measured by DMA and static tensile testing. The room temperature storage and loss modulus increase with the increase HSWF; this is consistent with what is seen in the secant modulus from the tensile testing. These results are consistent with multiple other studies [11], [13], [31], [34], [57] [61]–[63]. The HSWF has an effect on the energy dissipative capacity, as seen by the tan(δ) curves. As the HSWF increases the tan(δ) curve decreases, indicating that material behaves more elastically and has greater potential for storing the load rather than dissipating it through heat. Since the hydrogen bonding seen in the hard phase would restrict molecular motion making the material stiffer.

From a failure perspective, increasing the HSWF increase fracture strength of the PUa formulations, but not consistent with the rest of the properties previously discussed. Increasing the HSWF from 20 to 30% HS increased the tensile strength at fracture by a factor of six, with a

small decrease in failure strain. Further increasing the HSWF did not increase the tensile strength but did see a dramatic decrease in the failure strain. This results in toughness that goes through a maximum at 30% HS and decreases with further increases in HSWF.

3.5 Conclusions

In this chapter, the intent was to formulate and characterize three model PUa's to study structure, properties, processing relationships as a function of HSWF. Three polyurea formulations were solvent-cast at three levels of HSWF, 20, 30 and 40 weight percent. Micro-phase separation in all three PUas was seen in the TEM images. FTIR showed that the reaction between the prepolymer and the amine blend had gone to completion. DSC showed shifts in the low temperature T_g and higher temperature transition related to the hydrogen bond structure within the hard phase. Upon heating and subsequent cooling both the low temperature Tg shift, and the high temperature transition disappeared indicating some thermal annealing occurred and that the original microstructure was non-equilibrium. Increases in the modulus as measured by DMA and tensile testing were seen with an increase in HSWF, but the toughness of the PUa increases to maximum at 30% HS and then decreases with further increases in HS. The model PUa will be used for subsequent GnP additions and viscoelastic modeling of PUa.

Chapter 4 - PUa-GnP Formulations

4.1 Introduction

In the previous chapter, model neat PUa formulations with 20, 30 and 40 percent hard segments were introduced and characterized using several thermomechanical and mechanical techniques. It was shown that the hard segment weight fraction (HSWF) strongly affected the viscoelastic properties of the PUa. As the HSWF is increased from 20% to 30% to 40%, the high-temperature storage plateau modulus (as measured in DMA tests) increases in a nonlinear fashion. The glass transition temperature of the soft phase changes only slightly (in both DSC and DMA measurements). Finally, the secant modulus in the tensile tests increases strongly between 20% and 30% polymers, but only slightly between 30% and 40% ones."

This chapter builds upon the earlier results by combining the polyurea polymers with nanofillers to create nanocomposites. In particular, exfoliated nano-graphene (GnP) additions of 0.5, 1.0, and 1.5 will be made to the model PUA formulations and the effect of hard segment weight fraction and GnP additions will be studied. Because we are only interested in the interactions between the PUa and the GnP without covalent bonding between the GnP and the PUa, care is taken to minimize or remove any functional groups that could react with the isocyanate and minimize any structural damage to the GnP. Functionalization of the GnP and its effects on the mechanical and viscoelastic properties is a subject of future research interests.

4.2 Composite Casting Process

The synthesis of the PUa-Neat materials is described in Chapter 3 and summarized here. The chemical constituents used were Isophorone diisocyanate (IPDI)-Vestanat from Evonik Corporation, Piscataway, NJ, USA; Jeffamine T5000 and D2000 polyetheramines from the Huntsman Corporation, The Woodlands, TX, USA; and the diethyltoluene diamine (DETDA)

(Lonzacure) chain extender from Lonza, Morristown, NJ, USA. Toluene was purchased from Fisher Scientific, Hampton, NH, USA. All the materials were employed in our research "as received", with no further processing. The formulations for the three neat PUas having hard segment weight fractions of 20%, 30%, and 40%, are provided in Table 4-1.

Table 4-1. Summary of chemical constituents and quantity used in the IPDI based PUa using the solvent cast process.

	Component	**IPDI-2k-20HS**	**IPDI-2k-30HS**	**IPDI-2k-40HS**
Isocyanate Prepolymer (A-Side)	**IPDI**	30.8 g	41.6 g	52.1 g
	T5000	14.5 g	12.1 g	10.1 g
	D2000	57.1 g	48.5 g	40.4 g
	Toluene	82.7 g (95 ml)	165.3 g (190 ml)	208.8 g (240 ml)
	%NCO	8.7 %	12.9 %	15.3 %
Amine Blend (B-Side)	**DETDA**	10 g	19.4 g	29.3 g
	D2000	90 g	80.6 g	70.7 g
Processing	**Index**	1.05	1.05	1.05
	Iso:Amine Vol Ratio	1.00	1.00	1.00
	Iso:Amine Weight Ratio	1.02	1.02	1.17
	%HS	20.2 %	30.2 %	40.0 %

For each of the three PUa formulations described in Table 4-1, four nanocomposites were then prepared, with the GnP weight percentage (wt%) varying from 0.5 to 1.5 wt% with increments of 0.5 wt%. For all the PUa-GnP nanocomposites, the process was identical to that for the neat systems with the following additional steps. Exfoliated nano-graphene (grade R-10, obtained from XG Sciences) was heat-treated at 400 °C in a nitrogen atmosphere for 1 h and allowed to furnace-cool. The required amount of GnPs was placed in a 500 mL beaker, toluene was added in the amounts shown in Table 4-1, to the beaker, and the slurry was simultaneously mechanically stirred and sonicated. The mechanical stirring was accomplished by magnetic stirring at 200 rpm. The sonication was accomplished using a Qsonica sonicator, manufactured by Qsonica L.L.C,

Newtown, CT, USA. The amplitude was set to 20 and the process time was set to 30 min with a pulse time of 10 s on and 10 s off. The temperature of the slurry never exceeded 32 °C, and the total run time was ~1 h. The total amount of energy input was 38,610 J. The weight of GnP added to the formulation is summarized as follows: for the 0.5 wt% GnP formulations, 1.02 g of GnP; for the 1.0 wt% GnP formulations, 2.04 g of GnP; and for the 1.5 wt% GnP formulation, 3.06 g of GnP.

4.3 PUA-GnP Characterization

The surface chemistry of the top 50–80 Å was determined with X-ray photoelectron spectroscopy (XPS). The measurements were performed using a PHI 5400 ESCA system. The base pressure of the instrument was less than 10^{-8} Torr. A 1 cm2 sample was mounted onto the sample holder with double-sided copper tape. The X-ray was a monochromatic Al source with a take-off angle of 45 degrees. Two types of scans were performed for each sample: a survey scan from 0–1100 eV taken with a pass energy of 187.85 eV and regional scans of each element at a pass energy of 23.70 eV. The data were fitted using the CASA XPS software package.

The GnP particle size and dispersion were characterized using a Hitachi 3700 SEM. The acceleration voltage was set to 5 keV to minimize charging effects. A 2-to-3-nanometer-thick gold coating was sputtered using a Quorum Q150R sputter coater. Geometric measurements of the GnP were performed utilizing PCI software, version 9.0.

Dynamic mechanical analysis was conducted using a TA Instruments (New Castle, DE, USA) RSA-G2 rheometer. The curing of the polymer was determined by measuring the change in storage modulus with respect to time. All film samples were loaded in tension. Temperature sweeps, at a rate of 3 °C/min, were conducted from −95 °C to a maximum temperature depending

on the polyurea formulation hard segment content. Six repeats per formulation were run for the temperature sweeps.

Tensile properties were measured on an Instron model number 5586A tensile tester. An Instron 1 kN load cell was used to measure the force and the extension was measured utilizing an Instron AVE-2 non-contact video extensometer. The crosshead speed was set to 200 mm/min. Finally, the ISO37 Type 3 tensile specimens were used. All tensile specimens were stamped using electromechanical stamper and a pre-certified stamping die.

4.3 Results and Discussion

4.3.1 Characterization of GnP via XPS and SEM

Scanning electron microscopy (SEM) was used to determine the effect of sonication on the GnP. Figure 4-1 shows SEM micrographs at various magnifications. Estimates of the particle diameter were produced by measuring the longest axis of the platelets, as shown in Figure 4-2. The average particle diameter before sonication was 15.4 +/− 6.3 μm (1σ). The average particle diameter after sonication was 15.0 +/− 4.5 μm (1σ). No change was seen in the morphology of the GnP. The GnP remained exfoliated throughout the sonication process and retained their shape and aspect ratio. Given that the technical data sheet for the R10 grade specified an average particle diameter size of approximately 10 μm, and accounting for the fact that the platelets in the images were at various angles, it is concluded that there was no difference between the as received and sonicated GnP.

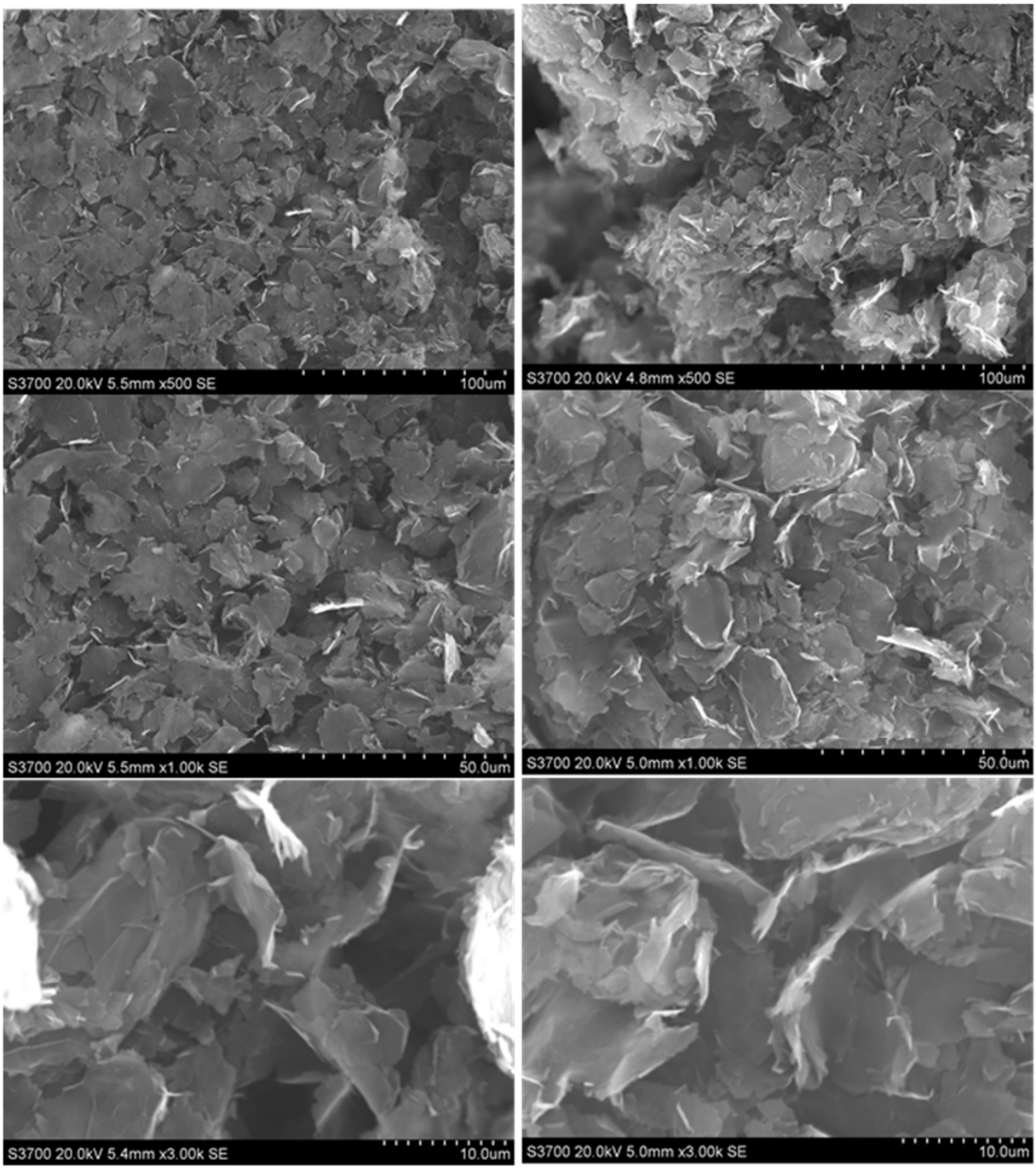

Figure 4-1. SEM images at various magnifications of the GnP before (left column) and after sonication (right column). The images indicate that there is no change in the morphology of the GnP with the sonication parameters used.

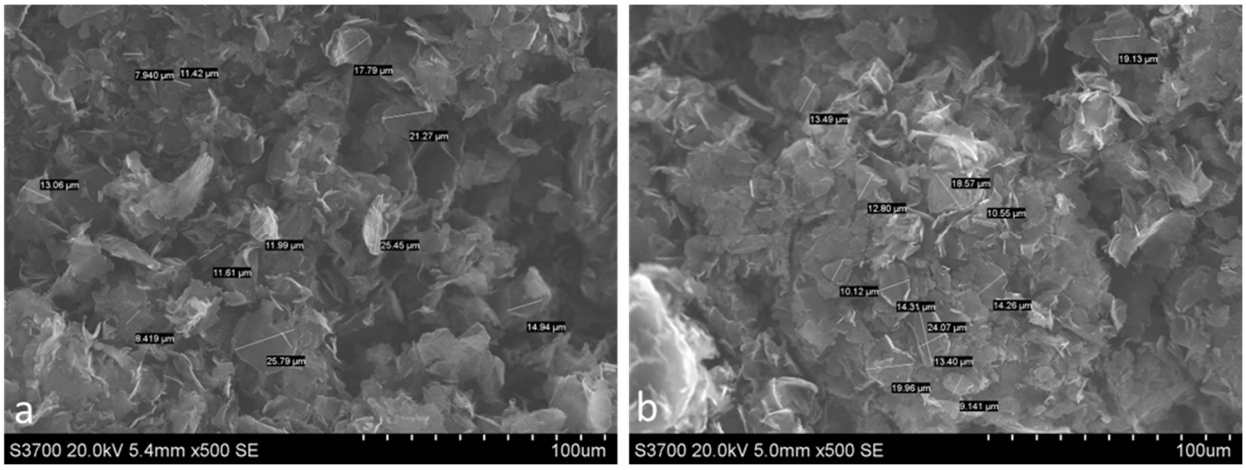

Figure 4-2. SEM micrographs showing the measurement of the estimated diameter of the GnP before sonication (a) and after sonication (b).

X-ray photoelectron spectroscopy (XPS) was used to evaluate the surface chemistry of the GnP after heat treatment and after sonication. Figure 4-3 shows a survey of both a heat-treated sample and heat-treated and sonicated sample. Both spectra showed two peaks. The first at 281.6 eV and 282.4 eV for the heat-treated and sonicated samples, respectively, are associated with the C 1s position. The second, at 530.4 eV for both heat-treated and sonicated samples is associated with the O 1s position. The atomic concentration was estimated and is presented in Figure 4-3.

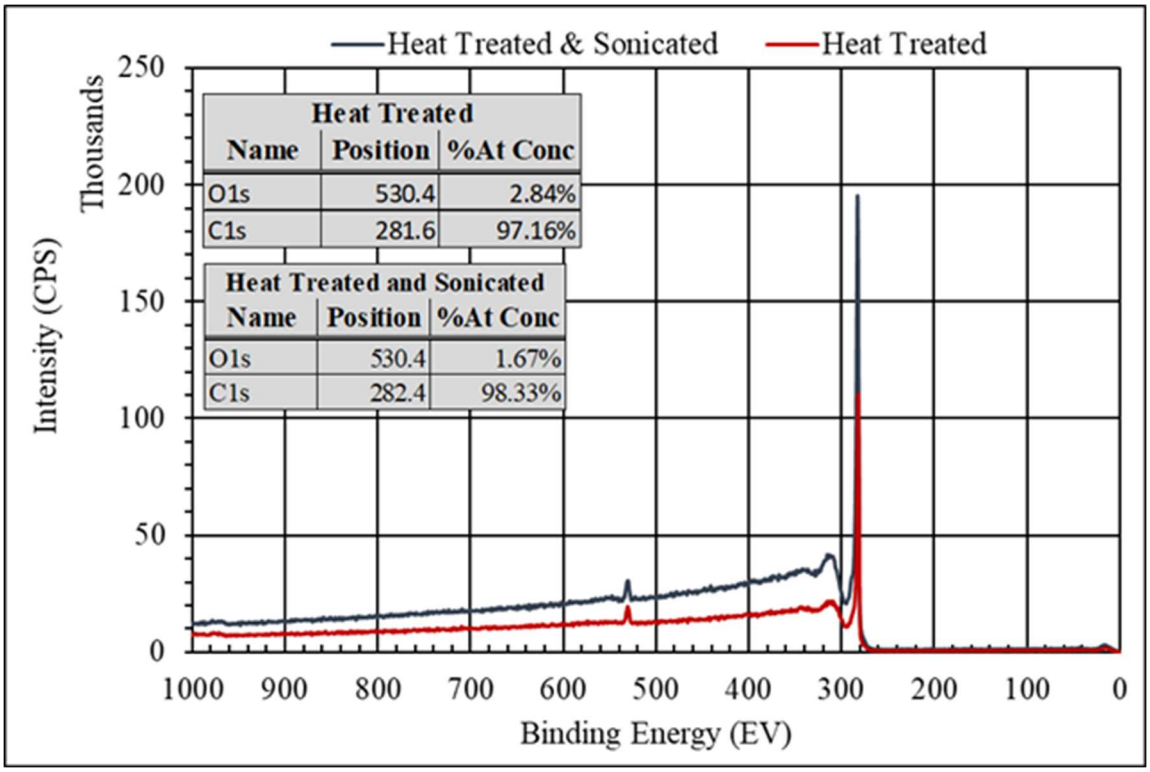

Figure 4-3. XPS survey of the GnP after heat treatment (red spectrum), and after heat treatment and sonication. The sonication did not cause any change to the surface chemistry of the GnP.

The atomic percentage of C was significantly higher than that of O for both heat-treated and heat-treated and sonicated samples. This is consistent with the expectation that the majority of the GnP was carbon with very little oxygen on the edges of the basal planes. The approximate 1% difference seen between the two treatments was not considered significant. To explore the source of the oxygen peaks, a deconvolution of the XPS spectra for the heat-treated sample and the heat-treated and sonicated sample in the binding energy region for C and O is shown in Figure 4-4 and Figure 4-5, respectively. From Figure 4-4a, the peak at 283.2 eV, the largest peak, was associated with the C=C double bonds of graphene. The remaining C 1s peaks were associated with hydroxyl 284.7 eV. The C 1s peak at 288.0 eV was associated with the C=O, and the C 1s peak at 289.7 was associated with a COOH/COOR [64]. From Figure 4-4b, the O 1s peak at 531.2 eV was associated with COOH and the O 1s peak at 532.7 eV was associated with the –OH functional group [65].

The deconvolution of the heat-treated and sonicated samples is shown in Figure 4-5. Similar to the analysis for the heat-treated samples, the peak at 283.2 eV (the largest peak in the spectrum) was associated with the C=C double bonds of graphene. The remaining C1s peak at 284.7 eV was associated with the –OH functional group. Likewise, the C 1s peak at 289.2 eV was associated with COOH/COOR functional groups (see Figure 4-4). In Figure 4-4b, the O 1s peak at 531.0 eV was associated with COOH, and the O 1s peak at 532.4 eV was associated with the –OH functional group. From the analysis above, one concludes that there was very little –OH or –COOH functionalization on the GnP. Furthermore, the sonication process had very little effect on the chemistry, nor did it reduce the particle size.

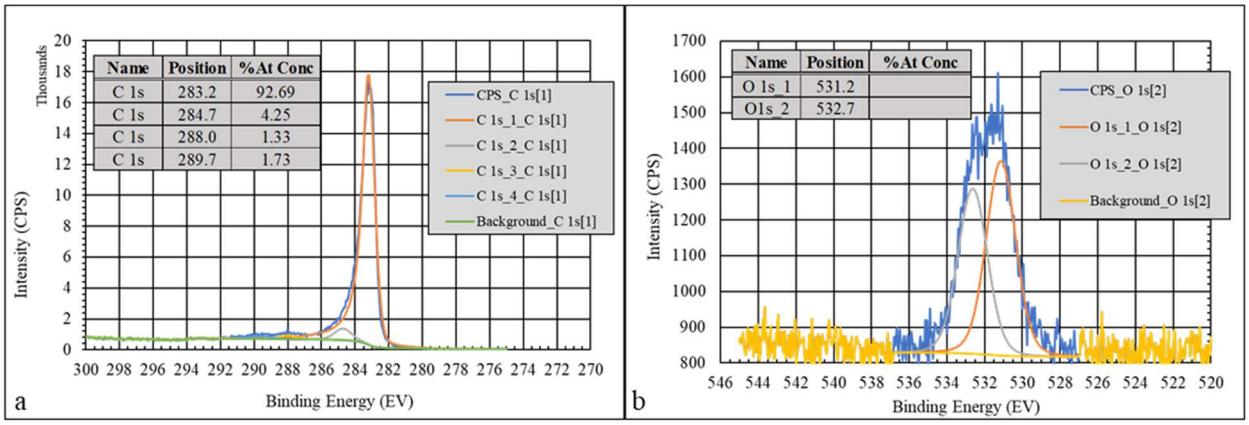

Figure 4-4. Deconvolution of the XPS spectrum, for the heat-treated GnP, in the binding energy region for C (a), and O (b).

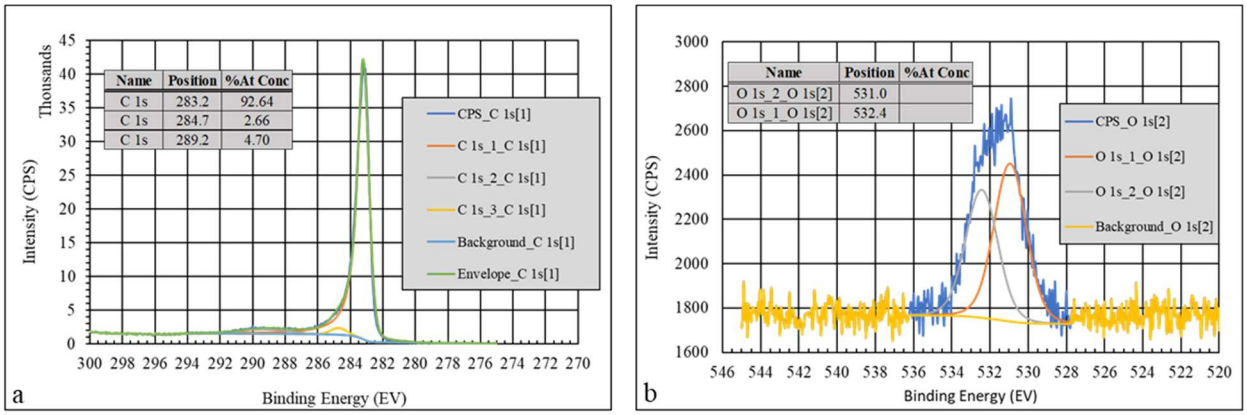

Figure 4-5. Deconvolution of the XPS spectrum, for the heat-treated and sonicated GnP and sonicated, in the binding energy region for C (a), and O (b).

To investigate particle dispersion at various concentrations of GnP, tensile samples were placed in liquid nitrogen for approximately 5 min and then snapped in half. SEM micrographs of the fracture surface were then used to study the nanoparticle dispersion in the polymer matrix. As can be seen in Figure 4-6 through Figure 4-8. In the lower-magnification micrographs, the GnP particles are seen as brighter, due to electron interaction with the jagged edges of the GnP, than the polyurea matrix; examples of GnP are highlighted by the arrows. No agglomeration or continuous networks of GnP were found in any of the formulations. Figure 4-6f and Figure 4-8f are higher-magnification micrographs (13 kX, and 10 kX respectively) of the GnP. The edges of the individual nano-platelets can be seen suggesting that GnP remained exfoliated throughout the sample preparation process.

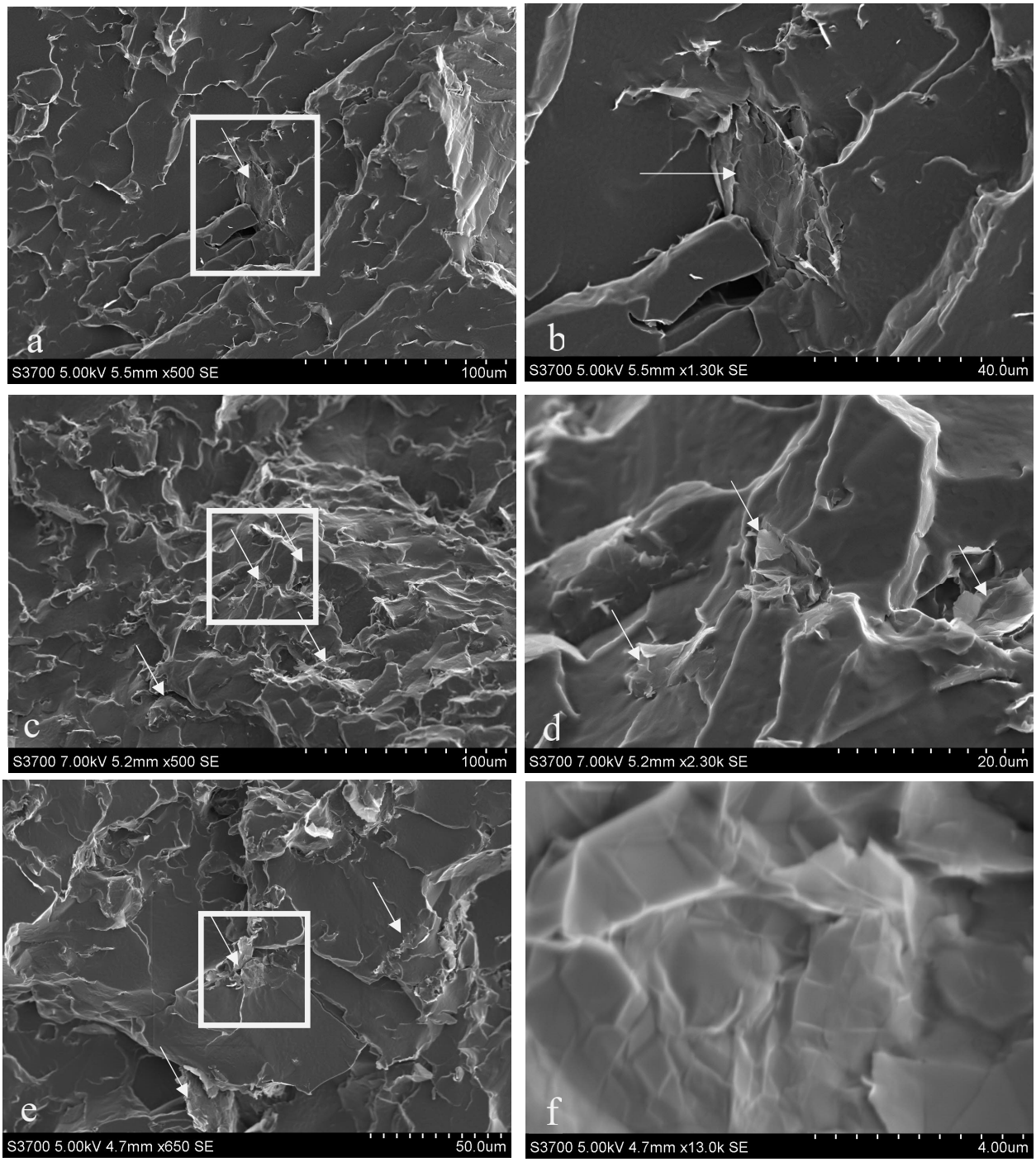

Figure 4-6. SEM photomicrographs of the fracture surface for all IPDI-2k-20HS GnP loadings: a) 0.5 wt% GnP loading at 500x, b) Photomicrograph of the white box in a. c) 1.0 wt% GnP loading at 500x, d) Photomicrograph of the white box in c. e) 1.5 wt% GnP loading. f) Photomicrograph of the white box in e. In all photomicrographs the arrows point to the GnP.

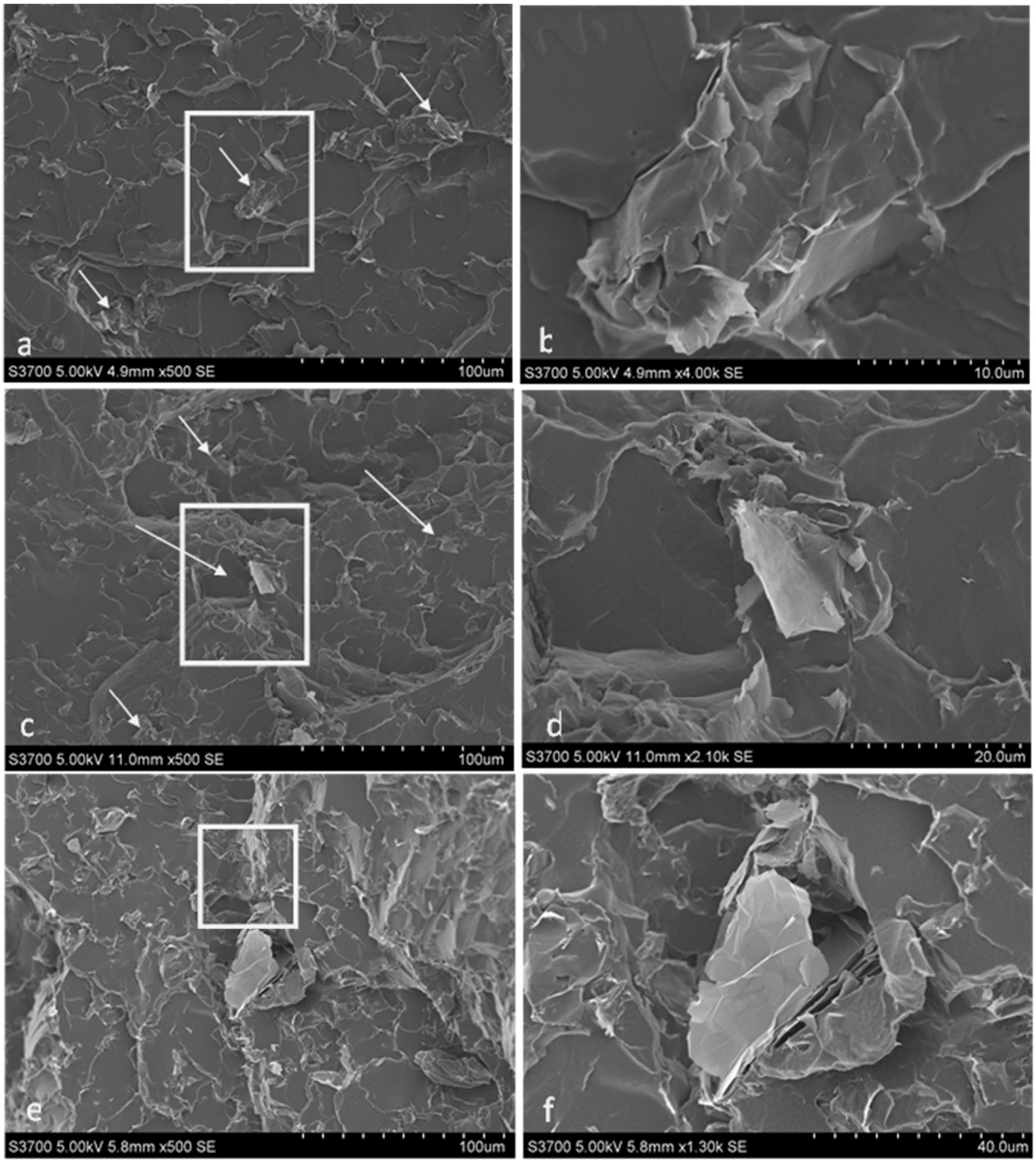

Figure 4-7. SEM photomicrographs of the fracture surface for all IPDI-2k-30HS GnP loadings: a) 0.5 wt% GnP loading at 500x, b) Photomicrograph of the white box in a. c) 1.0 wt% GnP loading at 500x, d) Photomicrograph of the white box in c. e) 1.5 wt% GnP loading. f) Photomicrograph of the white box in e. In all photomicrographs the arrows point to the GnP.

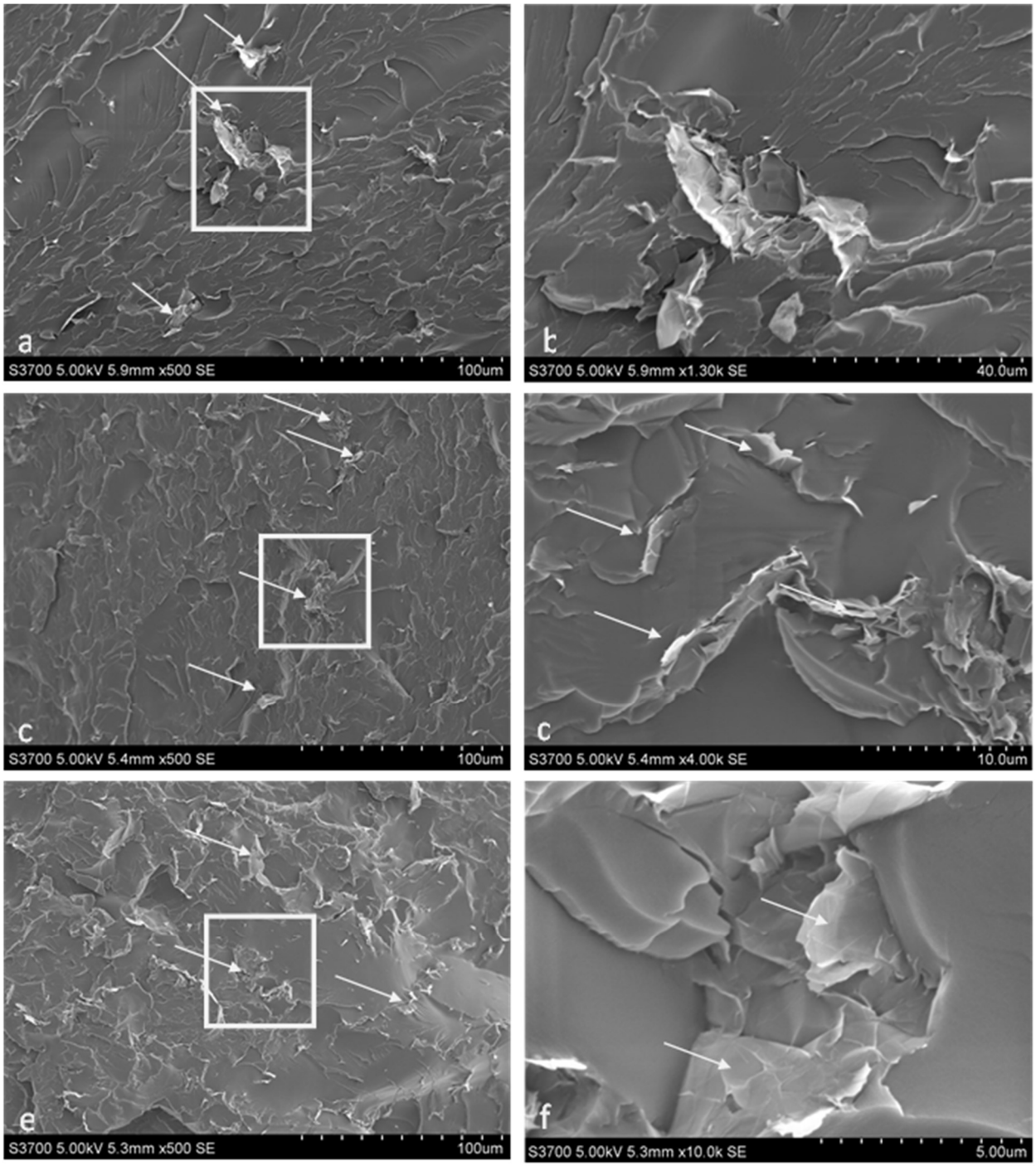

Figure 4-8. SEM photomicrographs of the fracture surface for all IPDI-2k-40HS GnP loadings: a) 0.5 wt% GnP loading at 500x, b) Photomicrograph of the white box in a. c) 1.0 wt% GnP loading at 500x, d) Photomicrograph of the white box in c. e) 1.5 wt% GnP loading at 500x. f) Photomicrograph of the white box in e. In all photomicrographs the arrows point to the GnP.

4.3.2 FTIR

Figure 4-9 shows the FTIR spectra for all IPDI formulations. In all neat cases the isocyanate peaks found at 2255 cm^{-1} are not observed (See Chapter 3 FTIR section for detailed analysis of the Neat FTIR Spectra) and the primary amine ones found between 3400-3500 cm^{-1} are now secondary peaks indicating the reaction has proceeded to completion. This is also true for the PUa-GnP composites for all the nanoparticle loadings. Therefore, the GnP did not interfere with the PUa reactions. In the case of the 20 and 30 percent hard segment formulations there was no shifting of any peak positions or appearance of any additional peaks for the nano-composites relative to the neat formulations. For the 40 percent hard segment two additional two absorption bands were seen at 1150 cm^{-1} and 1205 cm^{-1} are seen. These absorption bands are assigned to various vibrational modes of the oxy-propylene (C-O-C) in the main chain of both D2000 and the T5000. The absorption bands are present in all the 40% hard segment systems, regardless of GnP loading, with no shifting of the absorption bands with increasing percent nanofiller.

The fact that no additional absorption bands are seen between the neat samples and the nano-composite samples indicates that no covalent type bonding exists between the base PUa and the GnP.

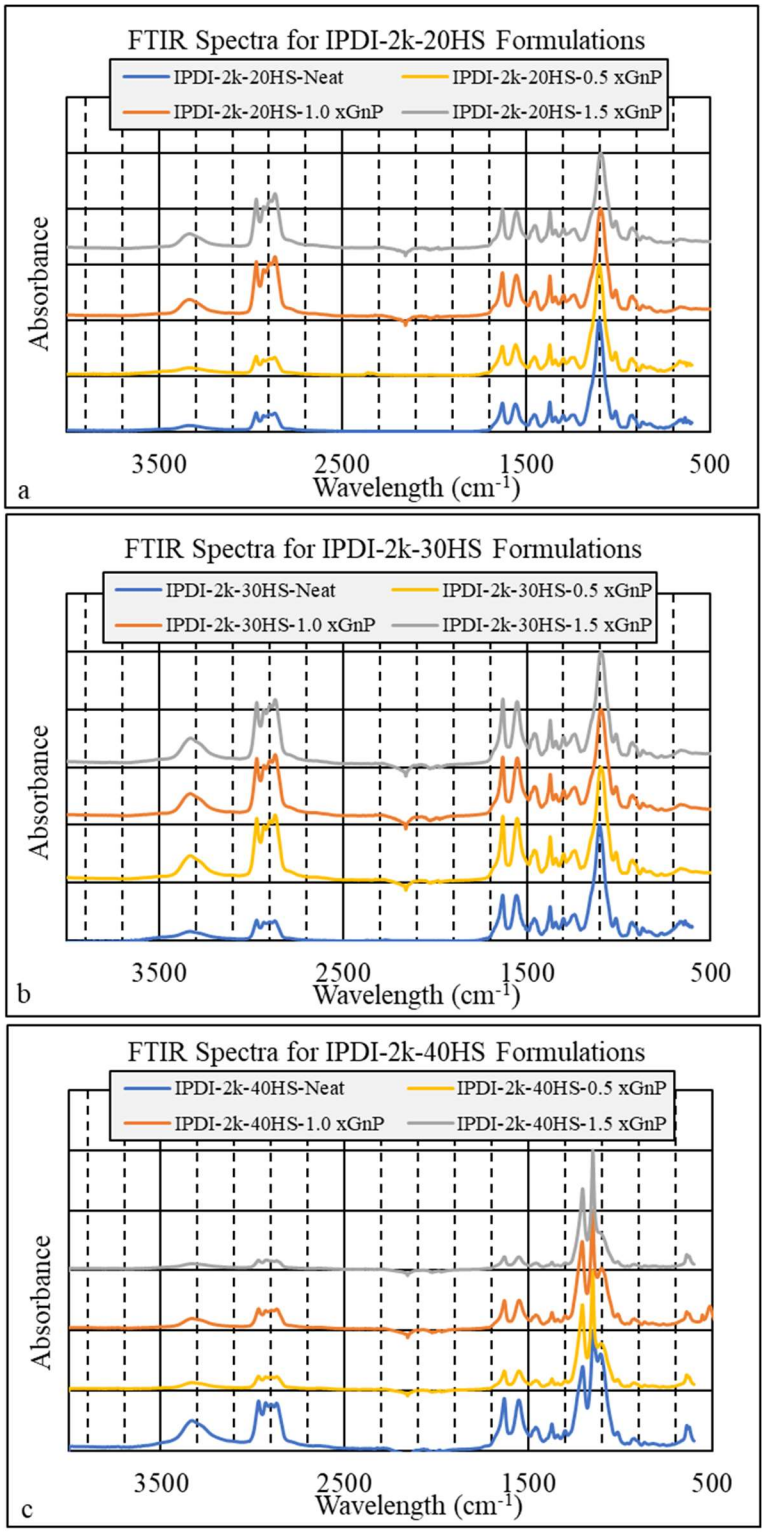

Figure 4-9. FTIR Spectra for all IDPI formulations. a) 20 percent HS based formulations, b) 30 percent HS based formulations, c) 40 percent HS based formulations.

4.3.3 TGA

Solvent extraction was verified by TGA. Figure 4-10 shows the TGA thermographs for all formulations. For all three formulations the weight loss at the boiling point of Toluene (110.6 °C) was less than 0.4 weight percent. The onset temperature, approximately 268 °C, is independent of the percent hard segment and nanofiller. The TGA experiments showed that the solvent was extracted and would not affect the remaining mechanical and thermomechanical experiments.

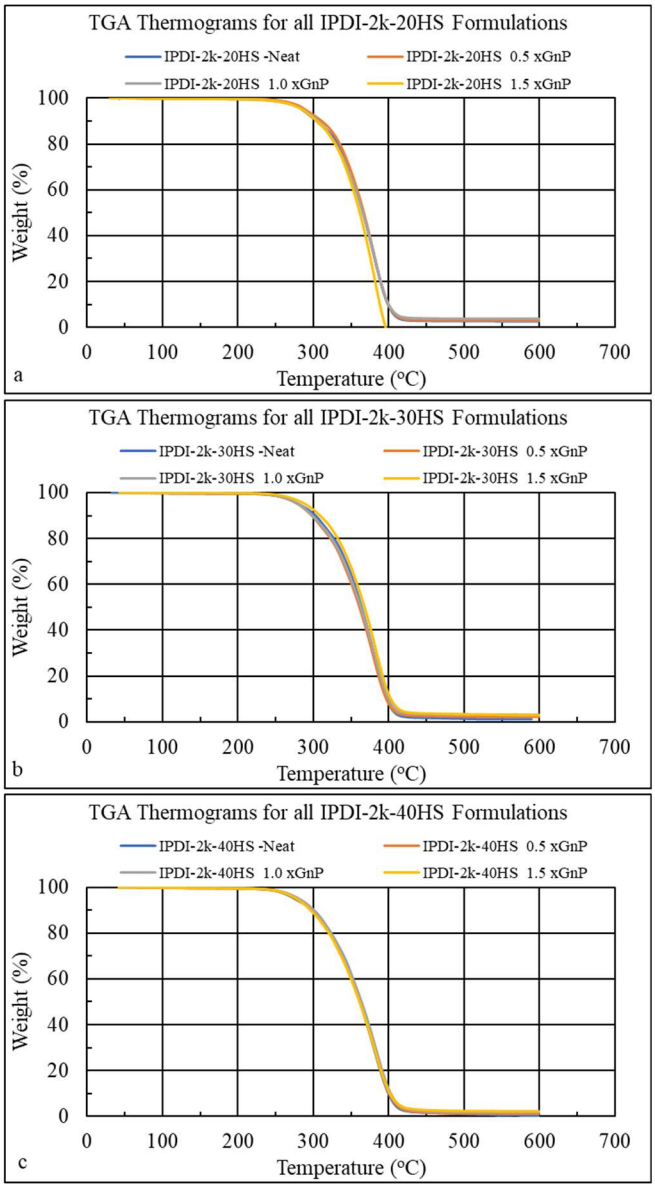

Figure 4-10. TGA Thermograms for all IPDI based formulations a) 20 percent HS based formulations, b) 30 percent HS based formulations, c) 40 percent HS based formulations.

4.3.4 DSC

Figure 4-11 through Figure 4-13 show the DSC scans for all the formulations and Table 4-2 summarizes the glass transition temperatures. The T_g during the first heating run decreases as the hard segment weight fraction (HSWF) is increased, which is attributed to an increase in hard segments dissolved in the soft phase [18]. The difference is significantly less pronounced in the cooling run and is practically invisible in the 2nd heating run. The same trend is seen for the nanocomposite formulations. The secondary transition at higher temperature was seen in all the formulations. This transition was exothermic for the 20% HS and 30% samples and endothermic for 40 percent hard segment formulations, see Table 4-2 for the enthalpy values. Note that identical trends existed for the nano-composite formulations. In fact, the GnP curves, regardless of loading lay on top of the neat formulations. This suggests that the GnP had no effect on the dissolved hard segments nor the percolated hard phase.

Table 4-2. Summary of the Tg DSC Scans for the neat and GnP nano-composite formulations.

Base Formulation	GnP Loading	T_g 1st heating run	ΔH (J/g) 1st Heating Run	T_g Cooling Run	T_g 2nd heating run
IPDI-2k-20HS	Neat	-60.7	5.4	-64.7	-62.2
	0.5 wt%	-61.4	7.1	-64.9	-62.2
	1.0 wt%	-60.7	8.6	-64.5	-62.9
	1.5 wt%	-61.5	8.1	-64.5	-62.4
IPDI-2k-30HS	Neat	-57.2	6.0	-65.1	-62.5
	0.5 wt%	-57.2	6.7	-65.2	-62.0
	1.0 wt%	-58.1	6.3	-64.9	-62.6
	1.5 wt%	-57.3	6.2	-64.8	-62.2
IPDI-2k-40HS	Neat	-52.8	-4.1	-65.9	-63.2
	0.5 wt%	-52.8	-2.1	-65.5	-63.2
	1.0 wt%	-53.6	-3.1	-65.7	-62.8
	1.5 wt%	-53.6	-2.8	-65.8	-63.5

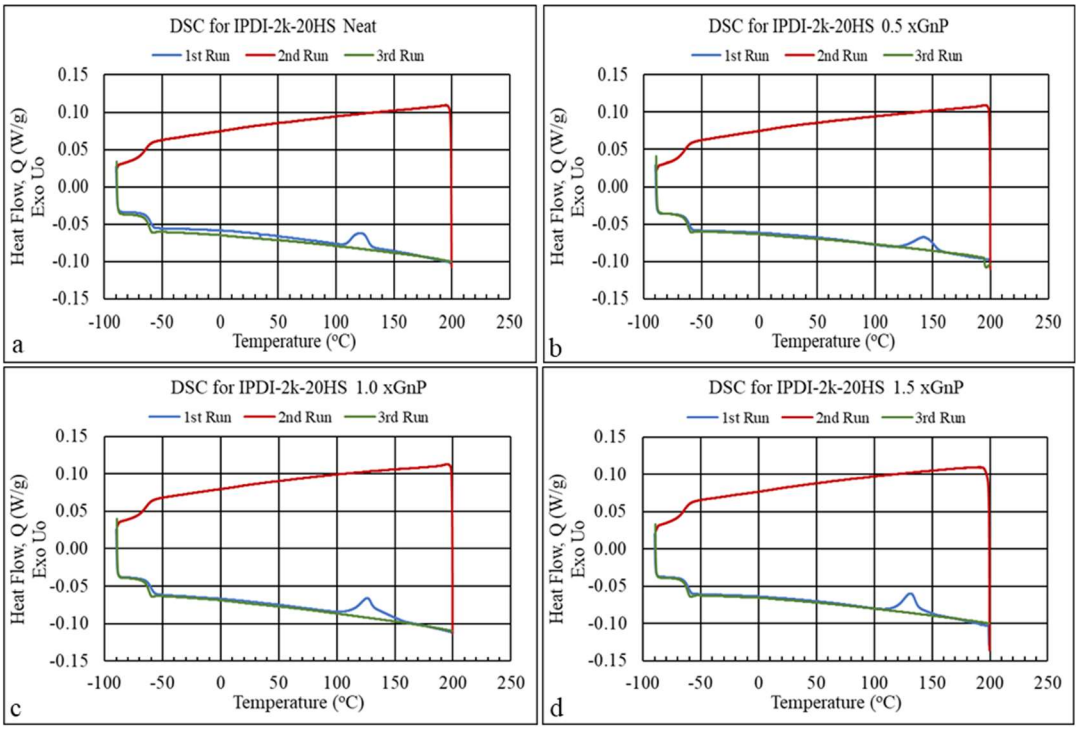

Figure 4-11. DSC for all IPDI-2k-20HS (20HS) formulations. a) neat, b) 0.5 GnP, c) 1.0 GnP, d) 1.5 GnP. Note 1st and 3rd run are heating, while the 2nd run is cooling.

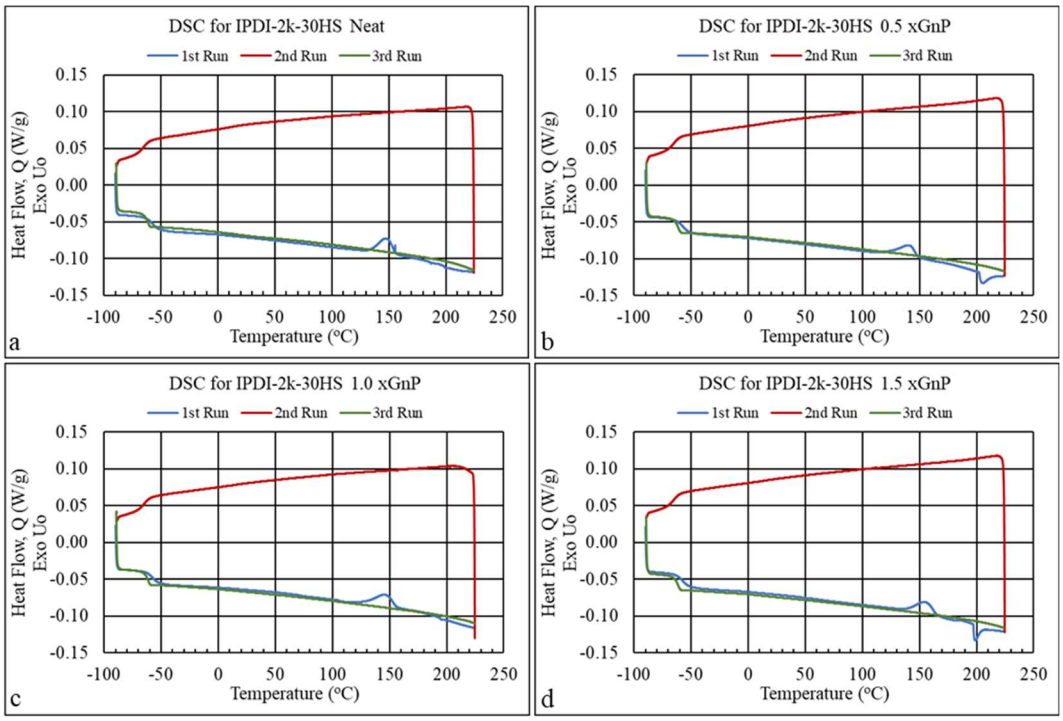

Figure 4-12. DSC for all IPDI-2k-30HS (30HS) formulations. a) neat, b) 0.5 GnP, c) 1.0 GnP, d) 1.5 GnP. Note 1st and 3rd run are heating, while the 2nd run is cooling.

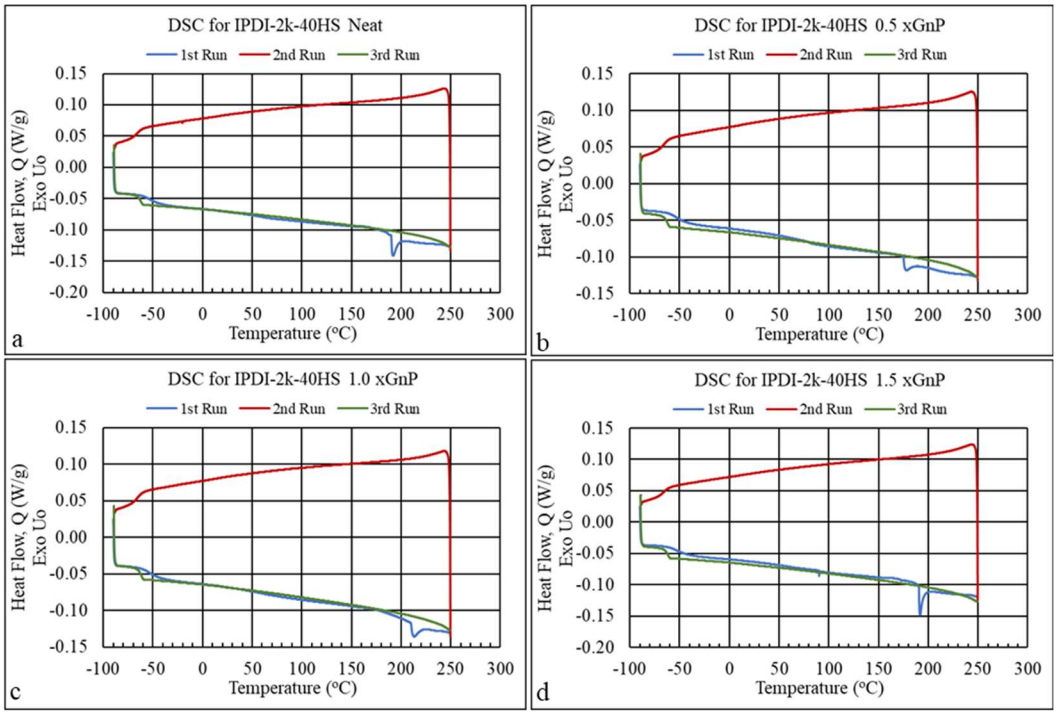

Figure 4-13. DSC for all IPDI-2k-40HS (40HS) formulations. a) neat, b) 0.5 GnP, c) 1.0 GnP, d) 1.5 GnP. Note 1st and 3rd run are heating, while the 2nd run is cooling.

4.2.4 DMA

Figure 4-14 through Figure 4-16 show the results of the temperature sweeps for all formulations, and Table 4-3 though Table 4-5 summarizes the key results of the DMA testing. For all cases of the HS the addition of GnP had no effect on the glass transition temperature. This is entirely consistent with the calorimetric T_g measured by DSC (see previous section). There was no effect on the low temperature storage modulus, this may be attributed to fact that the long chain diamines/triamines are the same regardless of formulations. This would tend to indicate that the GnP had little effect on the soft phase microstructure, i.e. no crystallizations or increase in the hydrogen bonding in the soft phase. The additions of GnP to the 30% HS formulations did increase the room temperature storage modulus slightly but had no effect on the 20 and 40 percent hard segment formulations. For the 20 and 30 percent hard segment samples the addition of GnP increased the temperature range of the plateau modulus while no effect was seen in 40 percent HS formulation, Figure 4-14a, Figure 4-15a, Figure 4-16a.

It is important to note that the viscoelastic properties of the base PUa are dominated by the change in hard segment weight fraction, with the additions of GnP playing only a secondary role. As previously shown in Chapter 3 and in Table 4-3 though Table 4-5 the HSWF can increase room temperature storage modulus by approximately 5 times from 20 to 30 weight percent HS and another 5 times from 30 to 40 weight percent hard segment.

Table 4-3. Summary of the IPDI-2k-20HS formulations. The hard segment weight fraction is 20 and the nano-loading ranges from neat to 1.5 wt% GnP.

IPDI 2k-20HS Formulations	**T_g (°C) E'**	**T_g (°C) E"**	**T_g (°C) tan (δ)**	**E' @ -90 °C (MPa)**	**E' @ 25 °C (MPa)**
Neat	-59.5 +/- 0.4	-57.2 +/- 0.3	-50.7 +/- 0.1	3439 +/- 700	11.8 +/- 1.9
0.5 wt% GnP	-59.6 +/- 0.2	-57.2 +/- 0.3	-50.7 +/- 0.1	3845 +/- 116	16.0 +/- 1.4
1.0 wt% GnP	-59.3 +/- 0.1	-56.4 +/- 0.4	-50.0 +/- 0.4	3398 +/- 173	11.0 +/- 1.1
1.5 wt% GnP	-59.9 +/- 0.1	-57.4 +/- 0.1	-50.5 +/- 0.3	4015 +/- 69	16.9 +/- 0.7

Table 4-4. Summary of the IPDI-2k-30HS formulations. The hard segment weight fraction is 30 and the nano-loading ranges from neat to 1.5 wt% GnP.

IPDI 2k-30HS Formulations	**T_g (°C) E'**	**T_g (°C) E"**	**T_g (°C) tan (δ)**	**E' @ -90 °C (MPa)**	**E' @ 25 °C (MPa)**
Neat	-58.9 +/- 0.5	-55.0 +/- 0.8	-48.1 +/- 0.7	3845 +/- 287	60.6 +/- 2.1
0.5 wt% GnP	-58.0 +/- 0.1	-53.9 +/- 0.0_2	-47.5 +/- 0.0_2	3613 +/- 160	72.2 +/- 3.4
1.0 wt% GnP	-58.5 +/- 0.1	-53.9 +/- 0.0_1	-47.7 +/- 0.3	3569 +/- 104	89.6 +/- 2.9
1.5 wt% GnP	-57.4 +/- 0.1	-53.6 +/- 0.1	-47.3 +/- 0.3	3238 +/- 211	87.0 +/- 5.0

Table 4-5. Summary of the IPDI-2k-40HS formulations. The hard segment weight fraction is 40 and the nano-loading ranges from neat to 1.5 wt% GnP.

IPDI 2k-40HS Formulations	**T_g (°C) E'**	**T_g (°C) E"**	**T_g (°C) tan (δ)**	**E' @ -90 °C (MPa)**	**E' @ 25 °C (MPa)**
Neat	-56.6 +/- 0.7	-49.5 +/- 1.0	-41.9 +/- 1.3	4043 +/- 294	308 +/- 35
0.5 wt% GnP	-57.5 +/- 0.5	-51.2 +/- 0.3	-43.9 +/- 0.5	3539 +/- 314	229 +/- 40
1.0 wt% GnP	-57.3 +/- 0.2	-51.1 +/- 0.3	-44.1 +/- 0.2	3606 +/- 178	237 +/- 22
1.5 wt% GnP	-57.0 +/- 0.3	-50.4 +/- 0.4	-42.6 +/- 0.6	3693 +/- 274	289 +/- 14

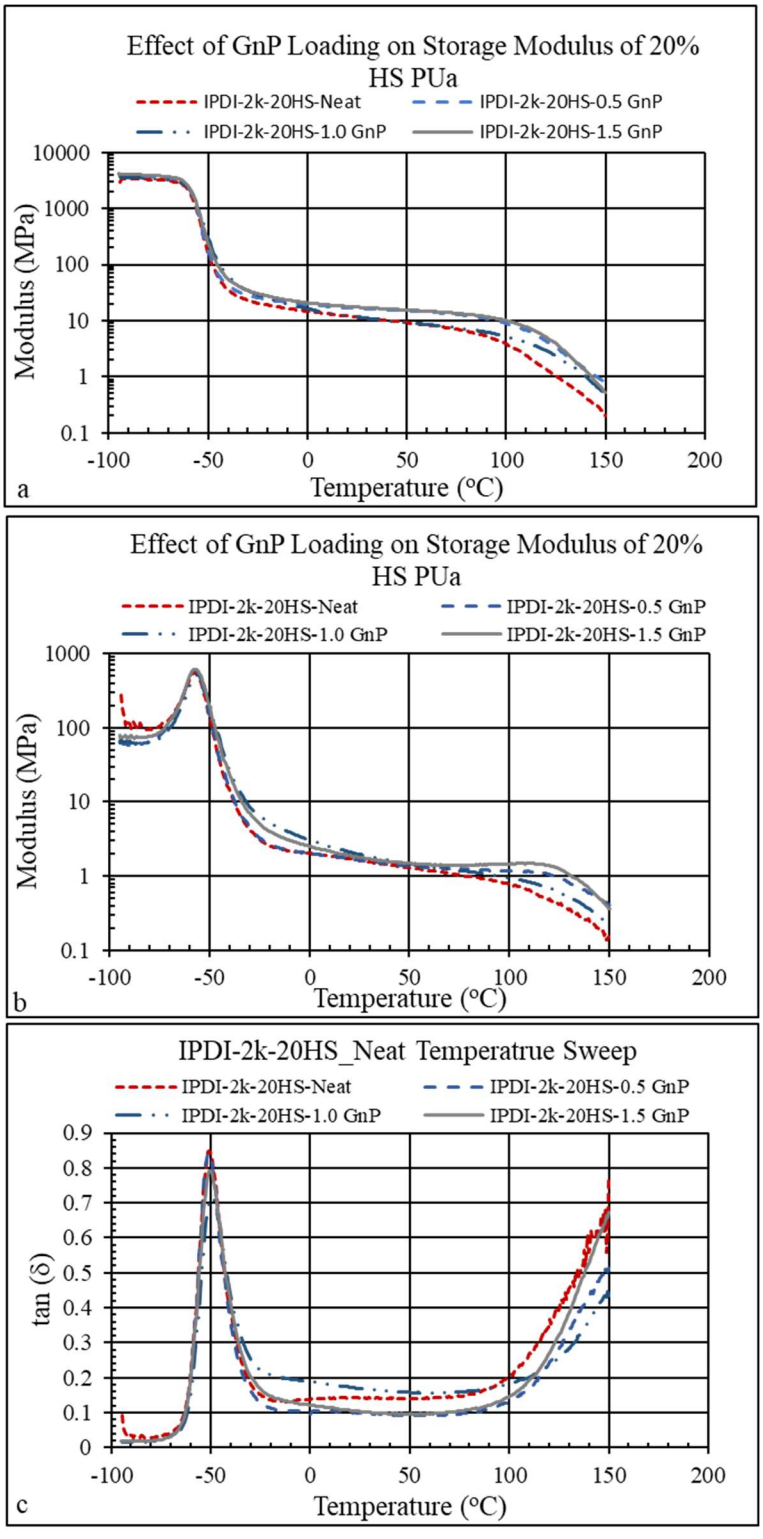

Figure 4-14. DMA curves for all IPDI-2k-20HS (20% HS) formulations. a) Storage modulus, b) Loss Modulus, c) tan(δ).

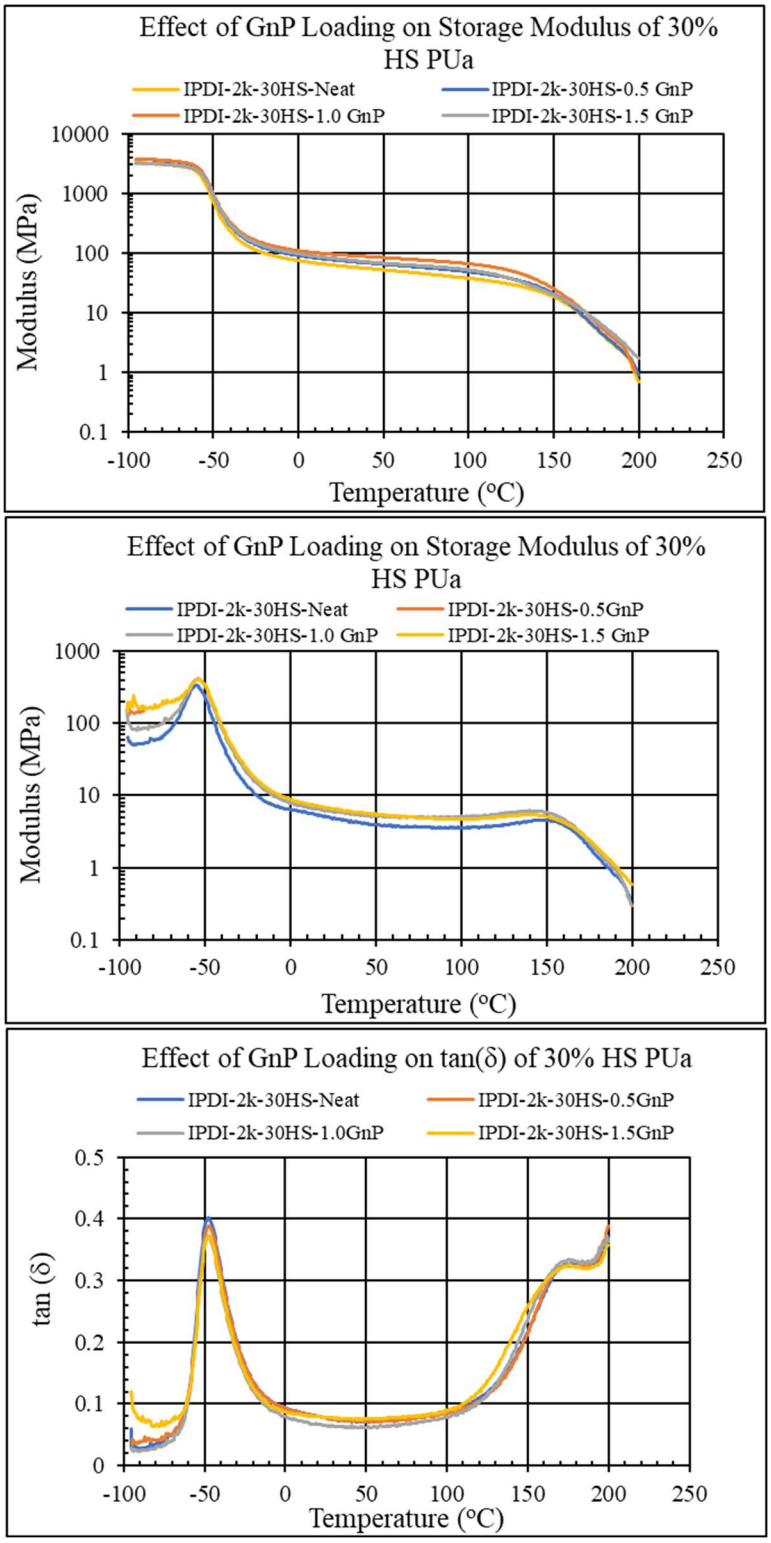

Figure 4-15. DMA curves for all IPDI-2k-30HS 30% HS) formulations. a) Storage modulus, b) Loss Modulus, c) tan(δ).

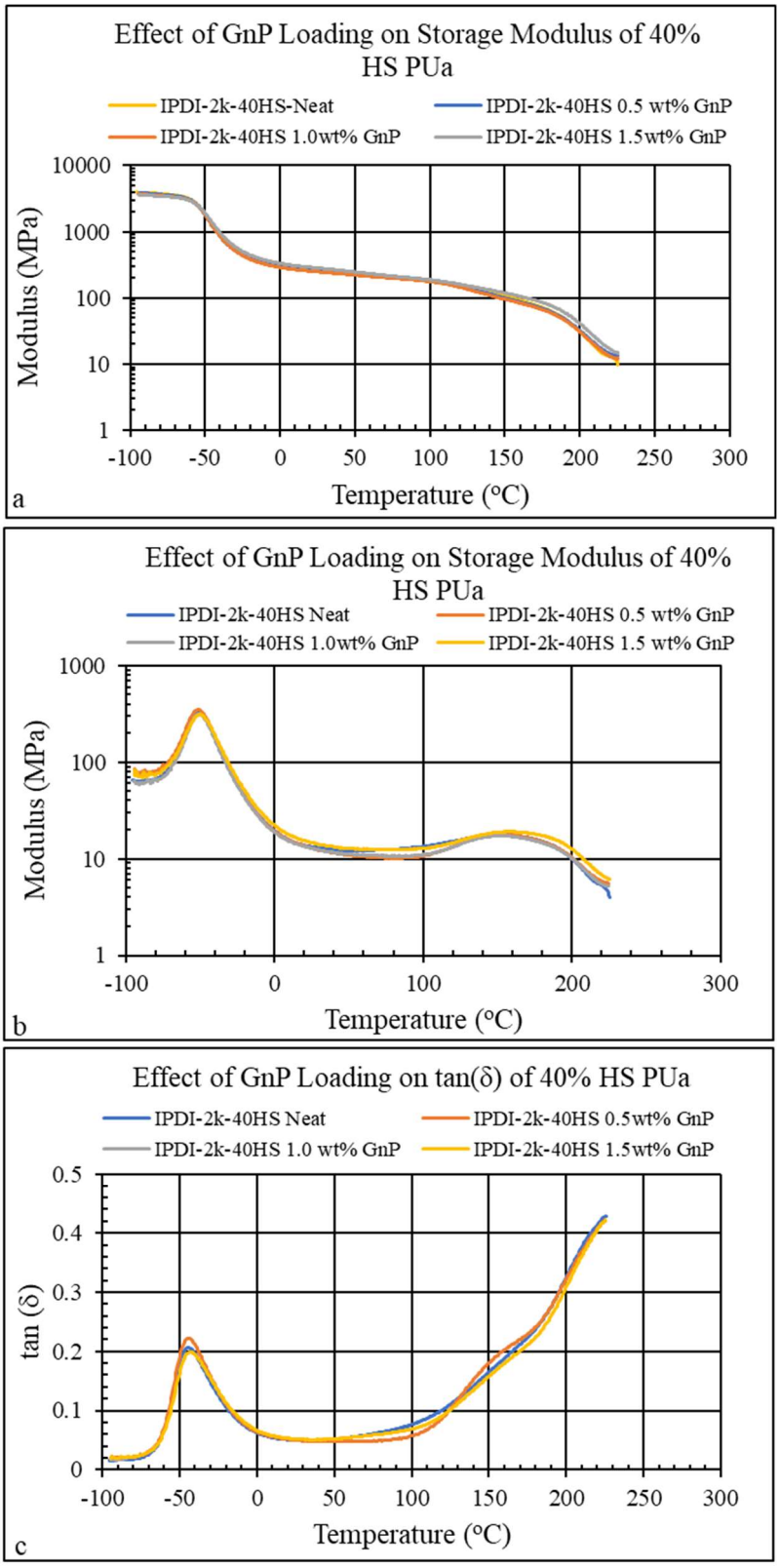

Figure 4-16. DMA curves for all IPDI-2k-40HS (40% HS) formulations. a) Storage modulus, b) Loss Modulus, c) tan(δ).

4.2.5 Tensile Data

Figure 4-17, Figure 4-18, and Figure 4-19 shows the results of the tensile testing for all formulations with different HSWF and GnP loadings; the results are also summarized in Table 4-6. The additions of GnP had the most impact on the lowest HSWF formulation. The secant modulus (for the 20 HSWF, 0.5% GnP) increased by a factor of approximately 3 relative to the neat PU; the tensile stress at failure increased by a factor of approximately 10 and the tensile strain to failure increased by approximately 130%. Additional increases in GnP weight fraction, however, resulted in decreased properties. Similar trends were observed of the 30 and 40 percent hard segments samples for the tensile strength but not necessarily for the secant modulus and the strain to failure.

The area under the tensile curve or the toughness can be a method of "normalizing" the tensile data into one single parameter that can describe a materials balance between strength and ductility. The toughness (U_T) was calculated for all formulations utilizing Equation 4.1.

$$U_T = \int_0^{\varepsilon_f} \sigma d\varepsilon \tag{4.1}$$

where ε_f is the failure strain, σ is the stress, ε is the strain. The integral was estimated using the trapezoidal rule to determine the area under the tensile curve. Examining the toughness values in Table 4-6 we see that for all formulation a maximum occurs at a nano loading of 0.5% GnP. The highest increase in toughness (4.5x) was seen in the 20 percent hard segment formulations, the more ductile formulations. The effect of the GnP nano additions diminished as percent hard segments are increased. A slight increase in toughness can be seen in the GnP addition for the 30 and 40 weight percent samples. Examining the tensile fracture surfaces can elucidate the drop in toughness.

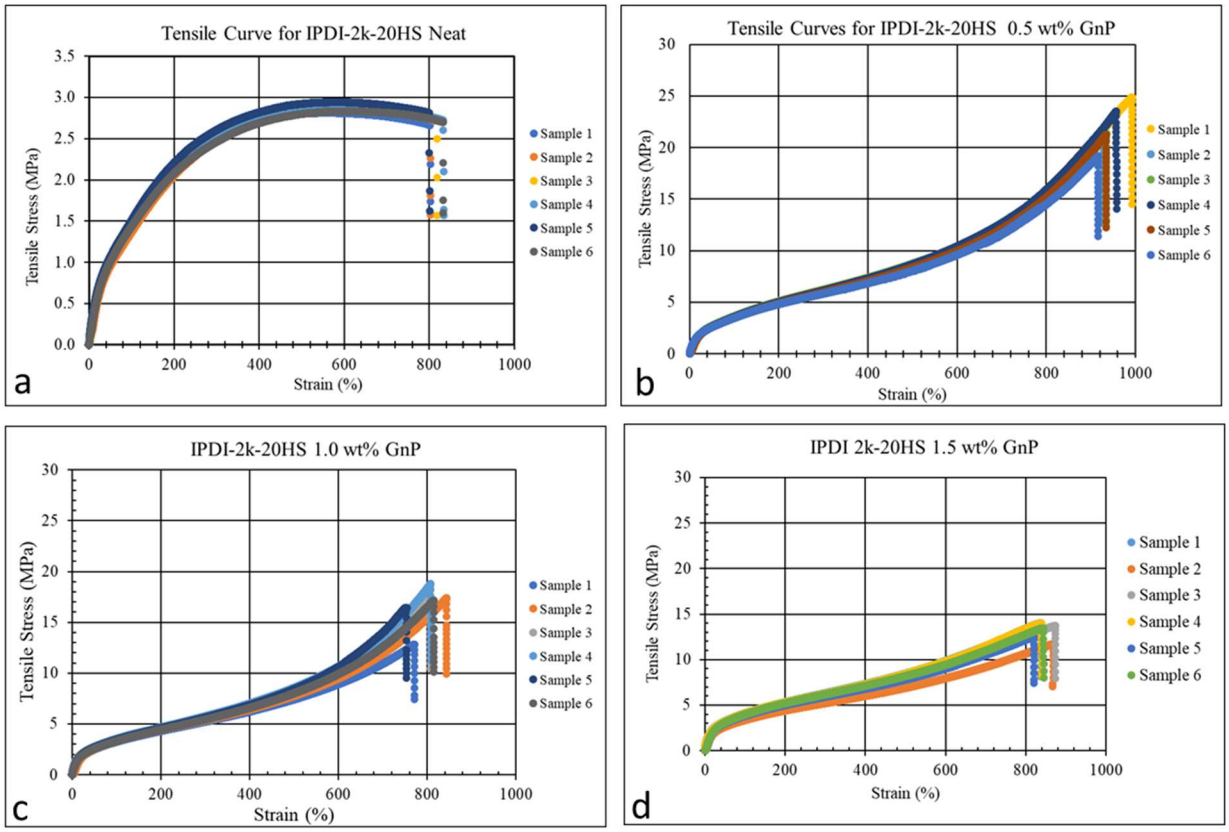

Figure 4-17. Tensile Curves for the IPDI-2k-20HS system. a) is the neat PUa, b) is the 0.5wt% GnP system, c) is the 1.0 wt% GnP system, and d) is the 1.5 wt% GnP system.

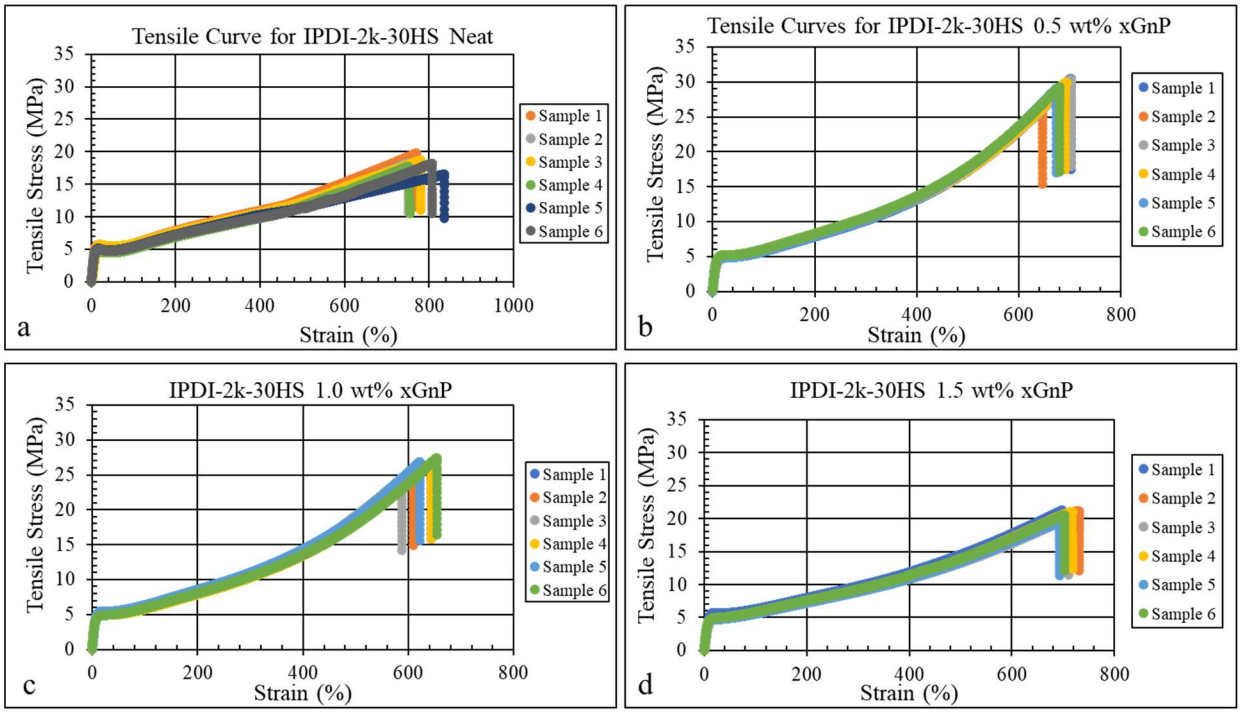

Figure 4-18. Tensile Curves for the IPDI-2k-30HS system. a) is the neat PUa, b) is the 0.5wt% GnP system, c) is the 1.0 wt% GnP system, and d) is the 1.5 wt% GnP system.

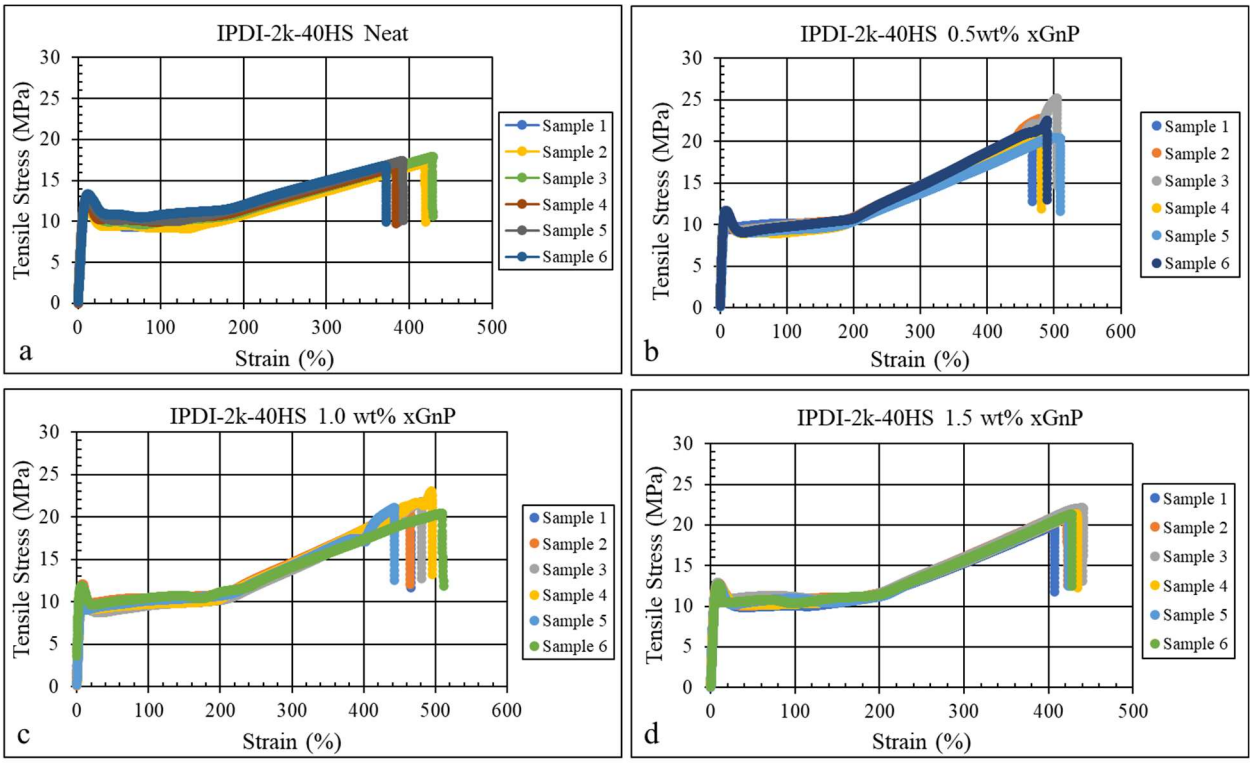

Figure 4-19. Tensile Curves for the IPDI-2k-30HS system. a) is the neat PUa, b) is the 0.5wt% GnP system, c) is the 1.0 wt% GnP system, and d) is the 1.5 wt% GnP system.

Table 4-6. Results for the Tensile testing.

Base Formulation	GnP Loading	Secant Modulus (2% Strain)	Tensile Stress @ Failure (MPa)	Tensile Strain @ Failure (%)	Toughness J/m^3
IPDI-2k-20HS	**Neat**	3.3 +/- 0.5	2.7 +/- 0.1	814 +/- 15	2.0 +/- 0.1
	0.5 wt%	11.1 +/- 0.2	22.0 +/- 2.0	944 +/- 27	9.3 +/-0.9
	1.0 wt%	11.4 +/- 0.5	16.8 +/- 2.2	799 +/- 33	6.0 +/- 0.6
	1.5 wt%	13.1 +/- 1.4	13.2 +/ 0.9	846 +/- 21	6.3 +/- 0.4
IPDI-2k-30HS	**Neat**	63.0 +/- 6.3	18.2 +/- 1.1	782 +/-33	8.2 +/- 0.5
	0.5 wt%	60.4 +/- 3.6	29.3 +/- 1.4	683 +/- 21	9.0 +/- 0.5
	1.0 wt%	75.5+/- 6.8	26.6 +/- 0.7	643 +/- 24	7.9 +/- 0.3
	1.5 wt%	71.8 +/- 9.2	20.5 +/- 0.7	709 +/- 14	7.9 +/- 0.4
IPDI-2k-40HS	**Neat**	203.9 +/- 8.9	17.1 +/- 0.5	397 +/- 22	4.9 +/- 0.3
	0.5 wt%	212.8 +/- 4.1	22.2 +/- 1.8	489 +/- 16	6.6 +/- 0.3
	1.0 wt%	222.8 +/- 3.5	21.2 +/- 1.0	475 +/-24	6.3 +/- 0.5
	1.5 wt%	248 +/- 10.1	21.2 +/- 0.7	425 +/- 11	5.8 +/- 0.3

The analysis begins with the fracture surface of the neat PUa. Figure 4-20 compares the fracture surfaces for all three neat formulations. For the 20% HS PUa, the fracture surface was relatively flat, and continuous, no identifiable fracture features such as hackle lines were seen. This suggests that the polymer did not exhibit any crack branching. It is possible that the crack developed and failed instantaneously with little or no crack propagation. The fracture mode is most likely through crazing, fibril formation and final crack in a single plane that is perpendicular to the tensile direction. The fracture surfaces for both the 30% and 40% HS samples showed hackle lines, “river patterns” pointing back to the fracture origin. For the fracture of 30% HS sample, Hackle lines were seen. These are outwardly divergent lines, “river patterns” along the fracture surface. The river patterns point back towards the bottom left corner which is the fracture

origin. The Hackle line represents the presence of multiple crack surfaces being formed during crack propagation and failure. The 40% HS sample also consisted of hackle lines pointing back to a pore in the bottom middle of the sample.

In comparing all the 30% HS and 40%HS samples the hackle lines are more intense and numerous in the 40%HS than the 30%HS. This indicates that the percolated hard phase, which are stiffer than the soft phase matrix may be providing a more torturous path for crack propagation. This is especially true when including the 20% HS sample, which exhibits no crack branching. The increase in crack branching is somewhat related to the PUa chain mobility. As the hard segments (or percolated hard phase) are increased, the PUa polymer chain mobility is decreased, as seen in dramatic increase of the storage modulus in the DMA curves of the previous section. With chain mobility decreasing, the crack front will branch to find a path of least resistance, torturous crack front. The addition of the GnP significantly changed the fracture modes of the tensile samples.

4.2

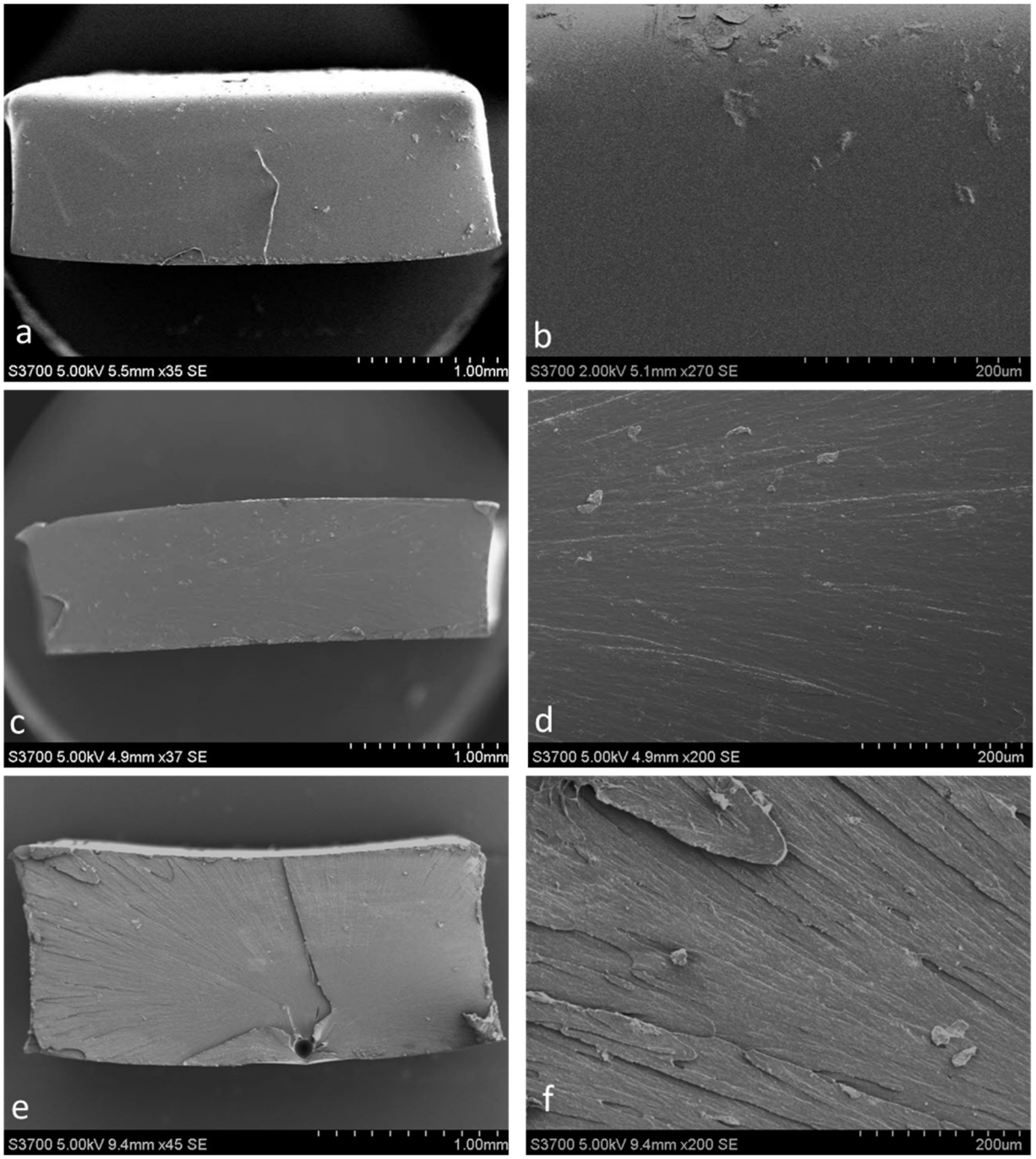

Figure 4-20. Comparison of the SEM macro-photographs for all three neat PUa formulations. a) & b) 20% HS, c) & d) 30%HS, e) & f) 40% HS. Note that the 20% HS showed no river patterns or any morphological features that would point toward the fracture origin. The 30% and 40 % showed river patterns with the 40% more than the 30%.

Figure 4-21 shows a series of SEM photographs the fracture surface the IPDI-2k-20%HS 0.5wt% GnP samples. Note in comparing in Figure 4-20 and Figure 4-21 the fracture surface has changed from a relatively flat, continuous surface with no crack branching to a rougher surface indicating multiple planes for crack propagation. Due to the electron beam interaction with fracture surface and GnP facets the PUa matrix polymer appears darker and the GnP's appear brighter, as highlighted in the higher magnification photographs in Figure 4-21b and c. Figure 4-21d shows a higher magnification of (a) further illustrating good dispersion of the GnP in the PUa matrix. The black arrow in Figure 4-21e and f show PUa matrix material still bonded to the GnP, while the inset (white box) of (f) highlights the GnP and the fact that individual facets of the GnP layers can be seen. The fact that PUa can still be seen attached to the GnP, even after failure indicates that good bonding existed between the PUa and the GnP. Figure 4-22 shows a higher magnification of the black box in Figure 4-21a. Here the crack fibril can be seen extending across the PUa giving further credence that the 20% PUa is fracturing through the initiation of crazes with crazes growing into fibril and then finally crack formation and failure. Figure 4-22 also shows that the crack is arrested by the GnP. A general trend that is seen is that the fracture surface is more faceted as the amount of GnP is increased, Figure 4-21, Figure 4-23 and Figure 4-24. The GnP only influences the crack branching that is seen and not necessarily the fracture mode of the matrix. PUa fibrils across crack fronts are seen, as well as PUa fibrils still attached to the GnP after fracture.

For the 30%HS formulations the addition of the GnP from 0.5 to 1.5 weight percent also increases the faceted look of the fracture surface. In the case of the 30% sample the GnP doesn't arrest the crack as is seen in the 20% samples. Figure 4-25 shows the fracture surface of the IPDI-2k-30HS 0.5 GnP. Note the fracture surface is faceted with different planes of fracture as opposed

to the Hackle lines seen in the neat sample (Figure 4-25c and d). Similar to the 20 percent hard segment formulations, good dispersion is seen in the 30 percent hard segment composite samples. The nanoparticle remained exfoliated and PUa fibrils can be seen still attached to the GnP even after the tensile loading indicated good bonding GnP and the PUa (black arrows in Figure 4-25e). The 30% HS regardless of nano-loading exhibited a different fracture phenomenon in vicinity of the GnP. Small cleavage facets can be seen emanating from the GnP as highlighted by the red arrows in Figure 4-25c. This indicates that fracturing is occurring from the GnP. As the nanoparticle loading increased from the 0.5 to 1.5 weight percent GnP. The faceted look of the fracture surface increased. Although some fibril can be seen branch across the PUa, as shown in Figure 4-25c and d.

For the 40 percent hard segment samples, Figure 4-28, Figure 4-29, and Figure 4-30 the fracture features were similar to the 30 percent hard segment with two notable exceptions. First, the faceted look of the fracture surface increases with cracking occurring along the tensile direction as well as the perpendicular to the tensile direction. Second no fibrils were seen bridging across the PUa or the GnP.

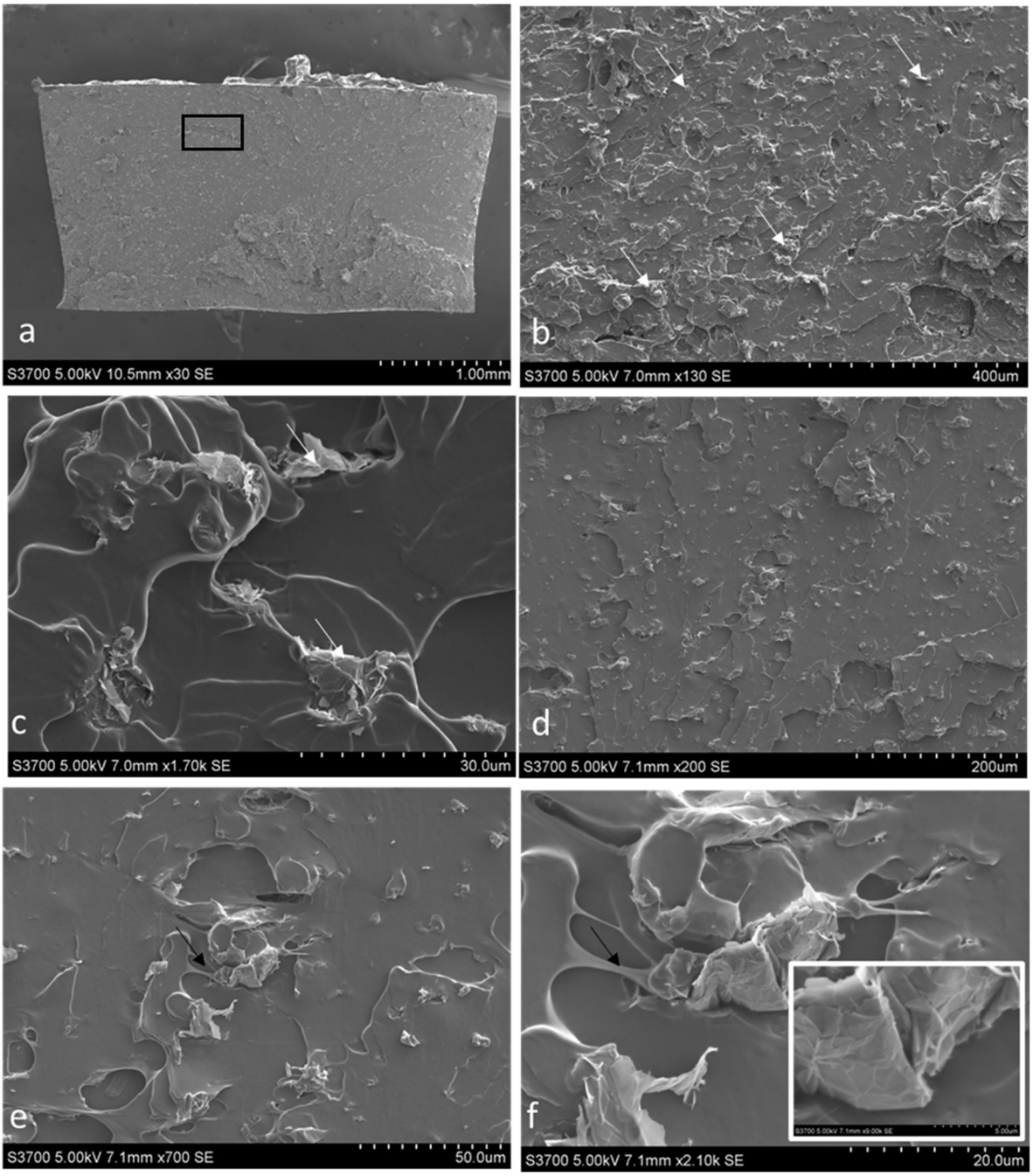

Figure 4-21. SEM fractography of the 20% HS with 0.5 wt% GnP added. a) overall view of the fracture surface. The white specs are showing are the GnP. b) and c) showing close ups of the GnP, highlighted by white arrows. d and e) another close of (a) but different region. The black arrow in (e) points to an area that the PUa is still bonded to GnP. f) close up of the GnP in (e) still bonded to the PUa. Note that the inset (white box) highlights the individual GnP platelets.

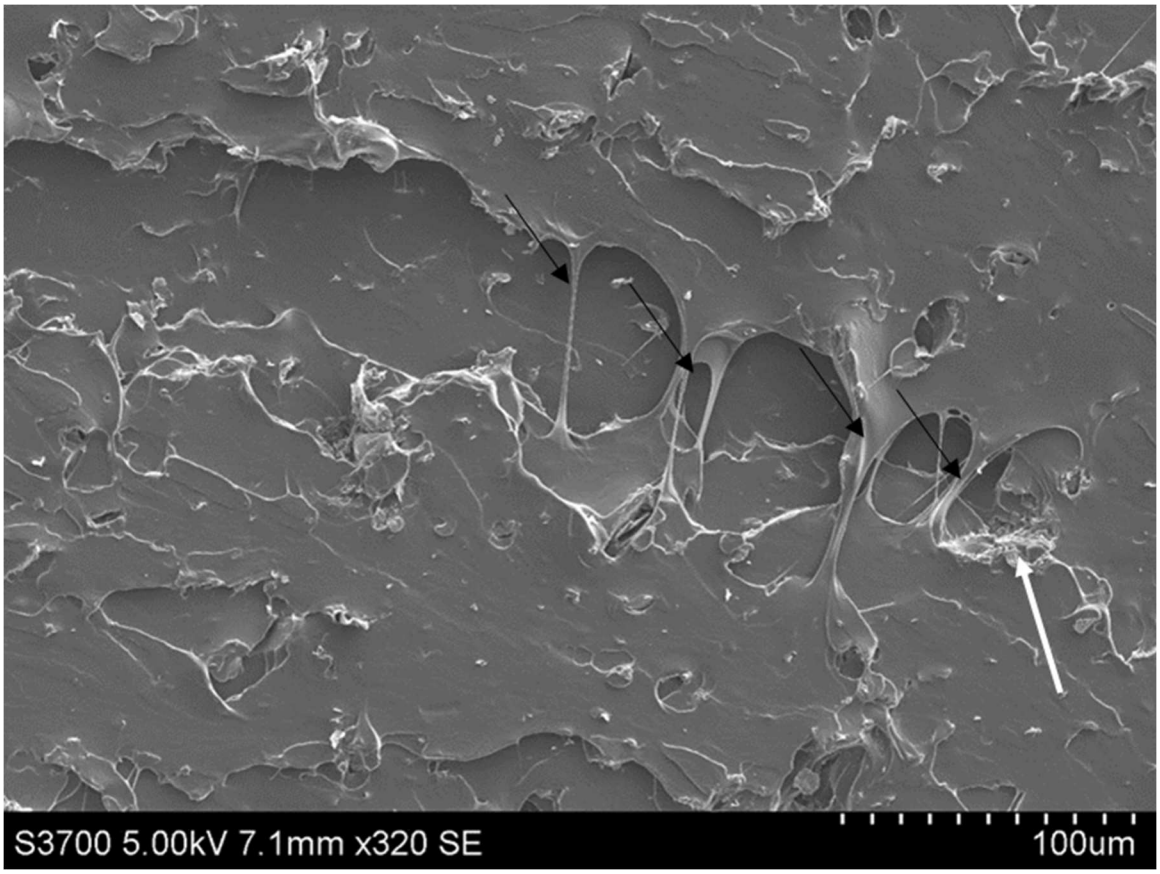

Figure 4-22. SEM photographs of black box from Figure 4-21 a. The black arrows highlight the PUa matrix still bridging the crack. The white arrow points to an GnP arresting the crack.

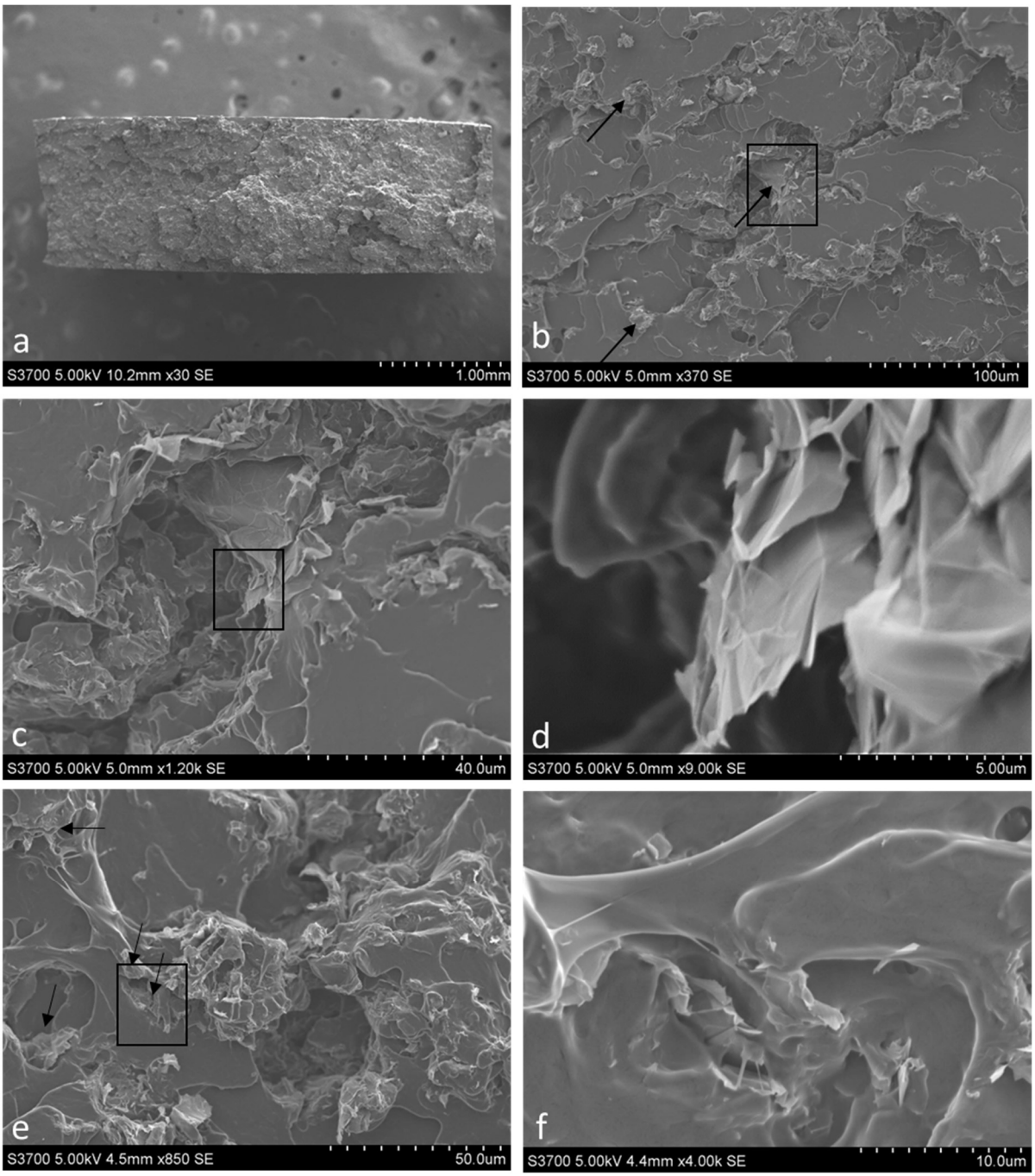

Figure 4-23 – IPDI-2k-20HS 1.0wt% GnP. a) Overall view of the fracture surface. The brighter specs are the GnP. b) higher magnification of (b). The arrows point to the GnP which are slightly brighter than the PUa matrix, c) Increased magnification of the boxed area. The arrows in the e) point to GnP, while f) is a higher magnification of the boxed area.

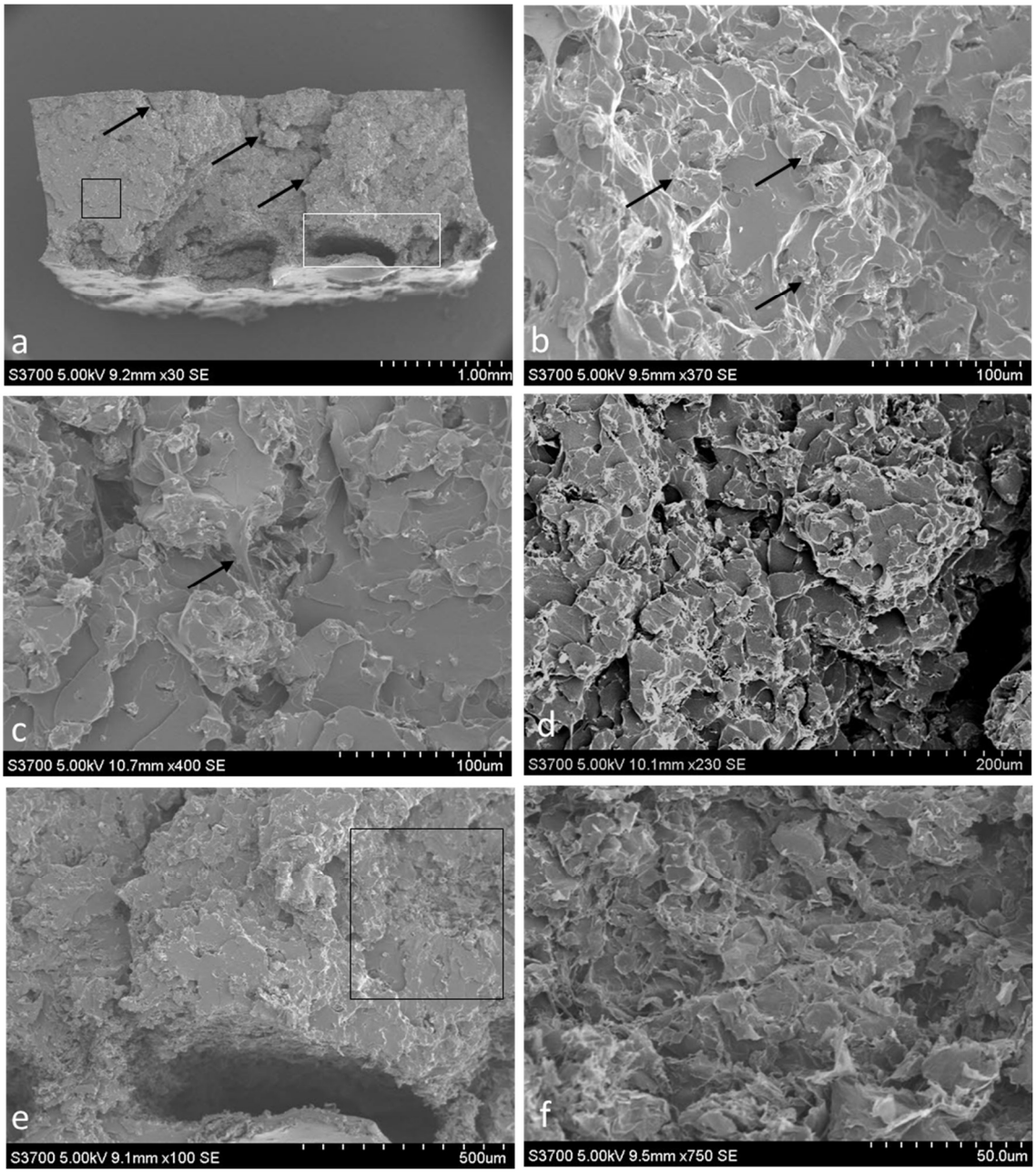

Figure 4-24. IPDI-2k-20HS- 1.5wt% GnP. a) Overall view of the fracture surface. The arrows point to cracks that appear to be longitudinal to the loading direction. As well as the primary traverse cracks. b) Increased magnification of the boxed area in (a). The black arrows point to the GnP. This is similar to the 1.0 wt% GnP seen in Figure 4-23, except slightly more faceted. c) photograph showing some bridging between the PUa and the matrix. d) another area from (a) showing the dispersion of nanoparticles, brighter objects, and the very small facets of Pua. e) Photograph showing an area of what seem to be an agglomeration of the GnP, which no bonding of the GnP to the film surface f) increase magnifications of the boxed area in (e).

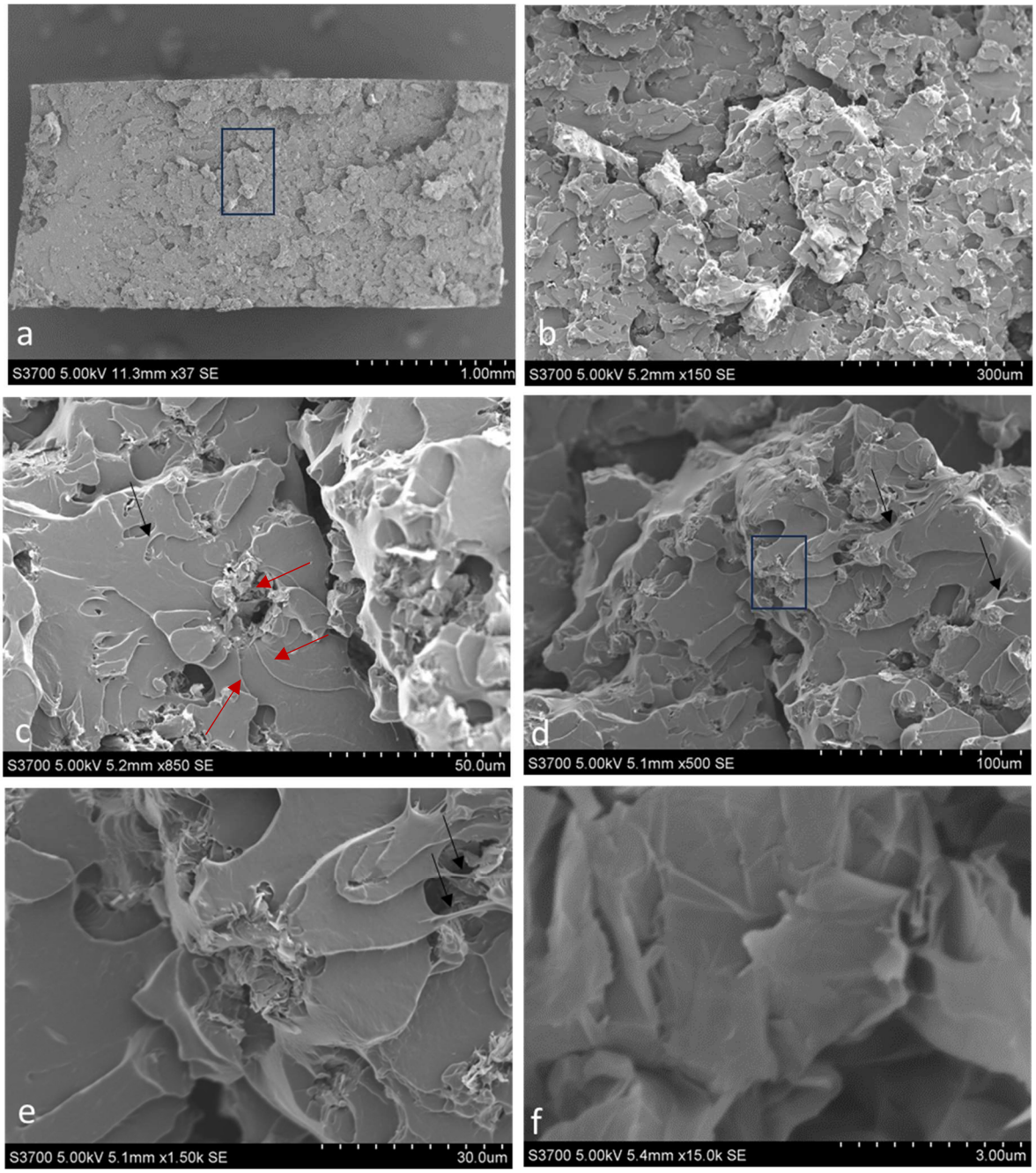

Figure 4-25. IPDI-2k-30HS 0.5wt% GnP. a) Overall view of the fracture surface. b) increased magnification of boxed areas in (a). Note that the fracture surface is much more faceted than the 20% 0.5 wt% GnP samples. Indicating that the fracture toughness of the base PUa will influence the brittle fracture appearance of the nano composite. c and d) Photograph showing another (random area) from (a). The arrow point to an example of the PUa bridging the facets (c) and GnPs in (d). e) increased magnification of (d). Again, the arrows point to fibrils of PUa bridging the GnP. f) showing a high magnification of the GnP in e). The individual GnP platelets are differentiated indicating the GnP remained exfoliated.

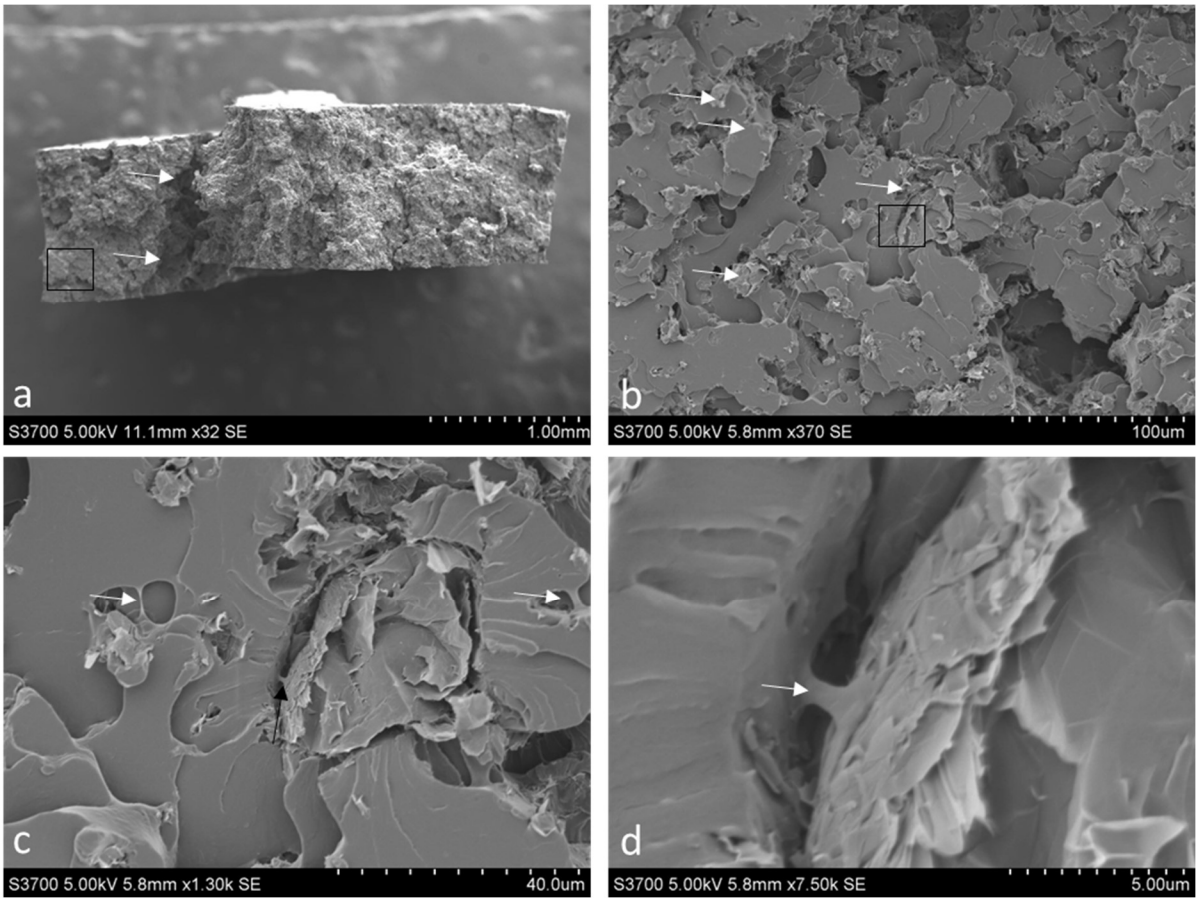

Figure 4-26. IPDI-2k-30 HS 1.0 wt% GnP. a) Overall view of the fracture surface. The arrow points to a longitudinal (to the loading direction) crack. b) The crack surface is highly faceted giving it a brittle appearance. b) Increased magnification of boxed area of (a). The GnPs are highlighted by the arrows and good dispersion of the GnP's is seen. c) is showing an increased magnification of the boxed area in (b). Note that the arrows point towards fibrils that are bridging the GnP to the PUa matrix. D) increase magnification of the fibril highlighted by the black arrow in (c). Also note the individual platelets of the GnP indicating the GnP has remained exfoliated.

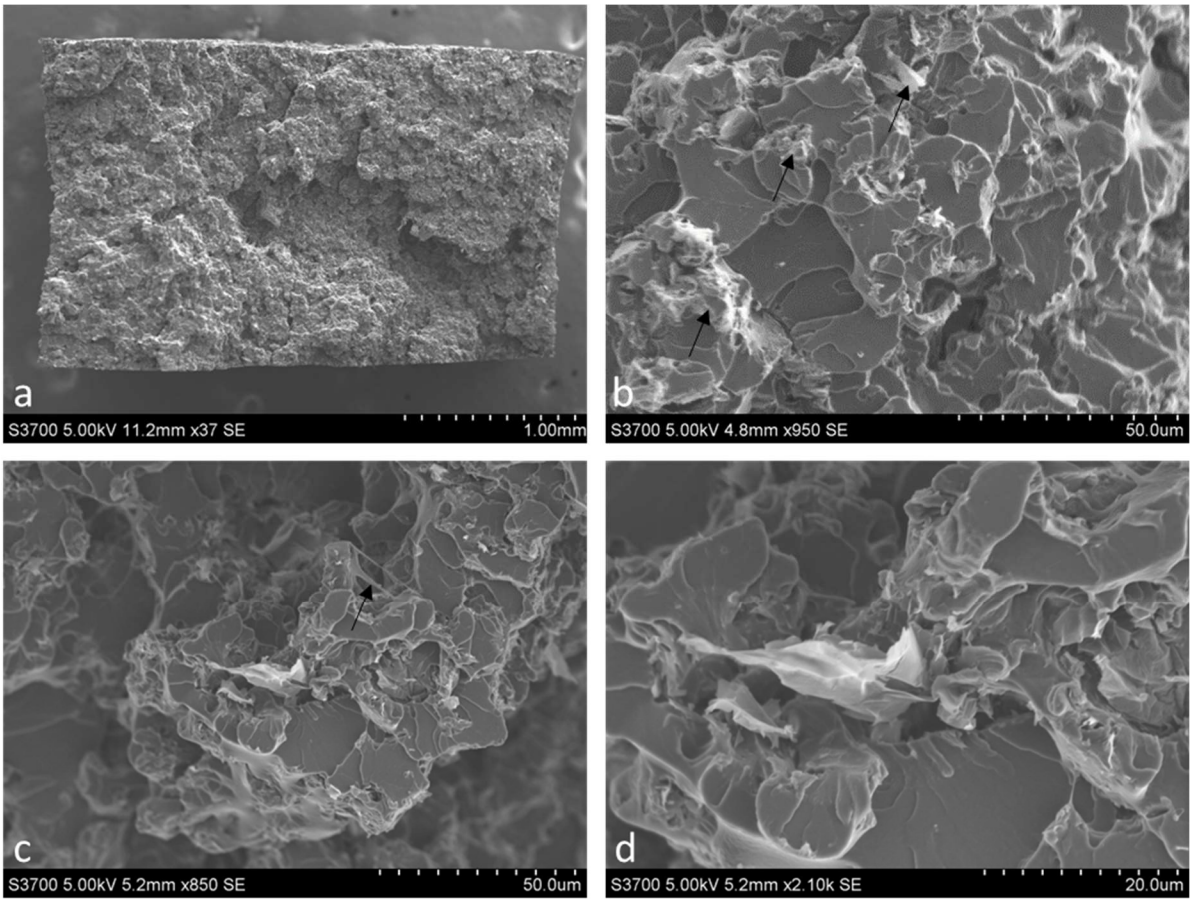

Figure 4-27. IPDI-2k-30 HS 1.5 wt% GnP. a) Overall view of the fracture surface. b) Increased magnification of the crack surface. The crack surface is highly faceted giving it a brittle appearance. The GnPs are highlighted by the arrows and good dispersion of the GnP's is seen. c) Increase magnification of (a) except at different location. The arrow points to fibrils spanning the GnP and PUa matrix. d) Increase magnification of the (c).

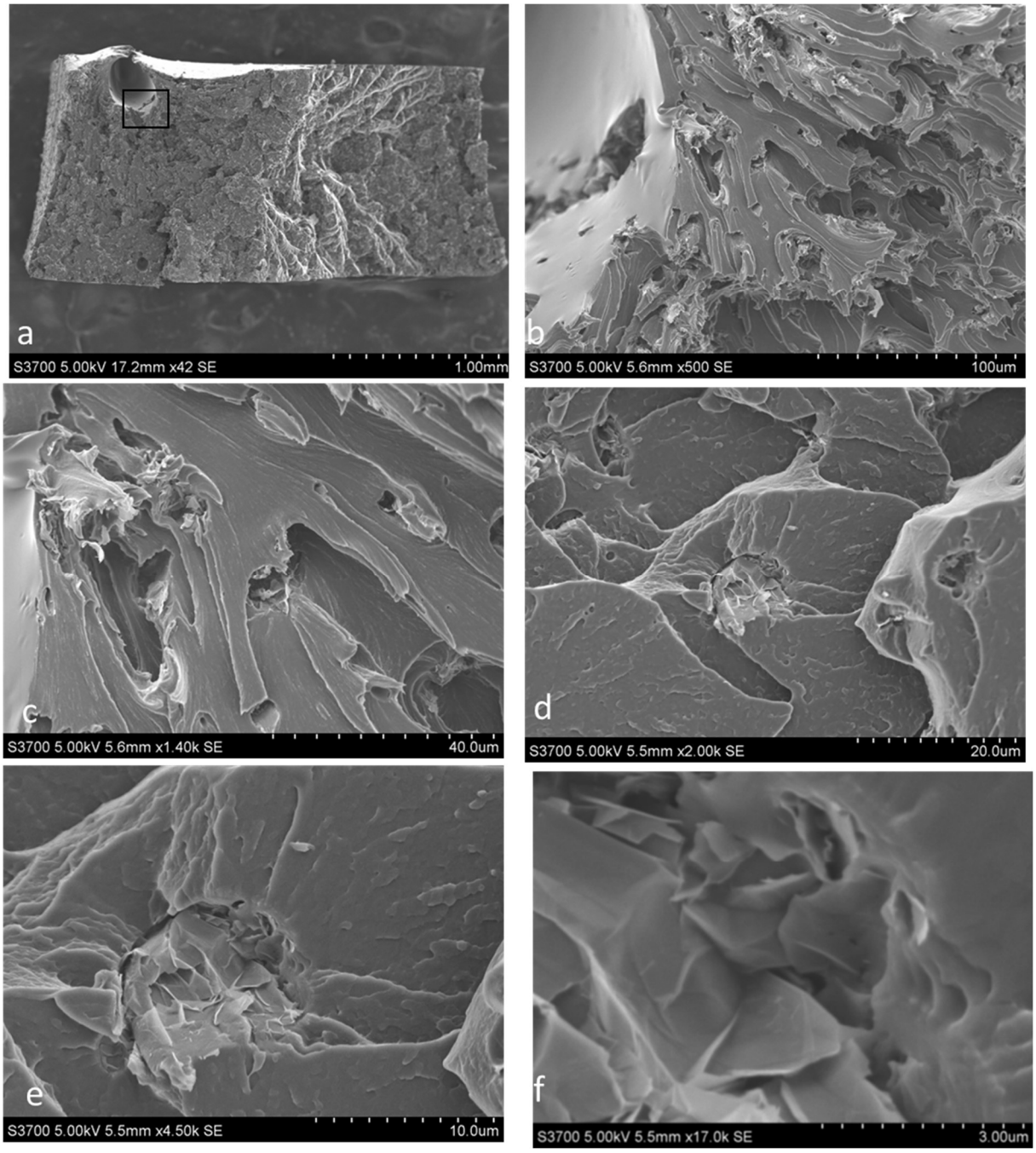

Figure 4-28. IPDI-2k-40 HS 0.5 wt% GnP. a) Overall view of the fracture surface. The fracture initiated from the large pore in the upper lefthand corner. There are two crack transverse crack surfaces on different planes. b) Increased magnification of the crack surface in the box area of (a). River patterns, highlighted by the arrows are seen which point back towards the pores. c) increased magnification of (b). d) and e) are series of photographs showing the fracture surface near the GnP. F) is a higher magnification photograph of the GnP in (e) showing that the PUa is bonded to the GnP. Individual platelets of the GnP can be seen indicating the GnPs remain exfoliated.

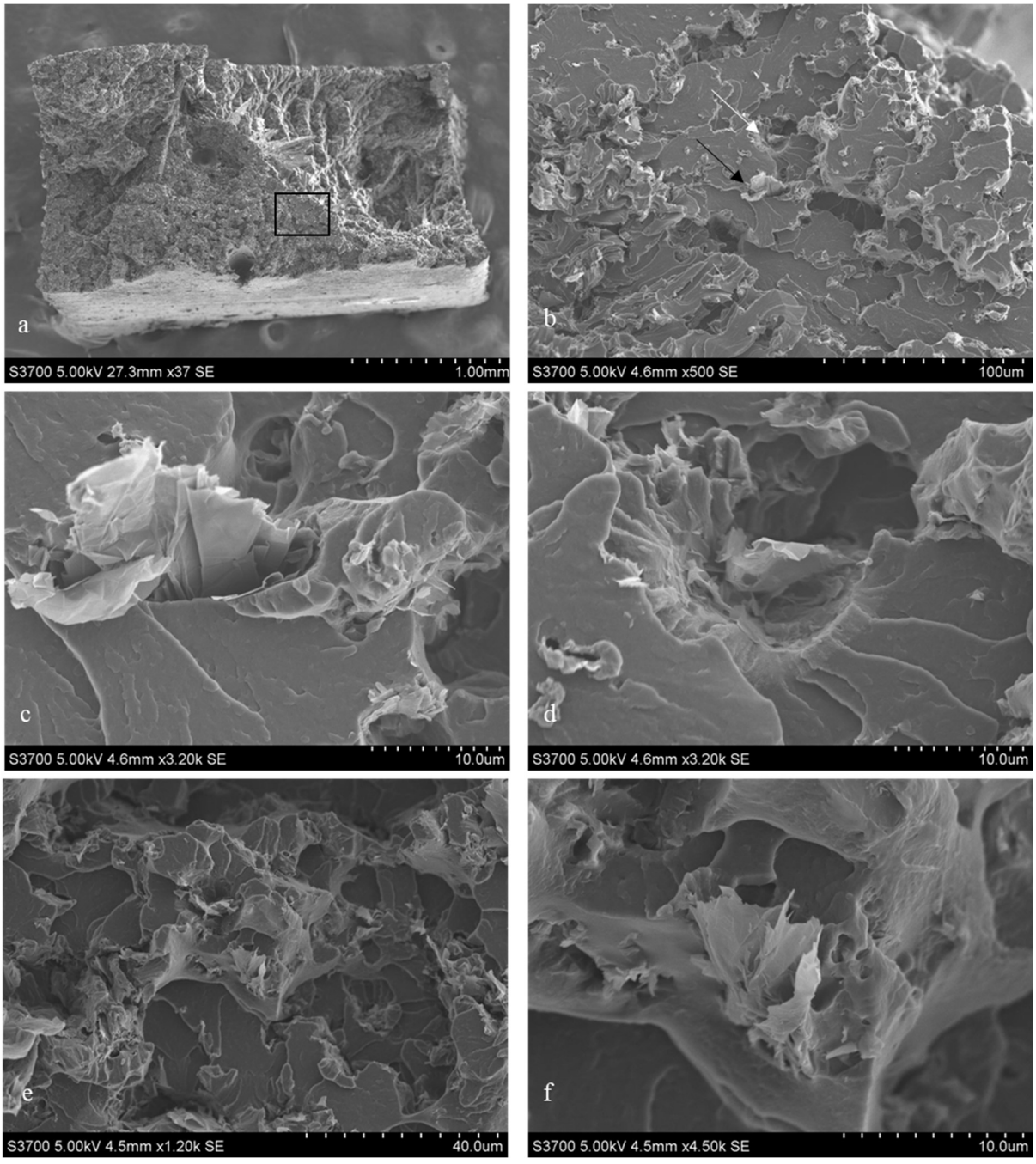

Figure 4-29. IPDI-2k-40 HS 1.0 wt% GnP. a) Overall view of the fracture surface. b) Increased magnification of the crack surface in the box area of (a). Black arrow points to the GnP which is highlighted in (c). The white arrow points the GnP highlighted in (d). c) increased magnification of (b) showing the GnP. The GnP remains exfoliated, and cleavage facets are seen emanating from the GnP. d) increased magnification of white arrow in (b). Showing many cleavage facets emanating from the GnP. e) showing that the PUa is bonded to the GnP. Individual platelets of the GnP can be seen indicating the GnPs remain exfoliated. f) increased magnification of (e).

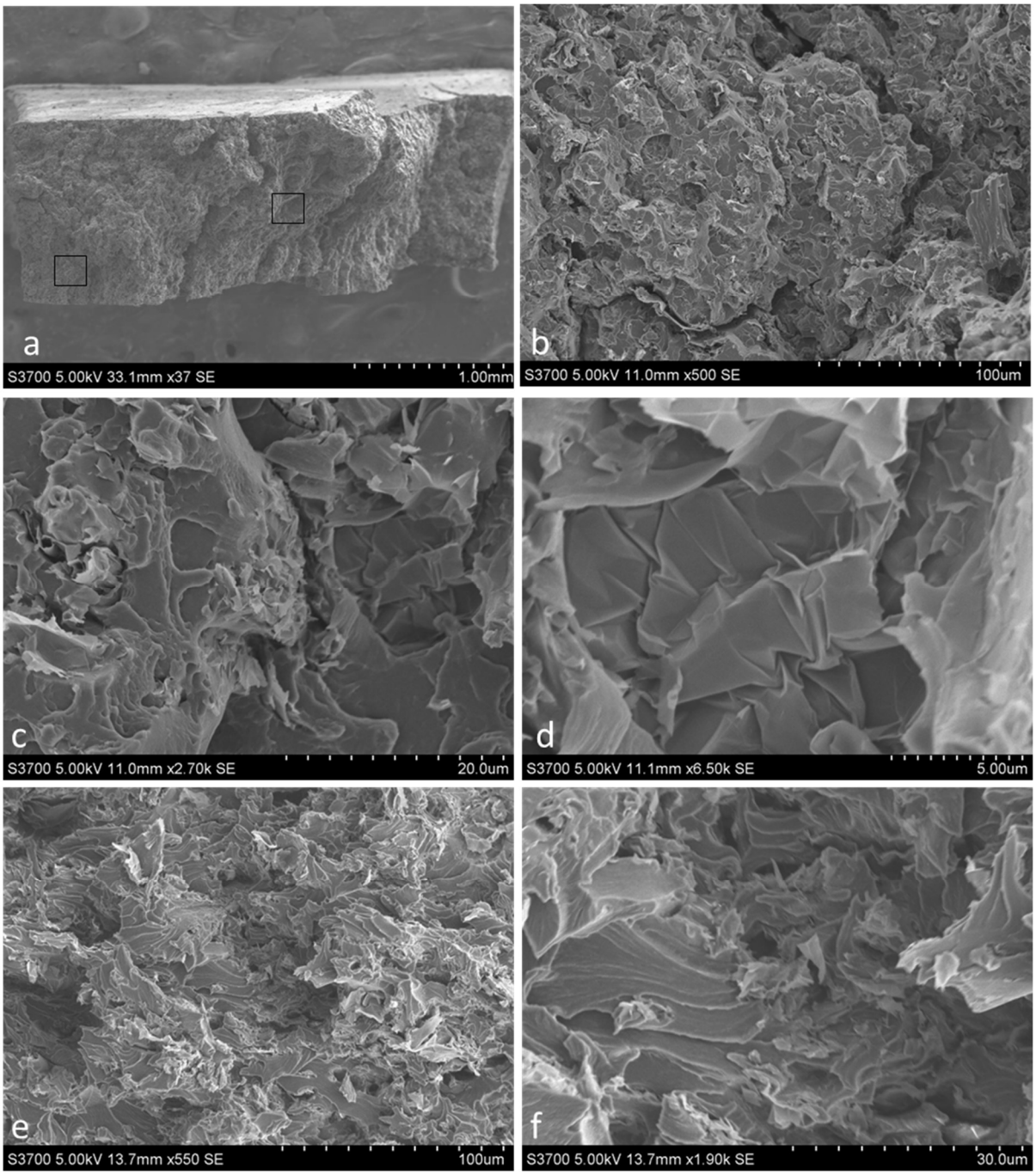

Figure 4-30. IPDI-2k-40 HS 1.5 wt% GnP. a) Overall view of the fracture surface. There are two crack transverse crack surfaces on different planes. b) Increased magnification of the crack surface in the box area of (a). River patterns, highlighted by the arrows are seen which point back towards the pores c) increased magnification of (b). d) and e) are series of photographs showing the fracture surface near the GnP. F) is a high magnification photograph of the GnP in (e) showing that the PUa is bonded to the GnP. Individual platelets of the GnP can be seen indicating the GnPs remain exfoliated.

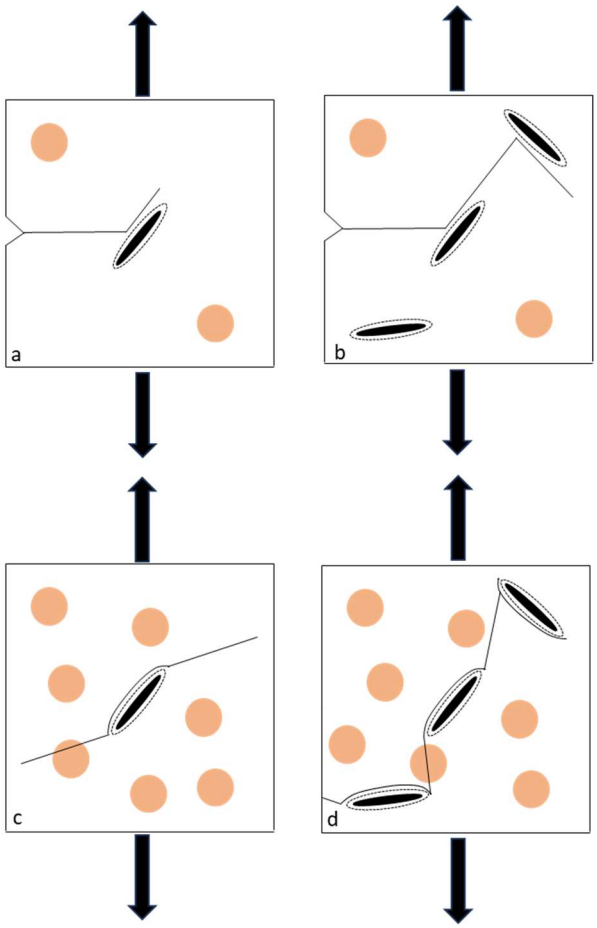

Figure 4-31. Schematic Representation of fracture occurring in the PUa nano composites.

To better explain the fracture mechanisms, a schematic representation of the microstructure is shown in Figure 4-31. Here the percolated hard phases are represented as the spheres and the GnP is represented by the elongated black ellipses. Figure 4-31a represents a crack front progressing through a PUa with low amount of percolated hard phase (e.g. the 20% hard segment). Polymer chain mobility is affected by the hard segment content [61]. A low hard segment PUa with increased polymer chain mobility allows for efficient stress transfer between the host polymer and GnP, resulting in possible enhancements in mechanical properties [66], [67]. As the failure initiates and the crack progresses through the PUa matrix the presence of GnP will create crack arresting mechanisms and their inherent stiff nature will force the crack to go around the GnP as

observed in Figure 4-31b or can even stop the propagation of the crack. This was observed in experimental fracture sample and is highlighted in the 20% hard segment 0.5 wt.% sample and shown in Figure 4-22 wherein a crack front is clearly observed being arrested by an GnP particle. As the nano-particle loading is increased, stress concentration occurring at the edges of multiple GnPs in close vicinity can lead to microcracks or initiation of failure. Furthermore, at low HSWF at high elongations, the chain mobility will cause the GnP particles to align along the loading direction bringing the GnP particles closer to each other. Eventually enough microcracks will form, then grow to bridge with each other causing final fracturing of the specimen. In PUa with high HSWF, the material response is governed by the properties of the hard segments. The influence of GnP appears to be minimal. A simple analogy is similar to continuous fiber composite with a matrix reinforced with GnP, wherein the matrix properties are considerably enhanced by the addition of GnP, but the composite properties are still governed by the carbon fiber [66]–[68]. Using the above analogy, it appears that hard segments control the behavior of PUa with high HSWF and the effect of GnP is less pronounced. Similarly, as mentioned earlier, the effect of GnP is more pronounced in low HSWF PUa. These observations are further confirmed by the toughness values shown in Table 4-6.

4.5 Conclusions

The intent of this chapter was to study the effect of adding GnP to a model PUa with varying weight fraction of hard segments. Throughout the solvent cast process, the GnP remained exfoliated, and no agglomeration was seen. The GnP contained no functionalization on the edges of the basal plane. Bonding between the GnP and the PUa was observed in both samples that were frozen in LN2 and fractured and as well as the tensile tested samples. The effect of the GnP on the mechanical properties decreased as the hard segment weight fraction increased. The most

dramatic effect was seen in the 20 percent hard segment formulations; it was also determined that the most efficient loading of the nano-particles was at 0.5.

Chapter 5 - Linear Viscoelastic Properties of Neat and Filled Polyurea – Modeling

5.1 Introduction

Chapter 4 compares the properties of both neat and filled PUa systems. It was shown that for the low-HSWF polyureas, there is a greater effect on the quasi-static properties, with the tensile failure mode changes within increase HSWF and increasing weight fraction of GnP. DMA temperature sweeps showed that very little changes in the Tg and the Storage modulus, above and below Tg. In this chapter, time-temperature-superposition (TTS) principle -- along with a novel approach in materials modeling known as the fractional calculus -- is used to elucidate the linear viscoelastic properties of neat and filled PUa. This material has been previously published in two peer-reviewed articles: (1) *Experimental and modeling studies of IPDI-based polyurea elastomers* [54] (2) *Polyurea–Graphene Nanocomposites—The Influence of Hard-Segment Content and Nanoparticle Loading on Mechanical Properties* [69].

Rathinaraj et al [40] utilized fractional calculus to describe the linear viscoelastic properties of multi-scale complex fluids (fractional Maxwell model or FMM, Equation 5.1)

$$\frac{E^*(\omega)}{E_o} = \frac{(i\omega\tau_c)^\alpha}{1+(i\omega\tau_c)^{\alpha-\beta}} \tag{5.1}$$

Here, E^* is the complex elastic modulus, E_o is a characteristic modulus (often called plateau modulus), τ_c is a characteristic relaxation time, α and β are power-law exponents. The real and imaginary parts can be split into the storage, E', and loss, E", modulus, Equations 5.2a and 5.2b respectively,

$$\frac{E'(\omega)}{E_o} = \frac{(\omega\tau_c)^\alpha \cos\left(\frac{\pi\alpha}{2}\right)+(\omega\tau_c)^{2\alpha-\beta}\cos\left(\frac{\pi\beta}{2}\right)}{1+(\omega\tau_c)^{\alpha-\beta}\cos\left(\frac{\pi(\alpha-\beta)}{2}\right)+(\omega\tau_c)^{2\alpha-\beta}} \tag{5.2a}$$

$$\frac{E''(\omega)}{E_o} = \frac{(\omega\tau_c)^\alpha \sin\left(\frac{\pi\alpha}{2}\right)+(\omega\tau_c)^{2\alpha-\beta}\sin\left(\frac{\pi\beta}{2}\right)}{1+(\omega\tau_c)^{\alpha-\beta}\cos\left(\frac{\pi(\alpha-\beta)}{2}\right)+(\omega\tau_c)^{2\alpha-\beta}} \tag{5.2b}$$

There are two notable special cases in the FMM class. The first case is the Fractional Maxwell Liquid (FML) where the exponent α is set to 1 and is used to describe complex fluid in the pre-gel state. The second case, the Fractional Maxwell Gel (FMG) describes the elastic behavior of viscoelastic materials beyond the gel point; in FMG, $b = 0$. In this work, a polyurea elastomer as a blend ("parallel" mixture rule) of two FMGs, one corresponding to the soft-phase matrix (with some dissolved hard segments and some isolated hard-phase domains) and the second one to the percolated hard phase (see Figure 5-1) is described. Thus, the overall model has six fitting parameters for each of the three polymers – the two plateau moduli, $E_{0,1}$ and $E_{0,2}$; the two relaxation times, $\tau_{c,1}$ and $\tau_{c,2}$; and the two power-law exponents, α_1 and α_2. In this chapter the effect of hard segment and GnP weight fractions on the fitting parameters will be elucidated and will be used to explain any microstructure changes.

To combine the DMA data for multiple temperatures, the time-temperature superposition (TTS) principle is utilized, and it is assumed that the horizontal shift factor, a_T, is the same for the hard and soft phases. The vertical shift factor is taken to be equal to unity. The master curves obtained in this fashion are then described using a two-FMG model,

$$E'(x) = \sum_{k=1}^{2} E_{0,k} \frac{(x\tau_k)^{\alpha} cos(\pi\alpha/2)+(x\tau_k)^{2\alpha}}{1+(x\tau_k)^{\alpha} cos(\pi\alpha/2)+(x\tau_k)^{2\alpha}} \tag{5.3a}$$

$$E''(x) = \sum_{k=1}^{2} E_{0,k} \frac{(x\tau_k)^{\alpha} sin(\pi\alpha/2)}{1+(x\tau_k)^{\alpha} cos(\pi\alpha/2)+(x\tau_k)^{2\alpha}} \tag{5.3b}$$

where $x = a_T\omega$, a_T being the shift factor.

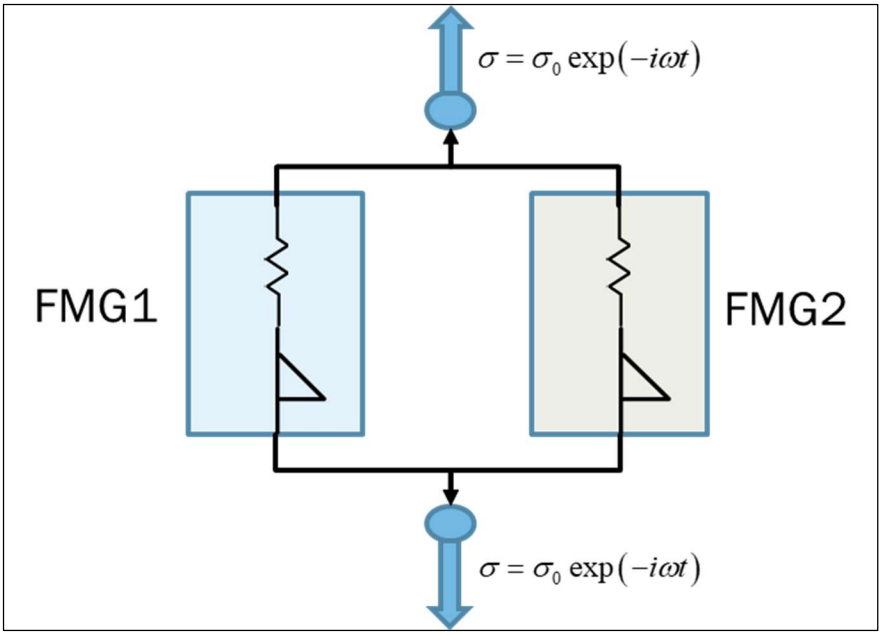

Figure 5-1. Schematic showing the two FMGs used to model the polyurea. FMG1 is taken to be the filled soft phase, while FMG2 is the percolated hard phase. Each FMG is a combination of an elastic spring and a "springpot", connected in series. Reproduced with permission from Ref. [54], copyright The Authors.

Figure 5-1 shows a schematic representation of the model for both the neat and filled systems. For the neat systems, two fractional Maxwell gels are used in parallel to represent the two phases, filled soft phase and percolated hard phase. FMG 1 represents the filled soft phase, while FMG2 represents the percolated hard phase. In the nanocomposites, there is a new phase introduced (GnPs), but the same two-FMG model is utilized, instead of introducing a third element. It is expected that the impact of the nanofillers would be only in modifying the parameters of one or both of the FMGs, at least at sufficiently low loadings (<1.5 wt%). In this case the impact of the nano-fillers on the actual microstructure of the PUa is explored.

5.2 Time-Temperature-Superposition (TTS) of Polyurea Polymers

In order to build the master curves, frequency sweeps from 0.1 to 10 Hz (with 5 points per decade) from a temperature range -80 ºC to 70 ºC every 10 ºC were run on a TA instruments RSA-G2 in tensile mode. See Chapter 3 for details in the DMA testing. In addition, a frequency sweep

was added for 25 ºC was also included since the reference of the master curves would be set at 25 ºC. Master curves were generated for all three polymers. Figure 5-2 show the master curves, while Figure 5-3 compare the various shift functions (WLF, Arrhenius, and TS2). The equations for the various shift functions, WLF is described Equation 5.2, Arrhenius is described by Equation 5.5, and TTS is described by Equation 5.6 were discussed in Chapter 1 and listed here for reference.

$$log(\alpha_T) = \frac{C_1(T-T_r)}{C_2+T-T_r} \tag{5.4}$$

$$\ln a_T = \left(\frac{E_a}{R}\right)\left(\frac{1}{T}-\frac{1}{T_r}\right) \tag{5.5}$$

$$ln(a_T) \equiv ln\left(\frac{\tau[T]}{\tau[T_o]}\right) = \frac{E_1}{RT} + \frac{E_2-E_1}{RT}\left(\frac{1}{1+exp\left\{\frac{\Delta S}{R}\left(1-\frac{T*}{T}\right)\right\}}\right) - \frac{E_1}{RT_o} + \frac{E_2-E_1}{RT_o}\left(\frac{1}{1+exp\left\{\frac{\Delta S}{R}\left(1-\frac{T*}{T_o}\right)\right\}}\right) \tag{5.6}$$

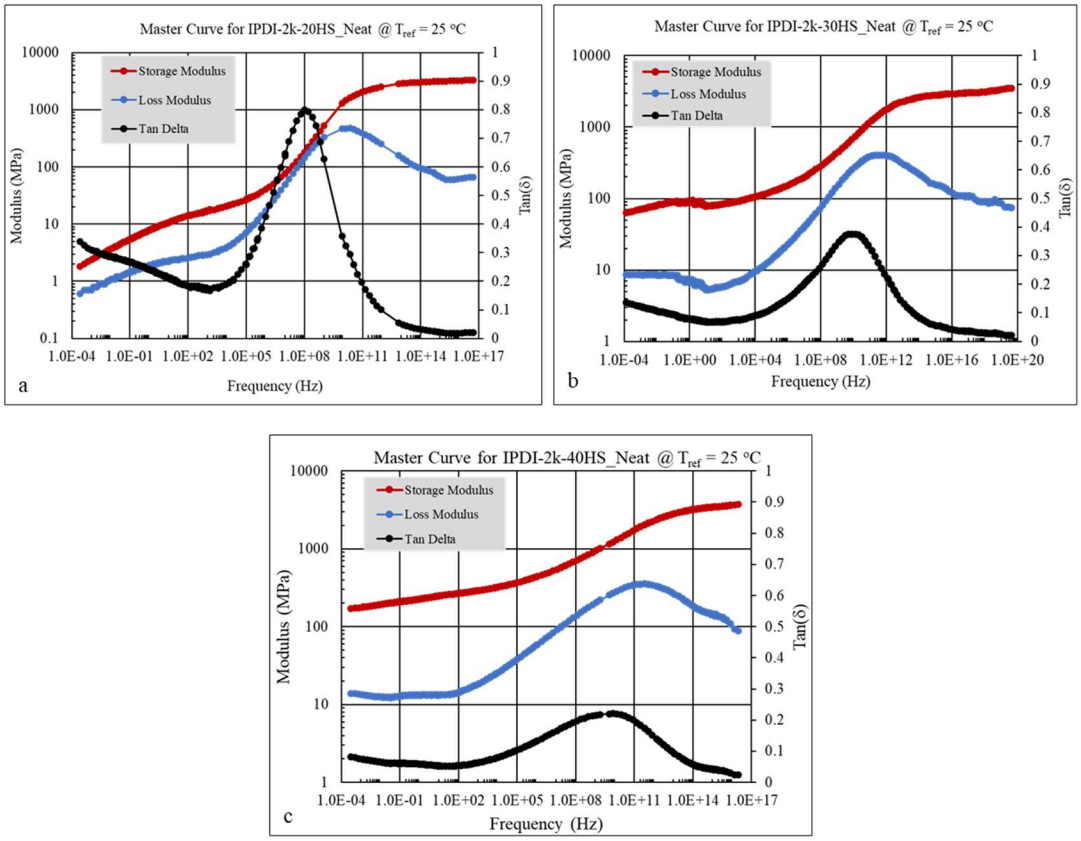

Figure 5-2. Master Curves for all three formulations. Reproduced with permission from Ref.[54], copyright The Authors.

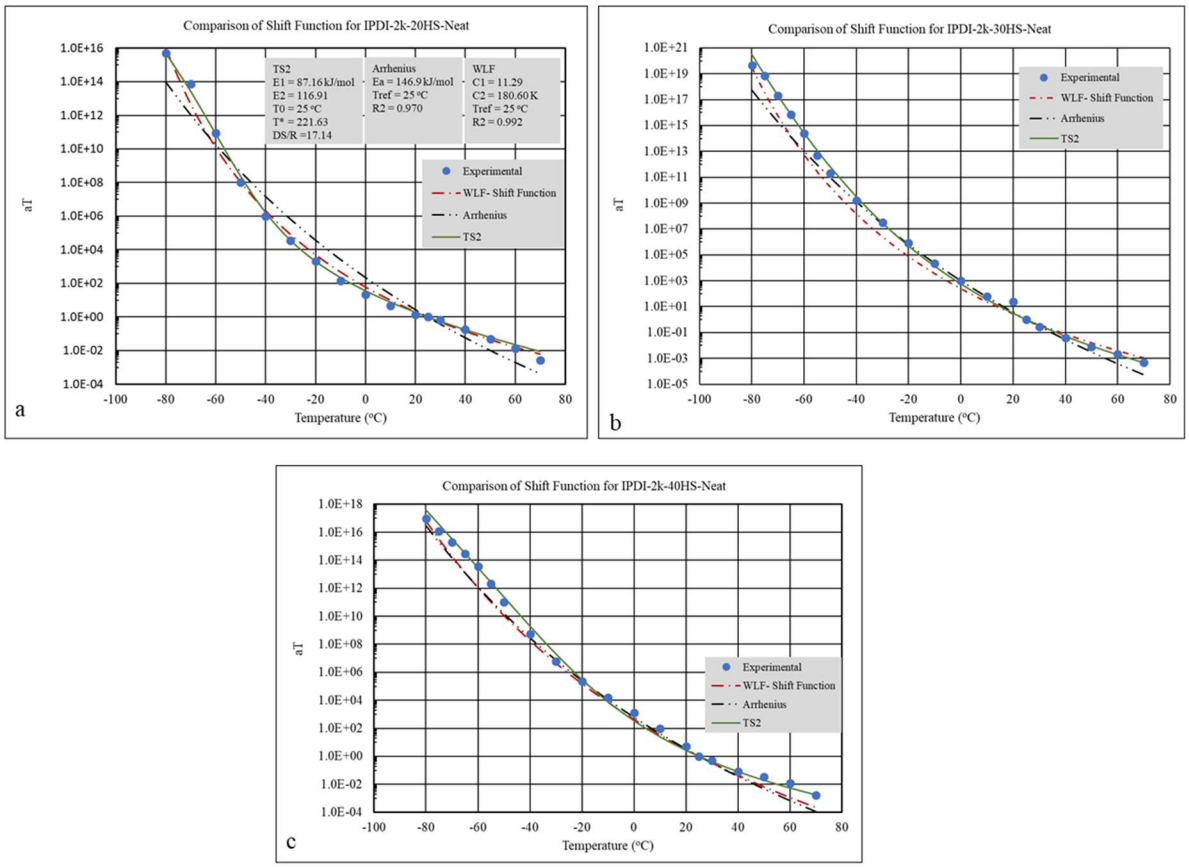

Figure 5-3. Comparison of various shift functions for all three PUa formulations. Reproduced with permission from Ref. [54] , copyright The Authors.

For the IPDI-2k-20HS formulation the WLF model tends to break down at temperatures lower than the T_g. and the Arrhenius model does not fit throughout the entire temperature range. For the IPDI-2k-30HS formulation both the Arrhenius and WLF model tend to break down at temperatures below the T_g. At higher temperatures the Arrhenius model holds well but WLF does not. For the IPDI-2k-40HS both WLF and Arrhenius break down at temperatures lower than the polymer T_g. For all three formulations the TS2 model holds throughout the temperature range. The TS2 calculated shift factors were used to generate the master curves for the storage modulus and tan(δ) across 24 decades of frequency, Figure 5-4.

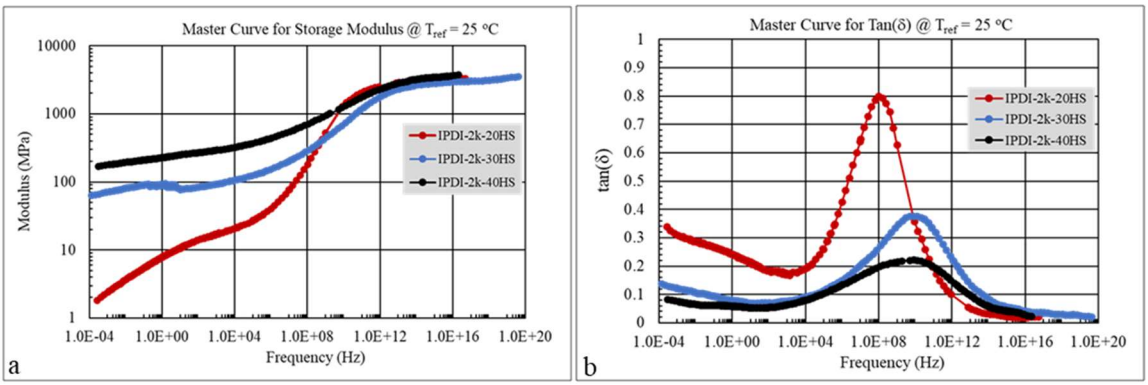

Figure 5-4. Comparison of Master Curves of Storage Modulus (a), and tan(δ) for all three formulations. Reproduced with permission from Ref. [54], copyright The Authors.

In all cases the storage modulus master curves exhibit transitions over several decades of frequency. The high-frequency plateau moduli are very close for all three materials. This was noted in the temperature sweeps of the PUa in Chapter 2 and 3 where it was discussed that at temperatures below temperature Tg the storage modulus is a function of the soft phase. In the lower frequency range, there is a larger effect on the modulus which is related to the role of hard domains, their structure and morphology [70]–[73]. From examining the tan(δ) master curves, a noticeable shift in the peak location (scaled frequency corresponding to the glass transition) between the 20% HSWF and the 30% HSWF is seen (for the latter two, the shape and location of the peak is almost the same). This difference indicates that after 30% HSWF, most of the "new" hard segments are no longer soluble in the soft phase and thus do not influence its glass transition temperature. The magnitude of the tan(δ) peak decreases as the HSWF is increased, indicating that the energy dissipation is stronger in the lower-HS polyureas and weaker in the higher-HS polyureas.

5.3 Mathematical Modeling and Optimization FMG and TS2

Table 5-1 shows the key identified parameters for the TS2 model. The values and standard deviations for the two-branch FMG parameters are shown in Table 5-2. The fractional order values, a_1 and a_2, show a consistent reduction in values as the concentration of the hard segments, HSWF,

is increased. Furthermore, small values for standard deviations across all stochastic optimization runs, indicating good reproducibility of the optimization runs even for the significantly large parameter bounds adopted was observed.

Table 5-1. TS2 model parameterization. Reproduced with permission from Ref. [54], copyright The Authors.

Parameters	IPDI-2k-20HS	IPDI-2k-30HS	IPDI-2k-40HS
E_1 (kJ/mol)	87.2	89.0	90.0
E_2 (kJ/mol)	116.9	162.4	128.5
$\Delta S/R$	17.1	5.6	10.8
T* (K)	221.6	230.4	249.3

Table 5-2. FMG 1 and FMG 2 parameters. Reproduced with permission from Ref. [54], copyright The Authors.

Model Parameters	IPDI-2k-20HS		IPDI-2k-30HS		IPDI-2k-40HS	
	FMG 1	FMG 2	FMG 1	FMG 2	FMG 1	FMG 2
E_o (Pa)	2789 ± 0.73	17 ± 0.02	2624 ± .36	99 ± 0.001	2813 ± .72	277 ± 0.42
τ_c (s)	1.9×10^{-12} ± 1.8×10^{-15}	1.2×10^{-2} ± 1.3×10^{-4}	1.7×10^{-23} ± 1.3×10^{-4}	7.5×10^{1} ± 1.1×10^{-1}	2.3×10^{-13} ± 1.3×10^{-15}	8.8×10^{1} ± 3.4
α	0.39 ± 1.1×10^{-4}	0.21 ± 1.7×10^{-4}	0.28 ± 3.3×10^{-5}	0.16 ± 3.8×10^{-5}	0.23 ± 2.2×10^{-4}	0.08 ± 1.7×10^{-4}

Figure 5-5 illustrates the two-branch FMG model fits to the experimental shifted data for all three formulations. For all formulations the FMG model fits the shifted experimental data well across all frequency scales, being able to capture the multiple power-law behaviors of both storage and loss moduli. Particularly for the 20 wt% hard segment sample, a slight deviation between the model and experimental data above the glass transition point in the loss modulus was observed.

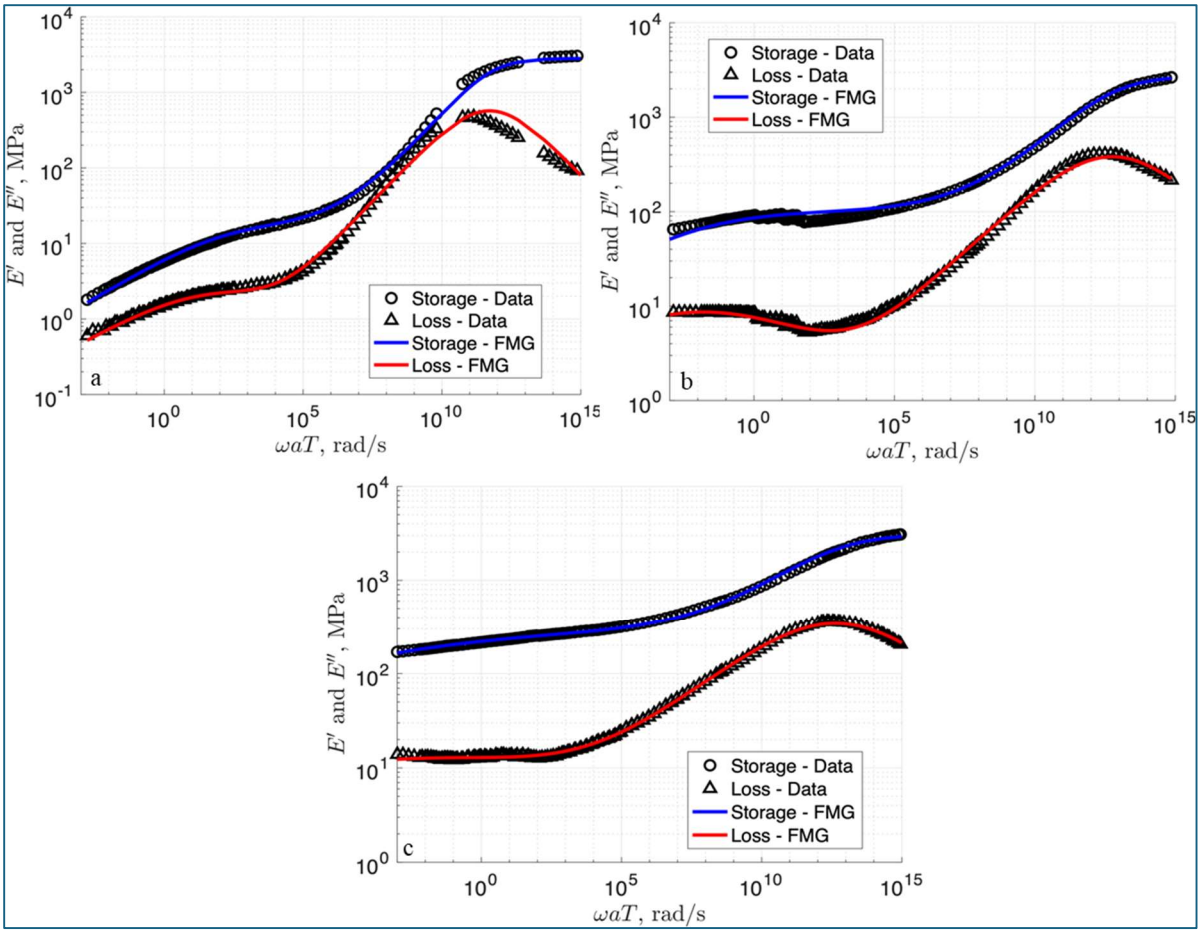

Figure 5-5. Comparison of the experimental shift data vs. the FMG model for both loss and storage module. a, b, c for hard segment weight 20, 30 and 40%, respectively. Reproduced with permission from Ref. [54], copyright The Authors.

In Figure 5.6, the FMG model fits for the DMA temperature sweep at the frequency of 1 Hz are compared with experimental data for the three polyureas with 20, 30, and 40% hard segments. The model agrees well with experimental in the temperature range between -70 °C and +70 °C (although there is more variability for the 30% system). At higher temperatures, the model fails to capture the dramatic softening of the material as the hard-phase domains melt and break up.

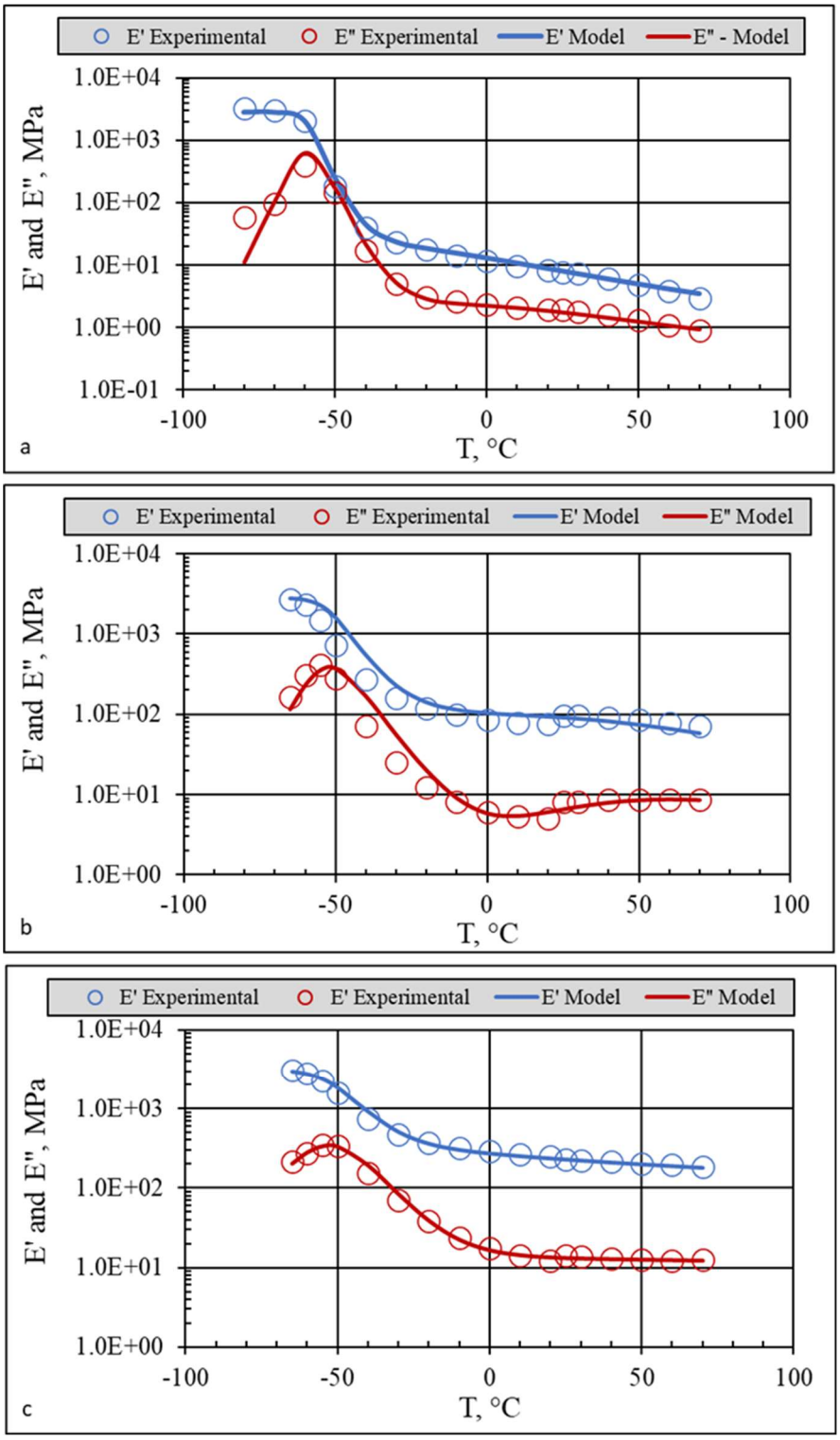

Figure 5-6. Comparison of the experimental temperature sweep, for all 3 PUa formulations, (See Chapter 2) to the FMG model temperature sweep. Note the frequency is at 1Hz for both model and experimental. Reproduced with permission from Ref. [54], copyright The Authors.

Figure 5-7a shows the effect of hard segment contents on the mean value of the characteristic modulus of the percolated hard phase, $E_{0,2}$. The characteristic modulus increases as the weight fraction of hard segments increases. This is consistent with both literature and the experimental data and can be attributed to the increase in the volume fraction of the percolated hard phases as well as in the improved "strength" of the hard domains (higher density of hydrogen bonds per domain) [70]. Consistent with these arguments the characteristic relaxation time for the percolated hard phase, $\tau_{c,2}$, also significantly increases with increase in HSWF, see Figure 5-7b. The power-law exponent α_2 decreases monotonically as HSWF is increased from 0.21 for the 20% system to 0.16 for the 30% and 0.08 for the 40% HSWF materials (see Table 5-4) recall that the provided mean values are obtained from the 10 different realizations of parameters obtained from the PSO algorithm.

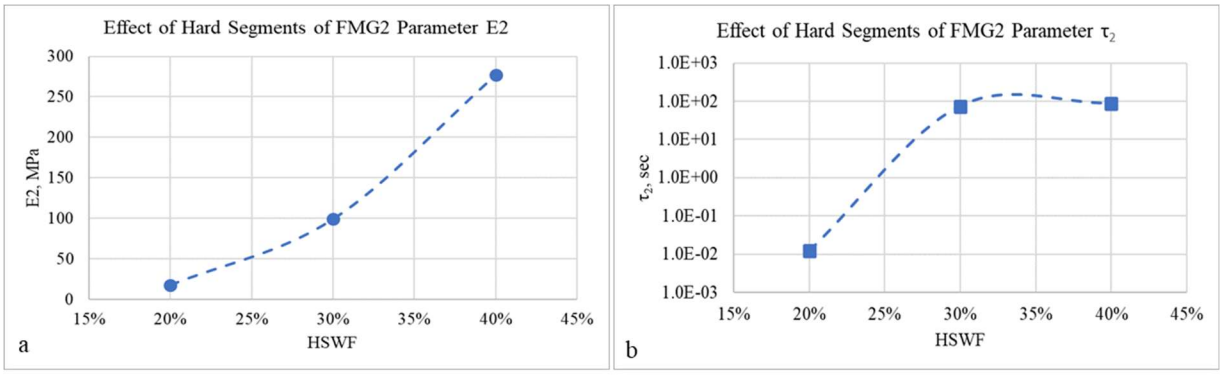

Figure 5-7. Effect of hard segments a) on the FMG parameter E0(2), b) on the characteristic relaxation time $\tau_c(2)$. Reproduced with permission from Ref. [54], copyright The Authors.

5.4 Mathematical Modeling and Optimization FMG and TS2 for filled systems

Figure 5-8 is a plot of the shift factor as a function of temperature for the IPDI-2k-20HS nanocomposites with (a) 0%, (b) 0.5%, (c) 1%, and (d) 1.5% GnP. The symbols are the results of the TTS shift of the data (as outlined above), and the lines are the TS2 equation fits. The addition of GnPs did not have a qualitative impact on the TTS or the temperature dependence of the shift

factor, although the model parameters (such as activation energies) changed slightly. Similar data and model fits for the IPDI-2k-30HS and IPDI-2k-40HS nanocomposites are presented in Figure 5-9, and Figure 5-10 and the TS2 model parameters are summarized in Table 5-3.

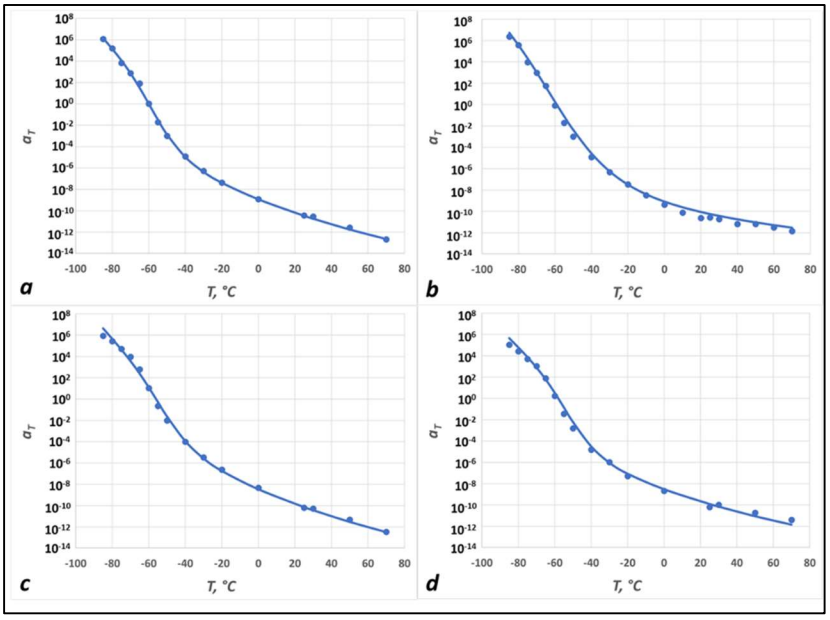

Figure 5-8. Experimental (symbols) and TS2 fit (lines) shift factors for 20HS polyureas with: (a) No added nanofillers; (b) 0.5 wt% GnP; (c) 1.0 wt% GnP; (d) 1.5 wt% GnP. Reproduced with permission from Ref. [54], copyright The Authors.

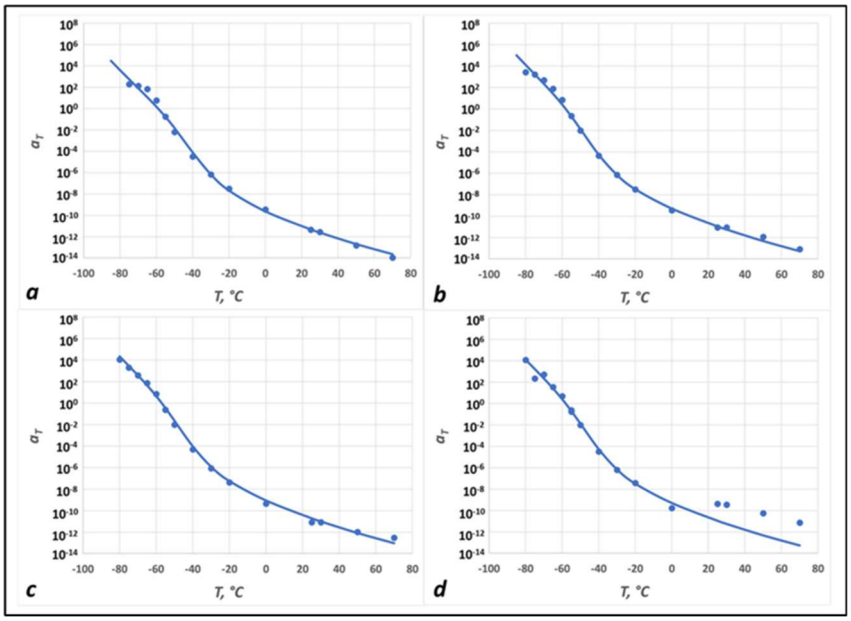

Figure 5-9. Experimental (symbols) and TS2 fit (lines) shift factors for 30HS polyureas with: (a) No added nanofillers; (b) 0.5 wt% GnP; (c) 1.0 wt% GnP; (d) 1.5 wt% GnP. Reproduced with permission from Ref.[69], copyright The Authors.

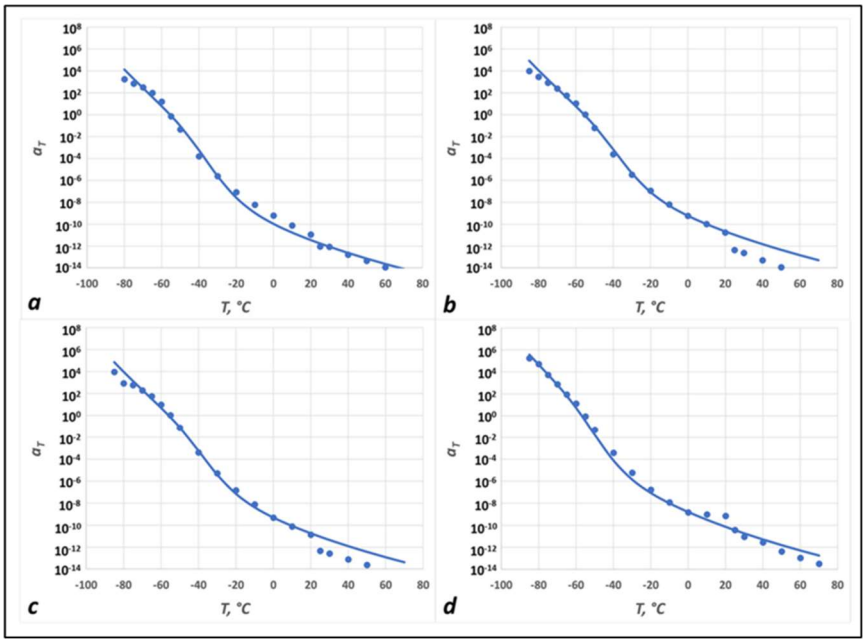

Figure 5-10. Experimental (symbols) and TS2 fit (lines) shift factors for 40HS polyureas with: (a) No added nanofillers; (b) 0.5 wt% GnP; (c) 1.0 wt% GnP; (d) 1.5 wt% GnP. Reproduced with permission from Ref. [69], copyright The Authors.

Table 5-3. TTS reference temperatures and TS2 fit parameters for all systems. Reproduced with permission from Ref. [69], copyright The Authors.

Polymer	% GnP	T_o (K)	E_1 (kJ/mol)	E_2, (kJ/mol)	ΔS/R	T* (K)
IPDI-2k-20HS	**Neat**	213	94.5	120.0	25.0	217.1
	0.5	214	94.5	121.1	25.0	218.5
	1.0	217	94.5	118.8	25.0	222.5
	1.5	215	94.5	116.5	25.0	222.8
IPDI-2k-30HS	**Neat**	214	99.9	120.0	25.0	233.8
	0.5	215	99.9	120.6	25.0	228.9
	1.0	216	99.9	120.6	25.0	228.9
	1.5	215	99.9	120.6	25.0	228.9
IPDI-2k-40HS	**Neat**	217	100.0	123.6	25.0	240.5
	0.5	218	100.0	120.4	25.0	238.5
	1.0	217	100.0	120.4	25.0	238.5
	1.5	216	100.0	120.8	25.0	225.6

In Figure 5-11, the storage and loss master curves are plotted for all nanocomposite systems: (a) IPDI-2k-20HS matrix, (b) IPDI-2k-30HS matrix; and (c) IPDI-2k-40HS matrix. Within each "family", all curves were very close to each other, with a possible exception of the IPDI-2k-20HS, 1% GnP (blue symbols in Figure 5-11a).

Table 5-4 provides the mean values and corresponding standard deviations for all six parameters in the two-FMG model. The optimization runs showed excellent convergence and reproducibility, as manifested in the low standard deviation values for all the systems considered.

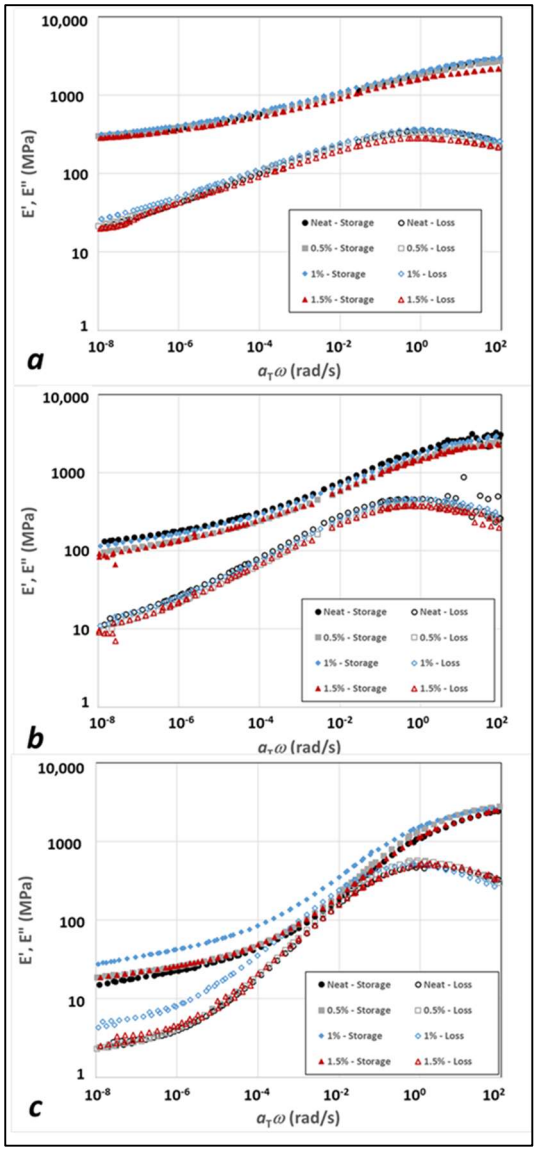

Figure 5-11. Master curves for the tensile storage (filled symbols) and loss (open symbols) moduli. (**a**) 40HS matrix with 0, 0.5, 1.0, and 1.5 wt % GnP. (**b**) Same as (**a**) for the 30HS matrix. (**c**) Same as (**a**) for the 20HS matrix. Reproduced with permission from Ref. [69] copyright The Authors.

Table 5-4. FMG 1 and FMG 2 parameters. Rows represent hard segment weight fractions of 20%, 30%, and 40%, while columns correspond to GnP weight fractions of 0.0%, 0.5%, 1%, and 1.5%. Reproduced with permission from Ref. [69], copyright The Authors.

Model Parameters		0.0% GnP		0.5% GnP		1% GnP		1.5% GnP	
		FMG 1	FMG 2	FMG 1	FMG 2	FMG 1	FMG 2	FMG 1	FMG 2
IPDI-2k 20HS	$E_{0,i}$ (MPa)	2815	64	3097	51	2871	118	2837	71
		$\pm 3.3 \times 10^{-6}$	$\pm 3.8 \times 10^{-7}$	$\pm 3.4 \times 10^{-6}$	$\pm 3.9 \times 10^{-7}$	$\pm 2.6 \times 10^{-6}$	$\pm 6.2 \times 10^{-7}$	$\pm 2.6 \times 10^{-6}$	$\pm 4.1 \times 10^{-7}$
	$\tau_{c,i}$ (s)	0.18	1.19	0.22	1.69	0.40	1.96	0.18	1.16
		$\pm 8.2 \times 10^{-10}$	$\pm 5.9 \times 10^{-10}$	$\pm 6.8 \times 10^{-10}$	$\pm 7.1 \times 10^{-9}$	$\pm 1.4 \times 10^{-9}$	$\pm 8.1 \times 10^{-9}$	$\pm 6.7 \times 10^{-10}$	$\pm 4.5 \times 10^{-9}$
	α_i	0.42	0.080	0.413	0.056	0.382	0.085	0.412	0.077
		$\pm 4.3 \times 10^{-10}$	$\pm 3.8 \times 10^{-10}$	$\pm 4.4 \times 10^{-10}$	$\pm 5.8 \times 10^{-10}$	$\pm 3.5 \times 10^{-10}$	$\pm 3.4 \times 10^{-10}$	$\pm 4.0 \times 10^{-10}$	$\pm 3.9 \times 10^{-10}$
IPDI-2k 30HS	$E_{0,i}$ (MPa)	2757	342	2405	278	2793	341	2203	301
		$\pm 1.8 \times 10^{-5}$	$\pm 1.7 \times 10^{-6}$	$\pm 3.4 \times 10^{-6}$	$\pm 1.5 \times 10^{-6}$	$\pm 2.5 \times 10^{-6}$	$\pm 1.2 \times 10^{-6}$	$\pm 1.9 \times 10^{-5}$	$\pm 8.9 \times 10^{-6}$
	$\tau_{c,i}$ (s)	1.14	3.23	0.68	2.00	0.66	1.90	0.89	2.41
		$\pm 4.1 \times 10^{-8}$	$\pm 1.0 \times 10^{-7}$	$\pm 5.8 \times 10^{-9}$	$\pm 1.2 \times 10^{-8}$	$\pm 2.7 \times 10^{-9}$	$\pm 6.3 \times 10^{-9}$	$\pm 2.7 \times 10^{-8}$	$\pm 3.0 \times 10^{-8}$
	α_i	0.314	0.054	0.307	0.061	0.307	0.061	0.312	0.071
		$\pm 1.1 \times 10^{-9}$	$\pm 3.6 \times 10^{-10}$	$\pm 5.7 \times 10^{-10}$	$\pm 3.4 \times 10^{-10}$	$\pm 3.4 \times 10^{-10}$	$\pm 2.2 \times 10^{-10}$	$\pm 2.5 \times 10^{-9}$	$\pm 2.0 \times 10^{-9}$
IPDI-2k 40HS	$E_{0,i}$ (MPa)	2635	604	2476	622	2843	687	2567	378
		$\pm 2.6 \times 10^{-6}$	$\pm 2.0 \times 10^{-6}$	$\pm 2.0 \times 10^{-6}$	$\pm 1.7 \times 10^{-6}$	$\pm 2.8 \times 10^{-6}$	$\pm 2.8 \times 10^{-6}$	$\pm 1.3 \times 10^{-5}$	$\pm 1.1 \times 10^{-5}$
	$\tau_{c,i}$ (s)	0.69	1.44	1.03	2.06	0.46	0.93	0.17	0.45
		$\pm 2.8 \times 10^{-9}$	$\pm 5.2 \times 10^{-9}$	$\pm 3.4 \times 10^{-9}$	$\pm 8.8 \times 10^{-9}$	$\pm 2.1 \times 10^{-9}$	$\pm 4.9 \times 10^{-9}$	$\pm 2.7 \times 10^{-9}$	$\pm 3.7 \times 10^{-9}$
	α_i	0.242	0.035	0.239	0.038	0.222	0.043	0.187	0.015
		$\pm 4.1 \times 10^{-10}$	$\pm 1.8 \times 10^{-10}$	$\pm 2.8 \times 10^{-10}$	$\pm 1.6 \times 10^{-10}$	$\pm 3.4 \times 10^{-10}$	$\pm 1.8 \times 10^{-10}$	$\pm 1.2 \times 10^{-9}$	$\pm 1.7 \times 10^{-9}$

Figure 5-12 through Figure 5-14 presents the two-FMG model fits to the experimental shifted data for IPDI-2k-20HS, IPDI-2k-30HS and IPDI-2k-40HS nanocomposites respectively. All fitted curves were generated using the model parameters values, since the standard deviation of each model parameter was negligible. For all the formulations, the relative error between the model and data was less than 3.1%, with data spanning a broad range of frequencies (between 10^{-4} and 10^{2} rad/s). However, for the 20 wt% hard segment sample at all nano-particle percentages, a minor deviation between the model and experimental data was observed above the glass transition point in the loss modulus, a phenomenon which was also noted for the neat 20% HWSF case.

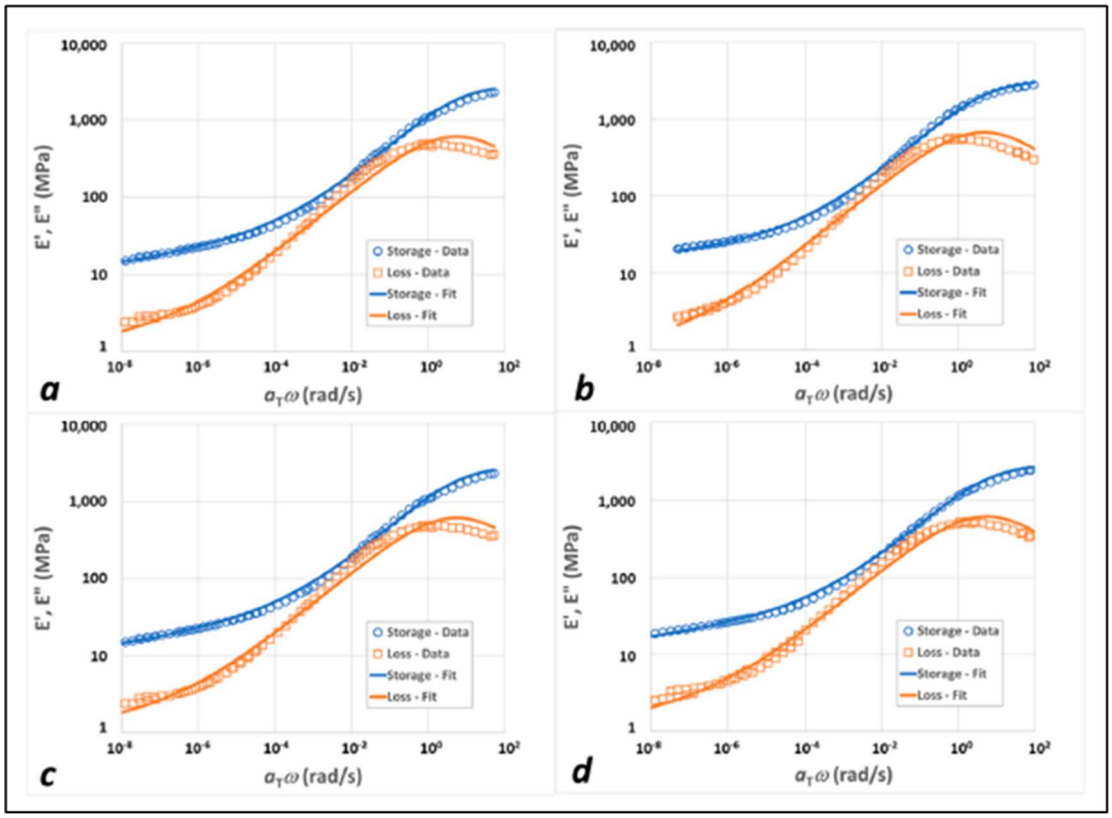

Figure 5-12. Experimental (symbols) and FMG-FMG fit (lines) master curves for 20HS polyureas with: (**a**) no added nanofillers; (**b**) 0.5 wt% GnP; (**c**) 1.0 wt% GnP; (**d**) 1.5 wt% GnP. Blue open circles represent storage modulus data NS blue lines are the storage modulus model fits; orange open squares correspond to the loss modulus data and orange lines are the loss modulus model fits. Reproduced with permission from Ref.[69], copyright The Authors.

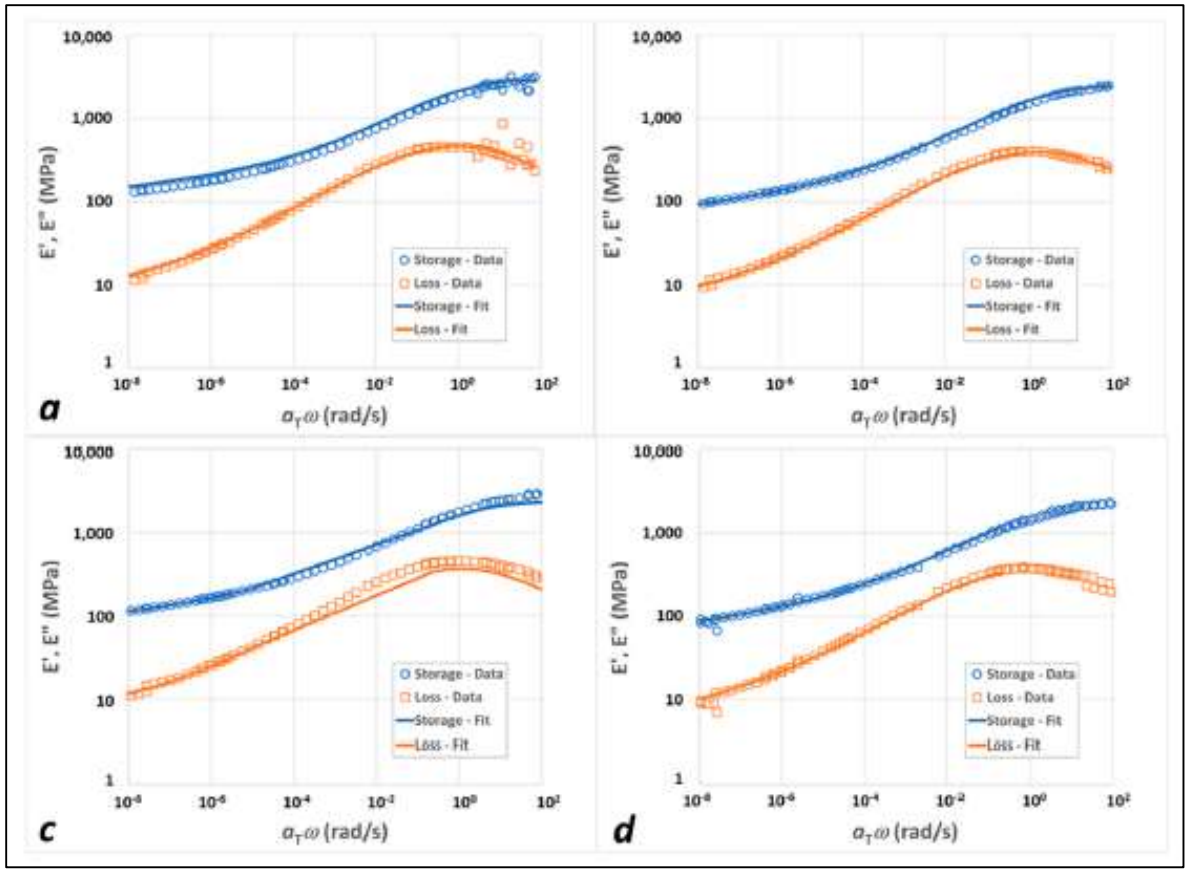

Figure 5-13. Experimental (symbols) and FMG-FMG fit (lines) master curves for 30HS polyureas with: (a) no added nanofillers; (b) 0.5 wt% GnP; (c) 1.0 wt% GnP; (d) 1.5 wt% GnP. Blue open circles represent storage modulus data NS blue lines are the storage modulus model fits; orange open squares correspond to the loss modulus data and orange lines are the loss modulus model fits. Reproduced with permission from Ref. [69], copyright The Authors.

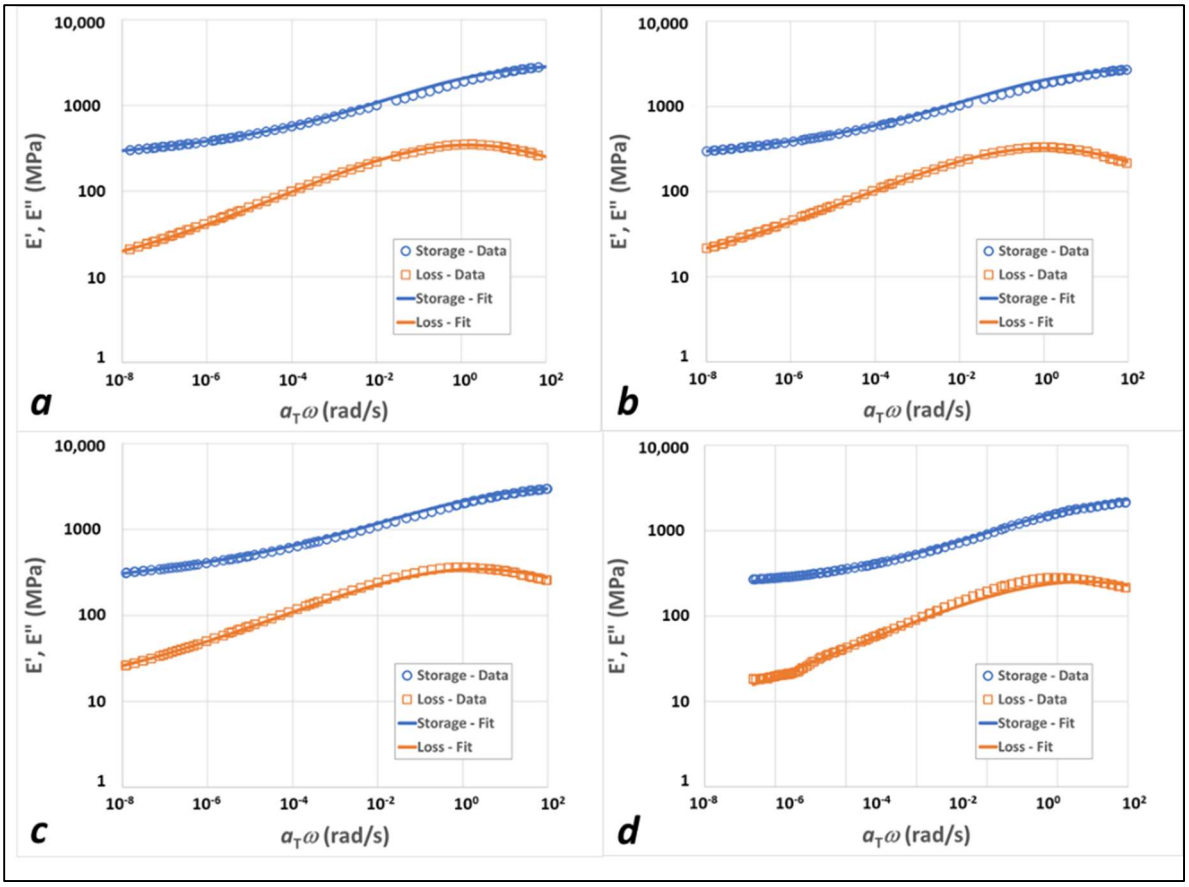

Figure 5-14. Experimental (symbols) and FMG-FMG fit (lines) master curves for 40HS polyureas with: (**a**) no added nanofillers; (**b**) 0.5 wt% GnP; (**c**) 1.0 wt% GnP; (**d**) 1.5 wt% GnP. Blue open circles represent storage modulus data NS blue lines are the storage modulus model fits; orange open squares correspond to the loss modulus data and orange lines are the loss modulus model fits. Reproduced with permission from Ref. [69], copyright The Authors.

Figure 5-15 a,b depict the influence of the nanofiller content on the mean characteristic modulus of both branches. In general, the effect was very small, except for the significant increase in $E_{0,2}$ for the 1% GnP in the IPDI-2k-20HS nanocomposite relative to the neat polymer. In that system, two factors contributed to the effect. First, the stiffness ratio between the filler and the matrix was the largest for the lower-HS polymers and became smaller as HSWF increased. Second, the impact of the fillers usually had a maximum as a function of filler loading. At low loadings, the effect was, obviously, very weak; at high loadings, on the other hand, the platelets aggregated, the aspect ratio decreased, and the overall effect decreased as well. Thus, 1% GnP in the IPDI-2k-

20HS represented the system corresponding to the maximum reinforcement in terms of both HSWF and %GnP.

In Figure 5-15 c,d, the variations in the relaxation times for both branches with respect to the filler weight fraction are shown. These variations are also fairly small and do not show a clear dependence on the nanoparticle loading. Finally, Figure 5-15 e,f show the power law exponents, α, for both branches. Again, the dependence of α_i on the GnP loading was fairly weak. The soft-phase exponent, α_1, showed a strong dependence on HSWF, decreasing as HSWF increased. This is consistent with the material becoming "more elastic" and the average loss tangent decreasing. The hard-phase exponent, α_2, was quite small for all twelve neat and nanocomposite systems, indicating that they were almost always nearly perfectly elastic.

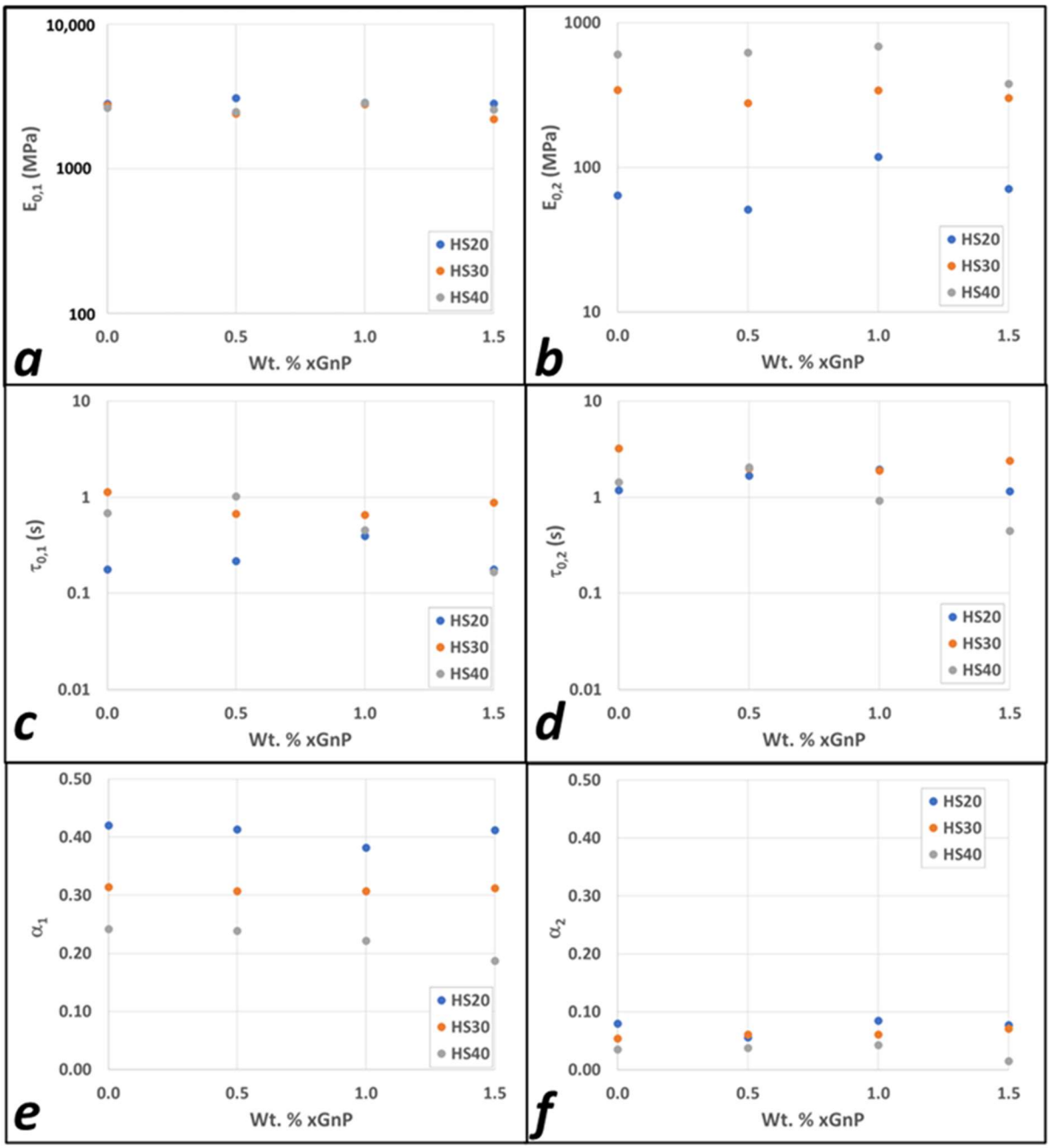

Figure 5-15. Effect of the nanofiller loading on the (**a**) characteristic modulus of the first branch ($E_{0,1}$) (**b**) characteristic modulus of the second branch ($E_{0,2}$), (**c**) characteristic time of the first branch ($\tau_{c,1}$), (**d**) characteristic time of the second branch ($\tau_{c,2}$), (**e**) power law exponent of the first branch (α_1), and (**f**) power law exponent of the first branch (α_2). Reproduced with permission from Ref. [69], copyright The Authors.

5.5 Discussion

In this chapter, a novel modeling approach to describe the linear viscoelasticity of polyurea polymers and their nanocomposites is outlined. Within this approach, a polyurea polymer is represented as a mixture in parallel of the two fractional Maxwell gels (FMG) to gain additional insight on the microstructure and the viscoelastic properties of PUa and its nanocomposite. Examining the FMG parameters provided a qualitative insight on the structure of both the filled soft phase and the percolated hard phase. In the three neat polymers, the chemistry is essentially the same across all the formulations. The same chemical constituents were used to make the PUa's, the difference being the ratios needed to obtain the desired number of hard segments. Thus, the filled soft phase (FMG 1) should be very similar across all three formulations. This is illustrated by fact that the thermophysical (DSC) T_g does not shift very much from formulation to formulation (See Chapter 2 and Chapter 3), and there is relatively little difference in the storage or loss modulus below $T_{g,}$ and indeed, the plateau modulus of the FMG 1, $E_{0,1}$, is fairly independent of HSWF and primarily corresponds to the glassy modulus of poly(propylene oxide). However, the other two FMG 1 parameters, $\tau_{c,1}$ and a_1, are more HSWF-sensitive. In the filled soft phase, there are multiple hard-phase "islands", with soft segments acting as bridges or loops [74]–[76]. The distribution of relaxation times depends on the average length of the hard segment, the balance between the "bridges" and "loops" (similar to the case of associative thickeners on nanoparticles [77], and the quality of the hydrogen bonds holding the hard-phase islands together. Developing a model to capture all these details remains a major challenge. Fortunately, for many practical applications, it remains a second-order effect, and the most significant impact comes from the percolated hard phase (FMG 2). As was discussed above, the FMG 2 modulus contribution, $E_{0,2}$, is determined by the volume fraction of the percolated hard phase multiplied by the modulus of the "ideal hard

phase" [39]. The dependence of $E_{0,2}$ on HSWF is thus consistent with earlier results. The dependence of $\tau_{c,2}$ on HSWF is likely the result of the "strengthening" of the hard phase as the average hard segment length is increased. Let us assume, in a somewhat simplistic fashion, that $\tau_{c,2}$ is related to the time corresponding to a pullout of a single chain out of the hard phase domain (again compare with the example of associating polymers in micelles or on nanoparticles [40], [42], [44], [77]–[80]), i.e., $ln(\tau_{c,2}) = A + \frac{H}{RT}$, where A is a constant, H is the hydrogen bonding energy, R is the gas constant, and T is temperature (in K). If $\tau_{c,2}$ increases by about five orders of magnitude between HSWF 20% and HSWF 40%, this implies that the hydrogen bonding strength increases by about $RTln(5)$, or approximately 29 kJ/mol or 6.8 kcal/mol (assuming T = 300 K). This is roughly consistent with molecular simulations performed for other hard segments like MDI-BDO or MDI-EG, [76], [81], [82] although more detailed analysis is needed.

The α parameter in both FMG 1 and 2 is related to the breadth of the relaxation spectrum and thus the distribution of the hard segments, both in the filled soft phase and the percolated hard phase. Fractional calculus has not been previously applied to describe segmented polyurethanes and polyureas; the approach is simply taking a previous micromechanical model [39], [70] and changing the elements from Hookean to fractional Maxwell gels (FMG). A perfect Maxwell element ($\alpha = 1$) implies a single relaxation time within the FMG, while $0<\alpha<1$ corresponds to a broad relaxation time spectrum, and $\alpha = 0$ depicts a purely elastic behavior. As discussed above, for the filled soft phase (FMG 1), as the HSWF is increased the α decreases. This is consistent with material behaving "more elastically", and reduced energy dissipation. For FMG 2, a similar trend is seen, but it is relatively minor, and the percolated hard phase behavior is primarily elastic for all three systems.

For the filled systems, the two variables of interest are the polyurea hard segment (HS) weight fraction and the exfoliated graphene nanoplatelet (GnP) loading. The hypothesis tested was that the polyurea hard segment and the nanofillers would interact strongly with each other and provide additional reinforcement by forming a "combined hard phase". Given the complex structure of any polyurea nanocomposite (soft-phase matrix, hard-phase islands, percolated hard-phase domains, exfoliated nanofillers, aggregated nanofillers, etc.), direct characterization, such as electron microscopy, is often inconclusive. Therefore, in utilizing the FMM and modeling the materials viscoelastic properties, information about the matrix-filler interaction can be inferred from the DMA results.

Similar to the previous study the neat system (discussed above) the DMA frequency sweeps in these systems are amenable to time–temperature superposition (TTS), with the TTS shift factors well-described by the TS2 [39] function. This was, in itself, a non-trivial result, since polyurea materials are multi-phase. The storage and loss master curves exhibited broad transition regions and thus could not be described with a single Maxwell model. Therefore, just as before the fractional Maxwell model (FMM) approach [40], [44], [80], [81], [83] to quantify the viscoelastic response and fit the master curve. In particular, the material was well-described using two fractional Maxwell gel (FMG) elements, one representing the soft phase (FMG1) and another one representing the percolated hard phase (FMG2). It was demonstrated that the plateau modulus of the percolated hard phase increased strongly with the hard segment weight fraction (HSWF), consistent with earlier studies [27]. For the filled systems the same approach is utilized to determine the combined impact of HSWF and GnP loading.

Based on the FMM analysis, the effect of the GnP was significantly less pronounced than the effect of the HSWF change. This result is consistent with expectations, as discussed above.

Further increases in the GnP loading likely resulted in at least some aggregation, thus blunting the effectiveness of the new fillers [50]. For polyureas with higher HSWF, the percolated hard-phase modulus is already quite high, and the contribution of the nanofillers becomes even less significant, regardless of their concentration. Thus, the addition of the nanofillers did not seem to offer a significant increase in the linear elastic properties of the polyureas studied here.

5.6 Conclusion

The focus of this chapter was to utilize DMA frequency sweeps and TTS to probe the microstructure of the neat and filled PUa. Master curves for the storage and loss modulus were obtained for both the neat and filled systems. A fractional Maxwell model was utilized to describe the linear viscoelasticity of the neat polyureas, at varying HSWF (20, 30 and 30%), and for the filled GnP PUa at three nano-loading (0.5, 1.0, 1.5 GnP). Within this framework, the TTS shift factor is modeled using the TS2 equation, and the master curves are described using the FMG micromechanical model. The framework resulted in a good agreement between theory and experiment. The physical meaning of the model parameter in the context of the standard hard-soft phase separation. For the neat systems the HSWF as represented by FMG2 has a significant effect on the overall viscoelastic performance. Increasing the HSWF, increased the characteristic modulus E_o, and the characteristic relaxation time, (τ_c), but decreased the power law exponent, α. This indicates that the as HSWF behave more elastically as the HSWF is increased.

The FMM model was then broadened to include the filled systems. Despite their structural complexity, PUa-GnP nanocomposites exhibit time–temperature superposition (TTS). For the first time, the TTS master curves were described by fractional calculus (FC)-based models with a small number of physically meaningful parameters (as opposed to the standard Prony-series modeling usually requiring twenty or more non-meaningful parameters). The modeling results confirmed

that the HSWF has a significantly more effect on the viscoelastic properties than the addition of GnP.

Chapter 6 - Conclusion & Future Research Needs and Recommendations.

6.1 Conclusion

The overall objective of this work was to enhance the understanding of the effects of GnP reinforcements on the structure-property relationship of polyurea. In the introduction, the three objectives were defined:

Do additions of GnP to polyurea impact its overall mechanical performance?

Does the addition of GnP in Polyurea affect its mechanical properties? If so, can we quantify it?

Despite the microstructural complexity of polyurea, which is further exacerbated by the addition of GnP, can the time-temperature-superposition (TTS) principle be applied, and can a mathematical model be developed to help elucidate the combined effect of HSWF and GnP additions?

If PUa is considered as a composite material consisting of hard and soft domains, which parameter has a more significant effect on the mechanical property: a) variation in HSWF or b) additions of GnP, or c) can they work synergistically?

If PUa is used as an adhesive, can Group I adhesive requirements (σ_{ult}>10 MPa & δ_{ult}>4mm) be achieved?

First, this work has successfully demonstrated that Group I adhesive requirements could be achieved by using PUa as an adhesive, as shown in Chapter 2. The PUa used were based on MDI and PTMO formulations. To the best of our knowledge, at the time of this dissertation, work on PUa as an adhesive was limited, and this is one of the unique and critical outcomes of this work. Further, HSWF had minimal effect on the max shear strength of the SLJ but did have an impact on the displacement at max load. For IPDI and MDI neat-based adhesives, the displacement at

max load decreased with increasing HSWF. Adding GnP in PUa adhesives did not result in any significant enhancement or detrimental effect on the resulting mechanical properties of the adhesive joints. This opens opportunities to introduce multifunctionality (thermally/electrically conductive adhesives) to the adhesive without detriment to the overall mechanical performance. Both tensile and DMA testing showed results similar to those of the SLJ. HSWF had a more substantial effect on the PUa than the GnP additions; this was seen in both the secant modulus (tensile testing) and room temperature storage modulus, and both dramatically increased with each 10% HSWF. One particular point of interest was the toughness of the material as a function of HSWF. The toughness increased with increasing HSWF up to 30% and then dropped with further increases in HSWF. Adding 0.5 wt% GnP to 20%, HSWF increased strength and ductility simultaneously, thereby increasing the overall toughness of the composite PUa. At higher HSWF the improvements in toughness were not as significant as observed in the 20% HSWF PUa formulations. Scanning Electron Microscopy provided insight into the crack propagation. At low HSWF, the inherently stiff GnP creates a crack-arresting mechanism, forcing the crack to go around the GnP or, in some cases, stop or pin the crack. When subjected to mechanical stresses, the effect of a stiff GnP particle in a relatively softer matrix leads to stress concentrations at the edges of the particles [66]. Hence, as the GnP loading in PUa increases, the stress concentrations in GnPs close to each other will merge to create microcracks. This can be further exacerbated when GnPs at higher elongations when sample deformation leads to GnP alignment along the loading direction. Eventually, microcracks bridge, causing a final fracture. This was evident in the highly faceted fracture surface of the higher GnP loadings at all levels of HSWF.

Overall, the influence of HSWF on the mechanical properties was more significant than the influence of GnP additions. As previously mentioned, while GnP addition did not significantly

enhance mechanical properties, it also did not have a negative effect, thereby providing the potential for adding multifunctionality (electrical conductivity, thermal conductivity, etc.) to polyurea.

Next, the focus was on dynamic mechanical analysis (DMA) and using time-temperature-superposition (TTS) to develop a mathematical/analytical relationship predicting the visco-elastic properties of neat and GnP-reinforced PUa. In general, DMA can be used to track changes in the glass transition and the moduli due to polymer compositional changes, cross-linking, phase changes, and or the introduction of fillers. TTS is used in conjunction with DMA to describe the viscoelastic properties over multiple decades of frequencies, which are not obtainable by a testing instrument. In this work, TTS was applied to both neat and filled systems. Various shift functions were used with a newer two-state, two-time scale shift function that provided the best correlation throughout the temperature range. Master curves for storage and tan(δ) were generated using the TS2 shift factors across 24 decades of frequency. Historically, a Prony series has been used to describe the master curves mathematically. The use of the Prony series can be cumbersome with upward of 20 constants, and these constants have no physical meaning. In this work, and for the first time, a fractional Maxwell model (FMM) with a small meaningful parameter was used to describe both storage and loss modulus master curves.

Starting with the neat polyurea systems, a two-branch FMG was used to describe the soft phase (FMG1) and percolated hard phase (FMG2). For the neat systems, the HSWF, as represented by FMG2, had a significant effect on the overall viscoelastic performance. Increasing the HSWF increased the characteristic modulus Eo and the characteristic relaxation time (τc) but decreased the power law exponent, α, for FMG2. This indicates that the hard phase behaves more elastically as the HSWF increases. Also, note that the FMG1 parameters were consistent throughout all three

formulations. This is due to the fact that the chemical constituents used for all three formulations were the same. The only difference was the compositions, wherein the side A: side B ratios were selected to obtain the desired number of hard segments. Thus, the FMG1 parameters for the filled soft phase (FMG 1) should be similar across all three formulations.

The FMM model was then broadened to include the filled systems. Despite their structural complexity, PUa-GnP nanocomposites exhibit time-temperature superposition (TTS). The modeling results confirmed that the HSWF has a more significant effect on the viscoelastic properties than the addition of GnP.

6.2 Future Work

Future work is divided into two parts, with short-term and long-term goals. 1) PUa-GnP nanocomposites, and 2) micro-mechanical modeling utilizing the FMM.

6.2.1 PUa-nanocomposites

In this work, a Group I adhesive was obtained using a neat polyurea as an adhesive and Aluminum 6061 substrates with an e-coat surface treatment. Only a cursory investigation into surface treatments was conducted as it was beyond the scope of this work. To further optimize the adhesive properties, a surface treatment based on substrates needs to be performed, and the adhesive thickness needs to be optimized. Therefore, in the short term, developing a surface treatment that can take advantage of the urea-urethane reaction is needed. This work also showed no detrimental effect on mechanical properties due to the addition of GnPs to the PUa. Future adhesive development should continue the MDI PUa work in the lower hard segment formulation regime. Based on this work, a Group 1 adhesive can already be achieved even with neat formulations. Additional characterization and feasibility studies must be performed to fully understand the material behavior. Recall that an MDI-based system is used as a blast mitigation

coating. Adding GnPs may have additional benefits at high strain rates, where attenuation of shock waves may occur due to the placement of GnP. Finally, additional characterization work is necessary in the fatigue regime. Structural adhesives in the ground vehicle domain not only undergo static and blast loading conditions but also experience fatigue loading. Particular interest is in the crack propagation through the PUa and how the GnP interacts and impedes crack formation and growth. Through this work, a fatigue limit can be defined. This experimentation would also apply to polyurethane/urea structures made by additive manufacturing.

Although not studied in this work, the results show promise towards developing multifunctional (thermally and electrically conductive) adhesives and coatings, where further thermo-mechanical characterization is performed beyond the percolation limit of the GnPs. Here, the questions to be answered are: (i) Do the trends in mechanical properties observed in this study extend beyond the percolation point of GnP? (ii) How can these be applied to thermal or electrically conductive adhesives and coating systems? (iii) Is there a tradeoff between electrical/thermal properties and mechanical performance at high strain rates? In doing this work, the first necessary step would be to verify the percolation limit for the GnP R10-PUa. The current work (SEM characterization in Chapter 4) shows that the percolation limit of the R10 GnP is near 1.5 wt.%. The exact percolation threshold can be calculated using electrical conductivity measurements with the current formulations and varying GnP loadings.

Another aspect of PUa-GnP nanocomposites is the functionalization of the GnPs with either amines or an isocyanate functional group; in this study, the GnPs were used without modification. In future work, the GnP can be functionalized with either an isocyanate and or amine; here, the GnPs can participate in the urea-urethane reactions, forming covalent bonds between hard segments and the GnP, for the case of an isocyanate or short chain amine

functionalization, and between the soft segment and GnP, in the case of a long chain amine functionalization.

Functionalization of the GnP can occur in two locations: 1) the edge of the GnP and 2) the basal plane of the GnP. In the first choice, the edge, there are a limited number of sites to functionalize so that the GnP can participate in the PUa reaction. In the second choice, functionalization on the GnP basal plane will result in the breaking of the π-π bonds, thus decreasing the modulus of the GnP. Another way to obtain a similar result would be to pick a chemical species that can be physiosorbed with the interaction between the π-π bonds of the GnP and the hard segment. Literature has shown that chemical species with two or three aromatic species can interact in such a manner with the GnP. A new type of chain extender could be introduced to the PUa, which would react to form the hard segment while simultaneously coating the GnP surface.

As seen in this work, the reaction between the isocyanate and the amine in polyurea is extremely quick, and its mechanical performance can be tailored through its chemical constituents. These advantages give rise to the development of PUa chemistry for additive manufacturing. Here, the long-term goal would be to develop a reaction nozzle that would thoroughly mix the isocyanate prepolymer and amine blends while simultaneously allowing for the proper chemical reaction between beads in a single layer and between layers.

6.2.2 Micro-mechanical Modeling

In this work, we also developed a framework using a fractional Maxwell model to describe the viscoelastic properties of PUa. This framework gives a good description of the microstructural characteristics of PUa through the FMG parameters. In this part, the short-term goal is to further study the FMG parameters, Eo, τc, and α, by changing the isocyanate and amine type. Here, we

are looking to understand better how the FMG parameters change with various changes in chemical constituents, which will affect the phase separation of the various polyureas. Typically, TTS is used to describe single phase systems. In this work TTS, in conjunction with the TS2 shift function and the FMM was successfully applied to describe a multiphase system. This begs the question, can this modeling framework be applied to other elastomeric-based systems like rubber, which can be filled and cross-linked? Furthermore, can the modeling framework be applied to nanoscale rheology where DMA is combined with AFM to determine viscoelastic properties of smaller samples (This is relevant to failure analysis of elastomeric materials) or individual phases?

BIBLIOGRAPHY

[1] M. Zheng-Dong, W. Hui, C. Yushun, D. Rose, A. Socks, and D. Ostberg, "Designing an Innovative Composite Armor System for Affordable Ballistic Protection," *25th Army Sci. Conf.*, 2006.

[2] R. Jensen, D. Deschepper, D. Flanagan, G. Chaney, and C. Pergantis, "Adhesives : Test Method , Group Assignment , and Categorization Guide for High-Loading- Rate Applications – Preparation and Testing of Single Lap Joints (Ver . 2 . 2 , Unlimited)," 2016.

[3] M. Szycher, "Szycher's handbook of polyurethanes." CRC Press, Boca Raton, FL, 2013.

[4] J. O. Akindoyo, M. Beg, S. Ghazali, M. R. Islam, N. Jeyaratnam, and A. R. Yuvaraj, "Polyurethane types, synthesis and applications–a review," *Rsc Adv.*, vol. 6, no. 115, pp. 114453–114482, 2016.

[5] A. Das and P. Mahanwar, "A brief discussion on advances in polyurethane applications," *Adv. Ind. Eng. Polym. Res.*, vol. 3, no. 3, pp. 93–101, 2020.

[6] M. F. Sonnenschein, *Polyurethanes: Science, Technology, Markets, and Trends*. Wiley, 2020.

[7] E. Sharmin, *Polyurethane*. Rijeka: IntechOpen, 2019.

[8] C. Hepburn, *Polyurethane elastomers*. 1982.

[9] D. J. P. Ii, "Polyurea-Based Coatings," vol. 5, 2015.

[10] R. Barsoum, *History of High Strain Rate Elastomeric Polymers (HSREP) Application*. Elsevier Inc., 2015.

[11] N. Iqbal, M. Tripathi, S. Parthasarathy, D. Kumar, and P. K. Roy, "Polyurea coatings for enhanced blast-mitigation: A review," *RSC Adv.*, vol. 6, no. 111, pp. 109706–109717, 2016, doi: 10.1039/c6ra23866a.

[12] Y. He, X. Zhang, and J. Runt, "The role of diisocyanate structure on microphase separation of solution polymerized polyureas," *Polymer (Guildf).*, vol. 55, no. 3, pp. 906–913, 2014, doi: 10.1016/j.polymer.2014.01.001.

[13] A. Pangon, G. P. Dillon, and J. Runt, "Influence of mixed soft segments on microphase separation of polyurea elastomers," *Polymer (Guildf).*, vol. 55, no. 7, pp. 1837–1844, 2014, doi: 10.1016/j.polymer.2014.02.009.

[14] J. Runt, A. Pangon, A. Castagna, Y. He, and M. Grujicic, *Phase Separated Microstructure and Structure-Property Relationships of High Strain Rate Elastomeric Polyureas*. Elsevier

Inc., 2015.

[15] G. L. O'Sickey, Matthew J., Lawrey, Bruce D., Wilkes, "Structure-Property Relationships of Poly(urethane-urea)s with Ultralow Monol COntent Poly(propylene glycol) Soft Segments. III Influence of MIxed Soft Segments of Ultralow Monol Poly(propylene glycol), Poly(tetramethylene ether glycol), and Tri(propylene ," *J. Applier Polym. Sci.*, vol. 89, pp. 3520–3529, 2002.

[16] M. J. O'Sickey, B. D. Lawrey, and G. L. Wilkes, "Structure-property relationships of poly(urethane-urea)s with ultra-low monol content poly(propylene glycol) soft segments. Part II. Influence of low molecular weight polyol components," *Polymer (Guildf).*, vol. 43, no. 26, pp. 7399–7408, 2002, doi: 10.1016/S0032-3861(02)00483-4.

[17] M. J. O'Sickey, B. D. Lawrey, and G. L. Wilkes, "Structure-property relationships of poly(urethane urea)s with ultra-low monol content poly(propylene glycol) soft segments: I. Influence of soft segment molecular weight and hard segment content," *J. Appl. Polym. Sci.*, vol. 84, no. 2, pp. 229–243, 2002, doi: 10.1002/app.10168.

[18] V. V. Ginzburg, J. Bicerano, C. P. Christenson, A. K. Schrock, and A. Z. Patashinski, "Theoretical modeling of the relationship between young's modulus and formulation variables for segmented polyurethanes," *J. Polym. Sci. Part B Polym. Phys.*, vol. 45, no. 16, pp. 2123–2135, 2007, doi: 10.1002/polb.21213.

[19] C. S. L. and T. A. V., "Properties of Linear Elastomeric Polyurethanes," *J. Appl. Polym. Sci.*, vol. 10, pp. 1837–1844, 1966, [Online]. Available: http://link.springer.com/10.1007/978-3-319-59379-1%0Ahttp://dx.doi.org/10.1016/B978-0-12-420070-8.00002-7%0Ahttp://dx.doi.org/10.1016/j.ab.2015.03.024%0Ahttps://doi.org/10.1080/07352689.2018.1441103%0Ahttp://www.chile.bmw-motorrad.cl/sync/showroom/lam/es/.

[20] J. T. Koberstein and R. S. Stein, "Small-angle x-ray scattering measurements of diffuse phase-boundary thicknesses in segmented polyurethane elastomers," *J. Polym. Sci. Polym. Phys. Ed.*, vol. 21, no. 10, pp. 2181–2200, 1983.

[21] J. T. Leung, Louis M, Koberstein, "Small-Angle Scattering Analysis of Hard-Microdomain Structure and Microphase Mixing in Polyurethane Elastomers.," *J. Polym. Sci. Polym. Phys. Ed.*, vol. 23, pp. 1883–1913, 1985, [Online]. Available: http://link.springer.com/10.1007/978-3-319-59379-1%0Ahttp://dx.doi.org/10.1016/B978-0-12-420070-8.00002-7%0Ahttp://dx.doi.org/10.1016/j.ab.2015.03.024%0Ahttps://doi.org/10.1080/07352689.2018.1441103%0Ahttp://www.chile.bmw-motorrad.cl/sync/showroom/lam/es/.

[22] C. W. Macosko *et al.*, "Dynamics of (Micro)phase Separation during Fast, Bulk Copolymerization: Some Synchrotron SAXS Experiments," *Macromolecules*, vol. 24, pp. 2883–2889, 1991, doi: 10.1021/ma00010a038.

[23] R. K. Agrawal and L. T. Drzal, “Adhesion mechanisms of polyurethanes to glass surfaces i. structure-property relationships in polyurethanes and their effects on adhesion to glass,” *J. Adhes.*, vol. 54, no. 1–4, pp. 79–102, 1995, doi: 10.1080/00218469508014383.

[24] R. K. Agrawal and L. T. Drzal, “Adhesion mechanisms of polyurethanes to glass surfaces. Part II. Phase separation in polyurethanes and its effects on adhesion to glass,” *J. Adhes. Sci. Technol.*, vol. 9, no. 10, pp. 1381–1400, 1995, doi: 10.1163/156856195X00068.

[25] R. K. Agrawal and L. T. Drzal, “Adhesion mechanisms of polyurethanes to glass surfaces. III. Investigation of possible physico-chemical interactions at the interphase,” *J. Adhes.*, vol. 55, no. 3–4, pp. 221–243, 1996, doi: 10.1080/00218469608009949.

[26] M. W. Matsen and F. S. Bates, “Origins of complex self-assembly in block copolymers,” *Macromolecules*, vol. 29, no. 23, pp. 7641–7644, 1996, doi: 10.1021/ma960744q.

[27] V. V Ginzburg, J. Bicerano, C. P. Christenson, A. K. Schrock, and A. Z. Patashinski, “Theoretical Modeling of the Relationship between Young’s Modulus and Formulation Variables for Segmented Polyurethanes,” *J. Polym. Sci. Part B Polym. Phys.*, vol. 45, pp. 2123–2135, 2007, doi: 10.1002/polb.

[28] N. Iqbal, M. Tripathi, S. Parthasarathy, D. Kumar, and P. K. Roy, “Polyurea spray coatings: Tailoring material properties through chemical crosslinking,” *Prog. Org. Coatings*, vol. 123, no. April, pp. 201–208, 2018, doi: 10.1016/j.porgcoat.2018.07.005.

[29] N. Iqbal, M. Tripathi, S. Parthasarathy, D. Kumar, and P. K. Roy, “Tuning the properties of segmented polyurea by regulating soft-segment length,” *J. Appl. Polym. Sci.*, vol. 135, no. 21, pp. 1–8, 2018, doi: 10.1002/app.46284.

[30] N. Iqbal, P. K. Sharma, D. Kumar, and P. K. Roy, “Protective polyurea coatings for enhanced blast survivability of concrete,” *Constr. Build. Mater.*, vol. 175, pp. 682–690, 2018, doi: 10.1016/j.conbuildmat.2018.04.204.

[31] N. Iqbal, D. Kumar, and P. K. Roy, “Emergence of time-dependent material properties in chain extended polyureas,” *J. Appl. Polym. Sci.*, vol. 135, no. 40, pp. 1–8, 2018, doi: 10.1002/app.46730.

[32] N. Iqbal, M. Tripathi, S. Parthasarathy, D. Kumar, and P. K. Roy, “Aromatic versus Aliphatic: Hydrogen Bonding Pattern in Chain-Extended High-Performance Polyurea,” *ChemistrySelect*, vol. 3, no. 7, pp. 1976–1982, 2018, doi: 10.1002/slct.201703176.

[33] D. Fragiadakis, R. Gamache, R. B. Bogoslovov, and C. M. Roland, “Segmental dynamics of polyurea: Effect of stoichiometry,” *Polymer (Guildf).*, vol. 51, no. 1, pp. 178–184, 2010, doi: 10.1016/j.polymer.2009.11.028.

[34] J. Yi, M. C. Boyce, G. F. Lee, and E. Balizer, “Large deformation rate-dependent stress-strain behavior of polyurea and polyurethanes,” *Polymer (Guildf).*, vol. 47, no. 1, pp. 319–

329, 2006, doi: 10.1016/j.polymer.2005.10.107.

[35] S. S. Sarva, S. Deschanel, M. C. Boyce, and W. Chen, “Stress-strain behavior of a polyurea and a polyurethane from low to high strain rates,” *Polymer (Guildf).*, vol. 48, no. 8, pp. 2208–2213, 2007, doi: 10.1016/j.polymer.2007.02.058.

[36] R. G. Barsoum, Ed., *Elastomeric Polymers with High Rate Sensitivity, Applications in Blast, Shockwave and Penetration Mechanics*, 1rst ed. Elsevier, 2015.

[37] A. . Frank, “Guidelines for Using TTS,” no. July. TA Intsruments, pp. 1–3, 2005.

[38] U. Gedde, *Polymer Physics*, 1st ed. London: Chapman and Hall, 1995.

[39] V. V. Ginzburg, “A simple mean-field model of glassy dynamics and glass transition,” *Soft Matter*, vol. 16, no. 3, pp. 810–825, 2020, doi: 10.1039/c9sm01575b.

[40] J. D. J. Rathinaraj, G. H. McKinley, and B. Keshavarz, “Incorporating rheological nonlinearity into fractional calculus descriptions of fractal matter and multi-scale complex fluids,” *Fractal Fract.*, vol. 5, no. 4, p. 174, 2021.

[41] K. Holzworth, Z. Jia, A. V. Amirkhizi, J. Qiao, and S. Nemat-Nasser, “Effect of isocyanate content on thermal and mechanical properties of polyurea,” *Polymer (Guildf).*, vol. 54, no. 12, pp. 3079–3085, 2013, doi: 10.1016/j.polymer.2013.03.067.

[42] M. Baumgaertel and H. H. Winter, “Determination of discrete relaxation and retardation time spectra from dynamic mechanical data,” *Rheol. Acta*, vol. 28, no. 6, pp. 511–519, 1989, doi: 10.1007/BF01332922.

[43] P. Sollich, “Rheological constitutive equation for a model of soft glassy materials,” *Phys. Rev. E - Stat. Physics, Plasmas, Fluids, Relat. Interdiscip. Top.*, vol. 58, no. 1, pp. 738–759, 1998, doi: 10.1103/PhysRevE.58.738.

[44] A. Jaishankar and G. H. McKinley, “Power-law rheology in the bulk and at the interface: quasi-properties and fractional constitutive equations,” *Proc. R. Soc. A Math. Phys. Eng. Sci.*, vol. 469, no. 2149, p. 20120284, 2013.

[45] J. R. Potts, D. R. Dreyer, C. W. Bielawski, and R. S. Ruoff, “Graphene-based polymer nanocomposites,” *Polymer (Guildf).*, vol. 52, no. 1, pp. 5–25, 2011, doi: 10.1016/j.polymer.2010.11.042.

[46] X. Zhao, Q. Zhang, D. Chen, and P. Lu, “Enhanced mechanical properties of graphene-based polyvinyl alcohol composites,” *Macromolecules*, vol. 43, no. 5, pp. 2357–2363, 2010, doi: 10.1021/ma902862u.

[47] J. . Halpin, J.C., Kardos, “The Halpin-Tsai Equations: A review,” *Polym. Eng. Sci.*, vol. 16, no. 5, pp. 344–352, 1976, [Online]. Available: http://link.springer.com/10.1007/978-3-

319-59379-1%0Ahttp://dx.doi.org/10.1016/B978-0-12-420070-8.00002-7%0Ahttp://dx.doi.org/10.1016/j.ab.2015.03.024%0Ahttps://doi.org/10.1080/07352689.2018.1441103%0Ahttp://www.chile.bmw-motorrad.cl/sync/showroom/lam/es/.

[48] S. K. Yadav and J. W. Cho, "Functionalized graphene nanoplatelets for enhanced mechanical and thermal properties of polyurethane nanocomposites," *Appl. Surf. Sci.*, vol. 266, pp. 360–367, 2013, doi: 10.1016/j.apsusc.2012.12.028.

[49] S. Rana, J. W. Cho, and L. P. Tan, "Graphene-crosslinked polyurethane block copolymer nanocomposites with enhanced mechanical, electrical, and shape memory properties," *RSC Adv.*, vol. 3, no. 33, pp. 13796–13803, 2013, doi: 10.1039/c3ra40711j.

[50] X. Qian, L. Song, Q. Tai, Y. Hu, and R. K. K. Yuen, "Graphite oxide/polyurea and graphene/polyurea nanocomposites: A comparative investigation on properties reinforcements and mechanism," *Compos. Sci. Technol.*, vol. 74, pp. 228–234, 2013, doi: 10.1016/j.compscitech.2012.11.018.

[51] X. Qian *et al.*, "One-pot surface functionalization and reduction of graphene oxide with long-chain molecules: Preparation and its enhancement on the thermal and mechanical properties of polyurea," *Chem. Eng. J.*, vol. 236, pp. 233–241, 2014, doi: 10.1016/j.cej.2013.09.061.

[52] G. Toader *et al.*, "New polyurea MWCNTs nanocomposite films with enhanced mechanical properties," *J. Appl. Polym. Sci.*, vol. 134, no. 28, pp. 1–7, 2017, doi: 10.1002/app.45061.

[53] D. J. P. Ii, "Technical Bulletin. Method for Calculation of Polyurea Spray Elastomer Systems." Primeaus Associates LLC.

[54] D. A. Tzelepis *et al.*, "Experimental and modeling studies of IPDI-based polyurea elastomers – The role of hard segment fraction," *J. Appl. Polym. Sci.*, vol. 140, no. 10, pp. 1–15, 2023, doi: 10.1002/app.53592.

[55] N. Samson, F. Mechin, and J. Pascault, "Relationships between synthesis and mechanical properties of new polyurea materials," *J. Appl. Polym. Sci.*, vol. 65, no. 12, pp. 2265–2280, 1997, doi: 10.1002/(sici)1097-4628(19970919)65:12<2265::aid-app2>3.3.co;2-s.

[56] Q. Zhou, L. Cao, Y. Yao, Z. Ouyang, Z. Su, and C. Xiaonong, "Investigation of the CUring Process of Spray Polyurea Elastomer by FTIR, DSC, and DMA," *J. Appl. Polym. Sci.*, vol. 125, no. 5, pp. 3695–3701, 2012, doi: 10.1002/app.36674.

[57] N. Iqbal, D. Kumar, and P. K. Roy, "Understanding the role of isocyanate dilution toward spraying of polyurea," *J. Appl. Polym. Sci.*, vol. 135, no. 9, pp. 1–8, 2018, doi: 10.1002/app.45869.

[58] C. P. Christenson *et al.*, "Model MDI/butanediol polyurethanes: molecular structure,

morphology, physical and mechanical properties," *J. Polym. Sci. Part B Polym. Phys.*, vol. 24, no. 7, pp. 1401–1439, 1986.

[59] K. Whitcomb, "Measurement of Glass Transition Temperatures by Dynamic Mechanical Analysis and Rheology." Accessed: Aug. 08, 2022. [Online]. Available: https://www.tainstruments.com/pdf/literature/RH100.pdf.

[60] Z. S. Petrović and J. Ferguson, "Polyurethane elastomers," *Prog. Polym. Sci.*, vol. 16, no. 5, pp. 695–836, 1991, doi: https://doi.org/10.1016/0079-6700(91)90011-9.

[61] C. G. Seefried, J. V. Koleske, and F. E. Critchfield, "Thermoplastic urethane elastomers. I. Effects of Soft-Segment Variations.," *J. Appl. Polym. Sci.*, vol. 19, no. 9, pp. 2493–2502, 1975, doi: 10.1002/app.1975.070190913.

[62] C. G. Seefried, J. V. Koleske, and F. E. Critchfield, "Thermoplastic urethane elastomers. II. Effects of variations in hard-segment concentration," *J. Appl. Polym. Sci.*, vol. 19, no. 9, pp. 2503–2513, 1975, doi: 10.1002/app.1975.070190913.

[63] C. G. Seefried, J. V. Koleske, and F. E. Critchfield, "Thermoplastic urethane elastomers. III. Effects of variations in Isocyanate Structure," *J. Appl. Polym. Sci.*, vol. 19, no. 9, pp. 3185–3191, 1975, doi: 10.1002/app.1975.070190913.

[64] X. Chen, X. Wang, and D. Fang, "A review on C1s XPS-spectra for some kinds of carbon materials," *Fullerenes Nanotub. Carbon Nanostructures*, vol. 28, no. 12, pp. 1048–1058, 2020, doi: 10.1080/1536383X.2020.1794851.

[65] Y. C. G. Kwan, G. M. Ng, and C. H. A. Huan, "Identification of functional groups and determination of carboxyl formation temperature in graphene oxide using the XPS O 1s spectrum," *Thin Solid Films*, vol. 590, pp. 40–48, 2015, doi: 10.1016/j.tsf.2015.07.051.

[66] M. Haq, R. Burgueño, A. K. Mohanty, and M. Misra, "Hybrid bio-based composites from blends of unsaturated polyester and soybean oil reinforced with nanoclay and natural fibers," *Compos. Sci. Technol.*, vol. 68, no. 15–16, pp. 3344–3351, 2008, doi: 10.1016/j.compscitech.2008.09.007.

[67] M. Haq, "HYBRID HIERARCHICAL BIO-BASED MATERIALS : DEVELOPMENT AND CHARACTERIZATION THROUGH EXPERIMENTATION AND COMPUTATIONAL SIMULATIONS By Mahmoodul Haq A DISSERTATION Submitted to Michigan State University in partial fulfillment of the requirements for the degr," Michigan State University, 2009.

[68] M. Haq, R. Burgueño, A. K. Mohanty, and M. Misra, "Hybrid bio-based composites from UPE/EML blends, natural fibers, and nanoclay," *Macromol. Mater. Eng.*, vol. 299, no. 11, pp. 1306–1315, 2014, doi: 10.1002/mame.201300473.

[69] D. A. Tzelepis, A. Khoshnevis, M. Zayernouri, and V. V. Ginzburg, "Polyurea–Graphene

Nanocomposites—The Influence of Hard-Segment Content and Nanoparticle Loading on Mechanical Properties," *Polymers (Basel).*, vol. 15, no. 22, p. 4434, 2023, doi: 10.3390/polym15224434.

[70] D. Ionita, M. Cristea, and C. Gaina, "Prediction of polyurethane behaviour via time-temperature superposition: Meanings and limitations," *Polym. Test.*, vol. 83, p. 106340, 2020.

[71] H. Vogel, "Das temperaturabhängigkeitsgesetz der viskosität von flüssigkeiten," *Phys. Z.*, vol. 22, pp. 645–646, 1921.

[72] G. S. Fulcher, "Analysis of recent measurements of the viscosity of glasses," *J. Am. Ceram. Soc.*, vol. 8, no. 6, pp. 339–355, 1925.

[73] G. Tammann and W. Hesse, "The dependence of viscosity upon the temperature of supercooled liquids," *Z. Anorg. Allg. Chem*, vol. 156, pp. 245–257, 1926.

[74] M. L. Williams, R. F. Landel, and J. D. Ferry, "The temperature dependence of relaxation mechanisms in amorphous polymers and other glass-forming liquids," *J. Am. Chem. Soc.*, vol. 77, no. 14, pp. 3701–3707, 1955.

[75] J. Bicerano, *Prediction of polymer properties*, 3rd ed. Boca Raton, FL: CRC Press, 2002.

[76] J. Zhao and G. B. McKenna, "The apparent activation energy and dynamic fragility of ancient ambers," *Polymer (Guildf).*, vol. 55, no. 9, pp. 2246–2253, 2014, doi: 10.1016/j.polymer.2014.03.004.

[77] H. Yoon and G. B. McKenna, "Testing the paradigm of an ideal glass transition: Dynamics of an ultrastable polymeric glass," *Sci. Adv.*, vol. 4, no. 12, p. eaau5423, 2018.

[78] H. Chen, L. R. Hart, W. Hayes, and C. R. Siviour, "Mechanical characterisation and modelling of a thermoreversible superamolecular polyurethane over a wide range of rates," *Polymer (Guildf).*, vol. 221, Apr. 2021, doi: 10.1016/j.polymer.2021.123607.

[79] A. D. Drozdov, "Fractional differential models in finite viscoelasticity," *Acta Mech.*, vol. 124, no. 1, pp. 155–180, 1997.

[80] J. L. Suzuki, M. Zayernouri, M. L. Bittencourt, and G. E. Karniadakis, "Fractional-order uniaxial visco-elasto-plastic models for structural analysis," *Comput. Methods Appl. Mech. Eng.*, vol. 308, pp. 443–467, 2016.

[81] M. D'Elia, M. Zayernouri, M. Gulian, and J. Suzuki, *Fractional Modeling in Action: A Survey of Nonlocal Models for Subsurface Transport, Turbulent Flows, and Anomalous Materials*. 2021.

[82] G. B. McKenna and S. L. Simon, "50th Anniversary Perspective: Challenges in the Dynamics and Kinetics of Glass-Forming Polymers," *Macromolecules*, vol. 50, no. 17, pp.

6333–6361, 2017, doi: 10.1021/acs.macromol.7b01014.

[83] A. Jaishankar and G. H. McKinley, “A fractional K-BKZ constitutive formulation for describing the nonlinear rheology of multiscale complex fluids,” *J. Rheol. (N. Y. N. Y).*, vol. 58, no. 6, pp. 1751–1788, 2014, doi: 10.1122/1.4892114.